A Method to Improve the Neutrino Energy Reconstruction in LArTPCs

Inauguraldissertation
der Philosophisch-naturwissenschaftlichen Fakultät
der Universität Bern

vorgelegt von

Patrick Koller

von Hochdorf LU

Leiter der Arbeit
Prof. Dr. M. Weber

Albert Einstein Centre for Fundamental Physics
Laboratory for High Energy Physics
Physics Institute

A Method to Improve the Neutrino Energy Reconstruction in LArTPCs

Inauguraldissertation
der Philosophisch-naturwissenschaftlichen Fakultät
der Universität Bern

vorgelegt von

Patrick Koller

von Hochdorf LU

Leiter der Arbeit
Prof. Dr. M. Weber

Albert Einstein Centre for Fundamental Physics
Laboratory for High Energy Physics
Physics Institute

Von der Philosophisch-naturwissenschaftlichen Fakultät angenommen.

Bern, 25th November 2021

Der Dekan:
Prof. Dr. Z. Balogh

Abstract

Precision measurements of the neutrino oscillation parameters allow to determine the potential violation of CP-symmetry in the leptonic sector. If the violation of CP-symmetry in the leptonic sector can be experimentally confirmed, this could become the preferred explanation in the Standard Model for the matter-antimatter asymmetry of the universe. The Deep Underground Neutrino Experiment (DUNE), which is being built by the Fermi National Accelerator Laboratory (FNAL) in the USA, aims to perform these measurements of the neutrino oscillation parameters using Liquid Argon Time Projection Chamber (LArTPC) detectors. Four massive multi-kt Far Detectors (FDs) are deployed together with a Near Detector (ND) that uses the same detector technology as the FDs. As a consequence of the high-intensity neutrino beam and the short distance to the neutrino source the ND will need ability to disentangle multiple overlapping events that happen within a single readout cycle. This is achieved with a LArTPC following the ArgonCube concept, which was developed at the University of Bern. The ArgonCube concept divides the detector volume into a number of identical, optically isolated and electrically isolated Time Projection Chamber (TPC) modules. The optical isolation reduces the pile-up of the scintillation light and allows for better localization of light signals.

The ND will need to measure the neutrino energy because neutrino oscillations occur as a function of the neutrino energy. Neutrons emerging from the neutrino interaction vertex can carry away more than 25 % of the neutrino energy, which is missed by applying the calorimetric method, because neutral particles are not reconstructed in LArTPCs. I have determined the bias and the uncertainty of the reconstructed neutrino energy due missed primary neutrons, based on simulations using the GENIE event generator. At the DUNE beam spectrum, primary neutrons will be involved in about 80 % of the neutrino-argon interactions. In those events with primary neutrons involved, a mean energy corresponding to $\sim 10\,\%$ of the parent neutrino's kinetic energy is carried away by primary neutrons, and the relative uncertainty on the reconstructed neutrino energy can exceed 13 %. I have developed a method to identify neutrons in LArTPCs by secondary charged particles that are produced if a neutron interacts with an argon nucleus. These neutrons appear as detached energy deposits, which prevents a trivial assignment to the correct interaction vertex, given the high event multiplicity at the ND site. Therefore, I further developed a method to assign detached energy deposits to neutrino interaction verices, exploiting the fast response of the light-readout systems. With a timing resolution at the $\mathcal{O}(1)$ ns, the light-readout systems easily allow to separate the light signals of individual events, which have a mean separation time of 179 ns. If the presented methods are used to veto neutrino interactions with primary neutrons, then the respective uncertainty on the reconstructed neutrino energy can be reduced to $< 10\,\%$.

Contents

List of Figures

List of Tables

Acronyms

3DST 3D Scintillator Tracker

AGS Alternating Gradient Synchrotron

ALICE A Large Ion Collider Experiment

ArCLight ArgonCube Light readout system

ASIC Application-Specific Integrated Circuit

BNL Brookhaven National Laboratory

CC Charged Current

CERN European Organization for Nuclear Research

CoG Center of Gravity

COH Coherent

DAQ Data Acquisition

DIS Deep Inelastic Scattering

DONUT Direct Observation of the Nu Tau

DUNE Deep Underground Neutrino Experiment

DUNE-PRISM DUNE Precision Reaction-Independent Spectrum Measurement

ECAL Electromagnetic Calorimeter

EM ElectroMagnetic

ES Elastic Scattering

FD Far Detector

FHC Forward Horn Current

FNAL Fermi National Accelerator Laboratory

FSI Final State Interactions

FV Fiducial Volume

GAr Gaseous Argon

GGD General Geometry Description

Hyper-K Hyper-KamiokaNDE

IO Inverted Ordering

JINR Joint Institute for Nuclear Research

J-PARC Japan Proton Accelerator Research Complex

Kamiokande Kamioka Nucleon Decay Experiment

KamLAND Kamioka Liquid scintillation AntiNeutrino Detector

KATRIN Karlsruhe Tritium Neutrino Experiment

LAr Liquid Argon

LArTPC Liquid Argon Time Projection Chamber

LBNF Long-Baseline Neutrino Facility

LBNL Lawrence Berkeley National Laboratory

LCM Light Collection Module

LEP Large Electron-Positron Collider

LSND Liquid Scintillator Neutrino Detector

LUT Look-Up-Table

MCS Multiple Coulomb Scattering

ME Medium Energy

MEC Meson Exchange Current

MI Main Injector

MicroBooNE Micro Booster Neutrino Experiment

MINERνA Main Injector Experiment for ν-A

MINOS Main Injector Neutrino Oscillation Search

MIP Minimum Ionising Particle

MSW Mikheyev-Smirnov-Wolfenstein

NC Neutral Current

ND Near Detector

NO Normal Ordering

NOνA NuMI Off-Axis ν_e Appearance

NuMI Neutrinos at Main Injector

OPERA Oscillation Project with Emulsion-tRacking Apparatus

PCB Printed Circuit Board

PDE Photon Detection Efficiency

PID Particle Identification

PIP-II Proton Improvement Plan-II

PMNS Pontecorvo-Maki-Nakagawa-Sakata

PMT PhotoMultiplier Tube

POT Protons On Target

PP Proton-Proton

QE Quasi-Elastic

RES Resonant

RHC Reversed Horn Current

RMS Root Mean Square

ROI Region Of Interest

SAND System for on-Axis Neutrino Detection

SBN Short-Baseline Neutrino

SiPM Silicon PhotoMultiplier

SLAC Stanford Linear Accelerator Center

SNO Sudbury Neutrino Observatory

SNU Solar Neutrino Unit

SSM Standard Solar Model

SURF Sanford Underground Research Facility

T2K Tokai To Kamioka

TPB TetraPhenyl Butadiene

TPC Time Projection Chamber

VUV Vacuum UltraViolet

WLS WaveLength Shifter

1. Introduction

In 1930, Wolfgang Pauli postulated a new, electrically neutral spin-$\frac{1}{2}$ particle with a mass comparable to that of the electron [1]. His intention was to save the law of energy conservation questioned by the continuous beta spectrum of $^{226}_{88}$Ra, that was observed by James Chadwick 16 years earlier [2, 3]. None of the by then known fundamental forces, neither electromagnetism nor gravitation, were capable to explain the existence of a particle with such properties. As a consequence, Enrico Fermi elaborated a quantitative theory of β-decay and weak interaction, which assumes the existence of such a particle, until the end of 1933 [4]. He named the particle, that he saw as a small version of the also electrically neutral neutron, a *neutrino*. Ultimately, the (anti)neutrino was discovered by Clyde Cowan and Frederick Reines in 1956, when they observed the absorption of antineutrinos produced in nuclear reactors in cadmium chloride [5]. Many neutrino experiments have been built since then and scientists from all over the world have contributed to understand the puzzling properties of the neutrinos. In Chapter 2, I will discuss the detection principles and results of historical experiments that essentially contributed to todays understanding of the neutrino.

Today we know that there are three neutrino types in terms of lepton flavor; electron, muon and tau neutrinos. Each flavor-type neutrino is a superposition of three massive neutrino eigenstates, whereby the fractional composition of the neutrino by means of massive eigenstates determines the probability to observe the neutrino in a specific flavor state [6]. That composition can change as neutrinos travel through space-time, and consequently, also the probability to observe the neutrino in a specific flavor state can change [6]. This phenomenon of neutrino flavor transitions is known as neutrino *oscillation*. As a consequence of neutrino oscillation, the neutrinos are different to the charged leptons as they violate the conservation of lepton flavor.

Neutrino oscillations are characterized by a set of constant oscillation parameters, and occur as a function of the neutrino energy [7]. More properly, they occur as a function of neutrino proper time, which is equal to L/E in the lab frame in an ultra-relativistic approximation. One of the oscillation parameters is a CP-violating phase, and measuring that phase with neutrino-oscillation experiments might reveal the violation of CP-symmetry in the leptonic sector [8]. If CP violation in the leptonic sector can be experimentally confirmed, this could become the preferred explanation in the Standard Model for the matter-antimatter asymmetry of the universe [9].

Another yet unsolved problem is that of neutrino mass hierarchy. Neutrino oscillations are only possible if the masses assigned with the massive neutrino eigenstates differ from each other [10]. The squares of the mass differences, the so-called mass splittings, characterize the length over which neutrino oscillations occur, and are derived from neutrino oscillation experiments too. Measurements have shown that two out of three

neutrino masses are very close (mass splitting $\simeq 7.4 \times 10^{-5}\,\mathrm{eV}^2$), while the third neutrino mass is farther away (mass splitting $\simeq 2.5 \times 10^{-3}\,\mathrm{eV}^2$) [11]. However, the hierarchy of the absolute neutrino masses, i.e. the question of which massive neutrino eigenstate is the lightest, has no yet been solved [11]. Here, the way of how the presence of matter affects the mixing of neutrinos can be exploited to get an answer. If neutrinos travel through dense materials, the mixing between flavor and mass eigenstates is changed differently for neutrinos and antineutrinos, and whether the mixing increases or decreases depends on the mass hierarchy [10]. In order to measure these effects with experiments, artificial beams of neutrinos and antineutrinos are being sent several hundred kilometers through the Earth's crust, and the derived oscillation parameters for neutrinos and antineutrinos are then compared to determine the neutrino mass hierarchy [12]. These experiments are referred to as long-baseline neutrino-oscillation experiments. Latest results from the Tokai To Kamioka (T2K) [13] and NOνA [14] experiments favor Normal Ordering (NO) [15].

Lower bounds on absolute neutrino masses can be set by oscillation data by zeroing the lightest massive neutrino eigenstate, while upper bounds can only be set by non-oscillation neutrino experiments [16]. The sum of the neutrino masses Σm_ν is probed by precision cosmology, the effective ν_e mass m_β is probed by β decay, and the effective Majorana mass $m_{\beta\beta}$ is probed by neutrino-less double beta decay ($0\nu\beta\beta$ decay, applicable if neutrinos are Majorana fermions) [17]. $0\nu\beta\beta$ decay has never been observed, and whether the neutrino is a Dirac fermion, i.e. neutrinos and antineutrinos are different particles, or the neutrino is a Majorana fermion, i.e. neutrinos are their own antiparticles, is still an open question [18]. The Karlsruhe Tritium Neutrino Experiment (KATRIN) has reported an upper limit $m_\beta < 1.1\,\mathrm{eV}$, and plans to advance the sensitivity down to 0.2 eV (90 % CL) after 5 years of measuring [19]. The so far most stringent upper bond on absolute neutrino masses has been derived from combined cosmological observations and particle physics experiments; $\Sigma m_\nu \lesssim 0.12\,\mathrm{eV}$ (95 % CL) [20].

Two future neutrino experiments with the capabilities to measure CP violation in the leptonic sector and to determine the mass hierarchy are currently being built; Hyper-KamiokaNDE (Hyper-K) [21] in Japan and the Deep Underground Neutrino Experiment (DUNE) [22] in the USA. Hyper-K will be hosted by the Tochibora mine near Kamioka town, about 295 km away from the Japan Proton Accelerator Research Complex (J-PARC) in Tokai, Japan. The detector will be placed at a depth of 650 m and will be the largest underground water Čerenkov detector in the world. New near detectors are considered to measure the un-oscillated beam in order to predict event rates at Hyper-K and to constrain systematic uncertainties.

As a personal member of the DUNE Collaboration, I will focus my studies on the DUNE experiment, which is being built at the Fermi National Accelerator Laboratory (FNAL) in Illinois, USA, and at the Sanford Underground Research Facility (SURF) in South Dakota, USA [22]. The oscillated signal will be measured with a massive Far Detector (FD) located 1300 km from the neutrino source, and will be composed of four cryogenic 10 kt Liquid Argon Time Projection Chamber (LArTPC) detectors. The un-oscillated signal at the FD will be predicted from measurements of the un-oscillated neutrino beam. These measurements will be performed with a Near Detector (ND) located 574 m

from the neutrino source, using a LArTPC as the detector's core component [23]. A high-intensity neutrino beam combined with the massive FD will provide enough neutrino interactions to determine the CP-violating phase for 50 % of all possible values at 5σ significance after about 10 years [22]. As a consequence, the ND will detect as many as ~ 55 neutrino events per beam spill. Since the charge-readout window in the DUNE ND is on the $\mathcal{O}(10)$ times longer than the beam spill, all events within the beam spill will be seen by the charge-readout as a single image; we call that *event pile-up*.

Wire-readout Time Projection Chambers (TPCs) reconstruct 3D images from multiple 2D projections, which introduces ambiguities [24]. These ambiguities pose a serious problem if it comes to the reconstruction of overlapping events, and consequently, projective wire readouts are not suitable for environments with a high event pile-up, such as the DUNE-ND site. An novel, pixelated charge-readout system [25], that was developed for the application in environments with high event multiplicities, and that will be applied to the DUNE-ND LArTPC, will be discussed in this work. This charge-readout system will enable true-3D and unambiguous event imaging, however, it will not be able to assign detached energy deposits to neutrino interaction vertices, which is essential for a precise neutrino-energy reconstruction in Liquid Argon (LAr).

Neutrino oscillations are a function of the neutrino energy, and in order to determine the oscillation parameters in long-baseline neutrino-oscillation experiments, the neutrino flavor as well as the neutrino energy needs to be measured with both the ND and the FD. A Charged Current (CC) Quasi-Elastic (QE) neutrino interaction with a single-nucleon target follows two-body kinematics, and the neutrino energy can be reconstructed from the lepton angle and energy independent of whether the nucleon is observed or not. That does not apply for multi-nucleon targets, e.g. LAr, because of the unknown initial state of the nucleus and Final State Interactions (FSI) [8]. Here, the calorimetric method is needed to reconstruct the neutrino energy, i.e. all energies carried away by particles produced in the neutrino interaction need to be measured and summed up. Neutrons emerging from the interaction vertex can carry away more than 25 % of the neutrino energy, which is missed by applying the calorimetric method because neutral particles are not reconstructed in LArTPCs.

A method to tag neutrino events for mis-reconstructed neutrino energy due to neutrons is the goal of this work. Neutrons can interact with argon nuclei and produce secondary charged particles that are visible in LArTPCs. In the DUNE ND, these charged particles show up as detached energy deposits that can not be assigned unambiguously to a neutrino interaction vertex, because the charge-readout will see multiple events piled-up. Here, the fast scintillation light in LAr, which can be detected with a timing resolution of the $\mathcal{O}(1)$ ns, can be exploited to make the association between the detached energy deposit and the neutrino interaction vertex. Accordingly, I plan to use a combination of the charge and the light signals produced in LArTPCs to assign neutrons by indirect detection to neutrino interaction vertices.

Such a method additionally requires spatial resolution provided by the light-readout system. Therefore, an optical simulation needs to be implemented in order to derive the spatial resolution of the light-readout system, which in turn can be used for a feasibility check of the proposed method of neutron tagging. I plan to provide the output of the

optical simulation in a compact format that allows a simplified handling for further studies of the optical detector-response, and that allows for a simple integration in high-level reconstruction software.

2. History of Neutrino Oscillation and Detector Techniques

In the early 20th century, the English physicist James Chadwick studied the momentum spectrum of β-particles emitted by $^{226}_{88}$Ra and its daughters. His intent was to determine the relative intensities of the discrete energies in the line spectrum. The results of the measurements were altogether unexpected to Chadwick; despite being able to identify a few of the most intense lines, the spectrum he found was a continuous spectrum. Chadwick's account on these results was published in April 1914 and no further communication appeared. [2, 3]

The idea of the neutrino was born in 1930, when Wolfgang Pauli desperately tried to save the law of energy conservation questioned by the continuous beta spectrum observed by Chadwick 16 years earlier. In his famous letter of the 4th December 1930 addressing the "*Radioactive Ladies and Gentlemen*", Pauli postulated a new, electrically neutral spin-$\frac{1}{2}$ particle with a mass comparable to that of the electron. He had no idea to what interaction it could couple to, but was right in the assumption that in a beta decay such a particle — Pauli called it a Neutron — is emitted in addition to the electron, such that the sum of their energies is constant. [1] James Chadwick discovered the actual neutron a bit more than a year later, in January 1932, when he observed a radiation of high penetrating power emitted in the disintegration of beryllium by α-particles. [26]

In 1933, further analyzing the shape of continuous β-emission spectra, Francis Perrin estimated the mass of the particle postulated by Pauli to be much lower than the electron mass, if not even zero. [27] In the same year, Enrico Fermi named the said particle a *neutrino* and, until the end of that year, elaborated a quantitative theory of β-decay and weak interaction, which assumes the existence of the neutrino. [4] In the following year, Hans Bethe and Rudolf Peierls estimated the size of the neutrino interaction cross-section σ, a measure for their interaction probability, based on the lifetime of β-radiating nuclei, to be less than $10^{-44}\,\mathrm{cm}^2$. They concluded that, even if one assumes a very steep increase of σ with increasing neutrino energy, there was no practically possible way of observing a neutrino, not event at cosmic-ray energies. [28]

In 1954, Raymond Davis Jr. tried to detect antineutrinos from nuclear reactors with a radiochemical method suggested by Bruno Pontecorvo in 1948. He deployed tanks containing 200 L and 3900 L of carbon tetrachloride next to the Brookhaven and Savannah River nuclear reactors, in attempt to induce the reaction

$$\bar{\nu} + {}^{37}\mathrm{Cl} \quad \rightarrow \quad {}^{37}\mathrm{Ar} + \mathrm{e}^- \tag{2.1}$$

with fission product antineutrinos. Davis did not measure an increase of the reaction close to the nuclear reactors compared to locations further away, and correctly concluded that neutrinos and antineutrinos must be distinct particles [29].

In 1956, more than two decades after its prediction, Clyde Cowan and Frederick Reines succeeded in detecting a neutrino for the first time in the so called Cowan-Reines-Neutrinoexperiment at the Savannah River nuclear reactor test site in South Carolina, USA. Cowan and Reines observed the antineutrino absorption reaction

$$\overline{\nu}_{\mathrm{e}} + \mathrm{p} \quad \rightarrow \quad \mathrm{e}^{+} + \mathrm{n} \tag{2.2}$$

in two 200-liter water targets, each placed between large liquid scintillation detectors. Cadmium chloride ($CdCl_2$) was dissolved in the water targets, with cadmium being a strong absorber of thermal-energy neutrons[1]. Their experimental setup was located near a powerful production fission-reactor, which provided an electron-antineutrino flux of $1.2 \times 10^{13}\,\mathrm{cm}^{-2}\,\mathrm{s}^{-1}$. The neutrino detection principle is illustrated in Figure 2.1. The positron created in the neutrino interaction slows down and annihilates with an electron in a time short compared to the detector's 0.2 µs resolving time. The two resulting 0.5 MeV annihilation gamma-rays are detected in prompt coincidence by the two scintillation detectors on opposite sides of the water targets. The neutron created in the neutrino interaction is moderated by the water and then captured by cadmium within a few microseconds. Again, the multiple gamma rays produced in the neutron capture are detected in prompt coincidence by the scintillation detectors, yielding a characteristic delayed-coincidence count with the preceding positron gammas. These tests demonstrated that reactor-associated events occurred at the rate consistent with expectations, and that the signal was not due to neutrons or gamma rays from the reactor. [5]

In 1957, the Wu-Experiment, conducted by and named after the Chinese-American physicist Chien-Shiung Wu, showed that the weak interaction, in contrary to the electromagnetic and strong interactions, violates parity conservation. [30] In the following year, Maurice Goldhaber was able to determine the helicity of the neutrino in the so-called Goldhaber-Experiment; he found that the neutrino is a *left-handed* particle, i.e. spin vector and momentum vector have opposite direction (negative helicity). [31]

In 1962, Leon Ledermann, Melvin Schwartz and Jack Steinberger reported the existence of two kinds of neutrinos, electron neutrinos and muon neutrinos, based on their observations in the Alternating Gradient Synchrotron (AGS) Neutrino Experiment at Brookhaven National Laboratory (BNL). They measured interactions of high-energy neutrinos with matter. The neutrinos were primarily produced by pion decay,

$$\pi^{+} \quad \rightarrow \quad \mu^{+} + \nu_{\mu} \quad \text{and} \quad \pi^{-} \quad \rightarrow \quad \mu^{-} + \overline{\nu}_{\mu}, \tag{2.3}$$

and interactions were studied in spark chambers, providing the possibility to distinguish muon events from electromagnetic showers. If one assumes that $\nu_{\mathrm{e}} = \nu_{\mu}$ ($\overline{\nu}_{\mathrm{e}} = \overline{\nu}_{\mu}$), then the number of observed muon events is expected at the same order as the number of

[1] Neutrons are considered thermal at kinetic energies comparable to the thermal agitation energy at room temperature, i.e. $E \approx kT \approx 1/40\,\mathrm{eV}$.

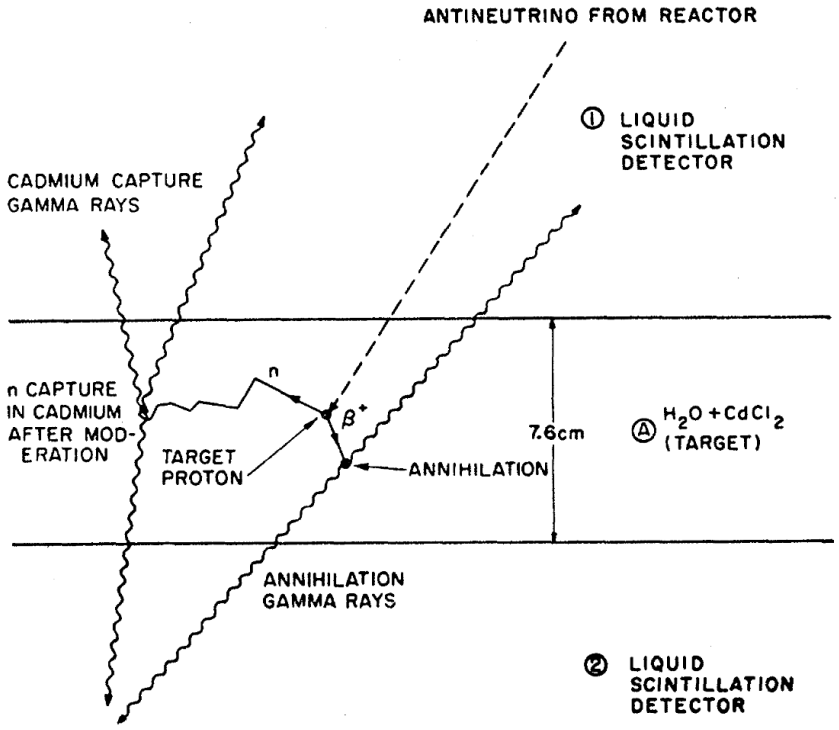

Figure 2.1.: The neutrino detection principle used in the Cowan-Reines-Neutrinoexperiment. A cadmium-chlorine doped water target is sandwiched by scintillation detectors. The positron (β^+) created in the neutrino interaction annihilates with an electron, and the resulting gamma-rays are detected in prompt coincidence by the scintillation detectors. The neutron (n) created in the neutrino interaction is moderated by water and captured by cadmium. Again, the resulting gamma rays are detected in prompt coincidence by the scintillation detectors, yielding a characteristic delayed-coincidence count with the preceding positron gammas. [5]

observed electromagnetic showers. However, Ledermann and his team measured 29 muon events but only 6 shower candidates of rather low quality, concluding that $\nu_e \neq \nu_\mu$ ($\overline{\nu}_e \neq \overline{\nu}_\mu$). [32]

In 1967, the Soviet physicist Andrei Sakharov formulated a possible explanation of matter-antimatter asymmetry in the hot model of the expanding universe by making use of effects of CP violation[2]. The theory of the expanding universe excludes the macroscopic separation of matter from antimatter; it must therefore be assumed that the universe is asymmetrical with respect to the number of particles and antiparticles (C asymmetry). According to Sakharov, the universe was neutral with respect to conserved charges but

[2]CP violation is the violation of combined C symmetry (charge symmetry) and P symmetry (parity symmetry).

C asymmetrical at the instant of its development. C asymmetry is the consequence of CP violation in the expansion of the hot universe caused by the difference between the partial probabilities of charge-conjugate reactions. [9] Up to now, CP violation has not yet been observed, but its measurement is subject of modern neutrino experiments and coming results might strengthen Sakharov's theory.

In the period 1965–1967, the Homestake Solar Neutrino Observatory was built at the Homestake Gold Mine in Lead, South Dakota, USA. Recent Standard Solar Model (SSM) calculations performed by John N. Bahcall had indicated a measurable flux of neutrinos from the decay of fusion products (predominantly ^{8}B) produced in the core of the Sun. Raymond Davis Jr. designed the experiment to measure this so-called solar neutrino flux on Earth based upon the neutrino capture reaction

$$\nu_{\mathrm{e}} + {}^{37}\mathrm{Cl} \quad \rightarrow \quad \mathrm{e}^{-} + {}^{37}\mathrm{Ar}, \tag{2.4}$$

which is sensitive to neutrinos with an energy above 0.814 MeV. The detection system was located in the Homestake Gold Mine 1478 m underground (4400 m water equivalent), which was essential to reject reactions by protons formed in cosmic-ray interactions. The neutrino detection depends upon removing the ^{37}Ar created according to Equation 2.4, and observing its decay in a proportional counter. This principle is illustrated in Figure 2.2. A cylindrical tank containing 390 000 l of liquid tetrachloroethylene (chlorine), C_2Cl_4, represents the sensitive core component of the detector. Liquid chlorine is extracted from the bottom of the tank (suction line) and pumped back to the tank trough a series of 40 eductors. The eductors aspirate helium from the gas phase above the liquid and mix it as small bubbles with the liquid in the tank, maintaining an effective equilibrium between the argon dissolved in the liquid and the argon in the gas phase. Argon is eventually extracted by circulating the helium gas from the tank through a charcoal trap. [33]

In 1968, Davis announced that the neutrino flux measured with the Homestake-Experiment was 2.56 ± 0.16 (stat) ± 0.16 (syst) Solar Neutrino Units (SNUs)[3]. This is less than one third of the SSM prediction (9.3 ± 1.3 SNUs) calculated by Bahcall. [34] Due to the large discrepancy between the measurement and the prediction this result became famous as the solar neutrino problem, which was not solved until 2002.

In 1975, Martin Perl et al. discovered the tau lepton (or tauon) at the Stanford Linear Accelerator Center (SLAC). The tauon is the heaviest of the three known leptons and charged counterpart of the, at that time not yet discovered, tau neutrino. [35, 36]

In 1988, the Kamiokande-II Collaboration reported on a deficit of the atmospheric muon-neutrino flux measured with the Kamioka Nucleon Decay Experiment (Kamiokande) detector in the Mozumi Mine in Kamioka, Japan. [37] Three years later, in 1991, the anomaly was confirmed by measurements performed with the IMB-3 detector located in a salt mine in Ohio, USA. [38] Both detectors were multi-kt water Čerenkov detectors originally designed for proton decay searches. In this type of detector, charged particles are detected via Čerenkov radiation, which is emitted if the particle's velocity v is greater than the speed of light in the respective medium c/n, where c is the speed of light in vacuum and n the refractive index of the medium. Čerenkov radiation is emitted

[3] One Solar Neutrino Unit corresponds to one interaction per 10^{36} target atoms per second.

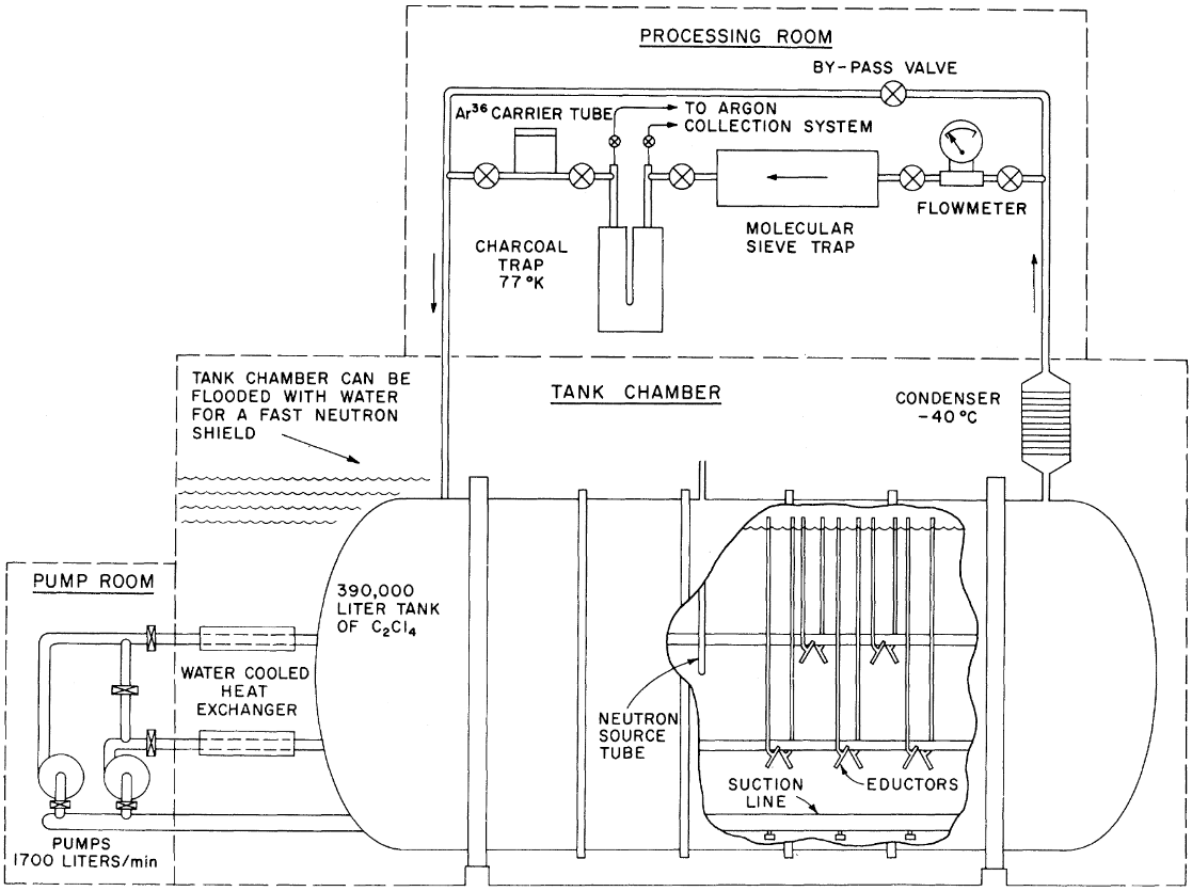

Figure 2.2.: The neutrino detection principle used in the Homestake-Experiment. A cylindrical tank containing 390 000 l of liquid tetrachloroethylene (chlorine), C_2Cl_4, represents the sensitive core component of the detector. Liquid chlorine is extracted from the bottom of the tank (suction line) and pumped back to the tank trough a series of 40 eductors. The eductors aspirate helium from the gas phase above the liquid and mix it as small bubbles with the liquid in the tank, maintaining an effective equilibrium between the argon dissolved in the liquid and the argon in the gas phase. Argon is eventually extracted by circulating the helium from the tank through a charcoal trap. [33]

cone-shaped around the particle's trajectory with a half-opening angle θ_c, which can be calculated from the relation

$$\cos(\theta_c) = \frac{c}{n(\lambda)v}. \tag{2.5}$$

Here, λ denotes the wavelength of the emitted photons. The total number of photons N emitted along a path length x can be calculated by integrating over the wavelength of the emitted photons,

$$\frac{dN}{dx} = 2\pi\alpha z^2 \int_{\lambda_1}^{\lambda_2} \left(\frac{\sin(\theta_c(\lambda))}{\lambda}\right)^2 d\lambda, \tag{2.6}$$

where α is the fine-structure constant and z the electric charge of the particle. Direction, momentum and type of the incident particle as well as the interaction time can be determined by analyzing the ring-like photon signal with light detectors covering the edges of the active medium. Neutrinos can be detected indirectly through the charged leptons $\ell = \mathrm{e}, \mu, \tau$ produced in CC interactions

$$\nu_\ell + \mathrm{n} \quad \rightarrow \quad \ell^- + \mathrm{p} \tag{2.7}$$

and

$$\bar{\nu}_\ell + \mathrm{p} \quad \rightarrow \quad \ell^+ + \mathrm{n}, \tag{2.8}$$

given the neutrino energy is large enough to provide the respective lepton mass. In addition, neutrinos of any lepton family can scatter elastically off the shell electrons of the target medium, according to the interaction

$$\overset{(-)}{\nu}_\ell + \mathrm{e}^- \quad \rightarrow \quad \overset{(-)}{\nu}_\ell + \mathrm{e}^-. \tag{2.9}$$

The recoiling electron can also be detected by Čerenkov radiation if the energy transferred by the neutrino is large enough. Protons produced in the neutrino Neutral Current (NC) interaction

$$\overset{(-)}{\nu}_\ell + {}^{16}_{8}\mathrm{O} \quad \rightarrow \quad \overset{(-)}{\nu}_\ell + {}^{15}_{7}\mathrm{N} + \mathrm{p} + \gamma \tag{2.10}$$

are below Čerenkov energy-threshold, for atmospheric neutrino energies. However, NC interactions can still be detected by measuring the de-excitation photons emitted by the residual target nuclei, or the photons emitted after the capture of a knocked-out neutron [39]:

$$\overset{(-)}{\nu}_\ell + {}^{16}_{8}\mathrm{O} \quad \rightarrow \quad \overset{(-)}{\nu}_\ell + {}^{15}_{8}\mathrm{O} + \mathrm{n} + \gamma. \tag{2.11}$$

Atmospheric neutrinos are a decay product of mesons produced by cosmic rays striking the atmosphere. While the atmospheric electron-neutrino flux observed with the experiments mentioned above was in good agreement with theoretical predictions, the measured atmospheric muon-neutrino flux was well below the expectation. The result became famous as the atmospheric neutrino problem.

Also in 1991, Kamiokande-II, an acronym for the Kamiokande in its second version, confirmed the solar neutrino problem. The collaboration performed directional measurements of ^{8}B solar neutrinos by neutrino-electron Elastic Scattering (ES). The directional

correlation with the Sun and the consistency of the differential electron energy distribution in shape and energy with that from ^{8}B decay confirmed the SSM. However, the measured solar neutrino flux was 0.46 ± 0.05 (stat) ± 0.06 (syst) times the prediction of Bahcall, and was consistent with the results from the Homestake-Experiment. [40]

In 1989, the total number of light neutrino families (flavors) was determined by the precise measurement of the Z-boson line shape at the Large Electron-Positron Collider (LEP)[4], operated by the European Organization for Nuclear Research (CERN). It was found that there are three neutrino families, light in terms of a neutrino mass less than half of the Z-boson mass. [41]

In 1998, the Super-Kamiokande Collaboration published measurements of the ratio between μ-like and e-like atmospheric neutrinos in the multi-GeV range, and the respective zenith-angle dependence. The measurements were performed with the Super-Kamiokande detector, a 50 kt water Čerenkov detector equipped with more than 13 000 PhotoMultiplier Tubes (PMTs) and located 1000 m underground (2700 m water equivalent) in the Mozumi Mine close to the Kamiokande detector. The total measured ratio (ν_μ/ν_e) was by a factor 0.66 ± 0.06 (stat) ± 0.08 (syst) lower than the expectation from simulations ($= 2$). Regarding the zenith-angle, the ratio of the number of upward-going to downward-going μ-like events was found to be $0.52^{+0.07}_{-0.06}$ (stat) ± 0.01 (syst) while the same ratio for the e-like events was consistent with unity. The collaboration concluded that the relative deficit of upward-going μ-like events from neutrinos that traveled a long distance through the Earth suggests the disappearance of ν_μ through neutrino oscillations. [42, 43]

Although the result provided a potential solution to the atmospheric neutrino problem, it was not yet a proof for neutrino oscillations. At Earth-scale baselines, muon neutrinos predominantly oscillate into tau neutrinos. The Super-Kamiokande detector was not sensitive to NC interactions but only to CC interactions, and consequently not able to measure tau neutrinos. In the NC interaction, the weak force is mediated by a neutral boson, Z^0, while in the CC interaction, the weak force is mediated by a charged boson, W^+ or W^-, as depicted by the Feynman diagrams shown in Figure 2.3. In the CC

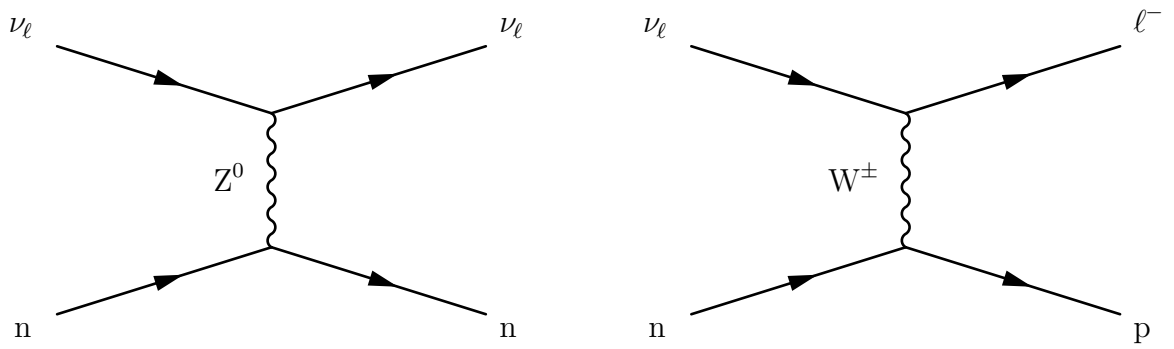

Figure 2.3.: NC neutrino-nucleus interaction (left) and CC neutrino-nucleus interaction (right). In the CC interaction, the neutrino needs to provide enough energy to create the respective lepton mass.

[4]Measurements were performed by the MARKII, L3, ALEPH, OPAL and DELPHI experiments [41].

interaction, the neutrino needs to provide enough energy to create the respective lepton mass. The CC interaction cross-section for ν_τ is greatly suppressed at low energies due to the large mass of the tauon ($1777\,\mathrm{MeV/c^2}$) and results in an energy threshold of 3.5 GeV. Furthermore, the tauon has a mean lifetime of 2.9×10^{-19} s and it decays very quickly after production. Because of these limitations, Super-Kamiokande was not able to measure tau neutrinos at that time. [44]

In 2000, the tau neutrino, predicted after the discovery of the tau lepton in 1975, was measured for the first time by the Direct Observation of the Nu Tau (DONUT) experiment at the FNAL in Illinois, USA. At neutrino energies used in the experiment, the produced tauon typically decays within 2 mm from its creation point into a lighter lepton or meson. Accordingly, the signal produced by a ν_τ interaction is a track with a kink. The interactions were observed with so-called emulsion detectors (stainless steel sheets interleaved with emulsion plates) which were able to provide the required tracking resolution. [45]

Finally, in 2002, the Sudbury Neutrino Observatory (SNO) was able to solve the solar neutrino problem. SNO is a spherical water Čerenkov detector located at a depth of 2100 m (6010 m water equivalent) in the Creighton Mine near Sudbury in Ontario, Canada. The detector was filled with heavy water (D_2O) and equipped with 9456 PMTs. It was sensitive to ^{8}B solar neutrinos through the reactions

$$\nu_\mathrm{e} + \mathrm{d} \quad \rightarrow \quad \mathrm{p} + \mathrm{p} + \mathrm{e}^- \qquad \text{(CC)}, \tag{2.12}$$

$$\nu_\ell + \mathrm{d} \quad \rightarrow \quad \mathrm{p} + \mathrm{n} + \nu_\ell \qquad \text{(NC)} \tag{2.13}$$

and

$$\nu_\ell + \mathrm{e}^- \quad \rightarrow \quad \nu_\ell + \mathrm{e}^- \qquad \text{(ES)}. \tag{2.14}$$

The CC reaction was sensitive exclusively to electron neutrinos while the NC reaction was equally sensitive to all three neutrino flavors $\ell = \mathrm{e}, \mu, \tau$. The ES reaction was sensitive to all flavors as well but with reduced sensitivity to ν_μ and ν_τ. CC and ES reactions were measured by Čerenkov radiation and NC reactions were measured by neutron capture on deuterium.

It was the first measurement of the total ^{8}B flux and it was in well agreement with the SSM, as evident from Figure 2.4. The dashed lines represent the $\pm1\sigma$ boundaries of the total flux predicted by the SSM and the solid blue band represents the $\pm1\sigma$ confidence-interval of the total NC flux measured by SNO. The red and green bands represent the respective SNO measurements for the CC and ES reactions. All bands intersect at the fit values for ϕ_e (electron-neutrino flux) and $\phi_{\mu\tau}$ (combined muon- and tau-neutrino flux), indicating that the combined flux is consistent with that one predicted by the SSM. As we will see in Chapter 3, this result was also consistent with the theory of neutrino oscillation in high-density environments, such as the core of the Sun. Consequently, this was not only the solution to the solar neutrino problem but also proof of neutrino oscillations first predicted by Bruno Pontecorvo in 1957 [47]. Furthermore, it was a

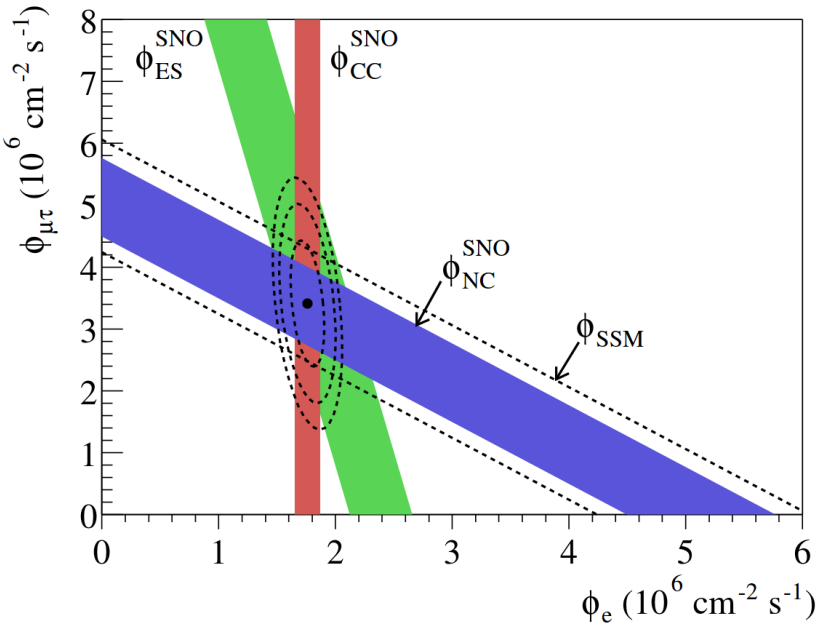

Figure 2.4.: Final result of flux measurements performed at SNO. The dashed lines represent the $\pm 1\sigma$ boundaries of the total flux predicted by the SSM and the solid blue band represents the $\pm 1\sigma$ confidence-interval of the total NC flux measured by SNO. The red and green bands represent the respective SNO measurements for the CC and ES reactions. All bands intersect at the fit values for ϕ_e (electron-neutrino flux) and $\phi_{\mu\tau}$ (combined muon- and tau-neutrino flux) indicating that the combined flux is consistent with that one predicted by the SSM. [46]

confirmation that neutrinos have non-zero mass, which is a requirement for neutrino oscillations to happen. [46]

Since SNO proved the concept of neutrino oscillations and consequently non-zero neutrino masses, many experiments around the globe contributed to a better understanding of the oscillation phenomena by measuring its governing parameters. In 1999, the KEK to Kamioka (K2K) [48] experiment begun its investigation of neutrino oscillations suggested by atmospheric neutrino observations. It was the first long-baseline neutrino-oscillation experiment and found oscillation parameters which were consistent with those measured by Super-Kamiokande [49]. The Kamioka Liquid scintillation AntiNeutrino Detector (KamLAND) [50] started to collect data in 2002. Combined with results from solar neutrino experiments, it has measured the mass splitting and mixing angle relevant for the oscillations observed from solar neutrinos, the so-called solar parameters. In 2006, the Main Injector Neutrino Oscillation Search (MINOS) long-baseline neutrino-oscillation experiment at FNAL measured the mass splitting and mixing-angle related to muon-neutrino disappearance, the so-called atmospheric parameters [51]. The Daya-

Bay [52], RENO [53] and Double Chooz [54] neutrino experiments have measured oscillation parameters from the disappearance of reactor electron-antineutrinos. They have set a relatively large value for the smallest of the three mixing angles; a non-zero value is required for violation of CP-symmetry. In 2012, the Daya-Bay experiment reported the discovery of the non-zero value for the smallest of the three neutrino-mixing angles, pushing experiments to further investigate in the potential violation of CP-symmetry in the lepton sector. In 2013, the NuMI Off-Axis ν_e Appearance (NOνA) long-baseline neutirno-oscillation experiment [55] at FNAL (successor of the MINOS experiment) started data taking, with the goal to precisely measure the parameters of muon neutrino and antineutrino disappearance, and the associated mass splitting, which allows strong constraints on the CP-violating phase and the neutrino mass hierarchy. Analogous measurements are performed by the T2K long-baseline neutrino-oscillation experiment [56] in Japan, which started operations in 2010. As of 2020, the T2K [13] and NOνA [14] experiments favor NO [15]. Latest results from T2K show an indication of CP-violation in the lepton sector [57]. Furthermore, T2K was the first experiment that observed neutrino appearance (electron neutrino appearance in a beam of initially muon neutrinos) [58], in 2011, and significantly contributed to the understanding of neutrino-nucleus interactions of various topologies by measuring their cross sections. In 2015, the Oscillation Project with Emulsion-tRacking Apparatus (OPERA) [59] experiment succeeded in measuring $\nu_\mu \rightarrow \nu_\tau$ oscillations by the detection of tau-neutrino CC-interactions in emulsion detectors.

3. Neutrino Theory

In Chapter 2, we saw that the SNO proved the concept of neutrino oscillations and, as a consequence, the existence of massive neutrinos. In Chapter 3, I am going to discuss the underlying theory of neutrino oscillations, and we will see why non-zero neutrino masses are a requirement for oscillations to happen. I will discuss different sources of neutrinos, and we will have a look on how state-of-the-art neutrino experiments measure the fundamental properties of neutrinos and investigate the laws of the weak interaction via neutrino oscillations.

3.1. Neutrino Oscillation in Vacuum

There are three types of neutrinos by means of how they interact weakly and to which of the three lepton families of electron, muon and tau they correspond. These are the so-called *flavor* eigenstates of the neutrino. On one hand, each flavor eigenstate is a composition of the three so-called *mass* eigenstates, which are distinguished by numerical indices. On the other hand, each mass eigenstate is a composition the three flavor eigenstates. The relation between flavor and mass eigenstates in vacuum is described by a three-dimensional orthogonal rotation that is defined by the unitary Pontecorvo-Maki-Nakagawa-Sakata (PMNS) matrix U:

$$\begin{pmatrix} \nu_\mathrm{e} \\ \nu_\mu \\ \nu_\tau \end{pmatrix} = U \begin{pmatrix} \nu_1 \\ \nu_2 \\ \nu_3 \end{pmatrix}. \tag{3.1}$$

The PMNS matrix, or simply called mixing matrix, shown in Equation 3.2,

$$U = \begin{pmatrix} c_{12}c_{13} & s_{12}c_{13} & s_{13}e^{-i\delta_\mathrm{CP}} \\ -s_{12}c_{23} - c_{12}s_{13}s_{23}e^{i\delta_\mathrm{CP}} & c_{12}c_{23} - s_{12}s_{13}s_{23}e^{i\delta_\mathrm{CP}} & c_{13}s_{23} \\ s_{12}s_{23} - c_{12}s_{13}c_{23}e^{i\delta_\mathrm{CP}} & -c_{12}s_{23} - s_{12}s_{13}c_{23}e^{i\delta_\mathrm{CP}} & c_{13}c_{23} \end{pmatrix} P \tag{3.2}$$

depends on the three mixing angles θ_{12}, θ_{13} and θ_{23}, where $s_{ij} \equiv \sin\theta_{ij}$ and $c_{ij} \equiv \cos\theta_{ij}$, and the Dirac CP-violating phase δ_CP [7, 60, 61]. P is either the identity matrix (in case when the neutrino is a Dirac fermion) or a diagonal matrix with the following form:

$$P = \begin{pmatrix} e^{i\alpha_1} & 0 & 0 \\ 0 & e^{i\alpha_2} & 0 \\ 0 & 0 & 1 \end{pmatrix} \tag{3.3}$$

containing the Majorana CP-violating phases α_1 and α_2 (in case when the neutrino is a

Majorana fermion)[1] [18]. According to Equation 3.1, the flavor eigenstate of a neutrino created in a CC weak interaction with a charged lepton $\ell_\alpha^\pm$ is a composition of the mass eigenstates ($k = 1, 2, 3$), weighted with the respective factors given in the mixing matrix U:

$$|\nu_\alpha\rangle = \sum_k U_{\alpha k}^* |\nu_k\rangle \qquad (\alpha = \mathrm{e}, \nu, \tau). \tag{3.4}$$

Under the assumption that the neutrino mass eigenstates evolve as plane waves in time, we can describe them at any given time t after their creation by

$$|\nu_k(t)\rangle = e^{-iE_k t} |\nu_k\rangle , \tag{3.5}$$

where

$$E_k = \sqrt{\vec{p}^2 + m_k^2} \tag{3.6}$$

is the neutrino energy defined in terms of the neutrino momentum p and the neutrino mass m_k. Analogously, we can express the temporal evolution of the neutrino flavor eigenstates as

$$|\nu_\alpha(t)\rangle = \sum_k U_{\alpha k}^* e^{-iE_k t} |\nu_k\rangle . \tag{3.7}$$

The mass eigenstates in Equation 3.7 can be decomposed into flavor eigenstates in turn. Here, we make use of the following relation

$$U^\dagger U = \mathbf{1} \quad \Longleftrightarrow \quad \sum_\alpha U_{\alpha k}^* U_{\alpha j} = \delta_{jk} \tag{3.8}$$

applied to the mixing matrix ($U^\dagger$ denotes the conjugate transpose of U), which allows us to write down the mass eigenstates in terms of flavor eigenstates as follows:

$$|\nu_k\rangle = \sum_\alpha U_{\alpha k} |\nu_\alpha\rangle . \tag{3.9}$$

Given that relation, we can substitute the respective mass eigenstates in Equation 3.7

$$|\nu_\alpha(t)\rangle = \sum_{\beta=e,\mu,\tau} \left(\sum_k U_{\alpha k}^* e^{-iE_k t} U_{\beta k} \right) \left|\nu_\beta\right\rangle , \tag{3.10}$$

which yields a relation for the temporal evolution of the flavor eigenstates α in terms of the the initial flavor eigenstates β. Accordingly, the probability to observe a neutrino in the final flavor eigenstate ν_β at any time t after a given initial flavor eigenstate ν_α is

$$P_{\nu_\alpha \to \nu_\beta}(t) = \left| \left\langle \nu_\beta \middle| \nu_\alpha(t) \right\rangle \right|^2 = \left| \sum_k U_{\alpha k} U_{\beta k}^* e^{-iE_k t} \right|^2 , \tag{3.11}$$

[1] Whether the neutrino is a Dirac fermion, i.e. neutrinos and antineutrinos are different particles, or the neutrino is a Majorana fermion, i.e. neutrinos are their own antiparticles, is still an open question.

which can be expanded as

$$P_{\nu_\alpha \to \nu_\beta}(t) = \sum_{k,j} U^*_{\alpha k} U_{\beta k} U_{\alpha j} U^*_{\beta j} e^{-i(E_k - E_j)t} \qquad (j = 1, 2, 3). \tag{3.12}$$

For ultrarelativistic[2] neutrinos, the energy relation in Equation 3.6 can be approximated by the second-order Taylor expansion

$$E_k \simeq E + \frac{m_k^2}{2E}, \tag{3.13}$$

where we assume the same momentum p for all neutrino mass eigenstates. In turn, the energy difference between two neutrino mass eigenstates

$$E_k - E_j \simeq \frac{\Delta m^2_{kj}}{2E} \tag{3.14}$$

becomes a function of the respective neutrino mass splitting

$$\Delta m^2_{kj} \equiv m_k^2 - m_j^2 \tag{3.15}$$

and of the generalized neutrino energy

$$E = |\vec{p}\,|. \tag{3.16}$$

Finally, the probability given in Equation 3.12 can be rewritten as

$$P_{\nu_\alpha \to \nu_\beta}(t) = \sum_{k,j} U^*_{\alpha k} U_{\beta k} U_{\alpha j} U^*_{\beta j} \exp\left(-i \frac{\Delta m^2_{kj} t}{2E}\right), \tag{3.17}$$

which we now call the oscillation probability for the transition from the flavor eigenstate α into the flavor eigenstate β. The oscillation probability of the channels with $\alpha = \beta$ is usually called *survival probability*, whereas the oscillation probability of the channels with $\alpha \neq \beta$ is usually called *transition probability*. [6] The probabilities do not only depend on the time but also the neutrino energy, the neutrino masses and the mixing angles, as we will see in the next section.

3.2. L/E Dependence and Mass Splitting

The propagation time t is not measured in neutrino oscillation experiments. Instead, the baseline L, i.e. the distance between the neutrino source and the detector, is known. Since ultrarelativistic neutrinos propagate nearly at the speed of light, it is possible to approximate $t = L$, leading to

$$P_{\nu_\alpha \to \nu_\beta}(L, E) = \sum_{k,j} U^*_{\alpha k} U_{\beta k} U_{\alpha j} U^*_{\beta j} \exp\left(-i \frac{\Delta m^2_{kj} L}{2E}\right). \tag{3.18}$$

[2] A particle is called ultrarelativistic when its speed is very close to the speed of light c, i.e. its energy is almost completely due to its momentum ($pc \gg mc^2$).

It is shown in [6], that in case of the survival probability, Equation 3.18 can be rewritten in the following simple form:

$$P_{\nu_\alpha \to \nu_\alpha}(L,E) = 1 - 4 \sum_{k>j} \left|U_{\alpha k}\right|^2 \left|U_{\alpha j}\right|^2 \sin^2\left(\frac{\Delta m^2_{kj} L}{4E}\right). \tag{3.19}$$

Expression 3.19 makes clear that the baseline L and the neutrino energy E are the two quantities that drive the phases of neutrino oscillations

$$\Phi_{kj} = \frac{\Delta m^2_{kj} L}{4E} = 1.267\, \Delta m^2_{kj}(\mathrm{eV}^2) \frac{L(\mathrm{km})}{E(\mathrm{GeV})}, \tag{3.20}$$

while the amplitudes of the oscillations are determined only be the elements of the mixing matrix, which are functions of the mixing angles and are constant. Moreover, the neutrino masses feed into the oscillation probabilities. Only if the neutrino mass splittings, i.e. the differences between the masses of the neutrino mass eigenstates, are greater than zero, then transition probabilities are non-vanishing. Therefore, neutrinos can only oscillate if at least two of them are massive. With a fixed baseline L and a fixed neutrino energy E, neutrino oscillation experiments can extract the parameters in the mixing matrix and the mass splittings by measuring survival and transition probabilities. The sensitivity on those parameters is usually characterized by a quantity that we call oscillation length, and which is defined as the distance at which the respective phase becomes equal to π, i.e. the distance between any two closest minima or maxima of the oscillation probability:

$$L^{osc}_{kj} = \frac{4\pi E}{\left|\Delta m^2_{kj}\right|} \simeq 2.48\,\mathrm{km}\, \frac{E(\mathrm{GeV})}{\left|\Delta m^2_{kj}\right|(\mathrm{eV}^2)}. \tag{3.21}$$

If $L \ll L^{osc}_{kj}$, then oscillations to not have enough time to evolve and $P_{\nu_\alpha \to \nu_\beta}(L,E) \simeq \delta_{\alpha,\beta}$. If $L \gg L^{osc}_{kj}$, then so many oscillations occur that only an averaged oscillation probability can be measured. The maximum sensitivity to oscillations and the respective parameters occur when $L \simeq L^{osc}_{kj}$, i.e. when $L/E \simeq \Delta m^2_{kj}$. [6, 10, 62]

Absolute neutrino masses can not be measured by oscillation experiments because oscillations are only sensitive to the mass splittings. Neutrino mass splittings, on the other hand, have been pinned down to fractions of meV^2. Measurements have shown that two out of three neutrino masses are very close ($\Delta m^2_{21} \simeq 7.4 \times 10^{-5}\,\mathrm{eV}^2$), while the third neutrino mass is farther away ($\Delta m^2_{3j} \simeq 2.5 \times 10^{-3}\,\mathrm{eV}^2$). However, it is still unknown whether ν_3 is heavier or lighter than the two other neutrino mass eigenstates, which is known as the problem of neutrino mass hierarchy. The problem is illustrated in Figure 3.1: on the left-hand side is shown what we call NO, i.e. ν_3 is the heaviest massive neutrino and $\Delta m^2_{3j} \equiv \Delta m^2_{31} > 0$. And on the right-hand side is shown what we call IO, i.e. ν_3 is the lightest massive neutrino and $\Delta m^2_{3j} \equiv \Delta m^2_{32} < 0$. The colors indicate the flavor composition of the three massive neutrinos according to the values in the PMNS matrix. [11]

It is important that neutrino oscillation experiments tune the ratio L/E with respect to the mass splittings in order to maximize their sensitivity for the parameters they want

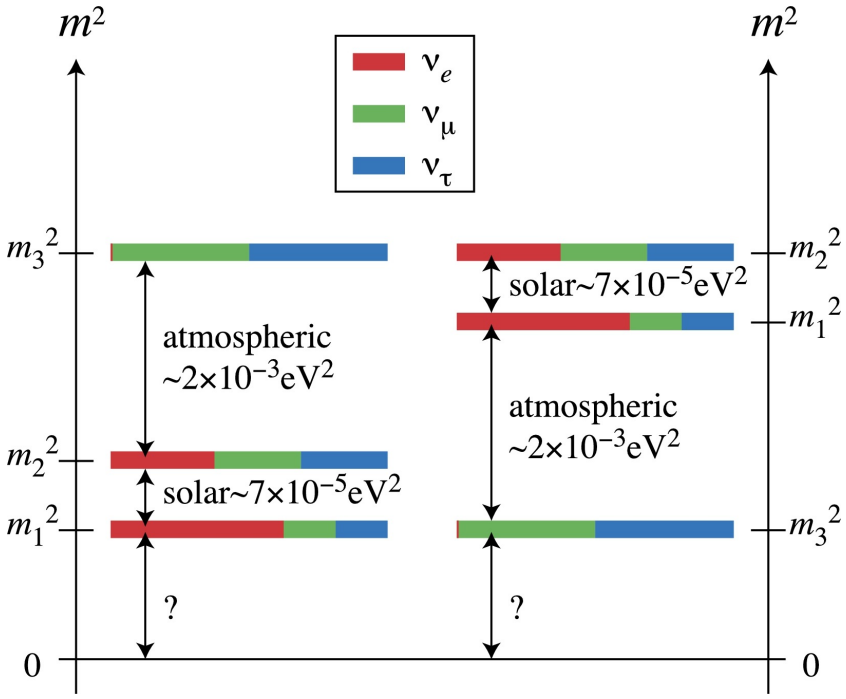

Figure 3.1.: Illustration of the problem of neutrino mass hierarchy: it is unknown whether ν_3 is heavier or lighter than the two other neutrino mass eigenstates. On the left-hand side is shown what we call NO, i.e. ν_3 is the heaviest massive neutrino and $\Delta m^2_{3j} \equiv \Delta m^2_{31} > 0$. And on the right-hand side is shown what we call Inverted Ordering (IO), i.e. ν_3 is the lightest massive neutrino and $\Delta m^2_{3j} \equiv \Delta m^2_{32} < 0$. The colors indicate the flavor composition of the three massive neutrinos according to the values in the PMNS matrix. [11]

to measure, i.e. what transitions they want to observe. As we will see in the next section, the neutrino energy is often defined by the neutrino source, which means that oscillation experiments predominantly need to tune their baselines.

3.3. Neutrino Sources

The energy of neutrinos in the universe depends on their source and varies by ~ 20 orders of magnitude in eV from cosmological neutrinos with $\sim 1 \times 10^{-4}$ eV to astrophysical neutrinos with $\sim 1 \times 10^{16}$ eV. Also the neutrino composition in terms of massive neutrinos depends on the neutrino flavor produced at the source. Understanding the neutrino production mechanism is crucial to predict what flavor ratios we can measure in our detectors. The fluxes of different neutrino sources as a function of the neutrino energy are summarized in Figure 3.2.

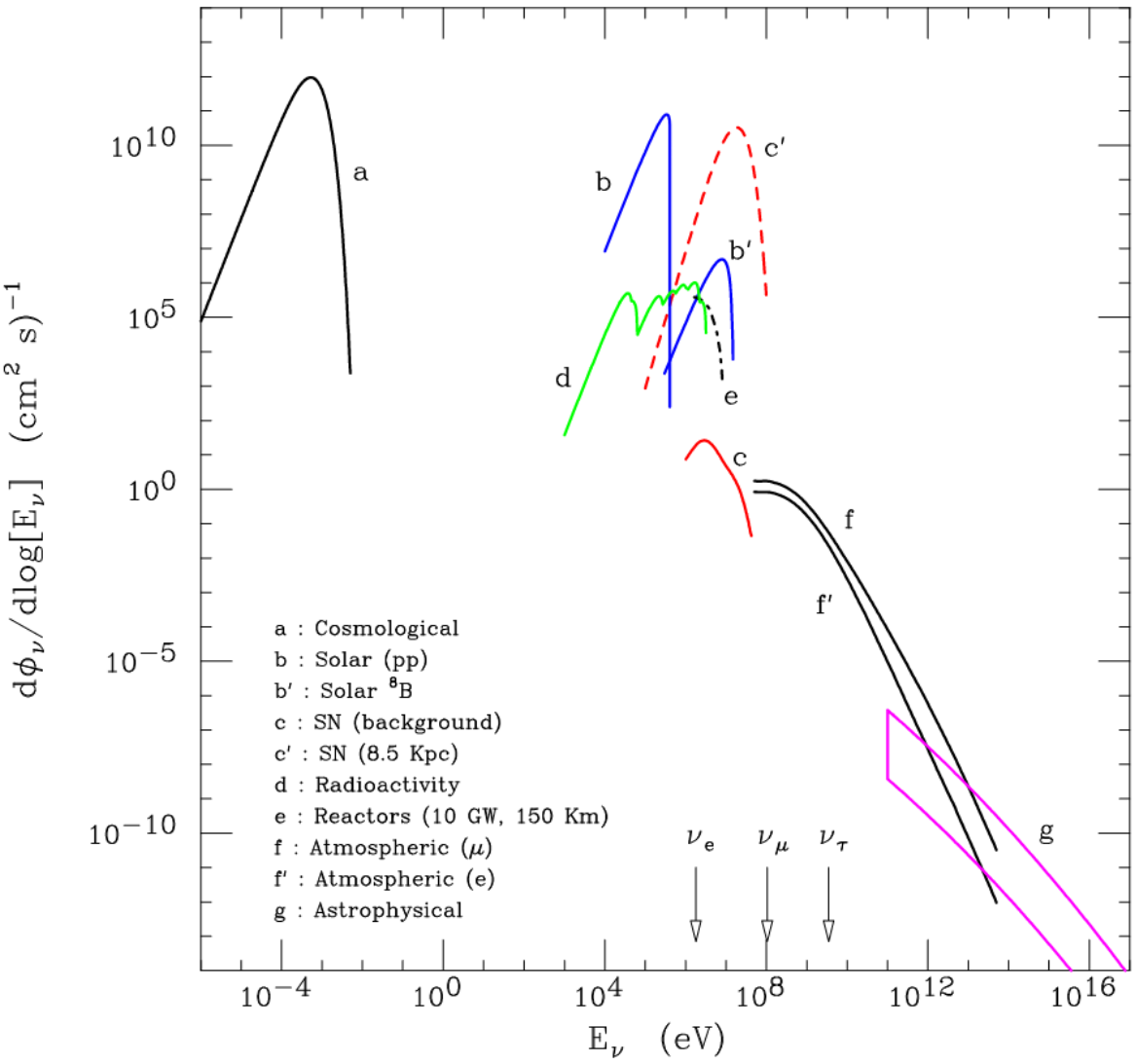

Figure 3.2.: Flux and energy of different neutrino sources in the universe. The arrows indicate the energy thresholds for CC interactions of ν_e, ν_μ and ν_τ on a free proton target. [10]

Many neutrino oscillation experiments are limited to a single source (or energy range) because the ratio L/E needs to fit the respective mass splitting, and the baseline L is usually fixed. For that reason, many neutrino oscillation experiments are not sensitive to the effect of three-neutrino mixing. In these cases, it is convenient to use the approximation of two-neutrino mixing, where only two massive neutrinos out of three and two flavor neutrinos out of three are considered. The flavor neutrinos can either be pure flavor neutrinos or linear combinations of pure flavor neutrinos. The mixing matrix simplifies to a two-dimensional rotation matrix with a single mixing angle θ:

$$U = \begin{pmatrix} \cos\theta & \sin\theta \\ -\sin\theta & \cos\theta \end{pmatrix}, \tag{3.22}$$

and oscillations depend on only one mass splitting,

$$\Delta m^2 \equiv m_2^2 - m_1^2, \tag{3.23}$$

with m_1 the mass of the lightest neutrino. The transition and survival probabilities for two-neutrino mixing can be derived from from Equation 3.17, leading to

$$P_{\nu_\alpha \to \nu_\beta}(L, E) = \sin^2(2\theta)\, \sin^2\left(\frac{\Delta m^2 L}{4E}\right) \tag{3.24}$$

and

$$P_{\nu_\alpha \to \nu_\alpha}(L, E) = 1 - \sin^2(2\theta)\, \sin^2\left(\frac{\Delta m^2 L}{4E}\right). \tag{3.25}$$

The PMNS matrix (Equation 3.2 in the Dirac case) can be rewritten as three orthogonal rotation matrices

$$U = \underbrace{\begin{pmatrix} 1 & 0 & 0 \\ 0 & c_{23} & s_{23} \\ 0 & -s_{23} & c_{23} \end{pmatrix}}_{atmospheric} \underbrace{\begin{pmatrix} c_{13} & 0 & s_{13}e^{-i\delta_{\mathrm{CP}}} \\ 0 & 1 & 0 \\ -s_{13}e^{i\delta_{\mathrm{CP}}} & 0 & c_{13} \end{pmatrix}}_{reactor} \underbrace{\begin{pmatrix} c_{12} & s_{12} & 0 \\ -s_{12} & c_{12} & 0 \\ 0 & 0 & 1 \end{pmatrix}}_{solar}, \tag{3.26}$$

where each rotation matrix describes the mixing between two massive neutrinos, similar to the two-neutrino mixing discussed above. Accordingly, each of the three matrices can be assigned a source of neutrinos which they describe at best. For historical reasons, these sources are the Sun, the atmosphere and nuclear reactors. It is now understood that the past solar-neutrino experiments did not actually measure oscillations but only the flavor composition of one massive neutrino eigenstate. On the other hand, atmospheric neutrinos have mainly been replaced by accelerator-based beam neutrinos nowadays. We will now have a closer look at these four types of neutrinos, which are the most relevant for neutrino oscillation measurements.

Solar Neutrinos

Solar neutrinos are produced in large quantities by fusion reactions in the core of the Sun. The total solar flux at the Earth is 6.5×10^{10} neutrinos per cm^2 and per second. More than 90 % of these neutrinos originate from the Proton-Proton (PP) chain, where four protons are fused into a helium core. The PP-chain reactions relevant for neutrino production are listed in Table 3.1. The third column shows the neutrino energy, the fourth

Table 3.1.: SSM (BP2000) solar neutrino predictions taken from Refs [34, 63, 64].

Reaction	Label	Energy [MeV]	Flux $[10^{10}\,\mathrm{cm}^{-2}\,\mathrm{s}^{-1}]$	Cl [SNU]
$\mathrm{p} + \mathrm{p} \rightarrow {}^2\mathrm{H} + \mathrm{e}^+ + \nu_\mathrm{e}$	pp	≤ 0.420	5.95	0.0
$\mathrm{p} + \mathrm{e}^- + \mathrm{p} \rightarrow {}^2\mathrm{H} + \nu_\mathrm{e}$	pep	1.442	1.40×10^{-2}	0.22
${}^3\mathrm{He} + \mathrm{p} \rightarrow {}^4\mathrm{He} + \mathrm{e}^+ + \nu_\mathrm{e}$	hep	≤ 18.8	9.3×10^{-7}	0.04
${}^7\mathrm{Be} + \mathrm{e}^- \rightarrow {}^7\mathrm{Li} + \nu_\mathrm{e}$	^{7}Be	0.861 (90 %)	4.77×10^{-1}	1.15
${}^8\mathrm{B} \rightarrow {}^8\mathrm{Be}^* + \mathrm{e}^+ + \nu_\mathrm{e}$	^{8}B	≤ 15	5.05×10^{-4}	5.76

column the flux at the Earth and the fifth column the neutrino absorption cross-section on chlorine, which was used as target in the Homestake-Experiment. The ^{8}B neutrino energies are at the order of 10 MeV. For $\Delta m^2_{21} \simeq 7.4 \times 10^{-5}\,\mathrm{eV}^2$ the oscillation length $L^{osc}_{21} \simeq 350\,\mathrm{km}$, whereas the distance from the Sun to the Earth is ~ 150 Million km. Consequently, what is measured on Earth are the averaged oscillation probabilities of ν_e in vacuum because $L \gg L^{osc}_{21}$. As we will see later in this Chapter, environments with very high matter densities (e.g. the core of the Sun) can change the effective neutrino-mixing angles. For that reason, ^{8}B neutrinos coming from the Sun are produced in a pure ν_2 mass eigenstate, and what we actually measure on Earth is the respective flavor composition of ν_2 in vacuum.

Atmospheric Neutrinos

Atmospheric neutrinos are part of cosmic-ray showers produced $\sim 30\,\mathrm{km}$ above the ground by high-energy particles (mostly protons) coming from the Sun or extragalactic sources. The characteristic composition of such a shower is shown in Figure 3.3. Short-lived mesons, most of them pions, are produced when high-energy particles strike the atomic nuclei in the upper atmosphere. The charged pions decay into muons and muon neutrinos, whereas the produced muons further decay into electrons and electron neutrinos, according to the reactions

$$\pi^+ \quad \rightarrow \quad \mu^+ + \nu_\mu \quad \rightarrow \quad \mathrm{e}^+ + \nu_\mathrm{e} + \overline{\nu}_\mu + \nu_\mu \tag{3.27}$$

and

$$\pi^- \quad \rightarrow \quad \mu^- + \overline{\nu}_\mu \quad \rightarrow \quad \mathrm{e}^- + \overline{\nu}_\mathrm{e} + \nu_\mu + \overline{\nu}_\mu. \tag{3.28}$$

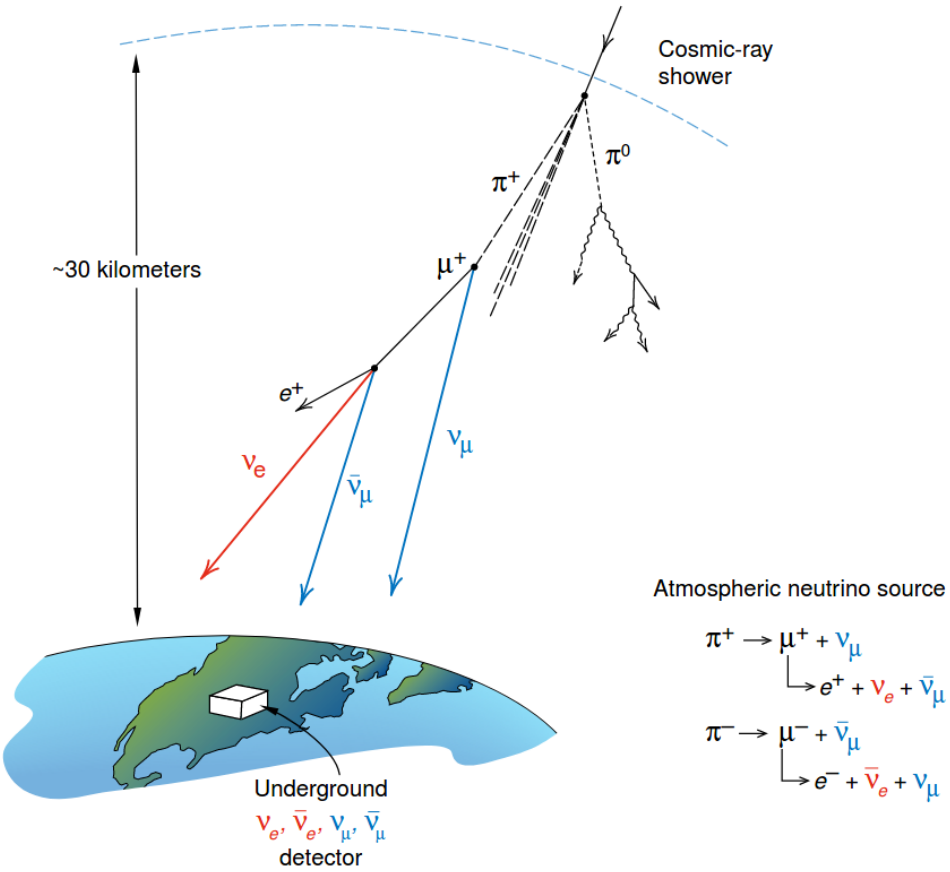

Figure 3.3.: Atmospheric neutrinos are produced by high-energy particles (mostly protons) coming from the Sun or extragalactic sources. Short-lived mesons, most of them pions, are produced when high-energy particles strike the atomic nuclei in the upper atmosphere. The charged pions decay into muons and muon neutrinos, whereas the produced muons further decay into electrons and electron neutrinos. [65]

From these reactions, it is evident that the flux of atmospheric muon (anti)neutrinos is roughly double the flux of atmospheric electron (anti)neutrinos. For $\Delta m^2_{3j} \simeq 2.5 \times 10^{-3}\,\mathrm{eV}^2$ and a typical neutrino energy around 1 GeV the oscillation length $L^{osc}_{3j} \simeq 1000\,\mathrm{km}$. Considering that atmospheric neutrinos are not only coming from above but are produced isotropically in the upper layers of the atmosphere, an average baseline for oscillations is represented by the Earth radius $R_\oplus = 6371\,\mathrm{km}$. Here, we are in the regime $L \simeq L^{osc}_{3j}$, which explains why Super-Kamiokande measured a zenith-angle dependent deficit of μ-like events in 1998.

Reactor Neutrinos

Reactor neutrinos are a decay product of the isotopes produced in nuclear-fission reactors. The fission fragments of heavy elements, like uranium or plutonium, usually show an excess of neutrons and undergo β^- decay as they become more stable, according to

$$ {}^{A}_{Z}\mathrm{E} \quad \rightarrow \quad {}_{Z-1}{}^{A}\mathrm{E}' + \mathrm{e}^- + \overline{\nu}_\mathrm{e}, \tag{3.29} $$

where A is the mass number and Z is the atomic number of an element E decaying into an element E'. As a result, the produced neutrinos are of a single flavor with a narrow energy range around 1 MeV. For $\Delta m^2_{3j} \simeq 2.5 \times 10^{-3}\,\mathrm{eV}^2$ the oscillation length $L^{osc}_{3j} \simeq 1\,\mathrm{km}$, and the neutrino flux at 1 km distance from a 1 GW reactor is as high as $\sim 2 \times 10^9$ neutrinos per cm^2 and per second. Unlike for solar- and atmospheric-neutrino experiments, the baseline is not predefined by the neutrino source but can be fine-tuned to fulfill the needs of the experiment. That allows reactor-neutrino experiments to precisely measure θ_{13} and the mass splitting between the lightest and the heaviest massive neutrino. In 2012, the Daya-Bay Reactor Neutrino Experiment has measured a non-zero value for the neutrino mixing angle θ_{13}, the by then last yet unknown neutrino mixing angle [66].

Beam Neutrinos

Beam neutrinos are the product of man-made neutrino beams. The source of a neutrino beam is a particle accelerator that accelerates protons to the desired kinetic energy. Next, the protons are deflected towards a target where they undergo strong interactions with the target material, yielding a forward-boosted bunch of pions aside from minor contributions of heavier mesons. The secondary particles pass one or several magnetic horns, where either the positively or negatively charged particles are focused towards a decay pipe, while the counter-charged particles are deflected off. The charged pions enter the decay pipe where they decay into muons and muon (anti)neutrinos (Equation 2.3) after a mean lifetime of 2.6×10^{-8} seconds. Any particles other than neutrinos are absorbed by a massive beam dump positioned at the end of the decay pipe; the result is a pure neutrino beam. Decay pipes have typical lengths of a few 100 m to prevent electron-neutrino contamination by muon decay.

Neutrino beams are of either nearly pure ν_μ or $\overline{\nu}_\mu$ composition, and what is typically measured in beam oscillation-experiments is the disappearance of μ-type and the appearance of e-type neutrinos. Both the neutrino energy (where a lower limit is set by the pion decay at rest) and the baseline can be chosen to fit the experiment. Same as for atmospheric neutrinos, the oscillation length $L^{osc}_{3j} \simeq 1000\,\mathrm{km}$ at 1 GeV neutrino energy.

Experiments with baselines of several 100 km length are referred to as long-baseline neutrino-oscillation experiments. Examples are the former MINOS experiment [67] (735 km baseline) and its successor the NOνA experiment [55] (810 km baseline), the T2K experiment (295 km baseline), or the future DUNE experiment with a 1300 km baseline.

Experiments with shorter baselines ($< 100\,\mathrm{km}$) are referred to as short-baseline neutrino-oscillation experiments. Former short-baseline neutrino-oscillation experiments (Liquid Scintillator Neutrino Detector (LSND) and MiniBooNE, among others) have measured

neutrino anomalies consistent with the mixing of the standard neutrinos with a fourth, non-weakly-interacting *sterile* species [68]. The Short-Baseline Neutrino (SBN) program, which is currently built at FNAL, addresses these anomalies and will carry out precision searches for new physics in neutrinos [68].

As we will see in the next section, the neutrino and antineutrino oscillation probabilities are different if CP symmetry is broken. Accordingly, long-baseline neutrino-oscillation experiments are well suited to probe CP violation in neutrino oscillations because they can be operated in both ν_μ and $\overline{\nu}_\mu$ mode.

3.4. Violation of CP-Symmetry

In Chapter 2, we saw that Daya Bay measured a non-zero value for the smallest of the three mixing angles, θ_{13}, which is a requirement for CP violation. In general, neutrino oscillations can violate the CP symmetry or the T symmetry:

$$P(\nu_\alpha \to \nu_\beta) \neq P(\bar{\nu}_\alpha \to \bar{\nu}_\beta) \qquad \text{(CP-symmetry violation)}, \tag{3.30}$$

$$P(\nu_\alpha \to \nu_\beta) \neq P(\nu_\beta \to \nu_\alpha) \qquad \text{(T-symmetry violation)}. \tag{3.31}$$

On the other hand, the CPT theorem implies that $P(\nu_\alpha \to \nu_\beta) = P(\bar{\nu}_\beta \to \bar{\nu}_\alpha)$. If CPT is a symmetry of nature, then the violation of CP symmetry implies the violation of T symmetry. To see how neutrino oscillations can violate the CP symmetry, we need to reformulate Equation 3.18 as

$$\begin{aligned} P_{\nu_\alpha \to \nu_\beta}(L,E) = \delta_{\alpha\beta} &- 4\sum_{k>j} \Re\left[U^*_{\alpha k} U_{\beta k} U_{\alpha j} U^*_{\beta j}\right] \sin^2\left(\frac{\Delta m^2_{kj} L}{4E}\right) \\ &+ 2\sum_{k>j} \Im\left[U^*_{\alpha k} U_{\beta k} U_{\alpha j} U^*_{\beta j}\right] \sin\left(\frac{\Delta m^2_{kj} L}{2E}\right). \end{aligned} \tag{3.32}$$

In case of antineutrino oscillations, the only difference is that we start with antineutrino flavor-states

$$|\bar{\nu}_\alpha\rangle = \sum_k U_{\alpha k} |\bar{\nu}_k\rangle \qquad (\alpha = \mathrm{e}, \nu, \tau) \tag{3.33}$$

in which the elements of the mixing matrix are complex conjugated with respect to the neutrino flavor-states in Equation 3.7. The respective antineutrino oscillation-probability can be reformulated as

$$\begin{aligned} P_{\bar{\nu}_\alpha \to \bar{\nu}_\beta}(L,E) = \delta_{\alpha\beta} &- 4\sum_{k>j} \Re\left[U^*_{\alpha k} U_{\beta k} U_{\alpha j} U^*_{\beta j}\right] \sin^2\left(\frac{\Delta m^2_{kj} L}{4E}\right) \\ &- 2\sum_{k>j} \Im\left[U^*_{\alpha k} U_{\beta k} U_{\alpha j} U^*_{\beta j}\right] \sin\left(\frac{\Delta m^2_{kj} L}{2E}\right). \end{aligned} \tag{3.34}$$

Comparing Equations 3.32 with Equation 3.34, we immediately see that they differ only in the terms depending on the imaginary parts of the quartic products of the elements of the mixing matrix:

$$\begin{aligned} A^{CP}_{\alpha\beta}(L,E) &\equiv P_{\nu_\alpha\to\nu_\beta}(L,E) - P_{\bar{\nu}_\alpha\to\bar{\nu}_\beta}(L,E) \\ &= 4\sum_{k>j} \Im\left[U^*_{\alpha k}U_{\beta k}U_{\alpha j}U^*_{\beta j}\right] \sin\left(\frac{\Delta m^2_{kj}L}{2E}\right). \end{aligned} \tag{3.35}$$

Neutrino oscillations can only violate CP symmetry if this term is non-zero. As a first consequence, CP asymmetry can be measured only in the transitions between different neutrino flavors, because for $\alpha = \beta$ the imaginary parts in Equation 3.35 vanish. And as a second consequence, CP asymmetry can only occur if the following three conditions are fulfilled (mathematical derivation in Ref. [10]):

1. The Dirac CP-violating phase δ_{CP} must be non-trivial, i.e. $\delta_{\mathrm{CP}} \neq 0$ and $\delta_{\mathrm{CP}} \neq \pi$.
2. All mixing angles must be non-vanishing: $\theta_{12} \neq 0$, $\theta_{13} \neq 0$ and $\theta_{23} \neq 0$.
3. All three phases $\Delta m^2_{kj}L/4E$ must be appreciably different from zero.

The Majorana CP-violating phases are common to an entire column of the mixing matrix. Consequently, neutrino oscillations are not sensitive to the Majorana phases as they cancel in the quadric products of the elements of the mixing matrix. This cancellation has to happen since the Majorana phases arise when a Majorana mass term that violates lepton number conservation is included, while neutrino oscillations conserve lepton number. [6, 10]

So far, we only discussed neutrino oscillations in vacuum. Another effect that leads to a different behavior of neutrinos and antineutrions arises when we look at how matter affects neutrino oscillations.

3.5. Neutrino Oscillation in Matter

In 1978, L. Wolfenstein [69] discovered that neutrinos propagating in matter are subject to a potential due to the coherent effect of elastic forward scattering with the electrons and nucleons in the medium. This potential can be seen as an index of refraction for neutrinos in matter that modifies the mixing of neutrinos. Interactions of neutrinos with matter can proceed by the exchange of a Z^0, resulting in the NC effective potentials:

$$V^{\mathrm{Z}}_{\nu_{\mathrm{e}}\mathrm{e}} = V_{\nu_\mu\mathrm{e}} = V_{\nu_\tau\mathrm{e}} = -\frac{\sqrt{2}}{2}G_F N_{\mathrm{e}}, \tag{3.36}$$

$$V_{\nu_{\mathrm{e}}\mathrm{p}} = V_{\nu_\mu\mathrm{p}} = V_{\nu_\tau\mathrm{p}} = +\frac{\sqrt{2}}{2}G_F N_{\mathrm{p}}, \tag{3.37}$$

$$V_{\nu_{\mathrm{e}}\mathrm{n}} = V_{\nu_\mu\mathrm{n}} = V_{\nu_\tau\mathrm{n}} = -\frac{\sqrt{2}}{2}G_F N_{\mathrm{n}}. \tag{3.38}$$

In addition, the electron neutrino can also interact by the exchange of a $W^{\pm}$, resulting in a CC effective potential:

$$V_{\nu_e e}^{W} = \sqrt{2} G_F N_e, \tag{3.39}$$

such that

$$V_{\nu_e e} = V_{\nu_e e}^{Z} + V_{\nu_e e}^{W} = -\frac{\sqrt{2}}{2} G_F N_e + \sqrt{2} G_F N_e, \tag{3.40}$$

where G_F is the Fermi coupling constant and N_e, N_p, N_n are the electron, proton and neutron densities of the medium. Crucial for matter effects is the difference of the total effective potentials between ν_e and ν_μ, ν_τ:

$$V \equiv V_{\nu_e} - V_{\nu_\mu} = V_{\nu_e} - V_{\nu_\tau} = \sqrt{2} G_F N_e. \tag{3.41}$$

It is also important to mention that for antineutrinos the effective potentials have a reversed sign:

$$V_{\bar{\nu}_\alpha} = -V_{\nu_\alpha} \qquad (\alpha = e, p, n). \tag{3.42}$$

The total NC effective potential is common to all neutrino flavors and therefore does not change the flavor evolution, whereas the CC effective potential only affects electron neutrinos and changes the evolution of $\nu_e \leftrightarrow \nu_\mu$ and $\nu_e \leftrightarrow \nu_\tau$ transitions. In other words, the potential difference V can be seen as having the effect of shifting the squared mass of the electron neutrino as follows:

$$E_\nu - V \simeq E_\nu + \frac{m^2}{2E_\nu} \tag{3.43}$$

leading to

$$m^2 \to m^2 + 2E_\nu V. \tag{3.44}$$

Quantitatively, the potential difference is equivalent to a shift in the mass splitting by

$$\Delta m^2(\nu_e) = +2E_\nu V \quad \text{and} \quad \Delta m^2(\overline{\nu}_e) = -2E_\nu V, \tag{3.45}$$

such that electron neutrinos acquire effectively a larger squared mass and electron antineutrinos acquire effectively a smaller squared mass. [10]

Let us consider the simple case of two-neutrino mixing in matter where ν_e is mixed with ν_μ or ν_τ. Here, the mixing angle in vacuum gets replaced by an effective mixing angle in matter θ_m, where

$$\sin^2(2\theta_m) = \frac{\sin^2(2\theta)}{\sin^2(2\theta) + (\cos(2\theta) - \xi)^2} \quad \text{with} \quad \xi = \frac{2VE}{\Delta m^2}, \tag{3.46}$$

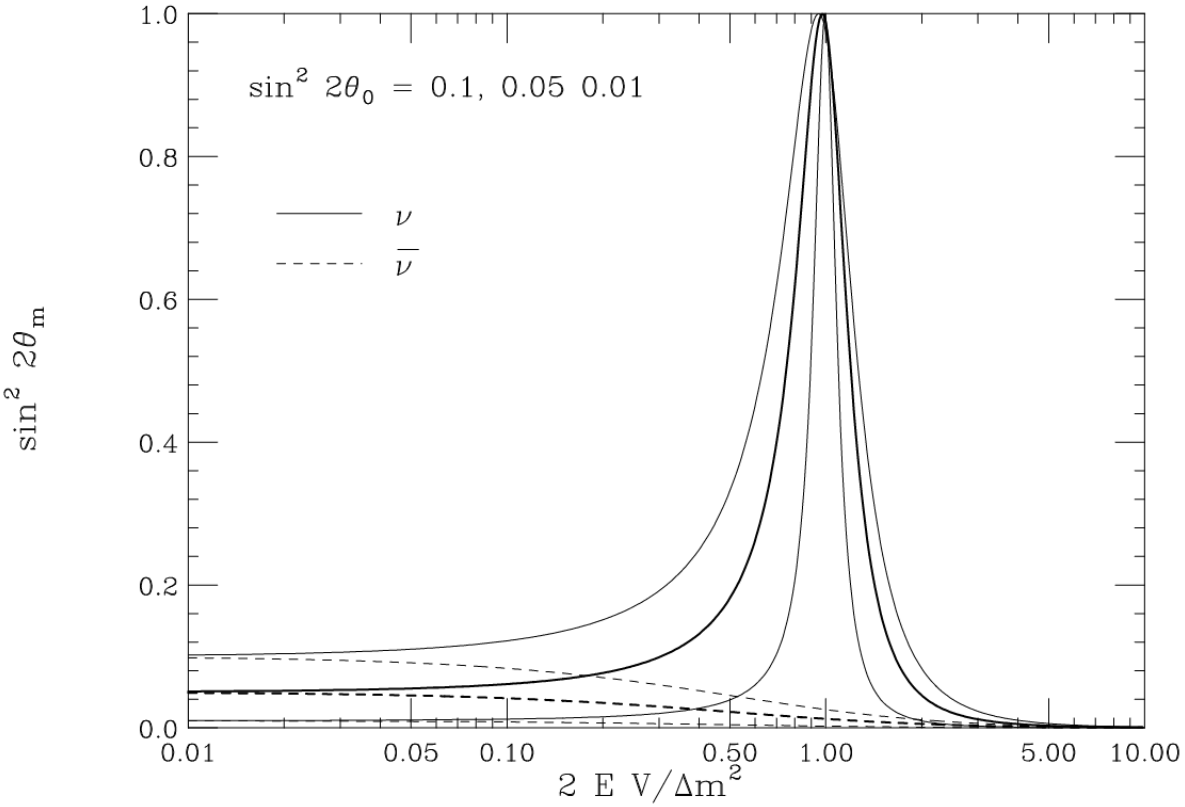

Figure 3.4.: Two-neutrino mixing in matter as a function of $\xi = 2VE/\Delta m^2$, for three different mixing angles θ_0 in vacuum. For $\xi \to 0$ the vacuum case recovers. For $\xi \to \pm\infty$ no mixing occurs and the neutrino flavor states appear as pure matter eigenstates. The maximum mixing occurs at $\xi = \cos(2\theta)$ (θ_m becomes $\pi/4$), at the so-called Mikheyev-Smirnov-Wolfenstein (MSW) resonance. [10]

and the effective mass becomes

$$\Delta m^2_{\text{eff}} = \Delta m^2 \times \sqrt{\sin^2(2\theta) + (\cos(2\theta) - \xi)^2}. \tag{3.47}$$

Figure 3.4 shows the behavior of the effective mixing angle in matter as a function of $\xi = 2VE/\Delta m^2$ for three different mixing angles θ_0 in vacuum. It is assumed that Δm^2 is positive if the mixing angle θ can vary in the interval $\theta \in [0, \pi/2]$. With this convention ξ is always positive for neutrinos and always negative for antineutrinos. In Figure 3.4, we see three particularly different regions:

1. $\xi \to 0$: The low-density region recovers the vacuum case.

2. $\xi \to \pm\infty$: For very high neutrino energies or at very high densities $\theta_m \to \pi/2$ for neutrinos and $\theta_m \to 0$ for antineutrinos. That means no mixing occurs and that ν_e (V>0) corresponds to ν_2 while $\overline{\nu}_e$ (V<0) corresponds to ν_1.

3. $\xi = \cos(2\theta)$: Maximum mixing occurs as θ_m becomes $\pi/4$. This is the so-called MSW resonance [69, 70]. The condition can be satisfied for neutrinos ($\xi > 0$) when $\theta < \pi/4$ and for antineutrinos ($\xi < 0$) when $\theta > \pi/4$.

An interesting aspect is that the MSW resonance appears for neutrinos only if the lightest mass state ν_1 is predominantly a ν_e, i.e. $\Delta m^2 > 0$ which corresponds to NO. On the other hand, the MSW resonance appears for antineutrinos only if $\Delta m^2 < 0$ which corresponds to IO. [10]

As was illustrated, the presence of matter affects the effective mixing angles and consequently the oscillations of neutrinos and antineutrinos in an opposite way depending on the mass hierarchy. A neutrino oscillation experiment with a baseline as long as the future DUNE can therefore probe the problem of neutrino mass hierarchy by comparing the oscillation probabilities of neutrinos with the oscillation probabilities of the respective antineutrinos. Following is a summary of all measured and unknown neutrino oscillation parameters.

3.6. Summary of Measured and Unknown Parameters

Neutrino oscillation parameters and uncertainties are obtained by fitting a set of unknown parameters, sometimes together with already known parameters, to the experimentally measured data. So-called global analysis take the data of many different experiments into account in order to obtain a combined and more profound fit result. Here, we are going to summarize the results from a global fit including new data released at the *Neutrino2020* conference performed by Esteban et al. [15]:

- The best fit of the global analysis disfavors IO at the 1.6σ level. Combined with the latest atmospheric-data analysis from Super-Kamiokande, IO is disfavored at the 2.7σ level.
- The best fit for the Dirac CP-violating phase it at $\delta_{\mathrm{CP}} = 195^\circ$. The CP-conserving value of 180° is allowed at the 0.6σ level. Restricted to IO, the best fit for δ_{CP} is close to maximal CP violation, with CP conservation being disfavored at $\sim 3\sigma$.
- The mixing angles and mass splittings for NO (best fit) and IO are listed in Table 3.2.

Table 3.2.: Three-flavor neutrino oscillation parameters obtained from a global analysis by Esteban et al. [15] including new data released at the *Neutrino2020* conference. Note that $\Delta m^2_{3j} \equiv \Delta m^2_{31} > 0$ for NO and $\Delta m^2_{3j} \equiv \Delta m^2_{32} < 0$ for IO.

Parameter	Normal Ordering (best fit)	Inverted Ordering
$\theta_{12}/^\circ$	$33.44^{+0.78}_{-0.75}$	$33.45^{+0.78}_{-0.75}$
$\theta_{23}/^\circ$	$49.0^{+1.1}_{-1.4}$	$49.3^{+1.0}_{-1.2}$
$\theta_{13}/^\circ$	$8.57^{+0.13}_{-0.12}$	$8.61^{+0.12}_{-0.12}$
$\delta_{\mathrm{CP}}/^\circ$	195^{+51}_{-25}	286^{+27}_{-32}
$\frac{\Delta m^2_{21}}{10^{-5}\,\mathrm{eV}^2}$	$7.42^{+0.21}_{-0.20}$	$7.42^{+0.21}_{-0.20}$
$\frac{\Delta m^2_{3j}}{10^{-3}\,\mathrm{eV}^2}$	$+2.541^{+0.028}_{-0.027}$	$-2.497^{+0.028}_{-0.028}$

3.7. Long-Baseline Neutrino Detection

As mentioned earlier in this chapter, CP violation can be probed with long-baseline experiments using beam neutrinos. And if the baseline is long enough, matter effects can help to solve the neutrino mass hierarchy problem. Here, we will discuss the general concept of long-baseline neutrino detection.

3.7.1. Beamline and Detectors

Long-baseline neutrino-oscillation experiments use beam neutrinos, that is an intense beam of nearly pure ν_μ or $\overline{\nu}_\mu$, which crosses a ND close to the beam source as well as a FD at few hundred kilometers downstream of the beam source. The neutrino beam is pointed towards the FD and therefore intersects with the Earth, which means that the neutrinos are subject to non-negligible matter densities compared to vacuum on their way to the FD. The neutrino energy E and the baseline L, i.e. the distance from the beam source to the FD, are tuned such that $L \simeq L^{osc}$. We already saw that beam neutrinos are of the same nature as atmospheric neutrinos. Therefore, the mass splitting relevant in long-baseline neutrino detection is $\Delta m^2_{3j} \simeq 2.5 \times 10^{-3}\,\mathrm{eV}^2$, such that Equation 3.21 becomes

$$L^{osc} \simeq 1000\,\mathrm{km}\,E(\mathrm{GeV}). \tag{3.48}$$

Near Detector

The ND is important to precisely measure the un-oscillated (anti)neutrino energy spectra of the beam and to constrain systematic errors. Neutrino NDs are exposed to relatively

high flux densities such that the detector dimensions are usually not driven by statistical considerations but rather by the topological aspects of the neutrino interactions, e.g. containment of the hadrons produced in neutrino interactions. But the high interaction rates can also pose a problem if the mean interaction period is less than a typical readout cycle of the detector. In that case, several neutrino interactions may overlap and need to be disentangled before they can be used for analysis. We refer to this phenomenon, when several neutrino interactions overlap, as event pile-up. Because of the low interaction probability of neutrinos with matter, neutrino event pile-up has never happened in a neutrino experiment before, but will be present in future experiments using high-intensity neutrino beams. Ultimately, the ND measurements are used to predict the un-oscillated energy spectra at the FD, which are sensitive to the oscillation parameters. Therefore, it is important that the ND shares the same target nucleus with the FD in order to prevent different cross sections and keep near-to-far predicted uncertainties as small as possible.

Far Detector

The FD measures interactions of the oscillated neutrino beam. Since beam neutrinos are produced by particle decay in flight, neutrino beams suffer a relatively large angular divergence, and consequently, the flux density at the FD is relatively low compared to the flux density at the ND. On the other hand, the interaction cross-sections of neutrinos are extremely small. Therefore, neutrino FDs are usually massive detectors that contain several tens or hundreds of kilo tonnes of active target material in order to acquire enough statistical significance within a few years of operation. The detectors are preferably located a few 1000 m of water equivalent underground to mitigated cosmic-ray backgrounds. Technically, the FD needs the ability to identify the flavor of the interacting neutrinos in CC events, or identify the events as NC interactions. Furthermore, it needs to measure the energy of the neutrinos since oscillations occur as a function of L/E.

3.7.2. Measurement Priciple

The neutrino being a neutrally charged lepton interacts with matter only by the weak interaction and gravitation, the latter non-relevant if one considers the negligibly small masses of the neutrinos. Consequently, the neutrinos can not be observed directly but only the secondary particles that are produced in the neutrino interactions with matter can be detected. Here, we are going to discuss the different channels of how neutrinos can weakly interact with matter and how these interactions look like by means of secondary particle topology. We will also see how the oscillation probabilities can be extracted from the neutrino interaction rates.

Neutrino Nucleus Interaction

We already saw in Chapter 2 that neutrinos can interact weakly by either the exchange of a $\mathrm{W}^{\pm}$ boson, referred to as a CC interaction, or by the exchange of a Z^{0} boson, referred to as an NC interaction. Let us assume that a neutrino ν_ℓ of any flavor ($l = \mathrm{e}, \nu, \tau$)

interacts with an atomic nucleus N. If the neutrino energy is below $\sim 1\,\mathrm{GeV}$, then the neutrino predominantly scatters off a single nucleon that is bound to the nucleus, and the nucleon stays intact. In the NC cases,

$$\nu_\ell + N \rightarrow \nu_\ell + N \tag{3.49}$$
$$\bar{\nu}_\ell + N \rightarrow \bar{\nu}_\ell + N, \tag{3.50}$$

we simply refer to it as elastic scattering, while in the CC cases,

$$\nu_\ell + \mathrm{n} \rightarrow \ell^- + \mathrm{p} \tag{3.51}$$
$$\bar{\nu}_\ell + \mathrm{p} \rightarrow \ell^+ + \mathrm{n}, \tag{3.52}$$

we refer to it as QE scattering or CC QE interaction, because of the kinematics similar to an elastic collision. At higher transferred momenta, the nucleons can be excited to resonant states which in turn decay inside the nucleus:

$$\nu_\mu + \mathrm{n} \rightarrow \mu^- + \Delta^+ \rightarrow \mu^- + \mathrm{n} + \pi^+ \tag{3.53}$$
$$\overline{\nu}_\mu + \mathrm{n} \rightarrow \mu^+ + \Delta^- \rightarrow \mu^+ + \mathrm{n} + \pi^-. \tag{3.54}$$

We call these interactions Resonant (RES), where Equations 3.53 and 3.54 are only two examples of many different possible RES interactions that can occur. These resonances are very short-lived such that detectors usually only see the final state particles. At even higher transferred momenta, the neutrino rather interacts with the quarks or partons than single nucleons. Hadronization destroys the respective nucleon while the nucleus N is changed or broken into a number of final fragments X:

$$\nu_\ell + N \rightarrow \nu_\ell + X \tag{3.55}$$
$$\bar{\nu}_\ell + N \rightarrow \bar{\nu}_\ell + X. \tag{3.56}$$

These highly inelastic interactions can occur by NC exchange, as shown above, as well as by CC exchange, and are referred to as Deep Inelastic Scattering (DIS). The opposite happens in the Coherent (COH) interaction. Here, the target nucleus stays in the ground state and the transferred momentum ends in the creation of a third particle, for example a neutral pion:

$$\nu_\ell + A \rightarrow \nu_\ell + A + \pi^0 \tag{3.57}$$
$$\bar{\nu}_\ell + A \rightarrow \bar{\nu}_\ell + A + \pi^0. \tag{3.58}$$

Another convention, referred to as $n\mathrm{p}n\mathrm{h}$, classes CC interactions by the number of nucleons (p) that take part in the interaction leaving a hole (h) in the nucleus. Accordingly, 1p1h corresponds to a CCQE interaction whereas in a 2p2h interaction a virtual meson is exchanged inside the nucleus, also called Meson Exchange Current (MEC).

Interactions With Shell Electrons

Neutrinos can interact in various ways with the shell electrons of atoms and molecules. A muon is produced in the so-called inverse muon-decay, which is only possible for μ-type neutrinos:

$$\nu_\mu + \mathrm{e}^- \quad \rightarrow \quad \mu^- + \nu_\mathrm{e} \tag{3.59}$$
$$\overline{\nu}_\mu + \mathrm{e}^- \quad \rightarrow \quad \mu^+ + \nu_\mathrm{e}. \tag{3.60}$$

The threshold energy for that reaction is relatively high because of the big mass difference between the electron and the muon, i.e. the squared four-momentum vector of the initial state has to be greater than the squared mass of the muon:

$$\begin{aligned} & (E_\nu + m_\mathrm{e})^2 - \boldsymbol{p}_\nu^2 \\ = \quad & E_\nu^2 + 2E_\nu m_\mathrm{e} + m_\mathrm{e}^2 - \boldsymbol{p}_\nu^2 \\ \simeq \quad & 2E_\nu m_\mathrm{e} + m_\mathrm{e}^2 \geq m_\mu^2 \end{aligned} \tag{3.61}$$

where E, m and $\boldsymbol{p}$ are the energy, mass and momentum of the respective particles, and the threshold energy becomes

$$E_\nu \geq \frac{m_\mu^2 - m_\mathrm{e}^2}{2m_\mathrm{e}} \simeq \frac{m_\mu^2}{2m_\mathrm{e}} = 10.92\,\mathrm{GeV}. \tag{3.62}$$

Accordingly, inverse muon-decay is suppressed in long-baseline experiments unless they operate at neutrino energies of tens of GeV. On the other hand, any flavor-type neutrino can elastically scatter on electrons by NC exchange:

$$\nu_\ell + \mathrm{e}^- \quad \rightarrow \quad \nu_\ell + \mathrm{e}^- \tag{3.63}$$
$$\bar{\nu}_\ell + \mathrm{e}^- \quad \rightarrow \quad \bar{\nu}_\ell + \mathrm{e}^-. \tag{3.64}$$

Additionally, elastic scattering on electrons is possible for ν_e and $\overline{\nu}_\mathrm{e}$ by CC exchange as well:

$$\nu_\mathrm{e} + \mathrm{e}^- \quad \rightarrow \quad \mathrm{e}^- + \nu_\mathrm{e} \tag{3.65}$$
$$\overline{\nu}_\mathrm{e} + \mathrm{e}^- \quad \rightarrow \quad \mathrm{e}^+ + \nu_\mathrm{e}. \tag{3.66}$$

The flavor dependence of neutrino-electron elastic scattering causes the difference in the total effective potentials in matter between electron flavor and muon/tauon flavor neutrinos. This potential difference gives rise to the already mentioned matter effects and reflects in different oscillation probabilities between neutrinos and antineutrinos.

Oscillation Measurement

Oscillation probabilities can not be measured by the FD directly. Instead, the neutrino interaction rates for the different flavors are measured as a function of the reconstructed neutrino energy at both the ND:

$$\frac{dN_\alpha^{ND}}{dE_{rec}} = \int \frac{\Phi_\alpha^{ND}(E_\nu)\,\sigma_\alpha(E_\nu)}{n^{ND}}\,T_\alpha^{ND}(E_\nu, E_\mathrm{rec})\,dE_\nu \tag{3.67}$$

and the FD:

$$\frac{dN_\alpha^{FD}}{dE_{rec}} = \int \frac{P_{\nu_\beta \to \nu_\alpha}(E_\nu)\, \Phi_\alpha^{FD}(E_\nu) \sigma_\alpha(E_\nu)}{n^{FD}}\, T_\alpha^{FD}(E_\nu, E_{\text{rec}})\, dE_\nu, \tag{3.68}$$

where

- α, β = neutrino flavors
- $P_{\nu_\beta \to \nu_\alpha}$ = oscillation probability
- N = event rate per target nucleus
- E_ν = true neutrino energy
- E_{rec} = reconstructed neutrino energy
- Φ = un-oscillated neutrino flux
- σ = neutrino interaction cross-section
- T = true-to-reconstructed neutrino energy transfer function
- n = number of target nuclei.

For simplicity, we assume that the target nucleus of the two detectors is identical. The un-oscillated neutrino flux at the FD needs to be predicted by simulations and feeds into the near-to-far flux ratio

$$R(E_\nu) = \frac{\Phi_\alpha^{FD}(E_\nu)\, n^{ND}}{\Phi_\alpha^{ND}(E_\nu)\, n^{FD}}, \tag{3.69}$$

such that Equation 3.68 can be rewritten in terms of the flux measured at the ND:

$$\frac{dN_\alpha^{FD}}{dE_{rec}} = \int \frac{R(E_\nu)\, P_{\nu_\beta \to \nu_\alpha}(E_\nu)\, \Phi_\alpha^{ND}(E_\nu)\, \sigma_\alpha(E_\nu)}{n^{ND}}\, T_\alpha^{FD}(E_\nu, E_{\text{rec}})\, dE_\nu. \tag{3.70}$$

Naively thinking, the oscillation probability can now be resolved as the ratio between Equations 3.70 and 3.67 weighted by the flux ratio:

$$\frac{dN_\alpha^{FD}}{dE_{rec}} \Big/ \frac{dN_\alpha^{ND}}{dE_{rec}} \simeq R(E_\nu)\, P_{\nu_\beta \to \nu_\alpha}(E_\nu). \tag{3.71}$$

However, as we will see in the next section, it is not possible to measure a pure near-to-far flux ratio because many effects do not cancel trivially. Even though we assumed identical target nuclei in the ND and the FD, the two detectors are not geometrically identical. Consequently, they will have different true-to-reconstructed neutrino energy transfer functions

$$T_\alpha^{ND}(E_\nu, E_{\text{rec}}) \neq T_\alpha^{FD}(E_\nu, E_{\text{rec}}) \tag{3.72}$$

such that

$$\frac{dN_\alpha^{FD}}{dE_{rec}} \Big/ \frac{dN_\alpha^{ND}}{dE_{rec}} \neq R(E_\nu)\, P_{\nu_\beta \to \nu_\alpha}(E_\nu). \tag{3.73}$$

3.7.3. Leading Uncertainties in Oscillation Measurements

We already saw that both the ND and FD need to measure the energy of the detected neutrinos. The energy is reconstructed from observed quantities and consequently a convolution of flux, cross section and detector response to the particles produced in the neutrino interaction. Uncertainties that are correlated among the ND and FD do cancel in the near-to-far predictions to a certain extent. Therefore, it is important to have the same target nucleus in both detectors and detection techniques as similar as possible. However, especially cross-section uncertainties and the detector response feed into the non-diagonal true-to-reconstructed neutrino energy transfer function, which is different for the ND and the FD. Therefore, it is an important task of the ND to provide the information that can be used to independently constrain the systematic errors of the flux, the cross section and the detector response. Following, we are going to characterize each of those three components to see how they can be constrained by measurements with the ND.

Flux

Neutrino flux uncertainties arise primarily from uncertainties in hadrons produced off the target and uncertainties in the beam parameters, e.g. horn currents and horn and target positioning. Hadron-production uncertainties dominate the absolute neutrino fluxes while uncertainties in the beam parameters dominate the near-to-far flux ratios. [8] Several techniques are used to constrain neutrino beam fluxes [22]:

- The total flux normalization and flux energy-spectrum or *shape* can be constrained by measuring neutrinos scattering off atomic electrons. The cross section of neutrino-electron elastic scattering can be calculated well because of its purely electroweak nature. On one side, counting neutrino-electron scatters allows to normalize the total neutrino flux. On the other side, the flux spectrum can be derived from the final state of the electron which is related to the neutrino energy by

$$1 - \cos(\theta) = \frac{m_\mathrm{e}(1-y)}{E_\mathrm{e}}, \tag{3.74}$$

  where θ is the angle between the incoming neutrino and the electron, m_e and E_e are the mass and the total energy of the electron and y is the fraction of the neutrino energy transferred to the electron.

- The ν_μ and $\overline{\nu}_\mu$ flux shapes can be constrained by the so-called low-ν scattering process, where low-ν refers to a low energy transfer between the neutrino and the target nucleus. Crucial for this method is that the CC inclusive[3] cross section of neutrinos does not depend on the neutrino energy in the limit where the energy transferred to the nucleus approaches zero (i.e. is less than a few 100 MeV). In

[3] Neutrino interaction cross-sections are called inclusive if any type and number of secondary particles aside the principle outgoing lepton are allowed.

that limit, the interaction rate is proportional to the flux and the flux shape can be derived by measuring the rate as a function of neutrino energy.

- Electron-neutrino contamination is an irreducible background in long-baseline neutrino oscillation experiments. The ν_e/ν_μ flux ratio can be constrained by beam simulations or by measurements requiring cross section universality.

Cross Section

Neutrino cross sections are modeled with neutrino interaction generators, such as *GENIE*, *NuWro* and *NEUT*. These generators try to model the various interaction channels that contribute to the total cross sections, which poses a highly non-trivial problem if the neutrino interacts with an atomic nucleus composed of several nucleons. Simply speaking, the neutrino-nucleus scattering process is usually factorized into an incoherent sum of hard scattering neutrino interactions with the single nucleons in the nucleus, and the effects of the nucleus are implemented as initial-state effects and FSI. Initial-state effects are related to the momentum and position distribution of the nucleons inside the nucleus, whereas FSI refers to the propagation and interaction of hadrons produced in the nucleon interaction through the nucleus. The nuclear system can carry away up to hundreds of MeV/c in the form of one or more heavy, non-relativistic particles. These particles typically carry off very little kinetic energy and consequently are invisible to the detector. [8]

The dominant uncertainties introduced by neutrino interaction generators (taken from Ref. [8]) are:

- initial state uncertainties
- hard scattering uncertainties and nuclear effects to the QE process
- hard scattering uncertainties in multi-nucleon (2p2h) processes
- hard scattering uncertainties in pion-production processes
- FSI uncertainties
- neutrino flavor dependent uncertainties

These uncertainties can be constrained by cross section measurements performed with the ND. In doing so, it is important that the target nucleus in the ND is the same as in the FD because neutrino interaction processes depend on the nuclear system of the target.

Detector

Neutrino detectors need the abilities to reconstruct the neutrino energy and identify the neutrino flavor in case of a CC interaction, or categorize the interaction as NC.

A neutrino CC QE interaction with a single-nucleon target follows two-body kinematics, and the neutrino energy can be reconstructed from the lepton angle and energy regardless of whether the nucleon is observed or not. That does not apply for multi-nucleon targets because of the unknown initial state of the nucleus and FSI. Here, the calorimetric method is needed to reconstruct the neutrino energy, i.e. all energies carried away by particles produced in the neutrino interaction need to be measured and summed up. Initial-state effects and FSI pose a big problem for calorimetry because they can not be identified by the detectors. Also neutral particles that carry away big amounts of energy from the vertex and stay undetected introduce serious errors to the reconstructed neutrino energy. These types of errors can be constrained by the true-to-reconstructed neutrino energy transfer function which is determined from detector simulations and unique to each detector. Obviously, these uncertainties do not cancel trivially in the near-to-far predictions because the ND is smaller and consists of more subsystems than the FD in order to fulfill its various tasks.

Another type of errors arises from the mis-identification of the interaction type, either by wrong reconstruction or by backgrounds. The same detection methods in the ND and the FD can help to mitigate interaction mis-identification because a bias in the identification efficiency as a function of neutrino energy will cancel between the two detectors. On the other hand, due to similarity, backgrounds characterized by the ND can be used to constrain backgrounds at the FD. [22]

3.8. Next-Generation Long-Baseline Neutrino Experiments

Now, that we learned about the design, working principle and difficulties of long-baseline neutrino-oscillation experiments, we are going to have a look at the two big next-generation long-baseline neutrino-oscillation experiments planned for the future. The first experiment is Hyper-K in Japan, the successor of the T2K experiment, and the second experiment is the new Deep Underground Neutrino Experiment (DUNE) in the USA.

3.8.1. Hyper-KamiokaNDE

Hyper-K is designed as a large-scale water Čerenkov neutrino detector. The 60 m tall, cylindrical tank with a diameter of 74 m contains 258 kt of highly transparent, purified water. The inner segment of the tank, referred to as Inner Detector, reflects the main active volume and is instrumented with 40 000 inward-facing 50 cm ⌀ photo sensors. The outer segment is called Outer Detector and monitored by 6700 outward-facing 20 cm ⌀

photo sensors. This part will be used as a veto for entering particles, such as cosmic ray muons. [21]

Hyper-K will be hosted by the Tochibora mine near Kamioka town, about 295 km away from the J-PARC in Tokai, Japan. The detector will be placed at a depth of 650 m and will be the largest underground water Čerenkov detector in the world. New near detectors are considered to measure the un-oscillated beam in order to predict event rates at Hyper-K and to constrain systematic uncertainties. The existing proton accelerator at J-PARC will be steadily upgraded to reach a 1 MW-beam. [21]

The Hyper-K technical design is illustrated in Figure 3.5. The cylindrical tank is 60 m

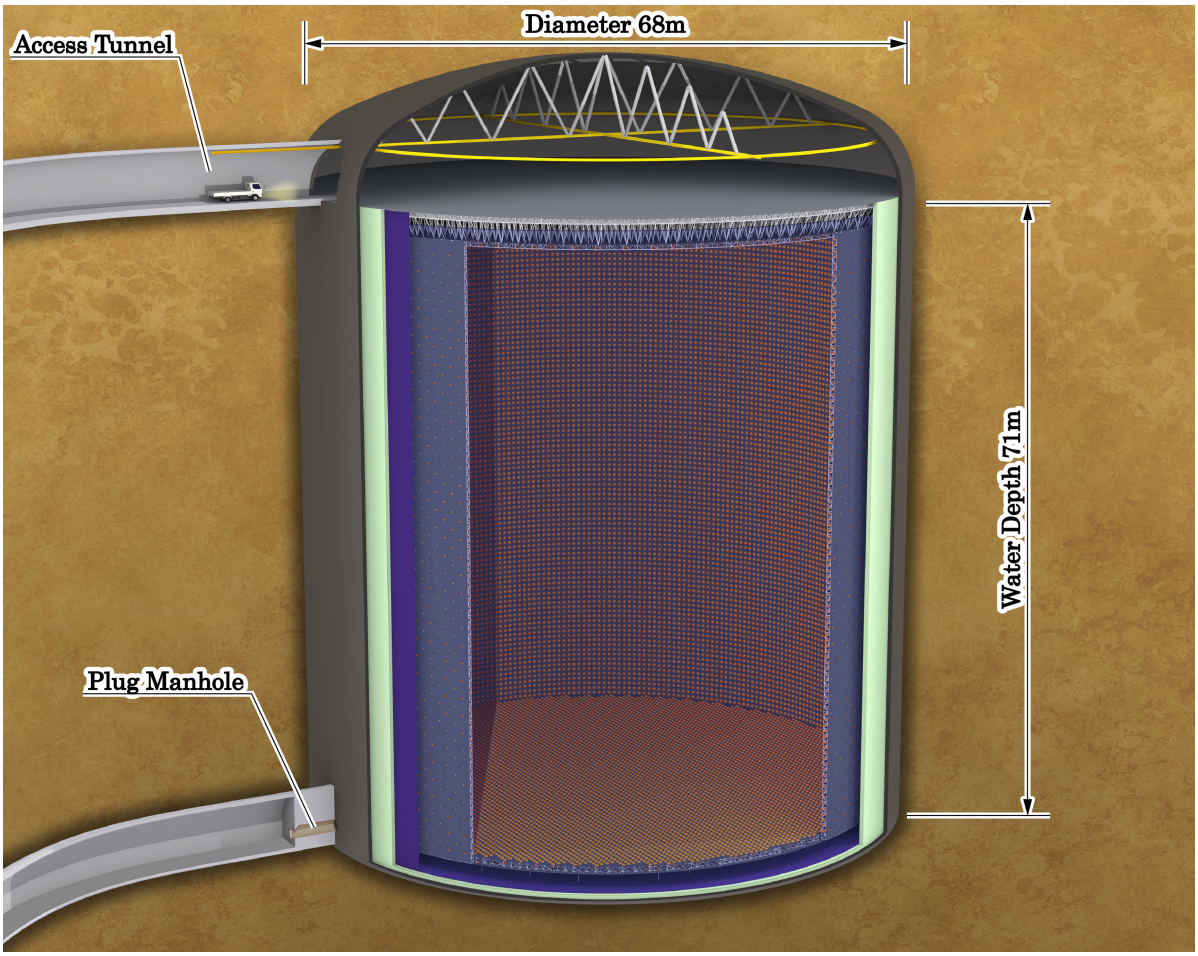

Figure 3.5.: The Hyper-K technical design. The cylindrical tank is 60 m tall and 74 m wide, and filled with 258 kt of highly transparent purified water (dimensions from Ref. [21]). 40 000 photo sensors with a diameter of 50 cm are facing the Inner Detector, and 6700 photo sensors with a diameter of 20 cm are facing the Outer Detector. [71]

tall and 74 m wide, and filled with 258 kt of highly transparent purified water. 40 000 photo sensors with a diameter of 50 cm are facing the Inner Detector, and 6700 photo

sensors with a diameter of 20 cm are facing the Outer Detector.

The key features of Hyper-K (taken from Ref. [21]) will be:

- capability to measure leptonic CP violation with highest precision
- excellent capability to search for proton decay
- atmospheric-neutrino measurements to determine the neutrino mass ordering
- detection of supernovae
- precision measurements of solar-neutrino oscillations

The Hyper-K project has officially been approved in 2020 and operations are planned to begin in 2027 [72].

3.8.2. Deep Underground Neutrino Experiment

DUNE is an international experiment hosted by FNAL in Illinois, USA. The massive FD will be composed of four cryogenic 10 kt LAr detectors resulting in a total active mass of 40 kt. The detection principle is that of TPCs enabling to reconstruct neutrino interactions with image-like precision and unprecedented resolution. A thorough discussion on the detection and working principles of LArTPCs will follow in Chapter 4. The FDs will be located $\sim$ 1.5 km underground at the SURF in South Dakota, 1300 km from the neutrino source. [22]

A composite ND will be built 574 m downstream of the beam source at FNAL. The core component of the ND is a segmented 50 t fiducial mass LArTPC constructed according to the *ArgonCube* technology originally developed at the University of Bern. Downstream, next to the LArTPC, will sit a Gaseous Argon (GAr) TPC with the main task to act as a spectrometer for particles that exit the LArTPC. The third component following further downstream will be a System for on-Axis Neutrino Detection (SAND). SAND will continuously monitor the neutrino beam and register any changes in the beam focusing or the beam composition. A unique feature of the DUNE ND is the so-called DUNE Precision Reaction-Independent Spectrum Measurement (DUNE-PRISM), which allows the LArTPC and the GAr TPC to move sideways and acquire data off the beam axis. [23]

The beamline will be provided by the Long-Baseline Neutrino Facility (LBNF) project, also hosted by FNAL. It will deliver the the world's most intense high-energy neutrino beam to the NDs and the FDs in an on-axis configuration. Particle accelerators will deliver a 1.2 MW beam of 120 GeV protons to the production target. A further planned upgrade to the accelerator complex could even provide up to 2.4 MW of proton beam power by 2030. [23]

The DUNE experimental setup and beamline are shown in Figure 3.6. Beam neutrinos are produced by a high-energy proton beam impinging an interaction target at the FNAL accelerator complex. A composite ND, also at FNAL, characterizes the un-oscillated neutrino beam 574 m downstream of the beam source. Four massive FDs at SURF

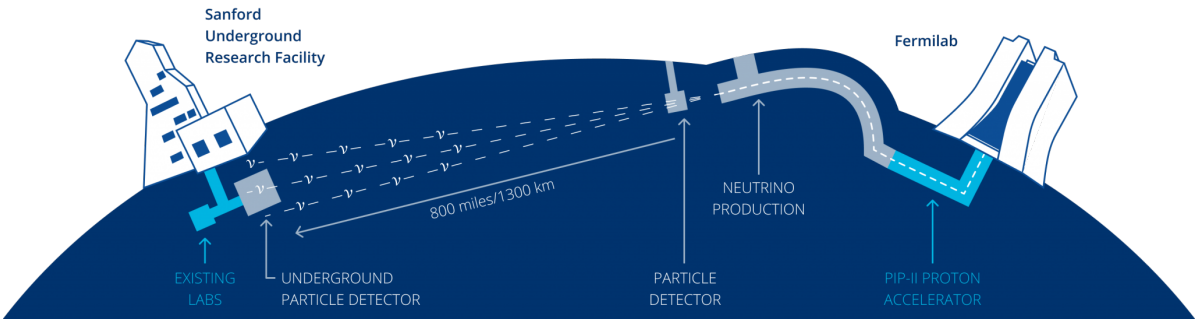

Figure 3.6.: The DUNE experimental setup and beamline. Beam neutrinos are produced by a high-energy proton beam impinging an interaction target at the FNAL accelerator complex. A composite ND, also at FNAL, characterizes the un-oscillated neutrino beam 574 m downstream of the beam source. Four massive FDs at SURF measure interactions of the oscillated beam 1300 km from the beam production site at FNAL. [73]

measure interactions of the oscillated beam 1300 km from the beam production site at FNAL.

The principle physics goals of DUNE (taken from Ref. [8]) are:

- observation of leptonic CP violation at the 3σ confidence level or better, over a wide range of possible values of δ_{CP}
- determination of the neutrino mass ordering
- measurement of the mixing angle θ_{23} and the determination of the octant in which this angle lies ($\theta_{23} < 45^\circ$ or $\theta_{23} > 45^\circ$)
- sensitive tests of the three-neutrino paradigm
- search for proton decay in several decay modes
- detect and measure the ν_{e} flux from a core-collapse supernova within our galaxy

On 21 July 2017 groundbreaking was held in South Dakota marking the start of excavation for LBNF, the future home to the international DUNE [74], and constructions begun in the mid 2020's.

3.9. Deep Underground Neutrino Experiment

The methods presented in this work apply to LArTPC neutrino detectors as they will be used by the DUNE ND. Accordingly, here, we are going to see how the DUNE beam looks like at the ND site, and we are going to have a detailed look at the ND itself. We will discuss the targeted sensitivities and allowed uncertainties of the DUNE ND to

achieve the DUNE physics goals. Furthermore, we will discuss in detail the technical requirements on the LAr component of the DUNE ND to fulfill these goals.

3.9.1. Near Detector Beam Environment

The DUNE neutrino-beam starts with a new purpose-built linear accelerator featured by FNAL's Proton Improvement Plan-II (PIP-II), which accelerates protons up to 800 MeV. Subsequently, the proton beam gains more energy as is proceeds through FNAL's chain of particle accelerators and eventually reaches 120 GeV in the largest accelerator, the Main Injector (MI). At this stage, the protons are ready for extraction in order to produce the world's most intense high-energy beam of neutrinos. The further path of the proton beam is illustrated in Figure 3.7. After the extraction point (at the right-hand side of the

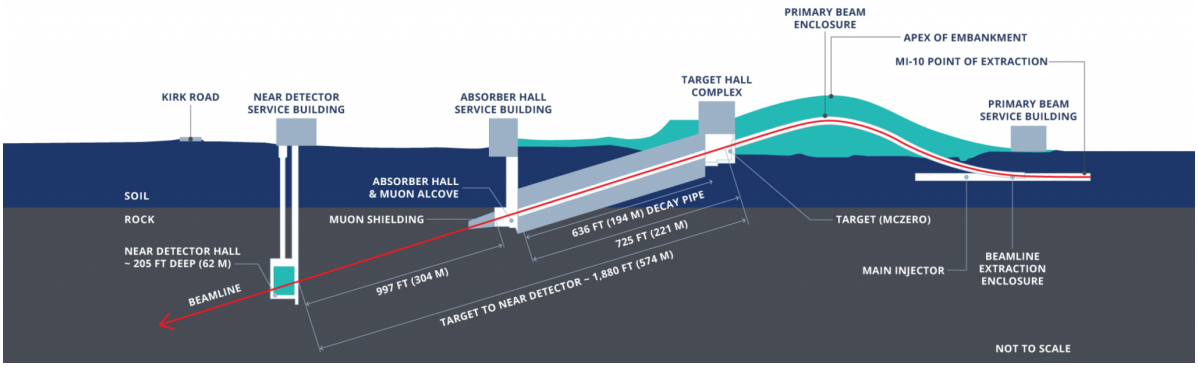

Figure 3.7.: The DUNE beamline at the ND site. After the extraction point (at the right-hand side of the figure), the proton beam passes a man-made hill with an apex 18.3 m from the ground where it is bent down by 7.2° towards a target. Mesons produced by the protons hitting the solid interaction target are focused by magnetic horns into a 194 m long decay pipe where they decay into muons and neutrinos. A muon shielding at the end of the decay pipe absorbs the muons and any other charged particle contaminations. Left over is a pure neutrino beam that intersects with the DUNE ND 574 m from the interaction target. [73]

figure), the beam passes a man-made hill with an apex 18.3 m from the ground, where it is bent down by 7.2° towards a target. Mesons produced by the protons hitting the solid graphite target are focused by magnetic horns into a 194 m long decay pipe, where they decay into muons and neutrinos. The magnetic horns can be run in both modes Forward Horn Current (FHC) (ν_μ mode) and Reversed Horn Current (RHC) ($\overline{\nu}_\mu$ mode). A muon shielding at the end of the decay pipe absorbs the muons and any other charged particle contaminations. What remains is a pure neutrino beam that intersects with the DUNE ND 574 m downstream from the interaction target. The focusing structure provides a wide band neutrino beam with neutrino energies from 0.5 GeV to 5 GeV to cover the first and second neutrino oscillation maxima at the distance of the FD. [75]

A comparison between the DUNE flux spectrum and the spectra of other neutrino oscillation experiments is shown in Figure 3.8. GENIE cross sections for the different

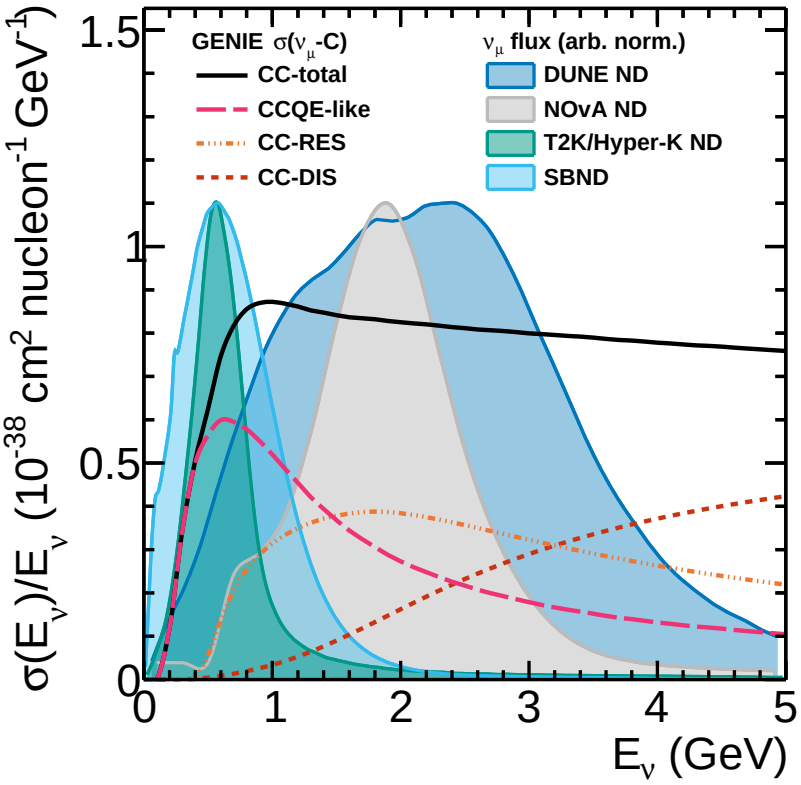

Figure 3.8.: Comparison between the DUNE flux spectrum and the spectra of other neutrino-oscillation experiments, overlaid with GENIE cross sections for the different CC neutrino-nucleus interaction channels, as a function of the neutrino energy. Plot by C. Wilkinson (LBNL).

CC neutrino-nucleus interaction channels are shown as a function of the neutrino energy. Compared to the T2K/Hyper-K ND, which mainly sees CC QE-like interactions, the DUNE ND will have to deal with large fractions of CC RES and CC DIS interactions.

The neutrino beam is structured into spills with a duration of 10 µs. Different beam designs with cycle times between 0.7 s and 1.2 s, and proton energies between 60 GeV and 120 GeV, have been considered. The current design uses a 1.2 MW beam of 120 GeV protons. A summary of the LBNF beam parameters for the phase I (1 MW power) and the planned phase II (2 MW beam power) of the DUNE experiment is given in Table 3.3. The numbers in the last column represent the expected event rates per tonne of LAr and per beam spill in the DUNE ND. While the event rate in the FD will be only ~ 3.4 beam neutrinos per hour, the event rate in the LAr ND will be as many as 15 (30) neutrinos every 10 µs beam spill. In contrast with the FD, the high multiplicity environment of the ND entailed a very different and novel approach to the LArTPC design in order to mitigate event pile-up. [75]

Table 3.3.: Summary of the LBNF beam parameters for the phase I (1 MW power) and the planned phase II (2 MW beam power) of the DUNE experiment. The numbers in the last column represent the expected event rates per tonne of LAr and per beam spill in the DUNE ND. [24, 75]

Phase	Proton Energy [GeV]	POT per Spill	Spill Period [s]	Beam Power [MW]	Event Rate [t_{LAr}^{-1}]
I	60	7.5×10^{13}	0.7	1.03	0.08
I	80	7.5×10^{13}	0.9	1.07	0.11
I	120	7.5×10^{13}	1.2	1.20	0.17
II	60	1.5×10^{14}	0.7	2.06	0.16
II	80	1.5×10^{14}	0.9	2.14	0.21
II	120	1.5×10^{14}	1.2	2.40	0.33

3.9.2. Near Detector

The ND site, which is shown in Figure 3.9, is composed of a surface building, the underground ND hall and a connecting service shaft with a diameter of ~ 12 m. The ND hall is at a depth of ~ 62 m reducing the flux of cosmic rays to an expected $\mathcal{O}(1)$ $m^{-2}\,s^{-1}$, which is about two orders of magnitude less compared to the flux at the surface. The ND itself is a complex of three primary detector components with two of those components having the capability to move off the beam axis. On one hand, each of the detector components has complementary standalone features, and on the other hand, they have overlapping functions to suffice the DUNE physics requirements. [23]

ND-LAr

The core component of the DUNE ND is the LArTPC constructed using the ArgonCube technology. This component is called ND-LAr. It uses the same target nucleus and the same fundamental detection principle as the FD, thus reducing the sensitivity to nuclear effects and detector-driven systematic uncertainties in the extraction of the oscillation signal at the FD. ND-LAr is massive enough to provide 1×10^8 ν_μ-CC events per year in the on-axis position and has a sufficient volume to provide containment of hadronic interactions. The detector is segmented into 35 individual, optically isolated TPCs (or modules) that will be discussed in detail in Chapter 5. In the latest design, these modules are arranged in an array of 7×5 modules, with the detector 7 modules wide and having 5 modules along the beam axis, as depicted in Figure 3.10. The modules are hosted in a common bath of purified LAr contained in a custom designed membrane cryostat. Being part of DUNE-PRISM, ND-LAr will have the capability to move off-axis for extended beam studies.

The standalone ND-LAr starts to lose acceptance for muons above ~ 0.7 GeV/c due to lack of containment. Because the muon momentum and charge are crucial for the neutrino

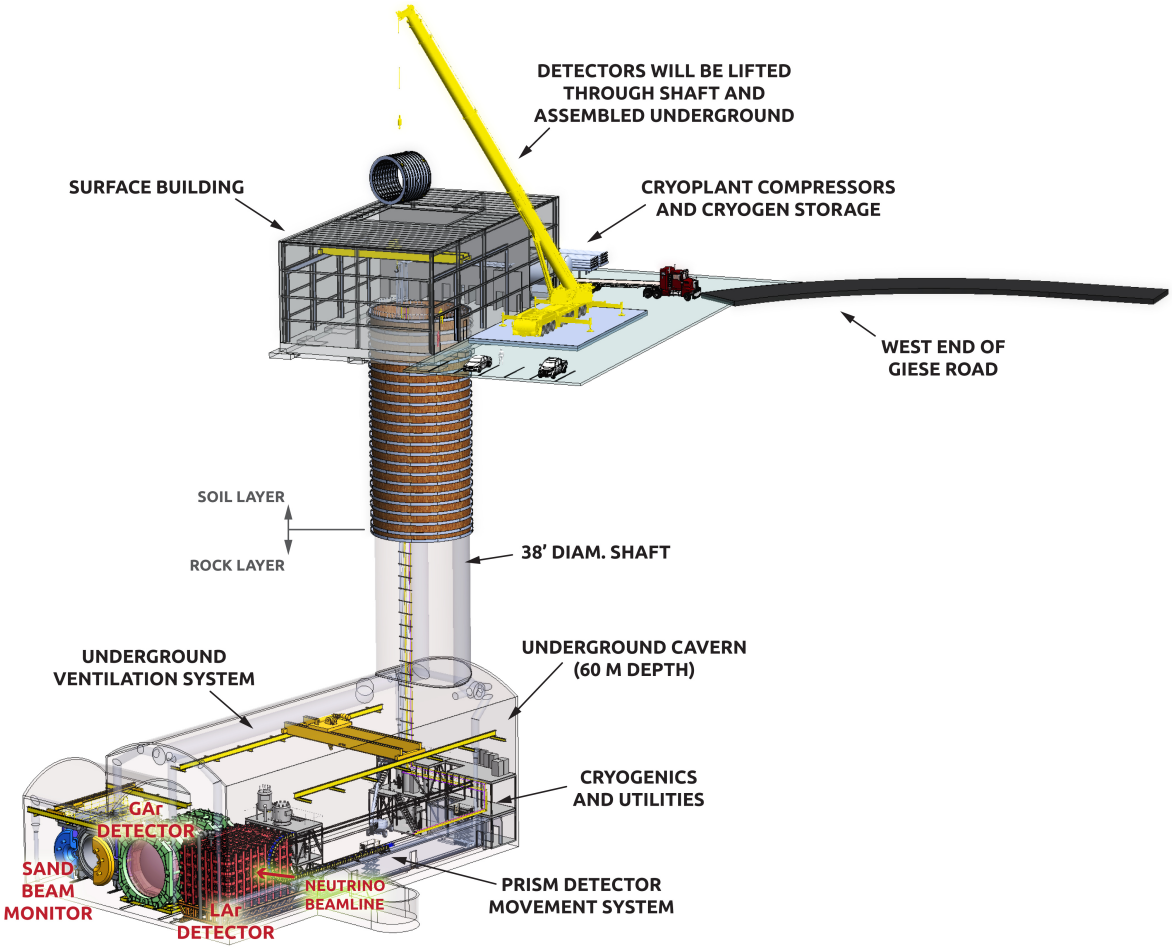

Figure 3.9.: Illustration of the DUNE-ND site, which is composed of a surface building, the underground ND hall and a connecting service shaft. The ND itself is a complex of three primary detector components (labeled *LAr DETECTOR*, *GAr DETECTOR* and *SAND BEAM MONITOR*), with two of those components having the capability to move off the beam axis (labeled *PRISM DETECTOR MOVEMENT SYSTEM*). [76]

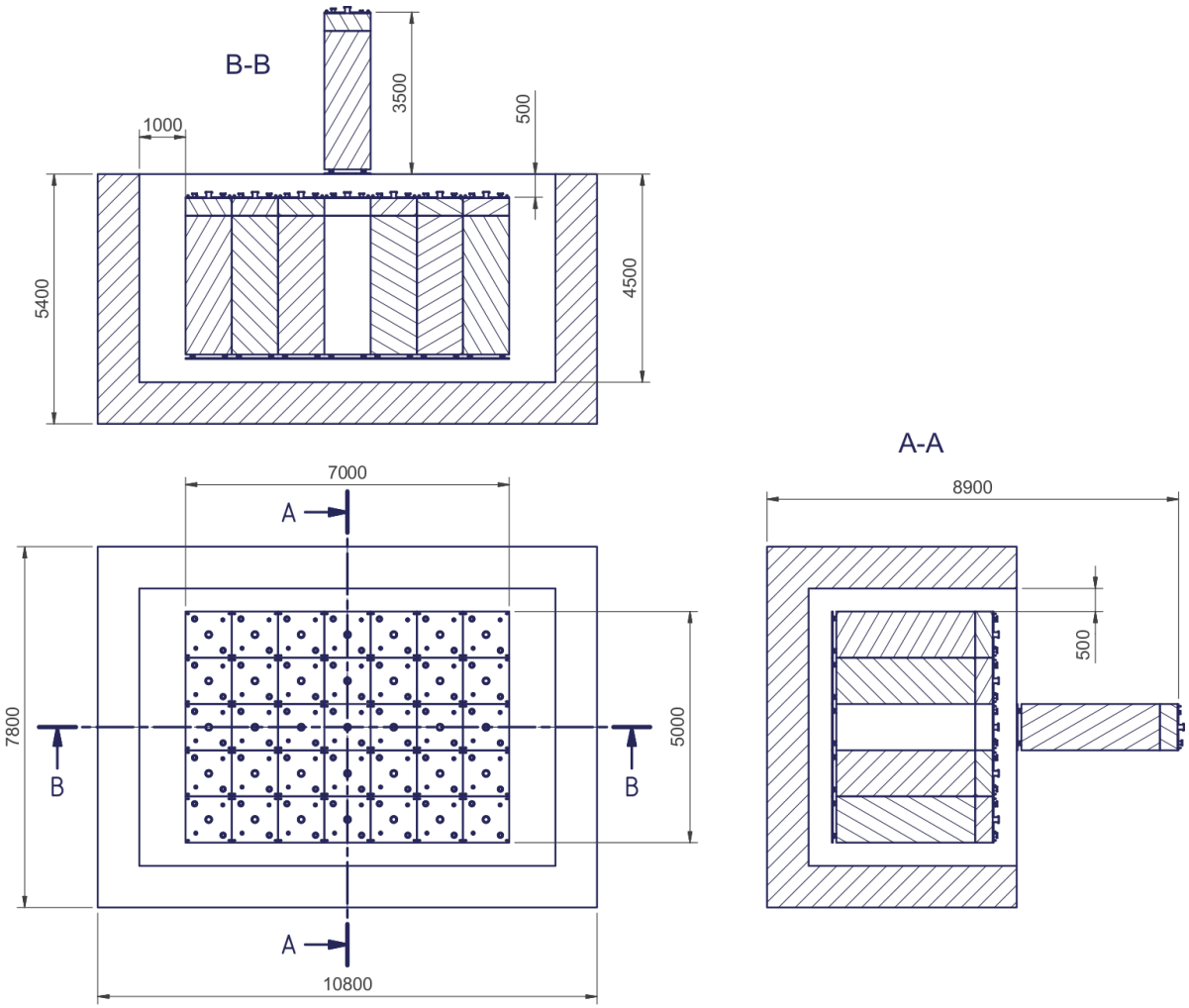

Figure 3.10.: Technical drawing of the module configuration in ND-LAr. The modules are hosted in a common bath of purified LAr contained in a custom designed membrane cryostat, where they are arranged in an array of 7×5 modules, 7 modules wide and 5 modules along the beam axis. [23]

energy reconstruction, a magnetic spectrometer is planned downstream of ND-LAr. This spectrometer uses gaseous argon and has the name ND-GAr. [23]

ND-GAr

ND-GAr is a magnetized composite detector (shown in Figure 3.11) that contains a central high-pressure GAr TPC as core component. The TPC is surrounded by an ECAL

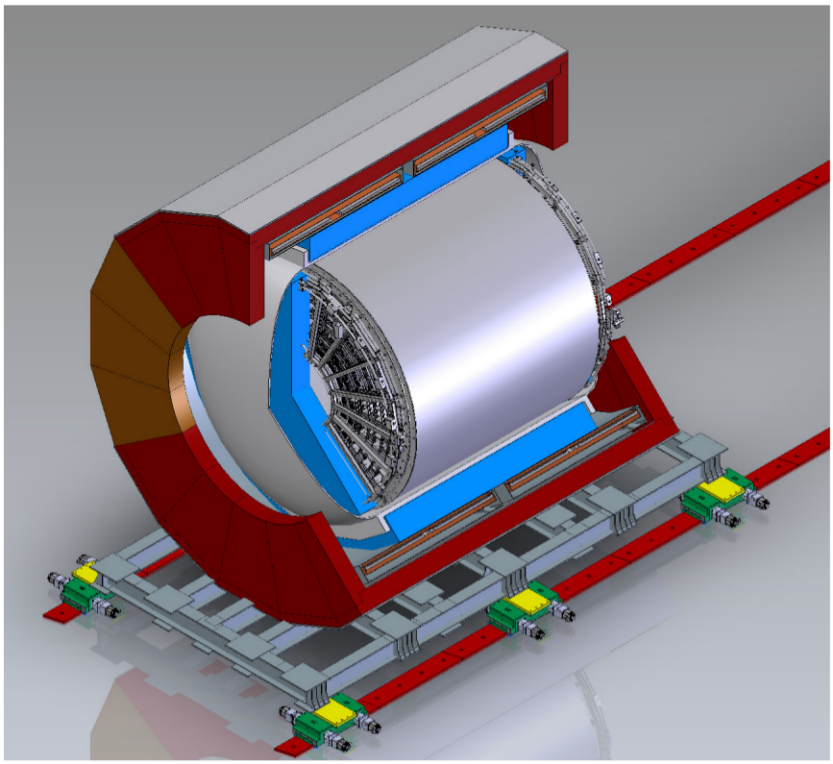

Figure 3.11.: Technical drawing of ND-GAr showing the central high-pressure GAr TPC (silver) surrounded by an Electromagnetic Calorimeter (ECAL) (blue), and with superconducting solenoid magnets (orange) providing the 0.5 T magnetic field. [23]

(blue). Both the GAr TPC and the ECAL are placed in a 0.5 T magnetic field which is provided by two superconducting solenoid magnets (orange). Further detectors planned for muon tagging are not shown in Figure 3.11. ND-GAr will be mounted to the same DUNE-PRISM movement system as ND-LAr providing the capability to move off-axis together with ND-LAr. [23]

ND-GAr extends and enhances the capabilities of the ND by providing a system that will measure the momentum and sign of charged particles exiting ND-LAr. Additionally, the gaseous argon in the TPC represents a target for neutrino interactions and allows to measure charged particles to lower energies than achievable in ND-LAr, and greatly extends particle identification. These capabilities enable further constraints of systematic uncertainties for oscillation analysis. [23]

SAND

The third primary detector of the DUNE ND is SAND, the System for on-Axis Neutrino Detection, which will be monitoring the beam-neutrino energy spectra in order to constrain flux uncertainties. The system will be magnetized and as such re-purpose the 0.6 T KLOE superconducting magnet, which comes already equipped with an ECAL. Inside the magnet will be an active tracking region made of many $1 \times 1 \times 1$ cm^3 plastic scintillator cubes, based on the *SuperFGD* design, developed for the T2K-ND upgrade [77]. Each cube is optically isolated and read out by three orthogonal wavelength-shifting fibers, providing three-dimensional tracking. Accordingly, this subsystem is named 3D Scintillator Tracker (3DST). The 3DST is surrounded on the top, bottom, and downstream sides by low-density tracking chambers that measure the charge and momentum of outgoing particles. The final design of the tracking chambers was not yet decided. A thin LAr target is also foreseen inside the magnetic volume between the tracking region and the upstream inner edge of the ECAL. A technical drawing of SAND highlighting the different subsystems is shown in Figure 3.12: the 3DST in the center (light green), low-density trackers (magenta), ECALs (green), the magnet coil (gold), and the return yoke (gray). [23]

SAND must be able to provide a statistically significant feedback on the beam spectrum, the beam profile, and the event rate over a time window of maximum one week. Herefore, it will measure CC neutrino interactions in the upstream ECAL as well as in the 3DST. The momentum and sign of the charged particles will be reconstructed from measurements in the low-density trackers.

SAND is the only of the three primary detector components that will not be able to move off-axis. The decision was made based upon two reasons. Firstly, the spectrum on the beam axis is more sensitive to some changes in the beam parameters than that of off-axis, and secondly, the constant on-axis monitoring helps to ensure that the changes in the off-axis flux are due to the movement of the detectors and not changes in the beam itself. [23]

3.9.3. DUNE PRISM

The relationship between the energy reconstructed from final state particles of neutrino interactions and the true energy of the incident neutrinos is currently not understood well enough to achieve the DUNE physics goals. That is primarily due to the missed energy from undetected particles and due to misidentified particles, which produces a shift towards lower reconstructed neutrino energy relative to the true energy. This shift does not cancel in the near-to-far flux ratio because the neutrino energy spectra at the ND and the FD are very different due to geometry and neutrino oscillations. [23]

We already learned that the observed quantities in neutrino detectors are a convolution of flux, cross section and detector response to the particles produced in the neutrino interactions, which means that the individual uncertainties contain correlated components. By measuring the neutrino beam at different off-axis positions, DUNE-PRISM will allow to deconvolve the flux and cross-section models and to constrain them separately. It will also provide a powerful handle for understanding the true-to-reconstructed neutrino

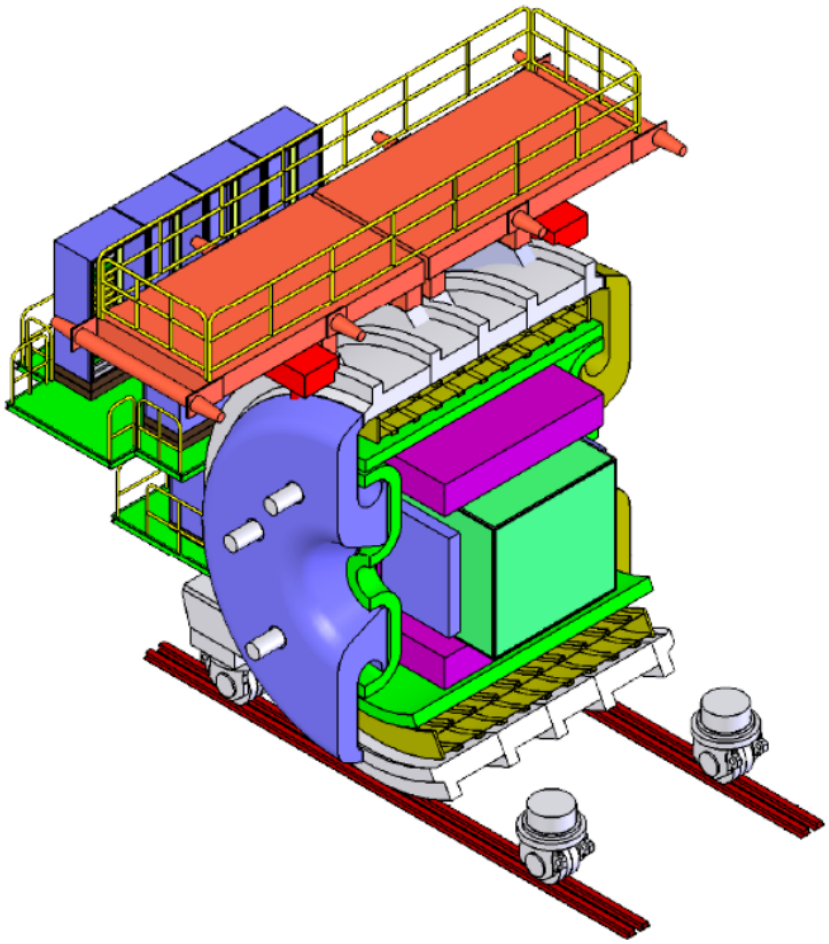

Figure 3.12.: Technical drawing of SAND showing the 3DST in the center (light green), low-density trackers (magenta), ECALs (green), the magnet coil (gold), and the return yoke (gray). [23]

energy mapping, which is applicable to the FD up to the degree to which ND-LAr and the FD are similar. A linear combination of the fluxes at different off-axis positions allows to create a data sample at the ND with an effective neutrino energy distribution that is close to that of the oscillated spectrum at the FD. Such procedure minimizes errors arising from the near-to-far flux difference, particularly those related to the neutrino interaction model. [23]

ND-LAr and ND-GAr will have the capability to move together off the beam axis up to 30.5 m ($\sim 3°$), while SAND will steadily monitor the beam neutrino flux on-axis. Figure 3.13 shows the expected neutrino energy spectra at different off-axis positions compared to the on-axis spectrum.

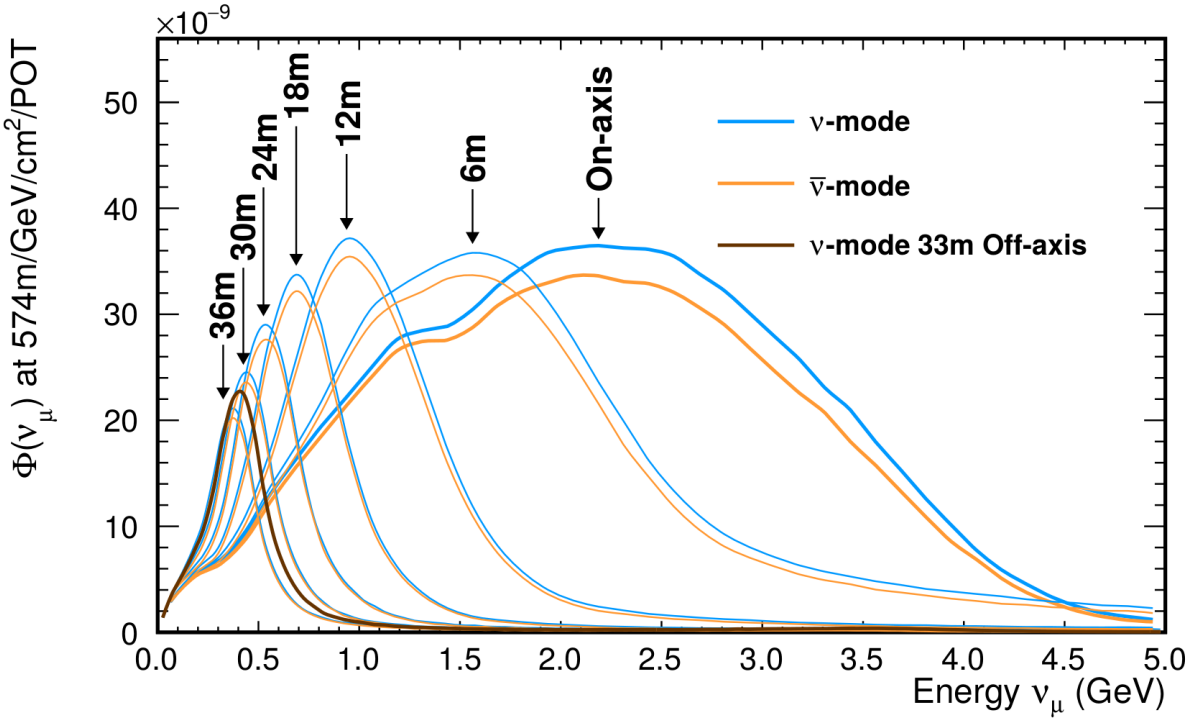

Figure 3.13.: DUNE-PRISM energy spectra at different off-axis positions w.r.t. the beam. A linear combination of the fluxes at different off-axis positions allows to create a data sample at the ND with an effective neutrino energy distribution that is close to that of the oscillated spectrum at the FD. The technique will allow to deconvolve the uncertainties arising from different sources, and to constrain them separately. [22]

3.9.4. Physics Sensitivities

The amount of statistically significant data acquired by long-baseline neutrino detectors is usually specified by the number of protons that impinge on the interaction target, and is referred to as Protons On Target (POT). DUNE assumes an annual 1.1×10^{21} POT using the 1.2 MW neutrino beam design. As a reference, Table 3.4 lists the expected

numbers of neutrinos interacting per 10^{20} POT and per tonne of LAr at the distance of the DUNE ND. [8]

Table 3.4.: Expected DUNE-ND interaction rates per 10^{20} POT and per tonne of LAr. [78]

Production Mode	ν_μ Events	$\overline{\nu}_\mu$ Events
CC QE ($\nu_\mu \mathrm{n} \to \mu^- \mathrm{p}$)	30 000	13 000
NC elastic ($\nu_\mu N \to \nu_\mu N$)	11 000	6700
CC resonant ($\nu_\mu \mathrm{p} \to \mu^- \mathrm{p}\pi^+$)	21 000	0
CC resonant ($\nu_\mu \mathrm{n} \to \mu^- \mathrm{n}\pi^+$ or $\nu_\mu \mathrm{n} \to \mu^- \mathrm{p}\pi^0$)	23 000	0
CC resonant ($\overline{\nu}_\mu \mathrm{p} \to \mu^+ \mathrm{p}\pi^-$ or $\overline{\nu}_\mu \mathrm{p} \to \mu^+ \mathrm{n}\pi^0$)	0	8300
CC resonant ($\overline{\nu}_\mu \mathrm{n} \to \mu^+ \mathrm{n}\pi^-$)	0	12 000
NC resonant ($\nu_\mu \mathrm{p} \to \nu_\mu \mathrm{p}\pi^0$ or $\nu_\mu \mathrm{p} \to \nu_\mu \mathrm{n}\pi^+$)	7000	0
NC resonant ($\nu_\mu \mathrm{n} \to \nu_\mu \mathrm{n}\pi^0$ or $\nu_\mu \mathrm{n} \to \nu_\mu \mathrm{p}\pi^-$)	9000	0
NC resonant ($\overline{\nu}_\mu \mathrm{p} \to \overline{\nu}_\mu \mathrm{p}\pi^0$ or $\overline{\nu}_\mu \mathrm{p} \to \overline{\nu}_\mu \mathrm{n}\pi^+$)	0	3900
NC resonant ($\overline{\nu}_\mu \mathrm{n} \to \overline{\nu}_\mu \mathrm{n}\pi^0$ or $\overline{\nu}_\mu \mathrm{n} \to \overline{\nu}_\mu \mathrm{p}\pi^-$)	0	4700
CC DIS ($\nu_\mu N \to \mu^- X$ or $\overline{\nu}_\mu N \to \mu^+ X$)	95 000	24 000
NC DIS ($\nu_\mu N \to \nu_\mu X$ or $\overline{\nu}_\mu N \to \overline{\nu}_\mu X$)	31 000	10 000
CC coherent π^+ ($\nu_\mu A \to \mu^- A\pi^+$)	930	0
CC coherent π^- ($\overline{\nu}_\mu A \to \mu^+ A\pi^-$)	0	800
NC coherent π^0 ($\nu_\mu A \to \nu_\mu A\pi^0$ or $\overline{\nu}_\mu A \to \overline{\nu}_\mu A\pi^0$)	520	450
NC elastic electron ($\nu_\mu \mathrm{e}^- \to \nu_\mu \mathrm{e}^-$ or $\overline{\nu}_\mu \mathrm{e}^- \to \overline{\nu}_\mu \mathrm{e}^-$)	16	11
Inverse Muon Decay ($\nu_\mu \mathrm{e}^- \to \mu^- \nu_\mathrm{e}$)	9.5	0
Total CC	170 000	59 000
Total NC+CC	230 000	84 000

The DUNE FD fiducial volume is planned to gradually increase as of the beginning of data taking, with an initial beam power of 1.2 MW:

- Start of data taking: two FD modules totaling 20 kt fiducial mass, 1.2 MW beam power.
- One year after start: add one FD module totaling 30 kt fiducial mass, 1.2 MW beam power.
- Three years after start: add one FD module totaling 40 kt fiducial mass, 1.2 MW beam power.
- Six years after start: upgrade to 2.4 MW beam power.

Figure 3.14 shows the significance at which DUNE will be able to measure CP violation given the above run plan with equal exposure times for FHC and RHC, and a dedicated

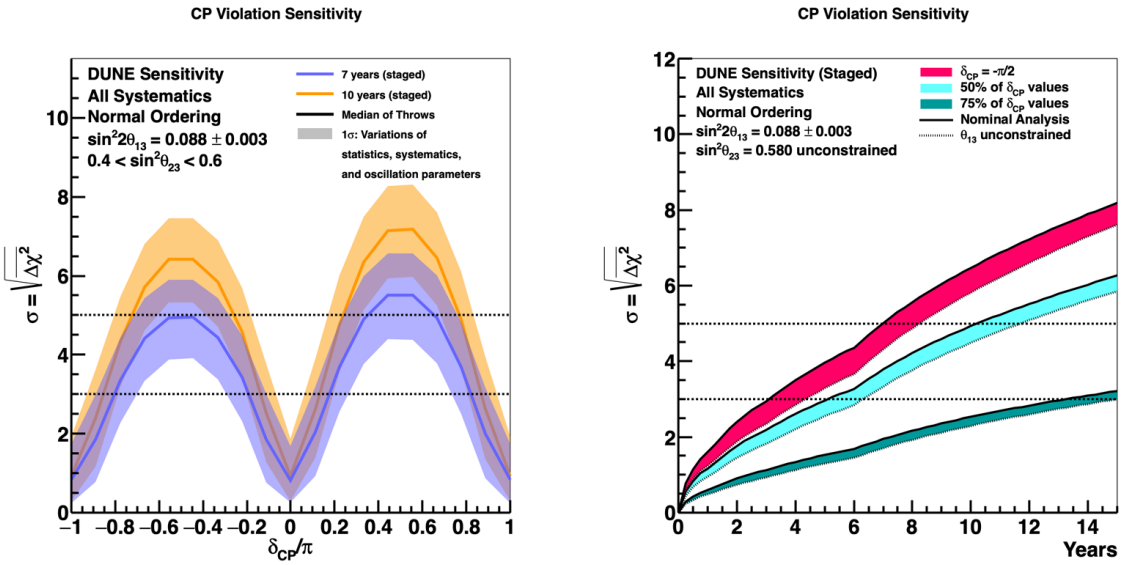

(a) **(b)**

Figure 3.14.: CP-violation sensitivity of DUNE as a function of exposure time (assuming equal exposure in FHC and RHC). The left-hand plot (a) shows the significance as a function of δ_{CP} for seven and ten years. Sensitivities drop to nearly zero at CP conserving phases ($\delta_{\mathrm{CP}} = 0$ or $\pm\pi$). The right-hand plot (b) shows the significance at which CP violation can be determined for 75 % and 50 % of δ_{CP} values , and when $\delta_{\mathrm{CP}} = -\pi/2$. CP violation can be observed with 5σ significance after about 7 years if $\delta_{\mathrm{CP}} = -\pi/2$ and after about 10 years for 50 % of δ_{CP} values. [8]

procedure to constrain systematic errors. The left-hand plot (a) shows the significance as a function of δ_{CP} for seven and ten years. The width of the transparent bands represent 68 % of fits when random throws are used to simulated statistical variations and select true values of the oscillation and systematic uncertainty parameters, and the solid line represents the median sensitivity. Sensitivities drop to nearly zero at CP conserving phases ($\delta_{CP} = 0$ or $\pm\pi$). The right-hand plot (b) shows the significance at which CP violation can be determined for 75 % and 50 % of δ_{CP} values , and when $\delta_{CP} = -\pi/2$, as a function of exposure time. The width of the bands show the impact of applying an external constraint on θ_{13}. CP violation can be observed with 5σ significance after about 7 years if $\delta_{CP} = -\pi/2$ and after about 10 years for 50 % of δ_{CP} values. [8]

Figure 3.15 shows the significance at which DUNE will be able to determine the neutrino mass ordering given the above run plan with equal exposure times for FHC and RHC and a dedicated procedure to constrain systematic errors. The left-hand plot

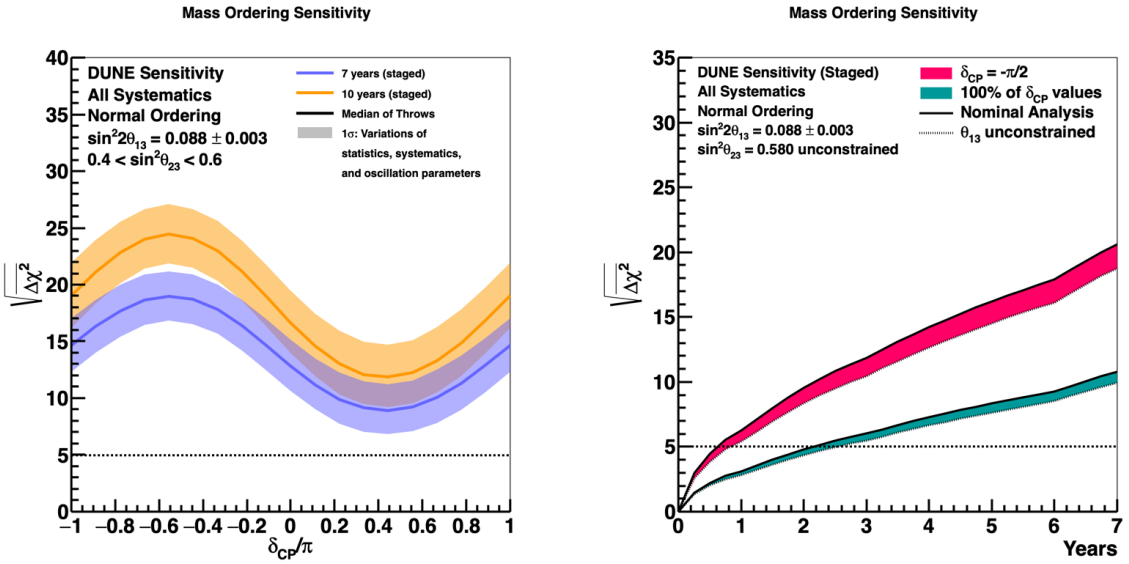

(a) **(b)**

Figure 3.15.: Mass-ordering sensitivity of DUNE as a function of exposure time (assuming equal exposure in FHC and RHC). The left-hand plot (a) shows the significance as a function of δ_{CP} for seven and ten years. The right-hand plot (b) shows the significance at which the neutrino mass ordering can be determined for 100 % of δ_{CP} values , and when $\delta_{CP} = -\pi/2$. DUNE will be able to determine the neutrino mass ordering at the 5σ level for 100 % of δ_{CP} values after between two and three years. [8]

(a) shows the significance as a function of δ_{CP} for seven and ten years. Same as in the CP-violation sensitivity, the width of the transparent bands represents 68 % of fits when random throws are used to simulated statistical variations and select true values of the oscillation and systematic uncertainty parameters, and the solid line represents the median sensitivity. The right-hand plot (b) shows the significance at which the neutrino

mass ordering can be determined for 100 % of δ_{CP} values , and when $\delta_{CP} = -\pi/2$, as a function of exposure time. The width of the bands show the impact of applying an external constraint on θ_{13}. DUNE will be able to determine the neutrino mass ordering at the 5σ level for 100 % of δ_{CP} values after between two and three years. [8]

Last but not least, we are going to list the requirements on the DUNE ND in order to reach the scope of sensitivities described above.

3.9.5. Near Detector Requirements

The ultimate overreaching requirement on the ND in the context of the long-baseline neutrino oscillation measurement is to predict the expected observable neutrino spectrum at the FD as a function of the oscillation parameters. Secondary ND requirements, needed to fulfill that ultimate goal, are:

1. ND measurements must be transferable to the FD, accounting for uncertainties regarding detector response, cross section and flux. Since the FDs are LArTPCs, the ND must be able to measure interactions on an argon target and must have a component that is a LArTPC.

2. The ND must sufficiently measure and constrain the uncertainties in the cross-section modeling to minimize their impact on the oscillation measurement.

3. The prediction of the neutrino flux is based on simulation and has significant uncertainties that must be constrained by the ND.

4. The ND must verify that its model predictions and constraints are robust by taking data with different neutrino spectra.

5. The ND must promptly detect variations in the flux and spectrum of neutrinos to minimize impact on the overall data quality.

6. The ND must be able to operate in a high-rate environment, i.e. must be able to separate cosmic rays, rock muons, and other beam-induced activity from the activity associated with neutrino interactions in the fiducial volume, including event pile-up.

There are two significant constraints which drive the design and requirements of the ND. Firstly, the choice of the LArTPC technology for the FD drives requirement #1. And secondly, the intense LBNF beam and the relatively shallow ND hall drive requirement #6. Since the methods presented in this work are exclusively applicable to TPCs operated with noble-gas liquids, we are only going to discuss the design requirements on the ND LAr component, which will be subject to Chapter 5. [23]

4. Liquid Argon Time Projection Chamber

In Chapter 4, I will discuss the working principle of TPCs that use LAr as the sensitive detector medium, and their application as particle detectors. In the first half of this chapter, we will see how different types of particles interact with matter, and I will describe the physical quantities and equations that are used to characterize these interactions and to calculate their interaction probabilities. In the second half, we will learn the basic functionality of the TPC with a focus on LArTPCs. We will see why LAr is a promising sensitive detector medium and how LArTPCs can track and identify different particle types and simultaneously determine their energy.

4.1. Passage of Particles Through Matter

Whenever particles pass through matter they loose energy by collisions with other particles, assuming the incoming particles are energetic enough that the target nuclei can be seen as at rest. The target nuclei themselves can be represented by entire molecules, atoms, atomic nuclei or even single nucleons. It is a non-trivial problem to describe such energy losses as the transferred momenta depend on many factors like the energy, mass and charge of the incoming particle, as well as the mass and charge distribution of the target nuclei. Semi-empirical equations have been elaborated for different categories of incoming particles: heavy charged particles with masses much greater than the electron mass, light charged particles (electrons and positrons), and the massless and uncharged photons.

4.1.1. Cross Section and Mean Free Path

There are two quantities commonly used in particle physics if it comes to the question on how frequent a particle interacts while passing through matter: the cross section σ and the mean free path λ. In order to get an idea of the physical meaning of the cross section, we want to assume that we have a uniform flux of identical particles that hit a target volume with unity thickness. Furthermore, we assume that several scatter nuclei are uniformly distributed within that target volume in a way that they do not overlap as seen from the flux direction. Such a setup is illustrated in Figure 4.1. Whenever an impinging particle hits one of the target nuclei, it is scattered away, whereby the size of the nuclei is only a hypothetical quantity meant to reflect the natural ratio between particles being scattered off and particles passing the target. From that point of view, the

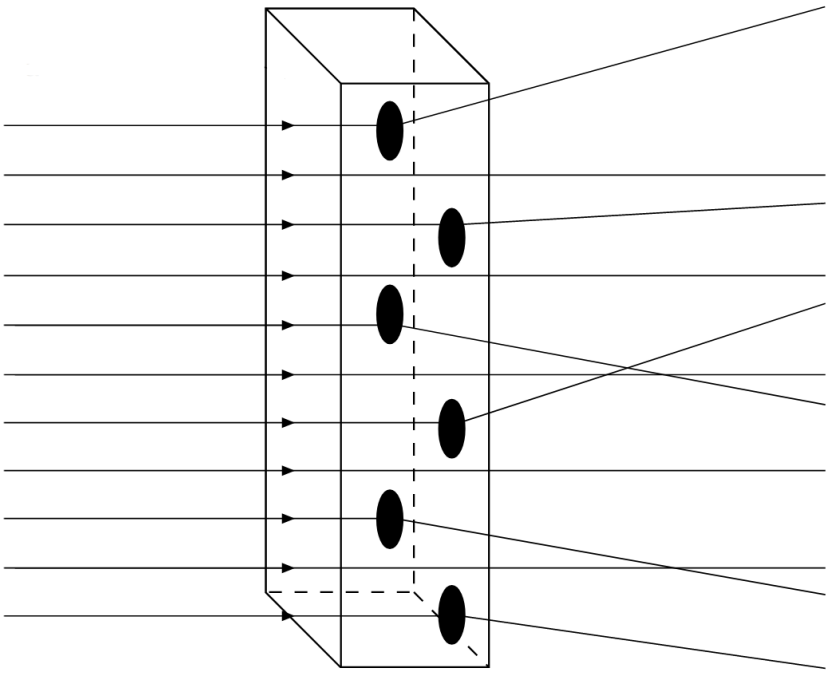

Figure 4.1.: Illustration of the scattering cross-section. A uniform flux of identical particles hit a target volume with unity thickness. Whenever an impinging particle hits one of the target nuclei, it is scattered away, whereby the size of the nuclei is only a hypothetical quantity meant to reflect the natural ratio between particles being scattered off and particles passing the target. From that point of view, the scattering cross section of a single nucleus is defined as the two-dimensional projection of its volume onto the plane perpendicular to the beam axis, thus having the dimension of an area. The figure is taken from Ref. [79] and modified.

scattering cross-section of a single nucleus is defined as the two-dimensional projection of its volume onto the plane perpendicular to the beam axis, thus having the dimension of an area.

For a target at rest, the scattering cross section depends on the energy of the incoming particle E as well as the scattering angle of the outgoing particle. For that reason, cross sections are often defined in the differential form

$$\frac{d\sigma}{d\Omega}(E,\Omega) = \frac{1}{\Phi}\frac{dN_s}{d\Omega}, \tag{4.1}$$

where Φ is the flux per unit area and per unit time, Ω is the steradiant and N_s is the average number of particles scattered into $d\Omega$ per unit time. The total cross section can be obtained by integrating the differential cross section over the full sphere of scattering angles:

$$\sigma(E) = \int \frac{d\sigma}{d\Omega} d\Omega. \tag{4.2}$$

If the flux source is a beam wider than the interaction target, then the number of particles scattering into $d\Omega$ can be obtained from the differential cross section by the multiplication

$$N_s(\Omega) = \Phi A_\perp N \delta x \frac{d\sigma}{d\Omega}, \tag{4.3}$$

where $A_\perp$ is the target area perpendicular to the beam axis, N is the number density of nuclei in the target and δx is the thickness of the target along the beam axis. On the other hand, the total number of scattering particles can be obtained from the total cross section by

$$N_{\text{tot}} = \Phi A_\perp N \delta x \sigma. \tag{4.4}$$

Now, let us have a look how things change if we assume a beam narrower than the interaction target. On one hand, the interaction probability P_{int} of a single particle within the target thickness δx is simply

$$P_{\text{int}}(\delta x) = N \delta x \sigma. \tag{4.5}$$

On the other hand, the general probability P of a particle surviving a distance x in the target material is exponential in distance:

$$P(x) = e^{x/\lambda}, \tag{4.6}$$

where λ is the mean free path. From Equation 4.6, we can see that the mean free path is by definition the length over which the fraction of particles not suffering an interaction reduces to $1/e$. In contrary, the probability of suffering an interaction anywhere in the distance x is

$$P_{\text{int}}(x) = 1 - e^{x/\lambda}. \tag{4.7}$$

For a small thickness δx, the interaction probability in Equation 4.7 can be approximated by Taylor's expansion dropping higher order terms of λ as

$$P_{\text{int}} = 1 - \left(1 - \frac{\delta x}{\lambda} + \dots\right) \approx \frac{\delta x}{\lambda}. \tag{4.8}$$

Comparing Equations 4.5 and 4.8 we find the useful relation

$$\lambda = \frac{1}{N\sigma}, \tag{4.9}$$

that we will make use of later in this chapter. [80]

4.1.2. Energy Loss by Heavy Charged Particles

The *Bethe-Bloch formula* describes the linear stopping power of moderately relativistic[1], charged heavy particles in matter due to ionization (collisions with shell electrons), with the linear stopping power defined as the average energy loss per unit path-length:

$$-\left(\frac{dE}{dx}\right)_{\text{coll}} = Kz^2\rho\frac{Z}{A}\frac{1}{\beta^2}\left[\frac{1}{2}\ln\left(\frac{2m_e c^2\beta^2\gamma^2 W_{\max}}{I^2}\right) - \beta^2 - \frac{\delta(\beta\gamma)}{2} - \frac{C}{Z}\right]. \tag{4.10}$$

Here,

$$K = 4\pi N_A r_e^2 m_e c^2 \tag{4.11}$$

is a constant with N_A Avogadro's number, m_e the electron mass, c the speed of light and r_e the classical electron radius defined as

$$r_e = \left(\frac{1}{4\pi\epsilon_0}\frac{e^2}{m_e c^2}\right), \tag{4.12}$$

with e the elementary charge and ϵ_0 the vacuum dielectric permittivity. z it the charge in units of e of the incident particle, ρ the density of the absorbing material and Z and A are the atomic number and the atomic weight of the absorbing material, respectively. The velocity v of the incident particle relative to the speed of light is defined by $\beta = \frac{v}{c}$, whereby the Lorentz factor γ is defined as

$$\gamma = \frac{1}{\sqrt{1-\beta^2}}. \tag{4.13}$$

$W_{\max}$ is the maximum energy transferred in a single collision, defined as

$$W_{\max} = \frac{2m_e c^2\beta^2\gamma^2}{1 + 2\gamma m_e/M + (m_e/M)^2}, \tag{4.14}$$

[1] When $0.1 \lesssim \beta\gamma \lesssim 1000$, with $\beta = \frac{v}{c}$ and γ the Lorentz factor according to Equation 4.13.

with M the mass of the incoming particle and I the mean excitation potential. Values of I for several materials have been deduced from actual measurements of dE/dx and can be obtained from semi-empirical equations for I vs. Z as given in Ref. [80]:

$$\frac{I}{Z} = 12 + \frac{7}{Z}\ \text{eV} \qquad Z < 13 \tag{4.15}$$

and

$$\frac{I}{Z} = 9.76 + 58.8\, Z^{-1.19}\ \text{eV} \qquad Z \geq 13. \tag{4.16}$$

δ and C are higher-order density and shell corrections to the Bethe-Bloch formula, which are important at high and low energies respectively. At sufficiently high energies, losses due to radiation become more important than losses due to ionization, for all charged particles. This radiative process, where electromagnetic radiation is emitted due to scattering of the charged particle in the electric field of a nucleus, is called *bremsstrahlung*, and will be discussed later.

In practice, it is often more convenient to use the mass stopping power

$$-\frac{1}{\rho}\left(\frac{dE}{dx}\right)_{\text{coll}} = z^2 \frac{Z}{A} f(\beta, I) \tag{4.17}$$

instead of the linear stopping power, because the mass stopping power is almost independent of the material type as both the ratio (Z/A) and $I(Z)$ vary very little for similar Z. Figure 4.2 shows the mass stopping power for different absorber materials as a function of particle momentum (normalized by the particle mass M and c). At non-relativistic energies, the ionization is dominated by the $1/\beta^2$ term and decreases with increasing energy up to $\beta \approx 0.96$, where the minimum

$$-\frac{1}{\rho}\left(\frac{dE}{dx}\right)_{\text{coll}}\Bigg|_{\text{min}} \approx 2\,\text{MeV}\,\text{g}^{-1}\,\text{cm}^2 \tag{4.18}$$

is reached. A particle that looses energy close to that minimum loss rate is called a Minimum Ionising Particle (MIP). At higher energies, one can observe a *relativistic rise* due to the logarithmic dependence of the Bethe-Bloch formula. This rise is partially canceled by the density correction.

The mass stopping power for mixtures and compounds is described by *Bragg's Rule*:

$$\frac{1}{\rho}\left(\frac{dE}{dx}\right)_{\text{coll}} = \sum_i \left[\frac{w_i}{\rho_i}\left(\frac{dE}{dx}\right)_{\text{coll},i}\right], \tag{4.19}$$

where

$$w_i = \frac{a_i A_i}{\sum_i a_i A_i} \tag{4.20}$$

is the weight fraction of the i-th element, a_i the number of atoms of the i-th element and A_i the atomic weight of the i-th element in the mixture or compound. [80]

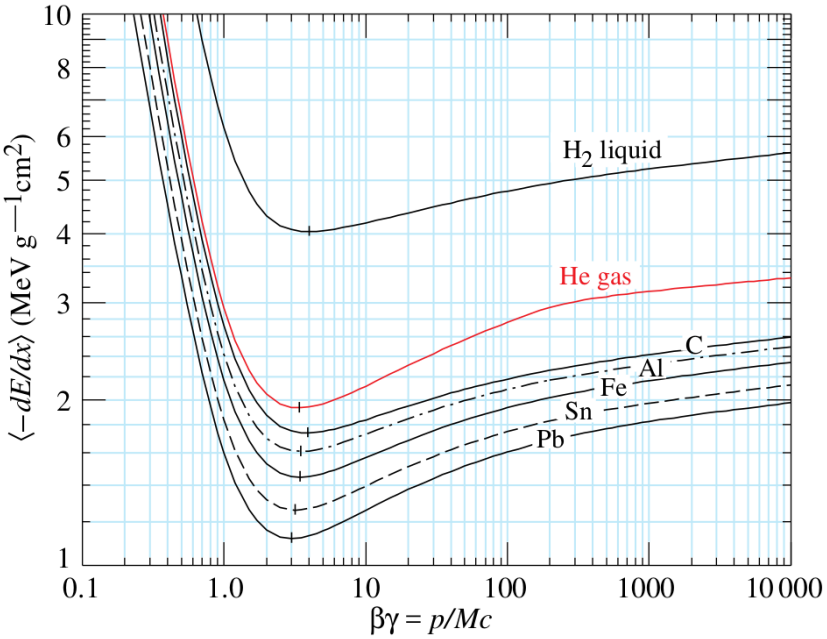

Figure 4.2.: Mass stopping power of charged particles with a mass M with respect to the particle momentum, for different absorber materials. At non-relativistic, energies the ionization is dominated by the $1/\beta^2$ term and decreases with increasing energy up to $\beta \approx 0.96$, where the minimum of $\sim 2\,\mathrm{MeV\,g^{-1}\,cm^2}$ is reached. At higher energies, one can observe a relativistic rise due to the logarithmic dependence of the Bethe-Bloch formula. This rise is partially canceled by the density correction. The figure is taken from Ref. [62] and modified.

4.1.3. Energy Loss by Electrons and Positrons

The stopping power for heavy charged particles (Eq. 4.10) does not apply for electrons and positrons, because of different kinematics, spin, charge and, in case of the electron, the identity of the incident particle with the electrons that it ionizes. Furthermore, in case of the positron, electron-positron annihilation must be taken into account. The total stopping power for electrons and positrons is the sum off the energy losses due to ionizing collisions and the energy losses due to radiation:

$$\left(\frac{dE}{dx}\right)_{\text{tot}} = \left(\frac{dE}{dx}\right)_{\text{coll}} + \left(\frac{dE}{dx}\right)_{\text{rad}}. \tag{4.21}$$

Semi-empirical approaches for the collisional energy losses are

$$-\left(\frac{dE}{dx}\right)_{\text{coll}} = \frac{1}{2}K\rho\frac{Z}{A}\frac{1}{\beta^2}\left[\ln\left(\frac{2m_ec^2\beta^2\gamma^2\{m_ec^2(\gamma-1)/2\}}{I^2}\right) + (1-\beta^2)\right. \tag{4.22}$$

$$\left. -\frac{2\gamma-1}{\gamma^2}\ln(2) + \frac{1}{8}\left(\frac{\gamma-1}{\gamma}\right)^2 - \delta(\beta\gamma) - 2\frac{C}{Z}\right] \qquad \text{(electrons)}$$

and

$$-\left(\frac{dE}{dx}\right)_{\text{coll}} = \frac{1}{2}K\rho\frac{Z}{A}\frac{1}{\beta^2}\left[\ln\left(\frac{2m_ec^2\beta^2\gamma^2\{m_ec^2(\gamma-1)\}}{2I^2}\right) + 2\ln(2)\right. \tag{4.23}$$

$$\left. -\frac{\beta^2}{12}\left(23 + \frac{14}{\gamma+1} + \frac{10}{(\gamma+1)^2} + \frac{4}{(\gamma+1)^3}\right) - \delta(\beta\gamma) - 2\frac{C}{Z}\right], \qquad \text{(positrons)}$$

and can be found in Refs [62, 80] among others. At energies below a few hundred GeV, electrons and positrons are the only particles for which energy losses due to radiation contribute substantially to the total energy loss of the particle.

Energy losses due to radiation (bremsstrahlung) are characterized by the so-called radiation length X_0, which is defined as the length over which the energy of the incident particle reduces to a fraction $1/e$:

$$-\left(\frac{dE}{dx}\right)_{\text{rad}} = \frac{E}{X_0} \quad \Longrightarrow \quad E = E_0 e^{-x/X_0}. \tag{4.24}$$

In the high-energy limit, where collisional energy losses can be ignored relative to radiative losses, the radiation length can be approximated as

$$\frac{1}{X_0} \approx 4\alpha r_e^2 \rho \frac{N_A}{A} Z(Z+1)\left[\ln\left(\frac{183}{Z^{1/3}}\right) - f(Z)\right], \tag{4.25}$$

with

$$f(Z) = a^2\left[(1+a^2)^{-1} + 0.20206 - 0.0369\,a^2 + 0.0083\,a^4 - 0.002\,a^6\right] \tag{4.26}$$

and $a = \alpha Z$, where $\alpha \approx \frac{1}{137}$ is the fine structure constant. The term $Z(Z+1)$ in Equation 4.25 reflects the two different contributions of the absorber material with $X_0 \propto Z^{-2}$ for the nucleus and $X_0 \propto Z^{-1}$ for the electrons. Same as for the mass stopping power, the radiation length of a mixture or a compound is described by Bragg's Rule:

$$\frac{1}{\rho X_0} = \sum_i \frac{w_i}{\rho_i X_i}, \tag{4.27}$$

where ρ_i is the density of the i-th element, X_i is the radiation length of the i-th element and w_i is the weight fraction of the i-th element in the mixture/compound as defined in Equation 4.19.

Beyond that, we can define the so-called critical energy E_c, at which energy losses due to collisions are at the same order as energy losses due to radiation:

$$\left(\frac{dE}{dx}\right)_{\text{coll}}\Bigg|_{E_c} = \left(\frac{dE}{dx}\right)_{\text{rad}}\Bigg|_{E_c}. \tag{4.28}$$

For electrons and positrons, E_c is at the $\mathcal{O}(10-100)$ MeV, depending on the absorbing material. Since the critical energy is proportional to the squared mass of the incident particle, radiative losses barely matter for particles other than electrons and positrons. A rough approximation for the critical energy of the muon

$$E_c(\mu^-) \approx E_c(\mathrm{e}^-) \left(\frac{m_\mu}{m_\mathrm{e}}\right)^2 \tag{4.29}$$

yields $E_c(\mu^-) \approx 400\,\mathrm{GeV}$, if we assume $E_c(\mathrm{e}^-) = 10\,\mathrm{MeV}$. [80]

4.1.4. Multiple Coulomb Scattering

Charged particles traversing a medium can be deflected by many small-angle scatters due to Coulomb scattering from nuclei. This effect is called Multiple Coulomb Scattering (MCS). The resulting net scattering and displacement can be approximated by Gaussian distributions. For MCS from a single material, the Root Mean Square (RMS) of the scattering distribution is

$$\theta^{\text{rms}}_{\text{space}} = \frac{13.6\,\mathrm{MeV}}{pv} z \sqrt{\frac{x}{X_0}} \left[1 + 0.038 \ln\left(\frac{xz^2}{X_0\beta^2}\right)\right], \tag{4.30}$$

where p, v, and z are the momentum, velocity, and charge number of the incident particle, and x is the thickness of the scattering medium. The scattering distributions projected onto planes along the direction of motion are assumed identical and independent of the plane orientation, such that the respective RMS

$$\theta^{\text{rms}}_{\text{plane}} = \frac{1}{\sqrt{2}} \theta^{\text{rms}}_{\text{space}}. \tag{4.31}$$

The distinct momentum dependence of MCS can be exploited to reconstruct the momentum of the incident particle, provided the angular resolution of the detector is good enough. [62]

4.1.5. Energy Loss by Photons

In optics, the intensity loss of light due to propagation in matter is described by an exponential decay characterized by the material specific mass attenuation coefficient μ. After a path length x, the initial intensity I_0 reduces to

$$I(x) = I_0 e^{-\mu x}. \tag{4.32}$$

In particle physics, this attenuation is usually characterized by the inverse of the attenuation coefficient, the so-called (electromagnetic) attenuation length

$$\lambda^{\mathrm{EM}} = \frac{1}{\mu}. \tag{4.33}$$

Here, we can make use of the relation 4.9 to express the attenuation coefficient in terms of the cross section (or vice-versa):

$$\mu = N\sigma, \tag{4.34}$$

where the number density of nucleons (atoms/cm^3)

$$N = \rho\frac{N_A}{A}. \tag{4.35}$$

There are three basic effects that contribute to energy losses by photons: the *photoelectric effect*, *Compton scattering* and *pair production*. In the photoelectric effect, energy from the photon is transferred to the electron shell of the absorbing material, while the atomic nucleus acts as a spectator only. For photon energies above the K-shell energy, it is almost always the K electrons which are involved in the photoelectric effect. Given that assumption for non-relativistic photons[2], the cross section can be calculated using a Born approximation:

$$\sigma_{\mathrm{ph}} = \sqrt{\frac{32}{\zeta^7}}\alpha^4 Z^5 \sigma_{\mathrm{Th}}, \tag{4.36}$$

with

$$\zeta = \frac{E_\gamma}{m_e c^2} \qquad \text{and} \qquad \sigma_{\mathrm{Th}} = \frac{8}{3}\pi r_e^2, \tag{4.37}$$

where E_γ is the photon energy and σ_{Th} the Thomson cross-section that describes scattering of photons by free electrons in the classical limit.

Compton scattering describes the scattering of photons by free electrons assuming the photon energy is high compared to the binding energy of the shell electrons. The Compton cross-section can be calculated from the Klein-Nishina formula and is the sum of the Compton absorption and the Compton scattering cross-sections:

$$\sigma_{\mathrm{C}} = \sigma_{\mathrm{C,a}} + \sigma_{\mathrm{C,s}} \tag{4.38}$$

$$= 2\pi r_e^2 \left[\frac{1+\zeta}{\zeta^2}\left(\frac{2(1+\zeta)}{1+2\zeta} - \frac{1}{\zeta}\ln(1+2\zeta)\right) + \frac{1}{2\zeta}\ln(1+2\zeta) - \frac{1+3\zeta}{(1+2\zeta)^2}\right], \tag{4.39}$$

[2]When the photon energy $h\nu \ll m_e c^2$, where h the Planck constant and ν the photon frequency.

where

$$\sigma_{\mathrm{C,s}} = 2\pi r_e^2 \left[\frac{1}{\zeta^3} \ln(1+2\zeta) + \frac{2(1+\zeta)(2\zeta^2 - 2\zeta - 1)}{\zeta^2 (1+2\zeta)^2} + \frac{8\zeta^2}{3(1+2\zeta)^3} \right] \tag{4.40}$$

is defined as the average fraction of the total energy transferred to the recoil electron, and

$$\sigma_{\mathrm{C,a}} = \sigma_{\mathrm{C}} - \sigma_{\mathrm{C,s}} \tag{4.41}$$

is defined as the average fraction of the total energy contained in the scattered photon.

Photons with energies equal to or above 1.022 MeV can undergo pair production. In this process the photon converges into an electron/positron pair by the presence of an atomic nucleus. Pair production can physically be seen an inverted process to bremsstrahlung. Accordingly, the pair production cross-section in the high-energy limit

$$\sigma_{\mathrm{pair}} = 4\alpha r_e^2 Z(Z+1) \left[\frac{7}{9} \ln\left(\frac{182}{Z^{1/3}} \right) - f(Z) \right], \tag{4.42}$$

where collision loss can be ignored relative to radiation loss, looks very similar to Equation 4.25. Same as the radiation length for bremsstrahlung, the mean free path for pair production

$$\frac{1}{\lambda_{\mathrm{pair}}} = N\sigma_{pair} \tag{4.43}$$

can be defined by using relation 4.9.

The total probability (per atom) for a photon interaction in matter is the sum of the individual cross sections discussed above:

$$\sigma = \sigma_{\mathrm{ph}} + Z\sigma_{\mathrm{C}} + \sigma_{\mathrm{pair}}, \tag{4.44}$$

where we have multiplied the Compton scattering cross-section by Z to take into account the Z electrons per atom. Same as for the radiation length, the mass attenuation coefficient of a mixture or a compound is described by Bragg's Rule:

$$\frac{\mu}{\rho} = \sum_i w_i \frac{\mu_i}{\rho_i}, \tag{4.45}$$

where μ_i is the mass attenuation coefficient of the i-th element, ρ_i is the density of the i-th element and w_i the weight fraction of the i-th element in the mixture/compound as defined in Equation 4.19.

For completeness, we also want to mention Rayleigh scattering, although this process does not contribute to energy losses. Rayleigh scattering describes the elastic scattering of photons by atoms as a whole, such that no energy is being transferred. [80]

4.1.6. Electron-Photon Cascades

So far we have seen that electrons/positrons can radiate bremsstrahlung, which is in the form of photons, and photons in turn can undergo pair production. Consequently, electrons (incl. positrons) and photons can evolve into electron-photon cascades that keep growing as long as the respective particle energies are above the thresholds of the underlying processes. The particles produced in the cascade keep diverging in a cone-shaped volume around the initial particle's direction of motion up to the point where the cascade stops. Because the involved interactions are of purely electromagnetic nature, and because of their cone-like shape, these cascades are usually referred to as ElectroMagnetic (EM) showers.

By comparing Equations 4.25 and 4.42 we see that the mean free path for pair production and the radiation length are nearly equal in size:

$$\lambda_{\text{pair}} = \frac{9}{7} X_0. \tag{4.46}$$

If we assume that both the electron and positron radiates a photon after an average distance of X_0, and that the photon undergoes pair production after an average distance X_0, then the total number of particles after t radiation lengths

$$N \approx 2^t, \tag{4.47}$$

given that we start with a single electron, positron or photon. If we further assume that the shower abruptly stops after t_{max} radiation lengths, at the point when the individual particles achieve critical energy E_c (see Eq. 4.28), such that

$$E(t_{\text{max}}) = \frac{E_0}{2^{t_{\text{max}}}} = E_c, \tag{4.48}$$

then we can define the total length of the shower expressed in units of the radiation length as

$$t_{\text{max}}\ [X_0] = \frac{\ln\left(\frac{E_0}{E_c}\right)}{\ln(2)}, \tag{4.49}$$

where E_0 is the energy of the initial particle. Accordingly, an estimate on the total number of particles involved in the shower at that point is

$$N_{\text{max}} \approx \frac{E_0}{E_c}. \tag{4.50}$$

The so-called *Moliere Radius*

$$R_{\text{M}} = \frac{E_s}{E_c} X_0 \tag{4.51}$$

is a measure for the transverse dimension of the EM shower, where

$$E_s = m_e c^2 \sqrt{4\pi/\alpha} = 21.1\,\text{MeV}. \tag{4.52}$$

Approximately 95 % of the EM shower is contained radially within a hypothetical cylinder with radius $R_{0.95} \approx R_M$ drawn around shower axis (trajectory of the initial particle). And approximately 95 % of the EM shower is contained longitudinally along the shower axis over a distance

$$L_{0.95}\ [X_0] \approx t_{\max} + 0.08\,Z + 9.6 \tag{4.53}$$

from the shower origin. [80, 81]

4.1.7. Hadronic Showers

Not only electromagnetism can lead to the formation of particle showers but also particles that interact via the strong interaction can initiate shower formations. These showers, referred to as hadronic showers, are considerably more complex than EM showers. A sizable amount of the available energy is usually converted into the excitation or breakup of atomic nuclei, and a major component of the secondaries are π^0s, which will propagate electromagnetically without any further nuclear interactions.

Hadronic cascades are characterized by the nuclear interaction length

$$\lambda_I = 37.8\,\mathrm{g\,cm^{-2}}\,A^{0.312} \tag{4.54}$$

to within 0.8 % for $Z > 15$ [62]. The maximum shower size expressed in units of the nuclear interaction length is

$$t_{\max}\ [\lambda_I] \approx 0.6 \ln(E_0\ [\mathrm{GeV}]) - 0.2. \tag{4.55}$$

Approximately 95 % of the hadronic shower is contained radially within a hypothetical cylinder with radius $R_{0.95} \approx \lambda_I$ drawn around the shower axis. And approximately 95 % of the hadronic shower is contained longitudinally along shower axis over a distance

$$L_{0.95}\ [\lambda_I] \approx t_{\max} + 4\,E^{0.15}\ [\mathrm{GeV}] \tag{4.56}$$

from the shower origin.

While EM calorimeters tend to be 15–30 X_0 deep, hadronic calorimeters are usually compromised at 5–8 λ_I. [62, 81]

4.1.8. Neutrons

Being electrically neutral charged particles, neutrons do not interact with the shell electrons of atoms or molecules but atomic nuclei directly. These interactions strongly depend on the neutron's kinetic energy and are either mediated by the weak force or the strong force. Therefore, neutrons are classed according to their kinetic energy into:

high energy neutrons at energies above $\sim 100\,\mathrm{MeV}$,

fast neutrons from a few hundred keV to a few tens of MeV,

epithermal neutrons between $\sim 0.1\,\mathrm{eV}$ and $\sim 100\,\mathrm{keV}$,

thermal or **slow neutrons** at energies comparable to the thermal agitation energy at room temperature, i.e. $E \approx kT \approx 1/40\,\mathrm{eV}$,

and **cold** or **ultra-cold neutrons** at energies of meV or µeV, respectively.

Typical neutron-nucleus interactions are [80]:

- Elastic scattering off nuclei $A(\mathrm{n},\mathrm{n})A$, which is the principle mechanism for energy loss of neutrons in the MeV region.
- Inelastic scattering off nuclei $A(\mathrm{n},\mathrm{n}')A^*$, $A(\mathrm{n},2\mathrm{n}')B$, $A(\mathrm{n},\mathrm{p})B$ etc. for neutrons with kinetic energies at the order of 1 MeV or more. In this reaction, the nucleus is left in an excited state which may later decay by radiative emission. At lower energies only elastic scattering occurs.
- Radiative neutron capture $n + (Z, A) \rightarrow \gamma + (Z, A+1)$ is most likely for neutrons at thermal energies or below as the cross section for this process goes approximately as $1/v$, with v the velocity of the neutron.
- Other nuclear reactions, in which the neutron is captured and charged particles are emitted, are most likely for neutrons with kinetic energies in the eV to keV region. The cross section of these processes also falls as $1/v$.
- Nuclear fission is most likely to happen for thermal neutrons.
- High-energy hadron shower production only occurs for very high energy neutrons with kinetic energies $> 100\,\mathrm{MeV}$.

The principal cross sections of neutrons in ^{40}Ar are shown in Figure 4.3, as a function of the neutron kinetic energy. A negative scattering resonance is present at $\sim 50\,\mathrm{keV}$, followed by a bunch of positive resonances up to $\sim 10\,\mathrm{MeV}$. Beyond these resonances, the neutron-argon ES cross-section is flat at $\sim 1\,\mathrm{b}$, which corresponds to a mean free path of $\sim 50\,\mathrm{cm}$ (see Eq. 4.9).

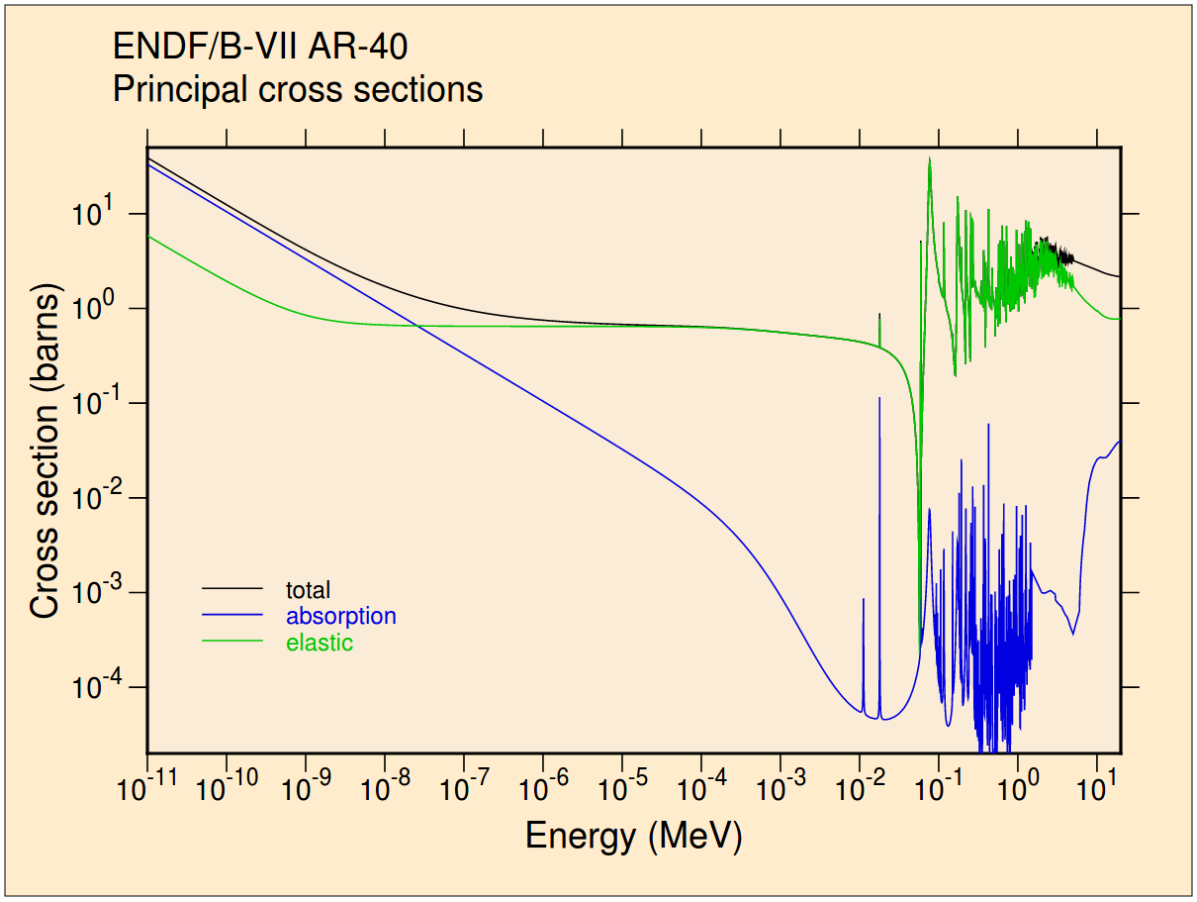

Figure 4.3.: Principal cross sections of neutrons in ^{40}Ar, as a function of the neutron kinetic energy. [82]

4.2. Basic Functionality of the Time Projection Chamber

A TPC is a 3D-tracking detector based on a gaseous or liquid noble gas element as the sensitive medium, developed by David R. Nygren in the 1970's [83]. The chamber consists of a cathode plane that is held on a negative electrical potential and a charge-readout plane (anode plane) at zero potential, whereas the noble gas inside the TPC acts as the active detector medium. A field-shaping structure that encircles the active volume helps to maintain a uniform electric field between the cathode plane and the anode plane.

The detection principle is based on ionizing collisions along the path of charged particles traversing the active medium in the TPC, leaving behind a trace of ionized/excited atoms and ionization electrons. Some fraction of ionized atoms and electrons recombines while the other fraction of charged particles starts to drift apart, ions towards the cathode plane and electrons towards the anode plane, as depicted in Figure 4.4. The ratio between

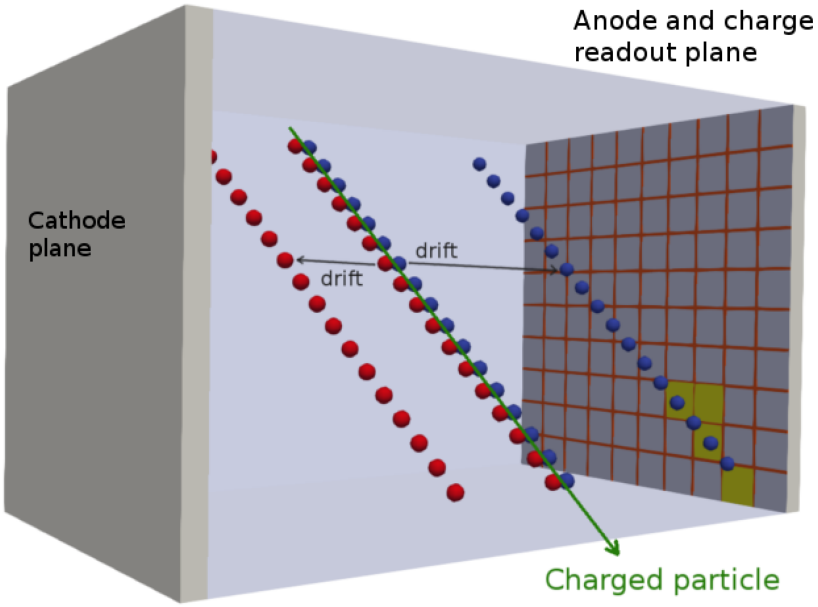

Figure 4.4.: Working principle of the TPC. Collisions along the path of charged particles traversing the TPC ionizes the active medium, leaving behind a trace of ionized/excited atoms and ionization electrons. Some fraction of ionized atoms and electrons recombines while the other fraction of charged particles starts to drift apart, ions (red) towards the cathode plane and electrons (blue) towards the charge-readout (anode) plane. The charge measured at the anode plane together with the arrival time allows for three-dimensional image reconstruction of traversing ionizing particles. [84]

the recombining and the drifting fraction depends on the strength of the electric field; the higher the electric field the lower the recombination. If the lifetime of a free electron in the sensitive medium is long enough, the electrons can drift all the way up to the

charge-readout plane, where charge is being measured. Therefore, only noble gases are suitable active media since only those can provide a long enough electron lifetime due to their low electronegativity. While the bare projection of the drift electrons onto the charged-readout plane only allows for two-dimensional imaging, the inclusion of charge arrival times enables three-dimensional track reconstruction of traversing charged particles.

An absolute position of the traversing charged particles can not be provided by the charge-readout system because of the unknown offset between the charge deposited closest to the readout plane and the readout plane itself. This issue can be solved by measuring the prompt scintillation light due to recombination which is emitted within at the $\mathcal{O}$ (1) ns after the ionization, thus being ~ 5 orders of magnitudes faster than a typical drift window. The corresponding time stamp, usually denoted by T_0, can be used to determine the absolute position of charge depositions along the drift axis.

4.2.1. Liquid Argon as a Detection Medium

In 1974, W. J. Willis and V. Radeka started to use LAr in ionisation chambers[3] because of the excellent properties of LAr as a detection medium [85]. Three years later, C. Rubbia applied the technique used by Willis and Radeka to the original TPC design of Nygren, proposing the LArTPC as a neutrino detector [86].

The key properties of LAr relevant for the application in TPCs and that make it a suitable target material for neutrino detectors are listed in Table 4.1. With a density higher than even heavy water, LAr is not only a suitable candidate for the sensitive detector medium but also heavy enough to compete with the aforementioned small neutrino-nucleus interaction cross-section, and thus a good candidate to be used as the target material for neutrino detectors. Charged particles traversing LAr produce a large amount of ionization electrons but also prompt scintillation light, and LAr is highly transparent to its own scintillation light, which means it can be detected and used for the determination of T_0. The electron drift velocity $v = E\mu$, where E the electric field strength, is reasonable high for electrons to survive drift lengths of the $\mathcal{O}(1)$ m. Drift electrons barely attach to argon atoms on their way towards the anode plane because argon being a noble gas element, and thus having a fully occupied outermost electron shell, does not possess electronegativity. Impurities with high electronegativities, e.g. oxygen and nitrogen, in the LAr are a severe issue on the performance of LArTPCs, however, argon is inert and can be purified fairly easy by using reactive filters. Ultimately, argon is present in the Earth's atmosphere (0.936 % [88]) and the fact that it is widely used in industry makes it cheap and available in large amounts, and thus applicable for large-scale LArTPC detectors. A drawback from the technical point of view is the low boiling point of LAr, which means that LArTPCs have to be realized as cryogenic detectors that need active cooling.

[3] An ionization chamber collects ionization electrons/ions that drift in an electric field between anode and cathode but without imaging capabilities.

Table 4.1.: LAr properties relevant for the application in TPCs, taken from Ref. [87]. *Electric field strength dependent values are given for $0.5\,\mathrm{keV\,cm^{-1}}$.

LAr Property	Symbol	Value	Unit
Boiling point (at 101 325 kPa)	T_B	87.303 ± 0.002	K
Freezing point (at 101 325 kPa)	T_F	83.8 ± 0.3	K
Density (at T_B)	ρ	1.396 ± 0.001	$\mathrm{g\,cm^{-3}}$
Electron mobility*	μ	320.2272	$\mathrm{cm^2\,V^{-1}\,s^{-1}}$
Electron drift velocity*	v	0.1601	$\mathrm{cm\,\mu s^{-1}}$
Longitudinal drift coefficient*	D_L	6.6270	$\mathrm{cm^2\,s^{-1}}$
Transversal drift coefficient*	D_T	13.2327	$\mathrm{cm^2\,s^{-1}}$
W-value for ionization	W_i	23.6 ± 0.3	eV/pair
Radiation length	X_0	14.0	cm
Nuclear interaction length	λ_i	85.7	cm
Critical energy	E_c	30.5	MeV
Minimum specific energy loss	$(dE/dX)_{MIP}$	2.12	$\mathrm{MeV\,cm^{-1}}$
W-value for scintillation	W_s	19.5	eV/photon
Scintillation emission peak	λ_{scint}	128 ± 10	nm
Scintillation decay time	τ_{scint}	6 ± 2, 1590 ± 100	ns
Index of refraction (at 128 nm)	n	1.38	-
Rayleigh scattering length (at 128 nm)	L_R	95	cm
Absorption length (at 128 nm)	L_A	>200	cm

4.2.2. Simultaneous Tracking and Calorimetry

LArTPCs combine the two capabilities to track charged particles and to measure their energy with calorimetric methods, i.e. by direct measurement of the energy deposited in the detector. Calorimetry works for charged particles that are fully contained in the TPC and for particle showers that are fully contained or partially contained up the point where no reasonable assumptions on the full shower extent can be met. The energy needed to produce an electron/ion pair is given by the W-value for ionization (see Tab. 4.1), and can be used as a norm to calculate how many ionization electrons are produced for a given amount of deposited energy. Some fraction of the freed electrons recombines with the surrounding ions, while the other fraction can be seen as potentially collectible (there is some remaining chance for electrons to be attached to impurities). Recombination introduces a non-linear relation between dE/dx and dQ/dx, where dQ is the summed charge of the electrons that do not recombine along dx. The recombination rate depends on the electric field strength, the higher the field strength the more electrons success to escape recombination with ions and the lower the scintillation light yield. Recombination can be parameterized by two empirical models, *Birks' model* and the *Box model* [89]. The parameters of these models are determined with measurements of stopping particles, where the energy at different waypoints can be traced back from the residual range of the particle tracks. Since cosmic muon tracks can be seen as nearly ideal MIPs, they provide a valuable independent handle on charge-readout calibration.

The purity is decisive for how many ionization electrons survive the drift path up to the charge-readout plane without being attached to any impurity. Therefore, the purity sets a lower limit on the energy resolution of the detector. Electrons in LAr are permanently colliding with the atoms of the surrounding medium such that their survival probability

$$\frac{Q}{Q_0} = e^{-\frac{t}{\tau_\mathrm{e}}} \tag{4.57}$$

decays exponential in time, where Q_0 is initial number of electrons, Q is the number of electrons left after the time t and τ_e is the mean lifetime of the electrons in the detector medium. Accordingly, the purity of the sensitive medium can be measured indirectly via the electron lifetime. Cosmic muon tracks are a good candidate for such measurements because of the a priori known energy-loss rate.

During the drift, the electron clouds also spread due to diffusion. The longitudinal (along drift) and transversal dimensions of an electron cloud after a certain time t are

$$\sigma_L^2(t) = \left(\frac{2D_L}{v_d^2}\right) t \tag{4.58}$$

and

$$\sigma_T^2(t) = \left(\frac{2D_T}{v_d^2}\right) t, \tag{4.59}$$

where v_d is the drift velocity and D_L and D_T are the longitudinal and transversal drift coefficients according to Table 4.1. [89] The electron diffusion sets a lower limit on

the potential spatial resolution of the charge readout and consequently on the imaging resolution of the detector.

Neutral particles pose a big problem in LArTPCs because they are not visible unless they produce secondary particles or recoils by interactions with atomic nuclei. Neutral particles that leave the active detector volume unseen can carry away big amounts of energy which will be missed in calorimetric energy measurements.

4.2.3. Two Components of Scintillation Light

Scintillation light is emitted by previously ionized atoms that recombine with electrons or by excited atoms. Argon ions recombine via dimer formation, which are bound states between two argon atoms, according to the reaction

$$e^- + {}^{40}Ar^+ + {}^{40}Ar \quad \rightarrow \quad {}^{40}Ar_2^*, \tag{4.60}$$

where the asterisk denotes that the dimer is in an excited state, sometimes also referred to as an excimer. The excimer is unstable and decays into two argon atoms under the radiation of a photon:

$${}^{40}Ar_2^* \quad \rightarrow \quad 2\ {}^{40}Ar + \gamma. \tag{4.61}$$

This mechanism of scintillation-light emission is called *recombination luminescence*. Excited argon atoms can build excimers too, which in turn decay into two argon atoms under the radiation of a photon:

$${}^{40}Ar + {}^{40}Ar \quad \rightarrow \quad {}^{40}Ar_2^* \quad \rightarrow \quad 2\ {}^{40}Ar + \gamma. \tag{4.62}$$

This second mechanism of scintillation light emission is called *self-trapped exciton luminescence*.

Both mechanisms emit Vacuum UltraViolet (VUV) photons in a narrow band around $\sim 128\,\text{nm}$ wavelength. Since photon sensors have a relatively bad efficiency to detect VUV light, many experiments use TetraPhenyl Butadiene (TPB) as a so-called WaveLength Shifter (WLS), which shifts VUV photons to photons in the optical blue.

There are two argon excimer states singlet and triplet, which refer to how the spin of the electron and the excimer couple in the atom. Both excimers decay exponentially but with different so-called scintillation decay times λ_{scint} (see Tab. 4.1). While the singlet state decays in $\sim 6\,\text{ns}$, the triplet state decays in $\sim 1600\,\text{ns}$. The ratio between singlet and triplet state formation is at the $\mathcal{O}\,(1)$. Regarding the different decay times, we refer to the *slow* and to the *fast* component of the scintillation light. [90]

4.2.4. Charge Readout

Conventional TPCs use projective wire readouts to reconstruct complex 3D images with multiple 2D projections of the charge signal. This principle is illustrated in Figure 4.5. The left-hand side of the figure shows a LArTPC with the cathode plane to the left in

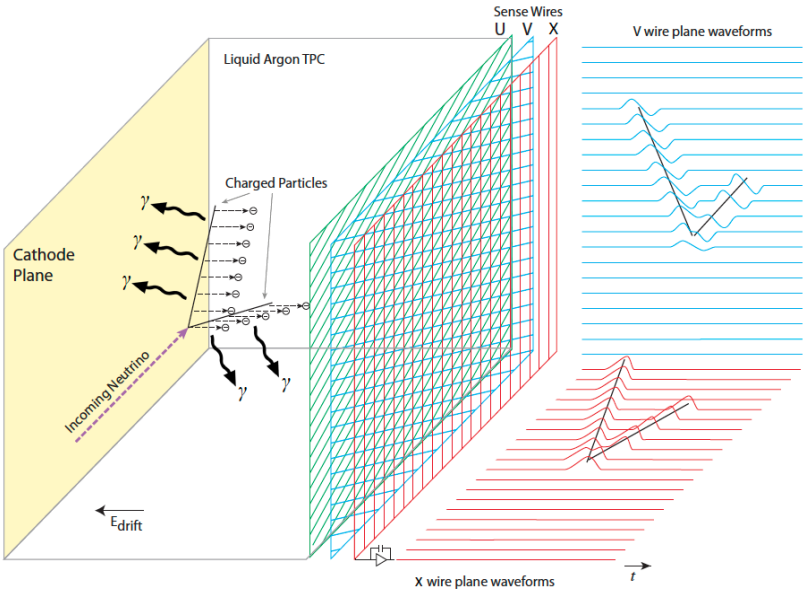

Figure 4.5.: Working principle of the traditional projective wire-readout TPC. An incoming neutrino produces two charged particles which in turn produce scintillation light (γs) and ionization electrons that drift towards the charge-readout plane. The first two wire planes (U and V) are operated at a small positive bias voltage such that the electrons pass the planes in between the wires and eventually are being collected at the X plane. While the U and V planes only see an induction signal the X plane sees the actual signal of the collected charge. 3D images are reconstructed from the three 2D projections provided by the three wire planes. [24]

yellow and the charge-readout plane, which is composed of three wire planes denoted U, V and X, to right. The wires are usually wrapped with different orientations building an angle of 60° between different wire planes. An incoming neutrino produces two charged particles which in turn produce scintillation light (γs) and ionization electrons that drift towards the charge-readout plane. The first two wire planes (U and V) are operated at a small positive bias voltage such that the electrons pass the planes in between the wires and eventually are being collected at the X plane. According to the produced signals, the first two wire planes are called induction planes and the third plane is called collection plane.

The right-hand side of Figure 4.5 illustrates how each wire plane sees its own projection of the charged tracks. While the U and V planes only see an induction signal the X plane sees the actual signal of the collected charge. Since the charge-readout planes are compounded with wrapped wires and the 3D images have to be reconstructed from the three 2D projections, many ambiguities arise from this technique. These ambiguities pose a serious problem if it comes to the reconstruction of overlapping events (event pile-up). While projective wire readouts are a good option for TPC operation in environments with low interaction rates, e.g. the DUNE FDs, projective wire readouts are not suitable for detectors in high-multiplicity environments, such as the DUNE ND site. An alternative charge-readout technique that was developed for the application in high-multiplicity environments and that will be applied to DUNE ND-LAr will be discussed in Chapter 5.

4.2.5. Particle Identification

If the TPC is realized within a magnetic field, then it allows to measure the charge and the momentum by deflection of the passing charged particles. Since the linear stopping power (Eq. 4.10) strongly depends on the particle momentum, it allows for Particle Identification (PID) if both dE/dx and the particle momentum are known. This technique for PID has successfully been applied by many particle physics experiments around the globe, one of them A Large Ion Collider Experiment (ALICE) at CERN. Figure 4.6 shows the linear stopping power as function of particle momentum measured with the magnetized ALICE TPC, overlaid by the theory curves for electrons (e), muons (μ), pions (π), kaons (K), protons (p), and deuterium (^{2}H) and tritium (^{3}H) cores. The application of PID by dE/dx is limited to the regions where these curves do not overlap, however. Other methods use the particle-specific phenomenology to distinguish different particles types, such as muons and pions that have similar masses and, as a consequence, whose dE/dx curves are relatively close together. While mouns appear as very clean tracks in TPCs, pions have a small but still observable tendency to shower. Such muon/pion-separation methods are very important in neutrino experiments because pions can pose a serious background for the primary muons produced in CC ν_μ interactions.

4.2.6. Issues With Conventional LArTPCs

We have seen many benefits of LArTPCs being used as particle detectors. These include the simultaneous tracking and calorimetry, the high transparency of LAr to its own

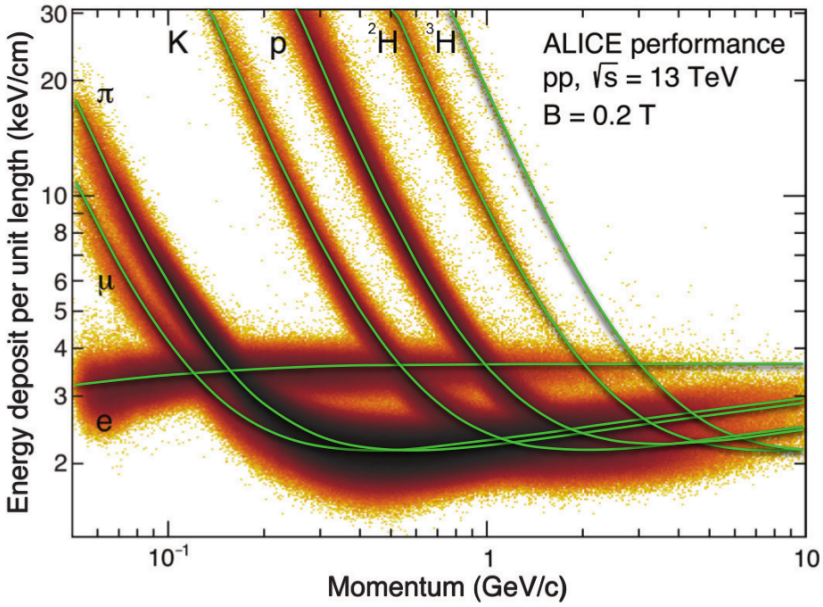

Figure 4.6.: PID with the ALICE TPC at CERN, taken from Ref. [62]. The plot shows the linear stopping power (dE/dx) as function of particle momentum measured with the magnetized ALICE TPC, overlaid by the theory curves for electrons (e), muons (μ), pions (π), kaons (K), protons (p), and deuterium (^{2}H) and tritium (^{3}H) cores

scintillation light, the fast light component to set an absolute time of the event, and the possibility of PID. Besides these benefits, there are some drawbacks that arise if we want to apply conventional LArTPCs in high-intensity beam environments:

- The electron drift speed is of the $\mathcal{O}(1)$ mm µs^{-1}, which favors event pile-up if the average event separation time is similar to or less than the drift time.
- Projective wire readouts introduce ambiguities because they reconstruct 3D images from multiple 2D projections measured with wrapped wires planes.
- The LAr scintillation process includes the emission of a slow component of scintillation light with a decay time of the $\mathcal{O}(1)$ µs.
- Uncontained scintillation light leads to optical pile-up and no way to disentangle the charge signals from different events in a high multiplicity environment.

The University of Bern put a lot of effort into detector research and development in order to address these issues listed. A modular LArTPC design with novel charge- and light-readout techniques has been elaborated and given the name ArgonCube. The ArgonCube concept was accepted very well and the international ArgonCube Collaboration was formed to improve the technical design with contributions from scientists and engineers

from more than 20 institutions around the world [4]. In Chapter 5, we will discuss the details of the ArgonCube concept and its application as the DUNE ND-LAr.

[4] https://www.argoncube.org

5. LArTPC in the DUNE ND

The ArgonCube concept addresses the issues with conventional LArTPCs that I discussed in the previous chapter. It is able to handle high-intensity beam environments and to disentangle piled-up events. Although the design was optimized to meet the requirements of the DUNE ND-LAr, it can be scaled to arbitrary detector dimensions, which makes it even applicable to multi-kt neutrino FDs. In this chapter, I will discuss the technologies used by the ArgonCube concept, and we will see how the concept is being realized to fulfill the requirements of the ND-LAr.

5.1. ArgonCube Principles

The ArgonCube concept divides the detector volume into a number of identical, optically isolated and electrically isolated TPC modules. The charge readout is achieved with pixelated anode tiles utilizing an Application-Specific Integrated Circuit (ASIC) to amplify and digitize charge signals at the anode. The pixelated anode eliminates the ambiguities associated with conventional wire-plane anodes. But the charge readout remains limited by the electron drift time, which is of the $\mathcal{O}(100)$ µs, and consequently, it is not able to resolve overlapping interactions that may have occurred at the $\mathcal{O}(100)$ ns apart. The light readout is achieved with dielectric WLS tiles/fibers coupled into Silicon PhotoMultipliers (SiPMs), which can be placed inside the electric drift-field to increase the light yield and to improve the localization of light signals. The contained scintillation light is vital for disentangling overlapping neutrino interactions and to associate detached energy deposits with interaction vertices. Additionally, the modules use a resistive field shell instead of traditional field shaping rings to minimize the dead material introduced through the modularization, to maximize the active volume and to minimize the power release in the event of an electric breakdown. [23, 91]

5.1.1. Modularization

The principle characteristic of the ArgonCube concept is the modularization. Each module represents a self-contained TPC that is electrically isolated among other modules. A central cathode splits each TPC into two optically isolated drift regions. In this way, the modularization reduces the drift length and therefore the charge-readout window to the extent of a single module. Shorter drift paths, in turn, allow operation at lower absolute cathode voltage and require less stringent purity conditions. Furthermore, the optical isolation reduces the pile-up of the scintillation light and allows for better localization of light signals, which I will exploit in the method presented in Chapter 6.

5.1.2. Pixelated Charge Readout

In 2018, Asaadi et al. [92] presented the first results from a pixelated LArTPC prototype, which was built and operated at the University of Bern. The prototype addressed the mechanical complexity of conventional wire readouts in the realization of large mass detectors and the intrinsic ambiguities in event reconstruction. It was shown that pixelated charge readouts are mechanically more robust than wire readouts and that pixelated LArTPCs are able to provide direct 3D readout to minimize reconstruction ambiguities. [92]

Cryogenic preamplifier ASICs were used to minimize the signal-to-noise ratio of the charge readout. These amplifiers, called LARASIC4* [93], were designed by the BNL for traditional wire readouts, which require fewer channels than a pixelated readout of equivalent dimensions and pitch. With only 16 channels per ASIC and given the 1008 pixels of the prototype cold digitization was disfavored due to power consumption constraints. Therefore, analogue multiplexing had to be used to minimize the channel numbers, with signals digitized at room temperature outside of the cryostat. The multiplexing scheme is shown in Figure 5.1. The pixel plane counts 1008 pixels realized by 900 µm vias printed on a Printed Circuit Board (PCB) at a pitch of 2.54 mm. Inductive focusing grids formed of 152.4 µm copper traces surround the pixels and split them into 28 Regions Of Interest (ROIs). There are 36 pixels per ROI and each ROI is defined as the pixels contained within a single section of the inductive focusing grid. The pixelated charge-readout prototype was operated in a cylindrical 60 cm-drift LArTPC with a radius of 10 cm. This so-called pixel demonstrator successfully reconstructed 3D tracks of crossing cosmic-ray muons. However, the existing wire-readout electronics in conjunction with the analogue multiplexing ambiguities complicated the reconstruction process. Also, the requirement of a high number of readout channels has not been addressed. [94]

As a result of this work, Lawrence Berkeley National Laboratory (LBNL) joined the ArgonCube collaboration and developed a pixel ASIC called LArPix [95], capable of cold amplification and digitization for 32 channels in LArTPCs. The LArPix ASICs are fabricated in 180 nm CMOS technology and dissipate as few as 61 µW of power per channel. [95] The low power dissipation is crucial to keep the heat introduced into the cryogenic system low, while the cold amplification and digitization drastically reduced the number of cryostat penetrations. To further reduce the number of cryostat penetrations, multiple LArPix chips can be daisy chained and communicated with using only two wires. A prototype pixel-board instrumented with a 28-chip readout assembly (896 channels) was operated at the University of Bern and has been used to successfully reconstruct true-3D images of cosmic-ray muons. The setup of the charge readout is shown in Figure 5.2. A total of 832 charge collecting pads were etched on a standard PCB (a) in ten different configurations in order to assess their relative performance. 28 LArPix ASICs were mounted on a second, so-called data PCB (b), located at the back-side of the pixel PCB. Each pixel pad was wire-bonded to a unique analog input of the ASICs through cavities cut into the data PCB. The pixel board was deployed in the same 60 cm-drift LArTPC as used in the pixel demonstrator test and convinced with an excellent performance. It surpassed the design targets for noise and power dissipation

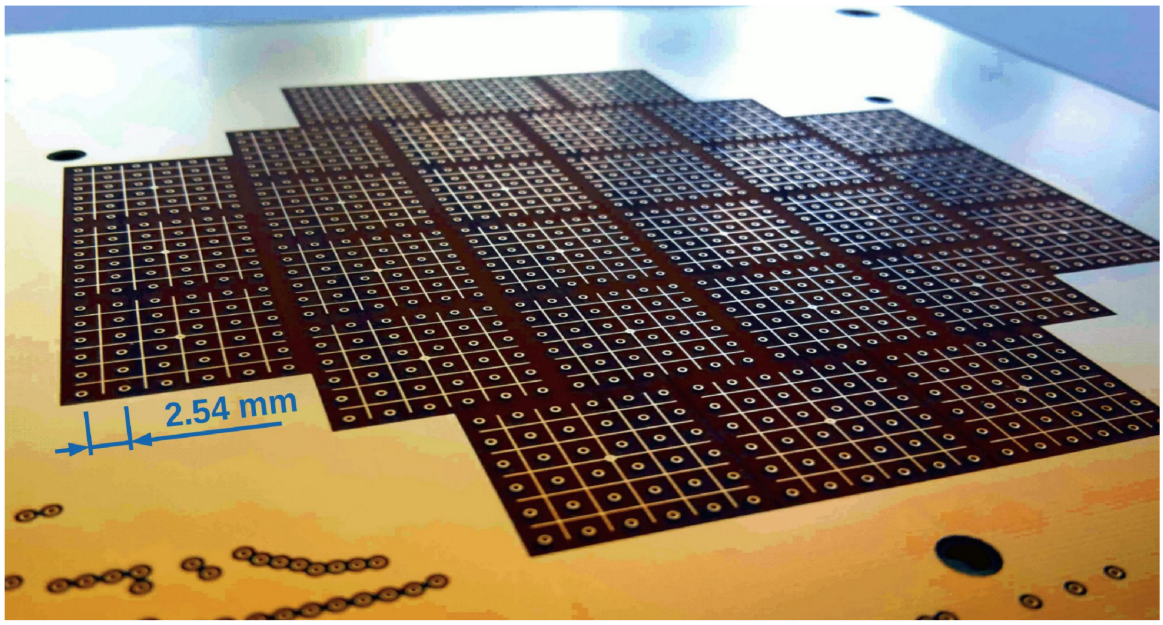

Figure 5.1.: Prototype of the pixelated anode PCB. The pixel plane counts 1008 pixels realized by 900 µm vias at a pitch of 2.54 mm. Inductive focusing grids formed of 152.4 µm copper traces surround the pixels and split them into 28 ROIs. There are 36 pixels per ROI and each ROI is defined as the pixels contained within a single section of the inductive focusing grid. [94]

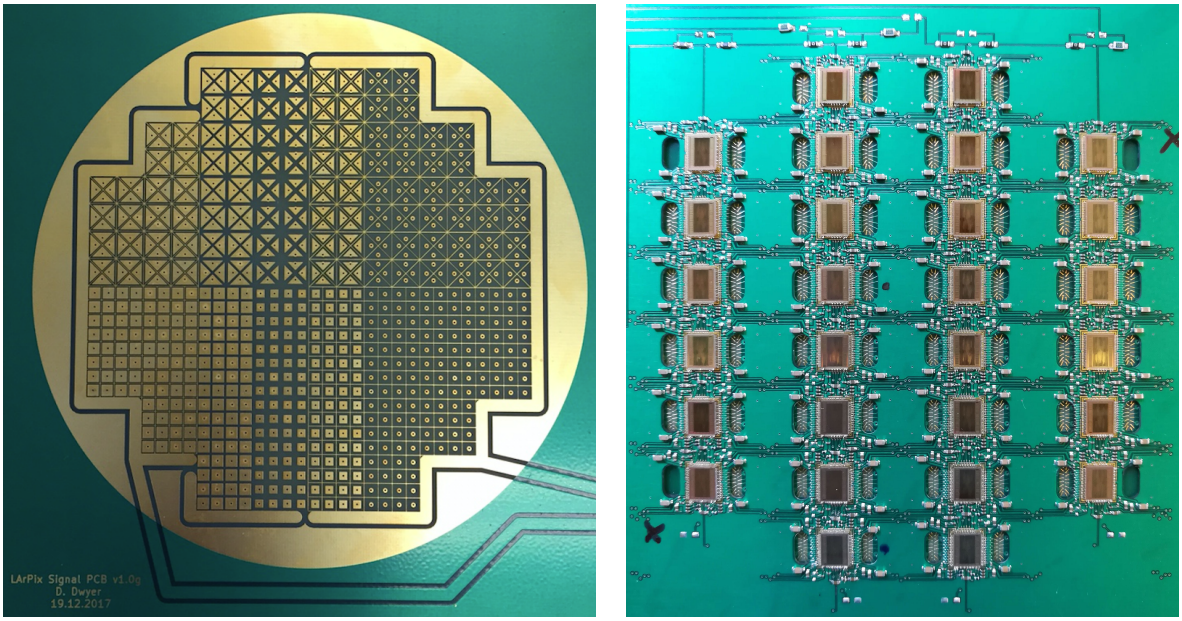

(a) **(b)**

Figure 5.2.: Prototype pixel-board instrumented with 28 LArPix ASICs (896 channels) operated at the University of Bern. A total of 832 charge collecting pads were etched on a standard PCB (a) in ten different configurations in order to assess their relative performance. 28 LArPix ASICs were mounted on a second, so-called data PCB (b), located at the back-side of the pixel PCB. Each pixel pad was wire-bonded to a unique analog input of the ASICs through cavities cut into the data PCB. [25]

and also met the requirements for cryogenic operation and digital multiplexing. Signals from cosmic-ray muons were imaged in true 3D with no evidence of spurious hits from noise.

A selection of events detected with the bespoken assembly is shown in Figure 5.3. The

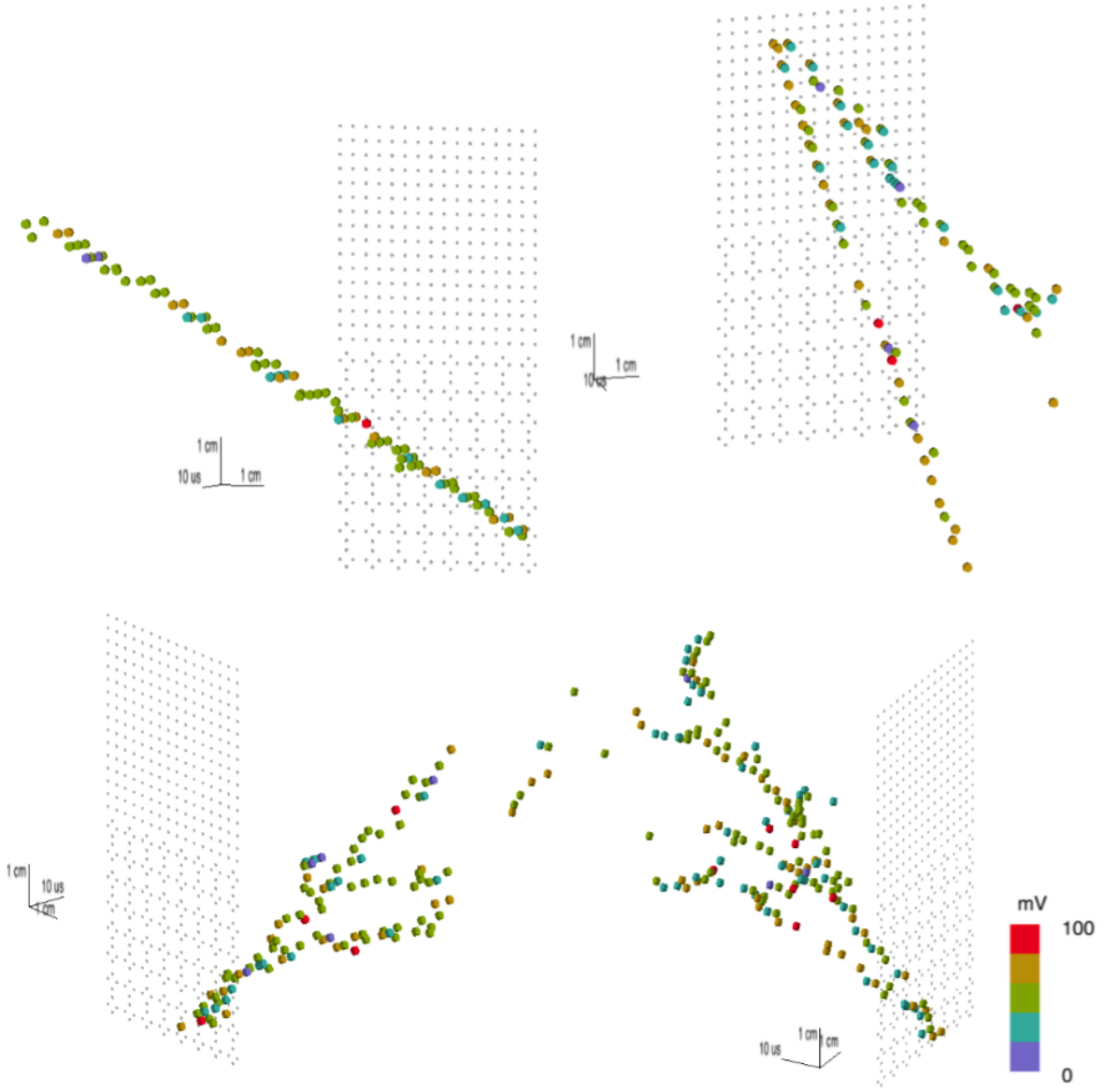

Figure 5.3.: Data collected with the 28-LArPix pixelated charge-readout assembly at the University of Bern. The two upper figures show relatively straight tracks from cosmic-muon candidates and the two lower figures show electromagnetic showers. The event displays show the raw data collected by the system with no filtering or enhancement applied. [25]

two upper figures show relatively straight tracks from cosmic-muon candidates and the

two lower figures show electromagnetic showers. The event displays show the raw data collected by the system with no filtering or enhancement applied. [25]

The successful demonstration of cold amplification and digitization provided by the LArPix ASIC in combination with digital multiplexing mitigates the lack of channels and multiplexing ambiguities associated with the readout used in the pixel-demonstrator test. Finally, true 3D-imaging without ambiguities makes pixelated LArTPCs a viable option for high-multiplicity environments, such as the DUNE-ND site.

5.1.3. Light Readout

The detection of fast LAr scintillation light is crucial in LArTPCs in order to provide an absolute time stamp (T_0) for each neutrino event. Two complementary detection systems that allow for the efficient use in cryogenic large-volume particle detectors are considered in the ArgonCube concept. Both systems are based on dielectric structures and can be deployed in electromagnetic fields with high field strengths (e.g. TPC drift-fields), avoiding the need for additional dead volume in the modular design of ArgonCube. LAr emits VUV scintillation light with 128 nm wavelength, where the efficiencies of currently available VUV-optimized photo sensors are typically fairly low, reaching at most 15 % [96]. Therefore, both systems use TPB to shift the LAr scintillation light to wavelengths of the visible spectrum, which in turn is being detected with SiPMs.

The first of the two light-readout systems with the name ArgonCube Light readout system (ArCLight) was developed at the University of Bern [97]. The detector consists of a 10 mm thick, solid and transparent polymer sheet doped with a WLS dye, and with reflective films laminated to each side, as depicted in Figure 5.4. The back face and edges are covered with a dielectric specular reflector foil, which has $\sim 98\,\%$ reflectance for the visible light spectrum. The front face is coated with a dichroic mirror film that is transparent in the blue and has high reflectance in the green range of the spectrum. A thin layer of TPB ($\sim 5\,\mu m$) is evaporated on top of the dichroic mirror facing the active area of the LArTPC. Hamamatsu S13360-6050CS SiPMs[1] with a sensitive area of 6 mm × 6 mm are coupled to the polymer sheet. These have a Photon Detection Efficiency (PDE) of $\sim 38\,\%$ in the range of the WLS-dye emission spectrum. [97, 98]

The ArCLight photon-detection principle, according to the numbers in Figure 5.4, is as follows: a VUV photon is absorbed by the TPB and a blue photon is emitted in turn (1), the blue photon passes the dichroic mirror and enters the WLS-doped plastic sheet (2), the blue photon is shifted to a green photon by the WLS dye in the plastic sheet (3), the green photon is reflected by the dichroic mirror (4) as well as the specular reflector foil (5) and eventually detected by one of the SiPMs (6). A photo of an ArCLight tile with the TPB layer facing upwards is shown in Figure 5.5a (a). The WLS-doped plastic sheet has a sensitive area of $\sim 30\,cm \times 30\,cm$ and is coupled to six SiPMs mounted on a PCB strip.

The second light-readout system with the name Light Collection Module (LCM) was developed at Joint Institute for Nuclear Research (JINR) in Dubna, Russia [99]. LCM

[1] https://www.hamamatsu.com/resources/pdf/ssd/s13360-2050ve_etc_kapd1053e.pdf

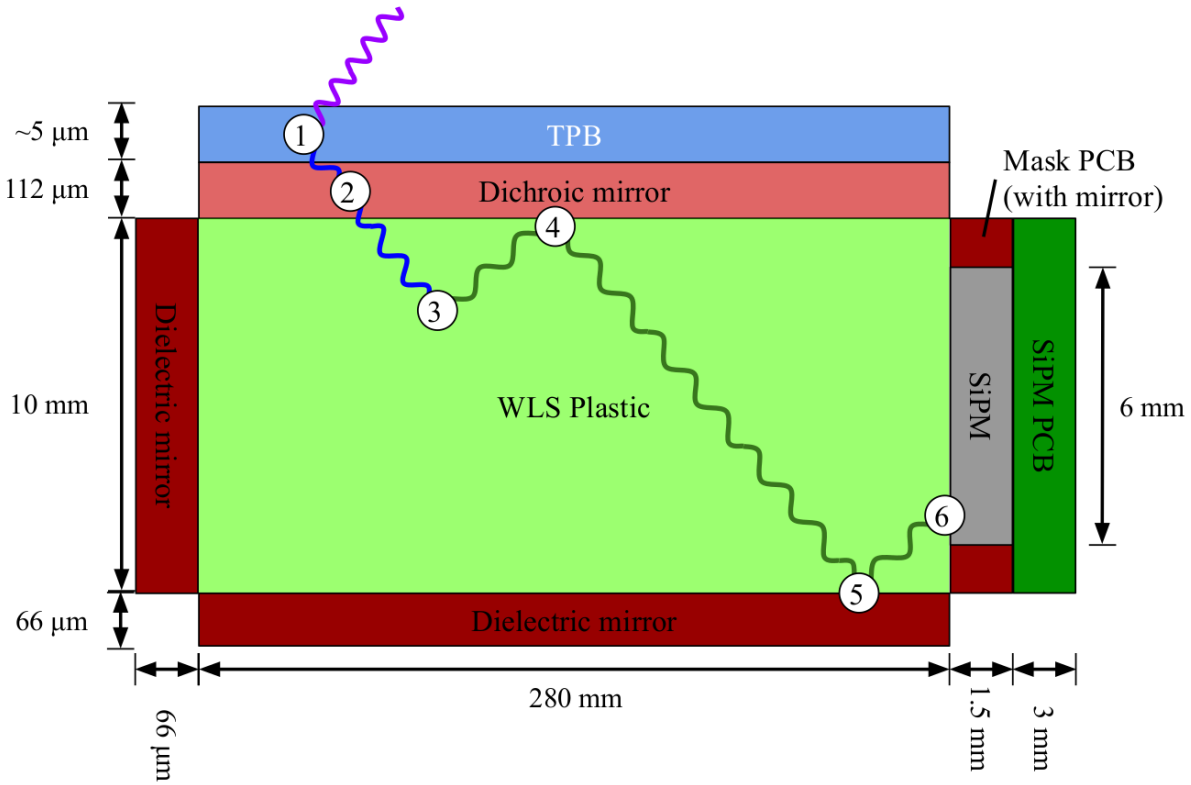

Figure 5.4.: The ArCLight photon-detection principle: a VUV photon is absorbed by the TPB and a blue photon is emitted in turn (1), the blue photon passes the dichroic mirror and enters the WLS-doped plastic sheet (2), the blue photon is shifted to a green photon by the WLS dye in the plastic sheet (3), the green photon is reflected by the dichroic mirror (4) as well as the specular reflector foil (5) and eventually detected by one of the SiPMs (6). [98]

(a) **(b)**

Figure 5.5.: Photos of the ArgonCube light-readout systems taken at the University of Bern. An ArCLight tile with the TPB layer facing upwards is shown in (a). The WLS-doped plastic sheet has a sensitive area of $\sim 30\,\text{cm} \times 30\,\text{cm}$ and is coupled to six SiPMs mounted on a PCB strip. An LCM tile is shown in (b). The TPB-coated fibers are aligned to cover an area as large as possible. Two SiPMs are mounted on a PCB strip and the fibers are bent by 180° such that the two open ends can be coupled to one of the two SiPMs each.

works in a similar way as ArCLight but uses WLS-doped fibers instead of a WLS-doped plastic sheet to trap the photons. The fibers are coated with TPB to shift VUV photons to blue photons and coupled to SiPMs, same as ArCLight. However, there is no need for reflective films because the gradient of refractive index in modern optical fibers prevents the photons from escaping once they are coupled in. A photo of an LCM tile is shown in Figure 5.5b (b). The TPB-coated fibers are aligned to cover an area as large as possible. Two SiPMs are mounted on a PCB strip and the fibers are bent by 180° such that each and is coupled to one of the two SiPMs.

Both light-readout systems have been tested at the University of Bern in highly purified LAr. These studies have shown that the PDE of ArCLight for LAr scintillation light is $\sim 0.2\,\%$ [98] and that of LCM is about $1-2\,\%$ [99]. Purpose-built frond-end electronics developed at JINR enable a timing resolution of the $\mathcal{O}(1)$ ns by analyzing the SiPM waveforms.

5.1.4. Resistive Field Shell

Conventional TPCs use field cages made of metal structures to shape a uniform electric drift-field between the cathode and the anode. Next-generation long-baseline neutrino experiments require detectors with active masses up to $\mathcal{O}(10^7)$ kg and drift lengths of several meters. The electrostatic energy stored in a TPC of such dimensions can be up to $\mathcal{O}(100)$ J [84]. An accidental discharge between the cathode or field cage and the grounded environment around the field cage could damage the readout electronics. The ArgonCube concept reduces the stored energy and it simplifies maintaining the electric-field stability. Additionally, the field cage is replaced by a so-called *resistive shell* that is a carbon-loaded polyimide foil laminated directly onto the cathode plane and the module walls. The polyimide foil has a resistance of $\mathcal{O}(1)$ GΩ per square at LAr temperatures and provides a continuous linear potential distribution along the drift direction. Compared to conventional field cages, the resistive shell drastically reduces the component count and, therefore, also the number of potential points of failure. And the resistive shell limits the power release in the case of an electric breakdown. [84, 100]

Measurements of the polyimid-foil resistance as a function of the electric field strength have been performed at SLAC, and are shown in Figure 5.6. These measurements shown that the resistance of the polyimide foil decreases with an increase in the electric field strength, and that a resistance $\geq 1\,\mathrm{G\Omega}$ per square can be maintained up to an electric field strength of $1\,\mathrm{kV\,cm^{-1}}$. That is true for electric fields applied parallel to the internal structure of the polyimid foil (labeled 0°) as well as for electric fields applied perpendicular to the internal structure of the polyimid foil (labeled 90°). [101]

A prototype resistive-shell LArTPC designed an operated at the University of Bern provided the proof of principle of this technique. The TPC is explained in Figure 5.7. The $7\,\mathrm{cm} \times 7\,\mathrm{cm} \times 15\,\mathrm{cm}$ drift volume is wrapped with a resistive shell along the 15 cm drift direction. Perforations in the polyimid foil allow for LAr recirculation. Also the cathode plane is laminated with polyimid foil and mechanically connected to the field shell providing a uniform electric potential. The charge-readout plane consists of two perpendicularly arranged layers of copper traces that are printed onto a Kapton foil and

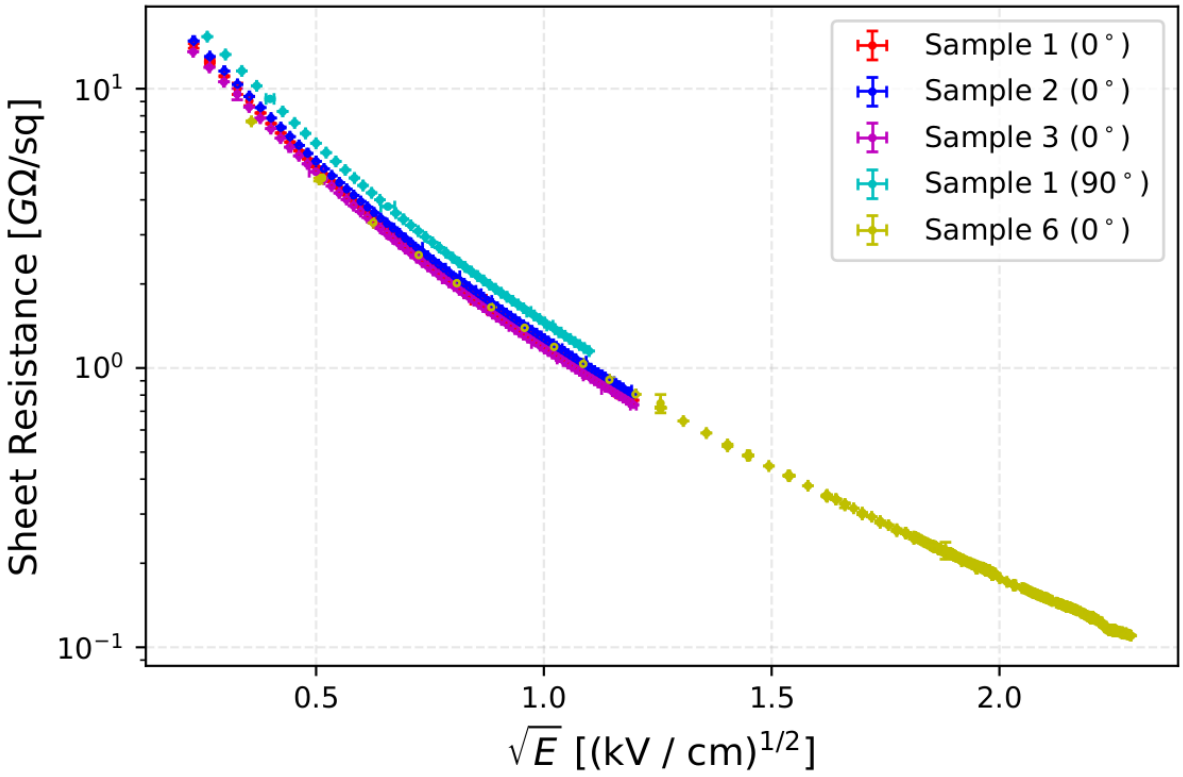

Figure 5.6.: Measurements of the polyimid-foil resistance as a function of the electric field strength performed at SLAC. The resistance of the polyimid foil decreases with an increase in the electric field strength. A resistance $\geq 1\,\mathrm{G\Omega}$ per square can be maintained up to an electric field strength of $1\,\mathrm{kV\,cm^{-1}}$. That is true for electric fields applied parallel to the internal structure of the polyimid foil (labeled 0°) as well as for electric fields applied perpendicular to the internal structure of the polyimid foil (labeled 90°). [101]

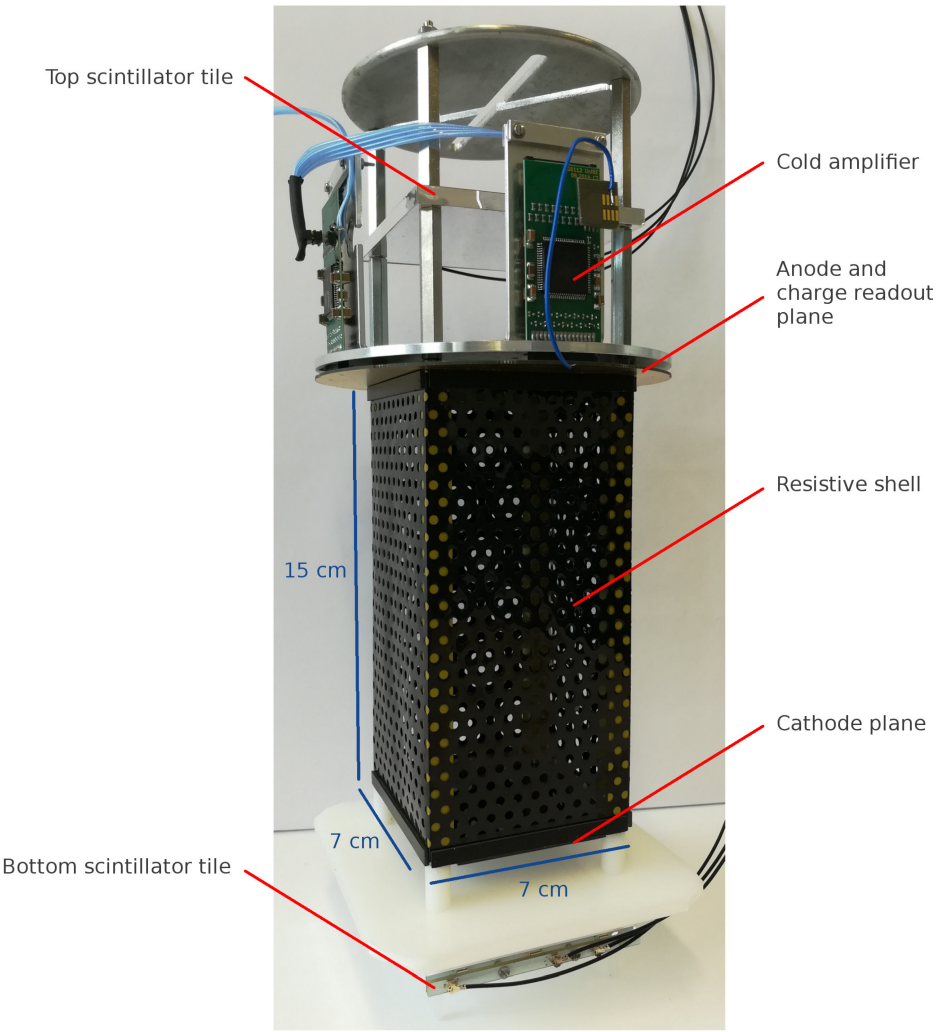

Figure 5.7.: Prototype of the resistive-shell LArTPC designed an operated at the University of Bern. The 7 cm × 7 cm × 15 cm drift volume is wrapped with a resistive shell along the 15 cm drift direction. Perforations in the polyimid foil allow for LAr recirculation. Also the cathode plane is laminated with polyimid foil and mechanically connected to the field shell providing a uniform electric potential. The charge-readout plane consists of two perpendicularly arranged layers of copper traces printed onto a PCB and read by a total of four LARASIC4* cold amplifiers. Two 7 cm × 7 cm × 0.4 cm scintillator tiles mounted above the charge-readout plane and below the cathode plane act as a small muon telescope and trigger for the charge readout. [84]

read by a total of four LARASIC4* cold amplifiers. Two $7\,\text{cm} \times 7\,\text{cm} \times 0.4\,\text{cm}$ scintillator tiles mounted above the charge-readout plane and below the cathode plane act as a small muon telescope and trigger for the charge readout.

5.2. ArgonCube Module

The ArgonCube module combines all principles discussed above in a rectangular shaped LArTPC, and represents an independent unit that can be used build large-scale detectors of arbitrary size and shape in multiples of modules. Figure 5.8 shows the drawing of a prototype module with a square footprint of $\sim 67\,\text{cm} \times 67\,\text{cm}$ and an active LAr volume of $\sim 63\,\text{cm} \times 63\,\text{cm} \times 126\,\text{cm}$. The active volume is split by the central cathode into two individual and identical TPCs. Each TPC is instrumented with a (2×4) array of pixel tiles (yellowish squares), with 4 tiles along the vertical axis, mounted onto the field-cage walls that are fabricated of G10 (epoxy fiberglass). Only one column of pixel tiles is visible in the drawing as it shows a central cut through the module. The inside of the walls perpendicular to the charge-readout planes are equipped with alternating ArCLight tiles and tiles made of three LCMs, starting from the top. High voltage (HV) is provided to the central cathode via the so-called HV-feedthrough, which is realized according to the design in Ref. [102]. The cathode, the inside faces of the field-cage bottom and top plates as well as the field-cage walls perpendicular to the charge-readout planes are laminated with highly resistive polyimid foil, forming together the resistive shell for the shaping of the drift field. The field cage is enveloped by a G10 sleeve, which is sealed onto a top steel-flange providing penetrations for instrumentation, and which is open at the bottom. An ullage volume right above the field cage allows for LAr leveling and pressure regulation and is separated form the top flange by a vacuum cavity made of steel to reduce the heat leak.

5.2.1. Cryogenic Scheme

The ArgonCube conc cryogenic scheme uses an external filtration-system to provide cold and pure LAr to the TPCs, which is needed to cool the readout electronics and to maintain the LAr purity. Several modules share a common cryostat filled with LAr. The LAr is extracted from the bulk volume below the modules, is cooled and filtered in an external system, and finally returned to the cryostat, where it is re-injected into the modules above the TPCs. From there, the cold and clean LAr flows down through gaps between the TPCs and the module sleeve to cool the readout electronics. Additionally, perforations in the field-cage bottom and top plates allow a flow through the TPCs to purify the active LAr volume. The module sleeve acts as a whir to contain the clear LAr in the module.

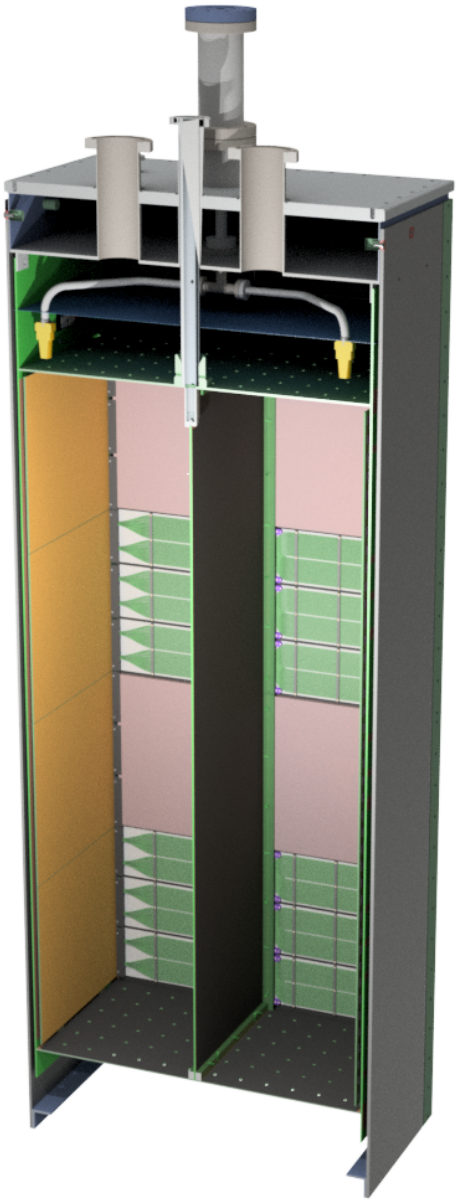

Figure 5.8.: ArgonCube Module0 technical drawing. The active volume is split by the central cathode into two individual and identical TPCs. Each TPC is instrumented with a (2×4) array of pixel tiles (yellowish squares) mounted onto the field-cage walls that are fabricated of G10 (epoxy fiberglass). The inside of the walls perpendicular to the charge-readout planes are equipped with light-readout tiles. High voltage (HV) is provided to the central cathode via the so-called HV-feedthrough. The field cage is laminated with highly resistive polyimid foil, forming the resistive shell for the shaping of the drift field. The field cage is housed in a G10 bucket which is sealed onto a top steel-flange providing penetrations for instrumentation. An ullage volume right above the field cage allows for LAr leveling and pressure regulation and is separated form the top flange by a vacumized cavity made of steel to prevent heat exchange with the outside.

5.2.2. Slow Control

Besides my personal contributions during the experimental activities at the University of Bern as a cryogenic an Data Acquisition (DAQ) expert, I set up a slow-control system for the monitoring of the detector hardware during laboratory operations. The monitored quantities cover temperatures, pressures, liquid levels, gas and liquid flows, high voltage as well as valve states. These quantities are fed into an open source time-series database[2], and in turn, are monitored in an open source analytics and interactive visualization web application[3]. A screen shot of the visualization that was used to monitor the LAr cryostat during the first run of the fully instrumented ArgonCube module, in March 2021, is shown in Figure 5.9.

Figure 5.9.: Slow-control visualization that was used to monitor the LAr cryostat during the first run of the fully instrumented ArgonCube module, in March 2021.

In order to reduce the wire count and noise introduced to the detector, I designed a PCB that allows to precisely read ten platinum resistive thermometers (Pt100[4]) at cryogenic temperatures. The PCB design is shown in Figure 5.10a; ten *MAX31865* resistance-to-digital converters digitize the values obtained from 4-point resistance measurements of the Pt100 sensors. The PCB can be plugged onto a *Raspberry Pi* single-board computer, which allows to select individual Pt100 channels and to feed the digitized measurements to the database via network link. A custom support structure was designed to house the PCB and *Raspberry Pi* computer, as shown in Figure 5.10b. The bottom plate is equipped with two D-Sub 25 connectors and can directly be plugged onto the detector

[2]InfluxDB version 1.8.3 (`https://www.influxdata.com/`).
[3]Grafana v5.4.2 (`https://grafana.com/`).
[4]Platinum resistor with 100 Ω nominal resistance at 0 °C.

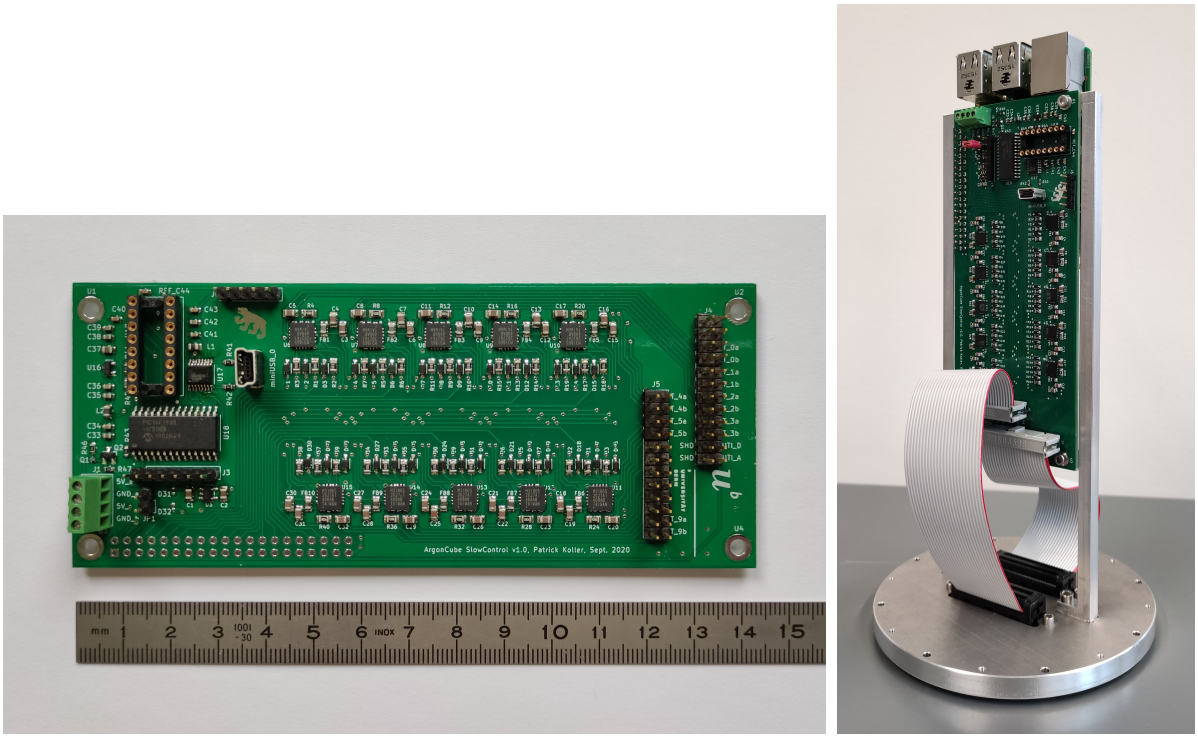

(a) **(b)**

Figure 5.10.: Slow-control PCB.

feedthrough. An aluminum cylinder with a cover (not shown) can be pulled over the construction to protect the sensitive electronics.

5.2.3. SingleCube

Several tests regarding the ArgonCube module design have been performed at the University of Bern. The design shown in Figure 5.8 makes obvious that each pixel tile serves one 16th of the module's active volume, having the shape of a cuboid with 30.3 cm × 31.0 cm × 31.0 cm side length each (30.3 cm along the drift axis). A cubic LArTPC of such dimensions equipped with a full-sized pixel board and an ArCLight tile was given the name SingleCube and operated at the University of Bern. The cubic TPC was submerged in a cryostat filled with purified LAr as shown in Figure 5.11a. A second

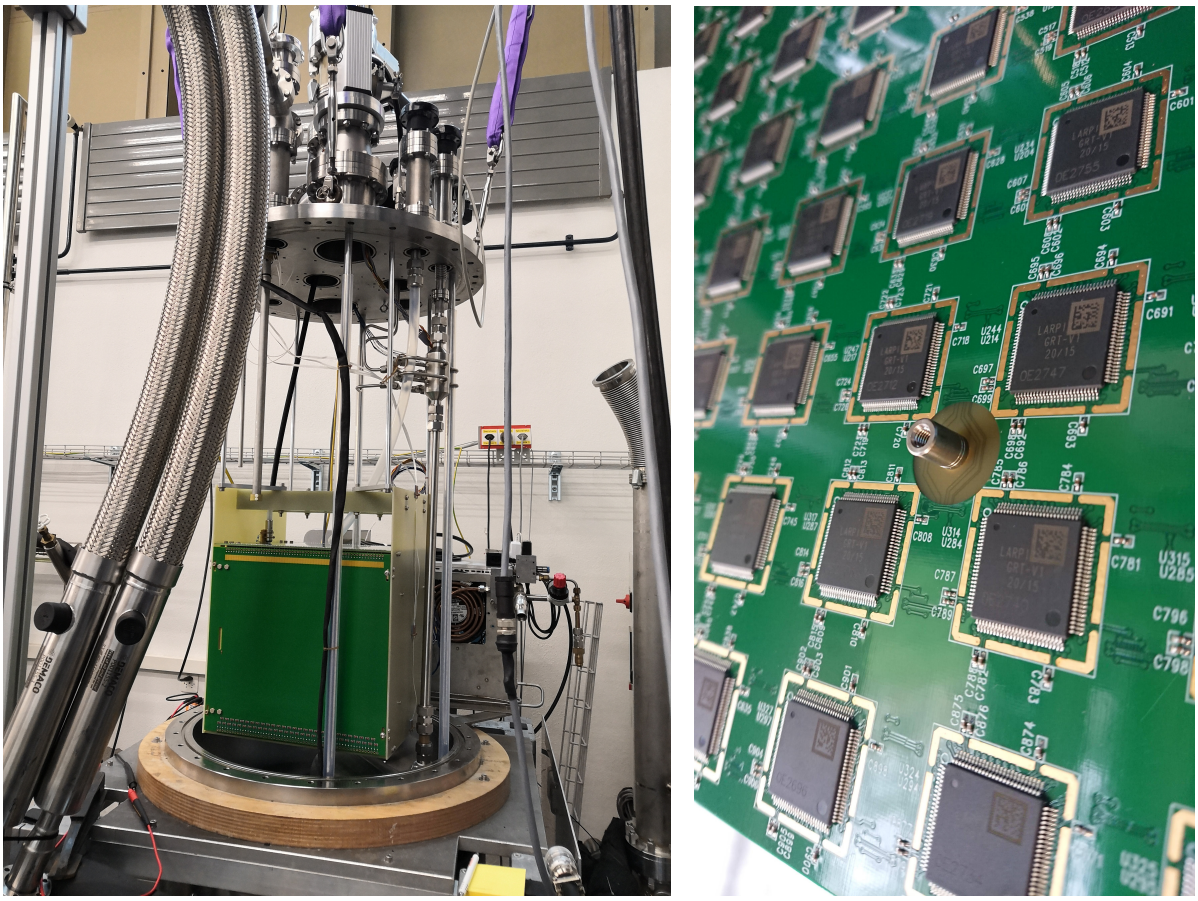

(a) **(b)**

Figure 5.11.: SingleCube experimental setup at the University of Bern (a) and LArPix second generation ASICs soldered to the back of the used pixel PCB (b).

generation of the LArPix ASIC encapsulated in epoxy package and directly soldered to the back of the pixel PCB, as it is shown in Figure 5.11b, has been used in this test. The used pixel board counts a total of 4900 charge-collecting pads with 4 mm × 4 mm size

that are arranged in a grid of 70×70 pixels with a pitch of $\sim 4.4\,\text{mm}$. A total of 100 ASICs are soldered in a 10×10 array to the back of the pixel board serving a section of 7×7 pixels each.

An external purpose-built LAr filtering-system submerged in liquid nitrogen was used to support the system with purified cold LAr. Therefore, a cryogenic pump was used extract LAr from the bottom of the cryostat, push it through the cooled external filter system and re-extract it in the cryostat right above the SingleCube TPC. With such a system, the LAr is not only being purified but simultaneously provides cooling to the readout electronics mounted in the TPC.

SingleCube was the first experiment that operated a full-sized pixel board in conjunction with ArCLight in a LArTPC. It successfully reconstructed 3D cosmic-ray events and demonstrated the interplay between the charge and the light read-out systems with the light read-out providing an external trigger to the charge read-out for event reconstruction. The TPC was operated in a cryogenic system that also provided a first test of the external LAr filtration system designed for the larger ArgonCube demonstrators. Further testes were needed to demonstrate the system's capabilities of maintaining the needed LAr purity in a full-sized module.

5.2.4. Module0

A first full-size ArgonCube module, given the name Module0, was equipped with only one pixel tile, one ArCLight tile and one LCM tile. Any un-instrumented areas were kept blank in the case of light readout or replaced with dummy anode-tiles in the case of charge readout. The main goal of this setup was to test the HV stability and to demonstrate the stable operation of the novel pixelated charge-readout system without damaging its sensitive electronics. The module was submerged in a cryostat filled with LAr and perforations in the bottom and top plates of the field cage allowed for liquid flow from and to the TPC. The same external filtration system previously tested in the SingleCube setup was used to filter the LAr and provide cooling power to the readout electronics inside the field cage. No HV related issues were detected and the charge readout successfully reconstructed 3D cosmic-ray events.

Finally, Module0 was fully instrumented and operated for the first time in early 2021. A total of 16 pixel boards were used to form the anode planes of the two TPCs represented by the ArgonCube module, and 8 ArCLight tiles and 8 LCM tiles (24 LCMs in total) seamlessly covered the field-cage walls parallel to the drift direction. Purpose-built front-end electronics developed at LBNL was used to daisy chain the LArPix ASICs of eight pixel boards (one TPC) each. Analogously, front-end electronics developed at JINR was used to simultaneously communicate with both light-readout systems, ArCLight and LCM, deployed in a single TPC.

The full instrumentation and respective cabling of the module introduces a big potential for spoiling the LAr. Accordingly, the testing of maintaining the LAr purity was the main issue of the first run. The used cryostat and the Module were carefully cleaned and vacumized before filling with ultra-pure LAr in order to register a potential degradation of the LAr purity due to water moisture, out-gassing of hydrocarbon cables or a lack of

filtration power by the external filtering system. The purity was indirectly measured via the electron lifetime of straight MIP-like cosmic-ray muons crossing the drift field. Clean tracks were registered from the first day on right after the filling process with an electron lifetime around 2 ms gradually increasing over the week of data taking. The temporal evolution of the electron lifetime measured with the fully instrumented Module0 is shown in Figure 5.12.

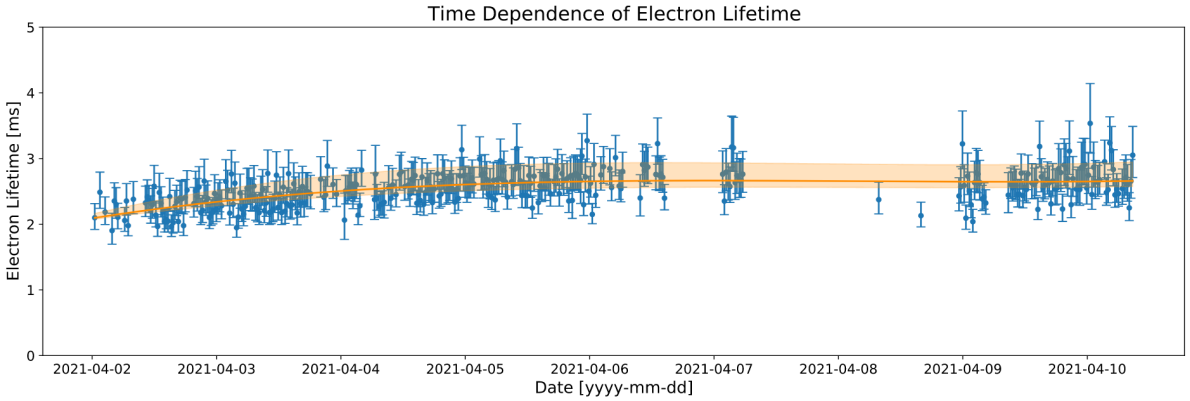

Figure 5.12.: Evolution of the electron lifetime measured with the fully instrumented Module0 prototype. The lifetime was 2 ms right after the filling process and gradually increased over one week of data taking. [103]

The Module0 test provided the proof of principle for the external filtration system by means of filtration power needed to maintain the targeted electron lifetime. In addition, it successfully demonstrated that the filtration system was able to provide enough cooling for continuous and stable operation of a full-sized pixel board over more than a week. The data collected with the Module0 is currently being processed and a DUNE Collaboration paper in order to publish the results in the near future is in preparation. A preliminary visualization of the charge data collected during the run looks very promising. Figure 5.13 shows a python-based event display that I set up to visualize cosmic-ray events reconstructed with the fully instrumented Module0. Charge signals collected with multiple pixel boards distributed among both TPCs of the module were successfully combined to form a complete image of the event.

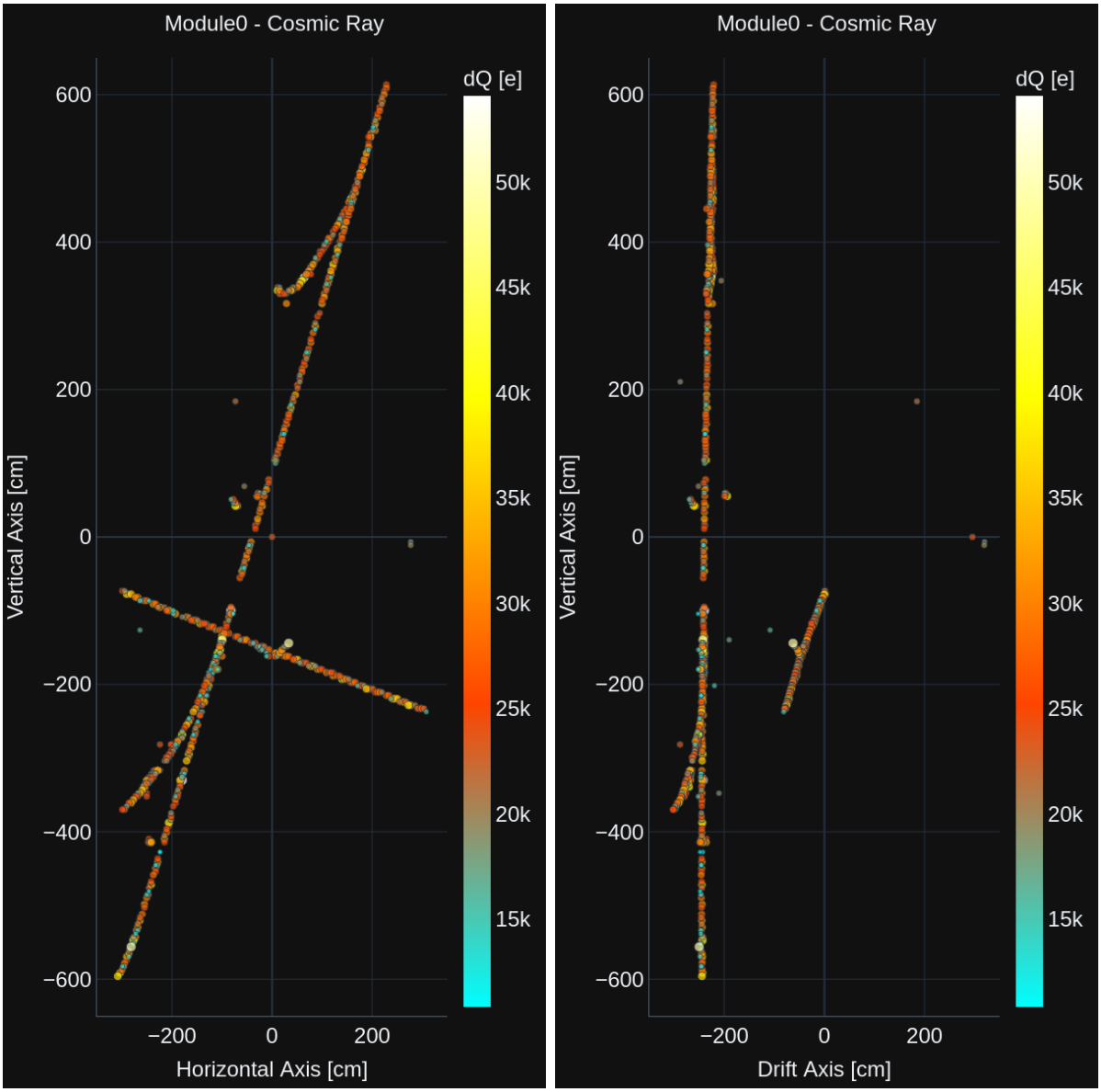

(a) **(b)**

Figure 5.13.: Visualization of a cosmic-ray event reconstructed with the fully instrumented Module0. Charge signals collected with multiple pixel boards distributed among both TPCs of the module were successfully combined to form a complete image of the event. [103]

5.3. Application in the DUNE Near Detector

The modular ArgonCube concept proofed its capability to provide large-scale LArTPCs with unambiguous true-3D imaging. Modularization keeps pile-up of both charge and light signals low yet minimizing the dead volume thanks to its novel dielectric light-readout system. Accordingly, ArgonCube is able to provide detectors with multiple tonnes of argon targets able to work in high-multiplicity beam environments, which makes it the perfect candidate for the required LAr component of the DUNE ND. In 2019, a modular LArTPC with pixelated charge readout, based on the ArgonCube concept, was incorporated into the DUNE ND design by the DUNE Collaboration.

5.3.1. ND-LAr

The ND-LAr detector design is shown in Figure 5.14. The detector consists of 35 modules, grouped into 7 rows of 5 modules, that are submerged in a common membrane cryostat filled with LAr. Each row shares a common cryogenic system for the supply of purified cold LAr, and is suspended under a section of insulation that forms the top flange of the cryostat. A row can be pulled as needed in order to repair or upgrade. The modules have a footprint of $1\,\mathrm{m} \times 1\,\mathrm{m}$ and are split into two TPCs of 3 m height with drift lengths of 50 cm, resulting in a total active mass of 147 t. A drift field with $\sim 0.5\,\mathrm{kV\,cm^{-1}}$ strength (comparable to the DUNE FD) is achieved with an applied cathode voltage of only 25 kV. The anode planes are formed of $30\,\mathrm{cm} \times 50\,\mathrm{cm}$ pixelated PCB-tiles with LArPix ASICs soldered to the back of the PCBs for cold amplification and digitization. Dielectric light-readout tiles, $30\,\mathrm{cm} \times 50\,\mathrm{cm}$ wide, cover the inside of the field-cage walls perpendicular to the charge-readout planes.

5.3.2. Detector Dimensions

The overall ND-LAr dimensions are defined through the hadron containment in neutrino cross-section measurements. Hadrons originating in the neutrino interactions must be fully contained in the LArTPC for a fraction of events up to 5 GeV neutrino energy. Simulations in LAr were used to evaluate the cross-section coverage for different detector dimensions. Neutrons were excluded from the hadronic energy calculation because only a small fraction of their kinetic energy is visible. Figure 5.15 shows the cross-section coverage as a function of detector height (left) and as a function of detector length (right), holding the other two dimensions fixed. It is desirable that the coverage does not vary rapidly with the detector dimensions to prevent model dependencies. Since the events are rotationally invariant about the beam axis, symmetries can be used to sample events. The optimal dimensions for hadron containment turns out to be $4\,\mathrm{m} \times 3\,\mathrm{m}$ transverse to the beam, and 5 m in the beam direction. The longer transverse dimension is chosen to be the width rather than the height because of the detector hall construction. Besides the hadron containment also to contain side-going muons is relevant for neutrino-energy reconstruction, where there is no coverage from the downstream spectrometer. For this

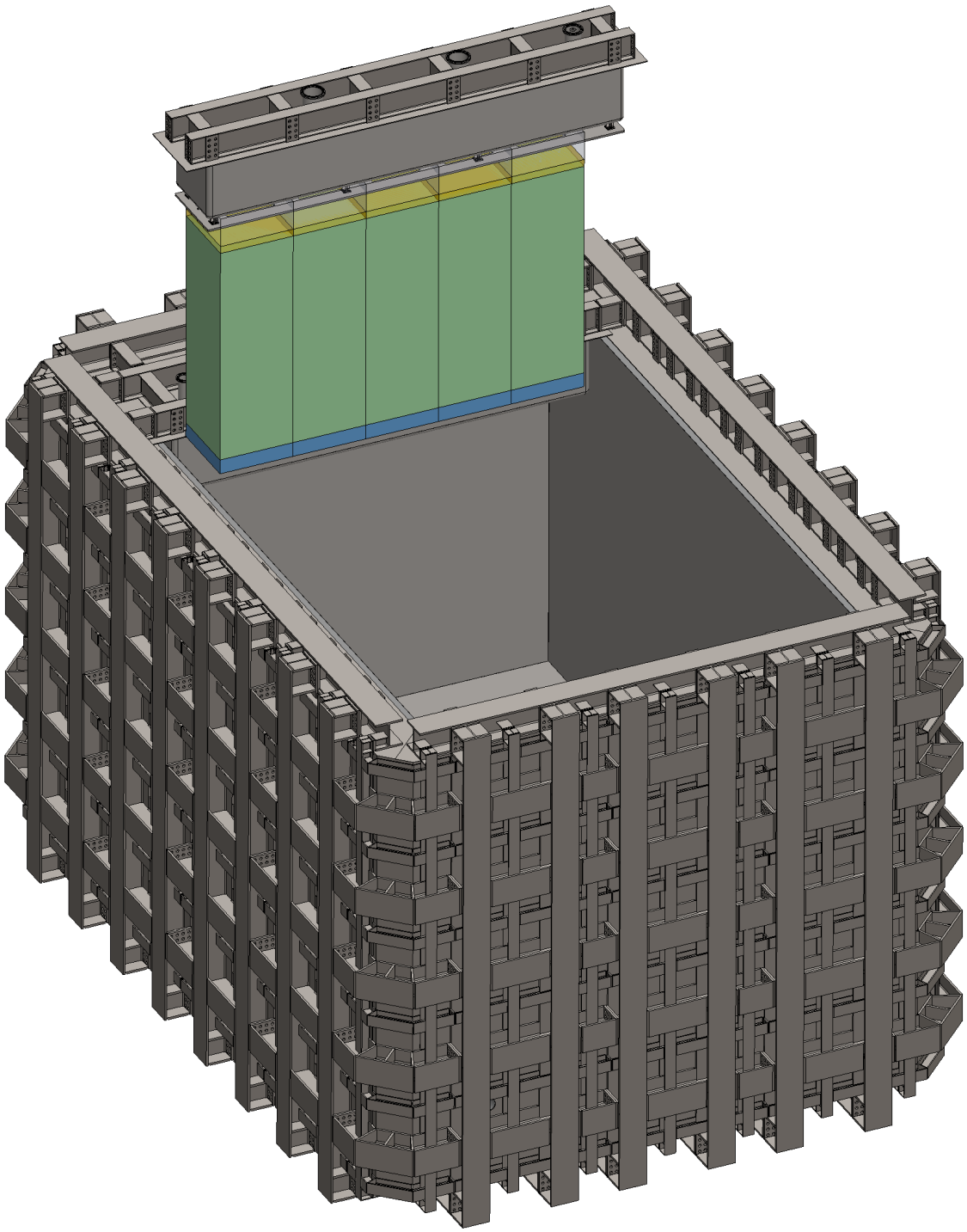

Figure 5.14.: The DUNE ND-LAr detector is comprised of 35 modules (green), grouped into 7 rows of 5 modules, that are submerged in a common membrane cryostat (gray) filled with LAr. Each row shares a common cryogenic system for the supply of purified cold LAr, and is suspended under a section of insulation that forms the top flange of the cryostat. A row can be pulled as needed in order to repair or upgrade.[104]

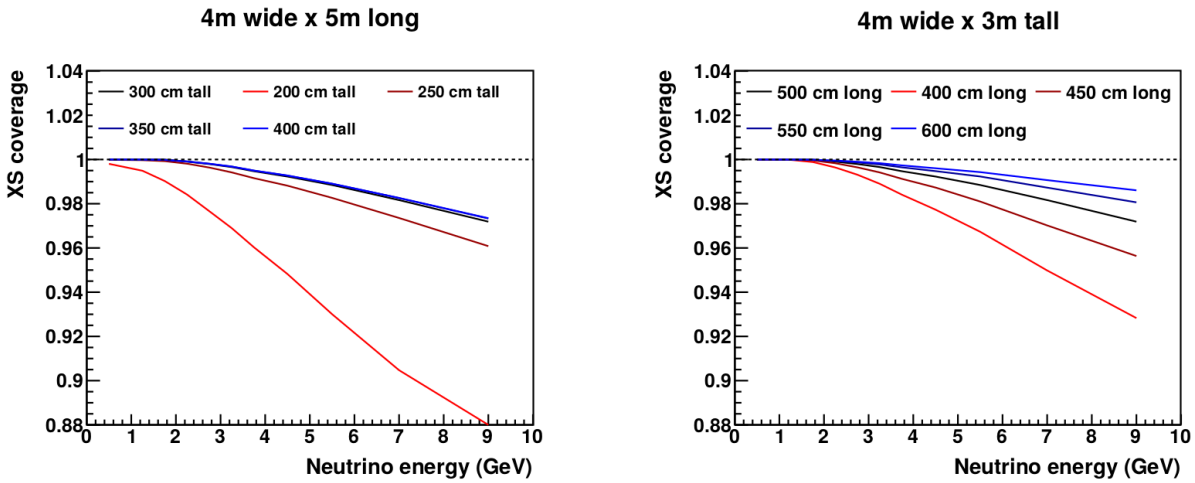

Figure 5.15.: The cross-section coverage by means of hadronic energy containment (neutrons excluded) is shown for various LArTPC heights (left) and widths (right) as a function of true neutrino energy. In each plot, the other two dimensions are held constant at the baseline values while the third dimension is varied. The optimal dimensions for hadron containment are determined to be 4 m × 3 m × 5 m. [23]

reason, the width of the final design has been increased from 4 m to 7 m, which also benefits flux constraints. [23]

5.3.3. Module Dimensions

The low cathode voltage and the efficient detection of fast scintillation light are driving the dimensions of the modules used in ND-LAr. A short optical path length is desired to reduce the light attenuation in LAr, and to minimize smearing of the photon arrival-time distribution due to Rayleigh scattering. Additionally, a short drift length allows for higher electric field strengths serving to suppress the slow component of the LAr scintillation light. A module with a 1 m × 1 m footprint splits the active volume among two TPCs with a drift length of 50 cm each, which allows the targeted electric field strength of 0.5 kV cm^{-1} with the cathode voltage limited to 25 kV. With such dimensions, the maximum optical path in the module is only 50 cm while the Rayleigh scattering length is about 1 m for scintillation light in LAr (see Tab. 4.1). A smaller module footprint would not yield significant physics improvements and is not desirable because of the increased number of readout channels, component count and inactive material. [23]

5.3.4. Handling of Pile-up

With a duration of $\sim$ 300 µs, the TPC drift-window at 0.5 kV cm^{-1} is relatively long compared to the 10 µs beam-spill length. Consequently, looking at the charge response will not reveal images of single interactions but the piled-up activity of all events happening

during the beam spill. For a spill at 1.2 MW beam power, a mean of 55 neutrino interactions are expected to deposit signals in the active volume of ND-LAr – including targets both internal and external to the LArTPC. Figure 5.16 illustrates the event pile-up of a spill at 1 MW beam power as seen by the charge readout of DUNE's ND-LAr, based on simulations. The top plot shows a side-view of all charge deposited within a single beam-spill, where charge deposits are colored according to the event number. The bottom plot shows the same beam spill but with charge deposits colored by the amount of deposited charge, as it will actually be seen by the ArgonCube charge-readout system.

The ability to handle event pile-up in a hight-rate environment, such as the DUNE-ND site, is one of the ND requirements listed in Section 3.9.5. Segmenting the detector volume into 70 TPCs (14 segments along the drift axis) reduces the number of neutrino interactions per spill from a total of 55 to 5 per segment. The modularization of ND-LAr also optically isolates each TPC from neighboring TPCs and contains scintillation light to reduce optical pile-up and improve the time response. The timing requirements of ND-LAr are set such that the pile-up of the $\mathcal{O}(100)$ events over 10 µs, resulting in an average spacing of the $\mathcal{O}(100)$ ns, can be separated using the optical signals in the detector. Simulations have shown that modularization drastically reduces optical pile-up. At 25 ns timing resolution, 3 % of the neutrino interactions within a TPC are within 25 ns of each other with modularization, whereas 30 % of the neutrino interactions are within 25 ns of each other with a monolithic TPC [23]. The ArgonCube light-readout system is able to provide absolute event time-stamps with a resolution of the $\mathcal{O}(1)$ ns. It is therefore vital for disentangling overlapping neutrino interactions in the expected high-rate environment and to match out-going muons between the ND-LAr and ND-GAr.

While pattern recognition using the charge signals from ND-LAr is expected to be a powerful handle to separate activity from piled-up neutrino interactions, the excellent timing capability of the light-readout system is the primary means by which beam activity can be separated from non-beam background. Additionally, the modularization provides localized timing information which plays an important role if it comes to the assignment between detached energy deposits and neutrino interaction vertices. Such procedures require commensurate timing synchronization between the LArTPC modules and are one of the key aspects that will be tested in a modular LArTPC prototype with the name ProtoDUNE-ND. [23]

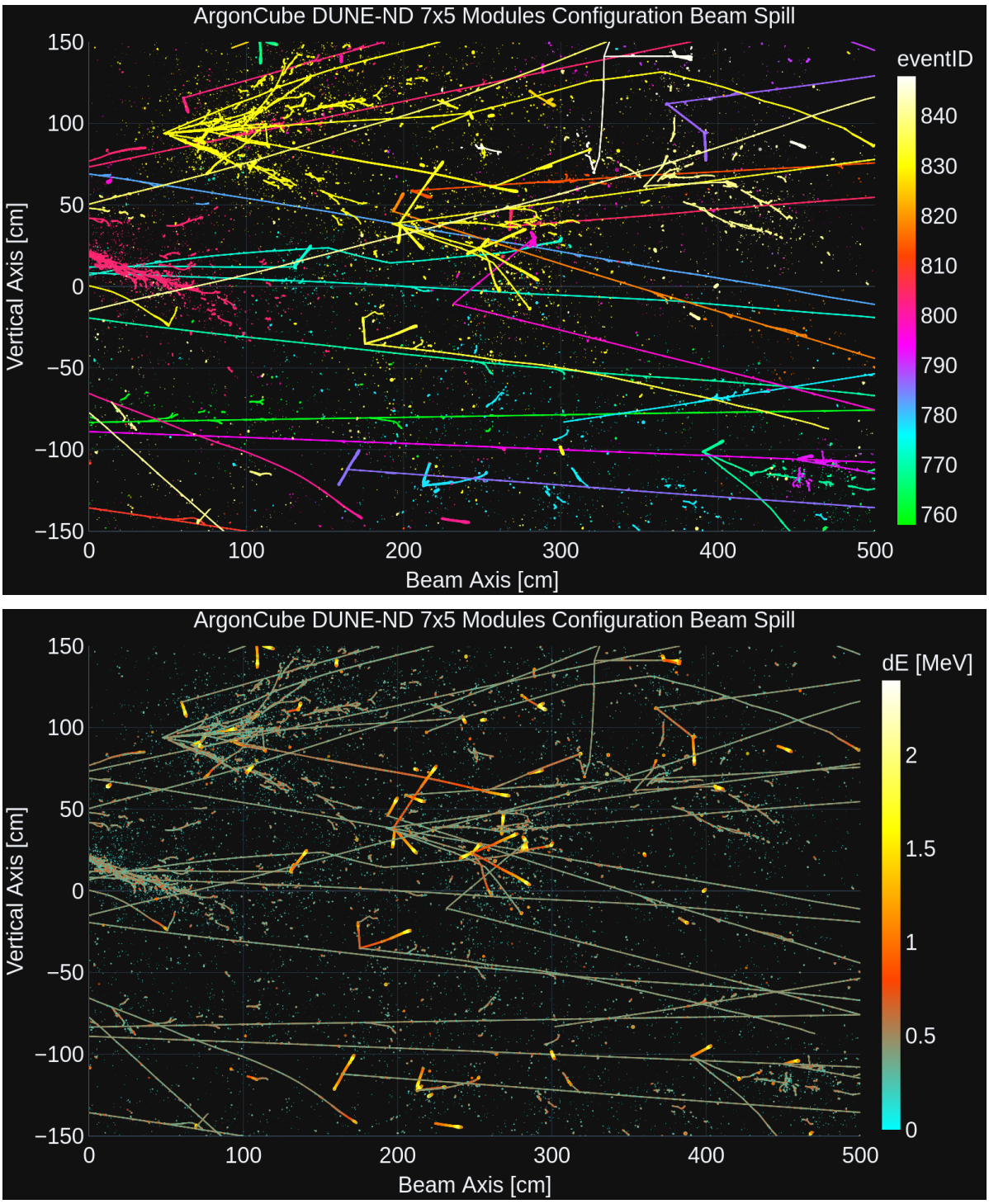

Figure 5.16.: Event pile-up in a 1 MW beam spill as seen by DUNE's ND-LAr based on simulations. The top plot shows a side-view of all charge deposited within a single beam-spill, where charge deposits are colored according to the event number. The bottom plot shows the same beam spill but with charge deposits colored by the amount of deposited charge, as it will actually be seen by the ArgonCube charge-readout system.

5.4. ProtoDUNE-ND

The last stage of the ArgonCube Research & Development (R&D) program is an intermediate-scale prototype of ND-LAr, the ArgonCube 2×2 Demonstrator, which has four modules arranged in a 2×2 grid. All four modules are identical and have the same design and dimensions as the Module0 discussed above, which means they are a little over half the size of the ND modules. Accordingly, the total active volume will be represented by eight self-contained LArTPCs and have the shape of a cube with almost 1.4 m side length. Each module can separately be extracted from and inserted into the shard purpose-built LAr cryostat, as shown in Figure 5.17.

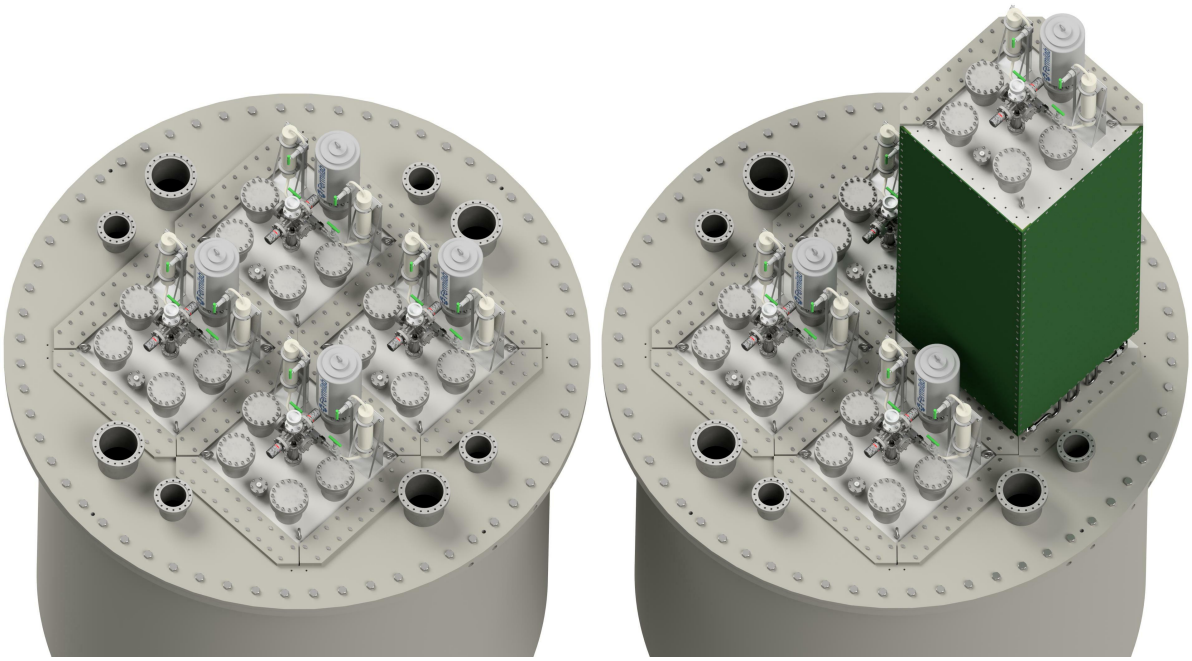

Figure 5.17.: ArgonCube 2×2 Demonstrator technical drawing. A purpose-built LAr cryostat will house for identical ArgonCube modules (same design as Module0) providing a total active volume of $\sim 1.4\,\mathrm{m} \times 1.4\,\mathrm{m} \times 1.4\,\mathrm{m}$ (left). Each module can separately be extracted from and inserted into the LAr cryostat (right). [105]

The ArgonCube 2×2 Demonstrator will be placed into the Neutrinos at Main Injector (NuMI) on-axis neutrino beamline at FNAL, to serve as the core component of a prototype detector for the DUNE ND with the name ProtoDUNE-ND. This will allow to study the detector response in a neutrino beam that is directly comparable to the neutrino beam of DUNE. Additional detector components (scintillator trackers as well as electromagnetic and hadronic calorimeters) will be placed upstream and downstream of the 2×2 Demonstrator and used for additional detector-physics studies.

5.4.1. Flux Studies

One of the primary concerns motivating the ProtoDUNE-ND program is how well the ND components will perform in a high-multiplicity environment. Neutrino flux studies have shown that the on-axis NuMI beam is the most suitable existing beamline for providing a useful neutrino-beam test for the proposed ND components. Figure 5.18 shows a comparison of the simulated fluxes (a) and event rates (b) as a function of neutrino energy for different existing neutrino beamlines at FNAL and the future DUNE beamline provided by the LBNF. The proposed LBNF flux is significantly more intense

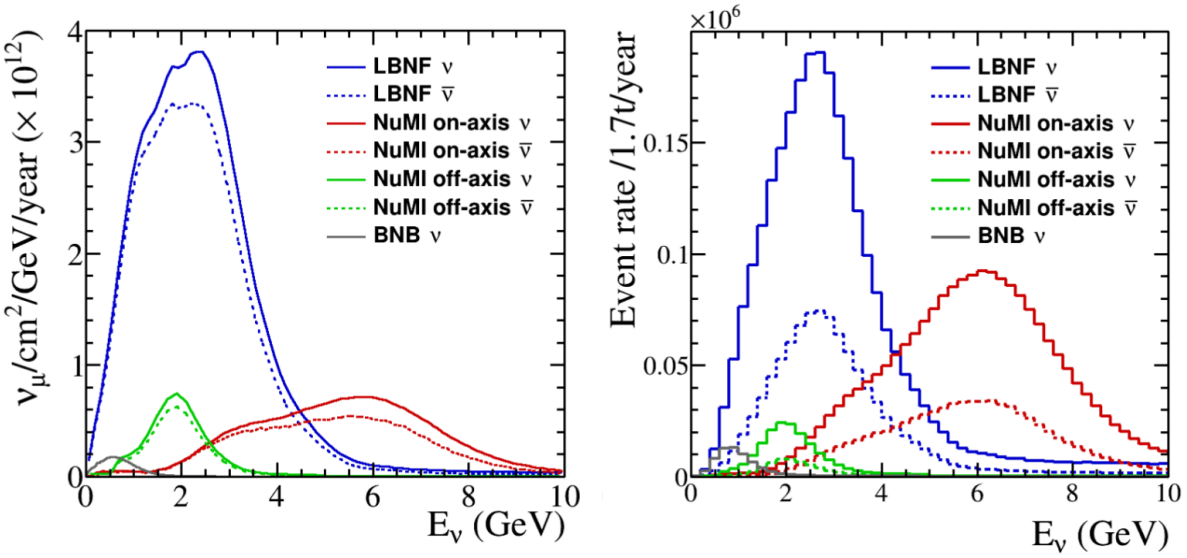

(a) Flux **(b)** Rate

Figure 5.18.: Comparison of the absolutely normalized fluxes for different neutrino beamlines at FNAL (a), and the expected yearly rates in the ArgonCube 2×2 Demonstrator's 1.7 t active LAr volume (b) as a function of neutrino energy (produced wit GENIE v2.12.10 with the "ValenciaQEBergerSehgalCOHRES" configuration). [105]

than the fluxes sampled at any existing experimental hall. However, due to the roughly linear relationship between neutrino energy and cross section, the measured rate from the on-axis NuMI beam in the ND hall of the former MINOS experiment is approximately the same as for the planned LBNF flux. [105]

5.4.2. Detector-Physics Studies

Basic detector stability checks as well as the testing of module extraction and insertion have been performed with a period of detector operation at the University of Bern. However, tests in Bern can only be performed using cosmic-ray muons, which have limited utility beyond basic detector stability checks. A selection of key detector-physics studies that could be performed with the ProtoDUNE-ND are:

- Combining light and charge signals among full-size ArgonCube modules in a comparably noisy environment to the DUNE ND.
- Event reconstruction in a modular environment, taking the gaps in particle tracks traversing multiple modules into account.
- Identify detached energy deposits in neighboring modules.
- Detection of neutrons with kinetic energies of the $\mathcal{O}(1)$ keV through neutron capture.
- Detection of fast neutrons with kinetic energies from the $\mathcal{O}(1)$ MeV to the $\mathcal{O}(1)$ GeV through recoiling charge particles after a collision of a neutron with a nucleus.
- Measuring the EM shower resolution using $\pi^0 \to \gamma\gamma$ decays.

Such studies would help to inform the final design of the DUNE ND, and aid in developing reconstruction algorithms suitable for neutrino interactions. [105]

5.4.3. Simulation

Simulations were used to check the feasibility of the proposed ProtoDUNE-ND studies. High statistics GENIE Monte Carlo samples were produced to compare the basic properties of neutrino interactions expected in the LBNF and NuMI Medium Energy (ME) beamlines. These events were then used to seed a GEANT4 simulation using the ArgonBox[5] software, in order to get a basic understanding of event shape and containment. Events were simulated in a $200\,\mathrm{m} \times 200\,\mathrm{m} \times 200\,\mathrm{m}$ box of LAr, and were then distributed randomly inside a volume with the correct spatial dimensions of the ArgonCube 2×2 Demonstrator active volume. Although the 2×2 geometry was not included in the simulation, this gives an acceptable estimate of the expected event rates and containment for the studies described above. Examples of the ArgonBox simulation with the basic ArgonCube 2×2 Demonstrator geometry superimposed can be seen in Figure 5.19 for a number of different neutrino energies.

I have performed a study that estimates the fraction of the incident neutrino energy that is contained in the active volume of the ArgonCube 2×2 Demonstrator. A fiducial volume was defined 30 cm (two radiation lengths in LAr) inwards from each side of the detector. Only neutrino interactions with the vertex inside the fiducial volume have been considered in the study, both ν_μ CC and NC. Figure 5.20 shows the fraction of contained neutrino energy as a function of the incident neutrino energy, colored by the number of events. In the left-hand plot, the energy carried away by any particles produced in the interaction has been taken into account, while in the right-hand plot, the energy carried away by primary muons produced in CC interactions has been ignored and subtracted from the neutrino energy. An event is classed as contained if $\geq 90\,\%$ of the incident neutrino energy is contained in the 2×2 active volume (events above

[5] `https://github.com/dadwyer/argon_box`

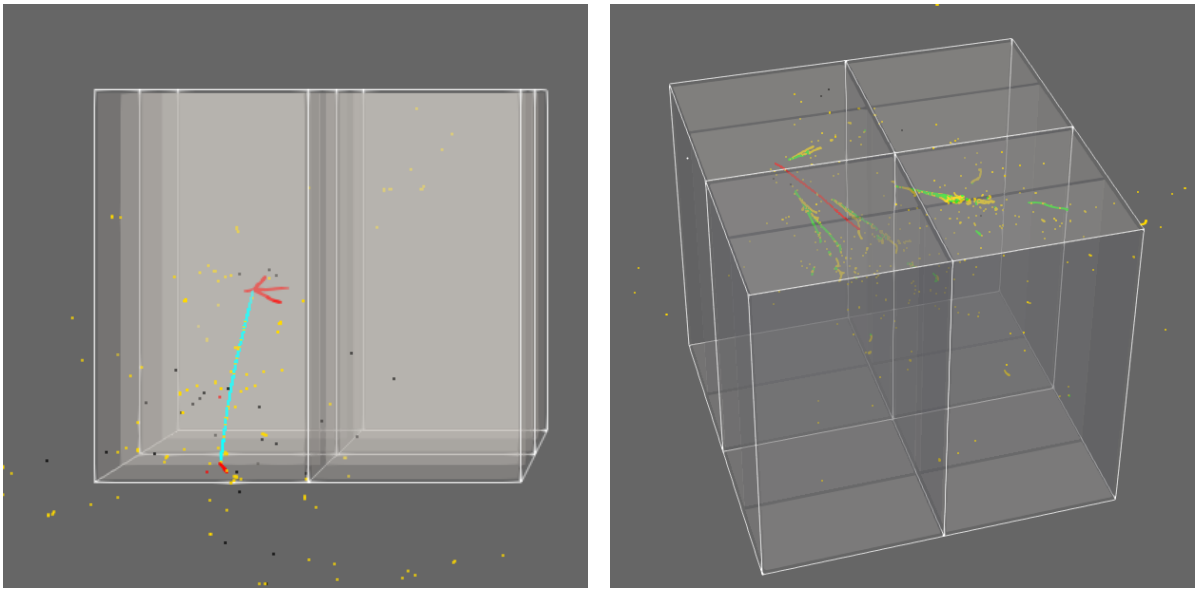

(a) $E_\nu = 2.6\,\text{GeV}$ **(b)** $E_\nu = 3.36\,\text{GeV}$

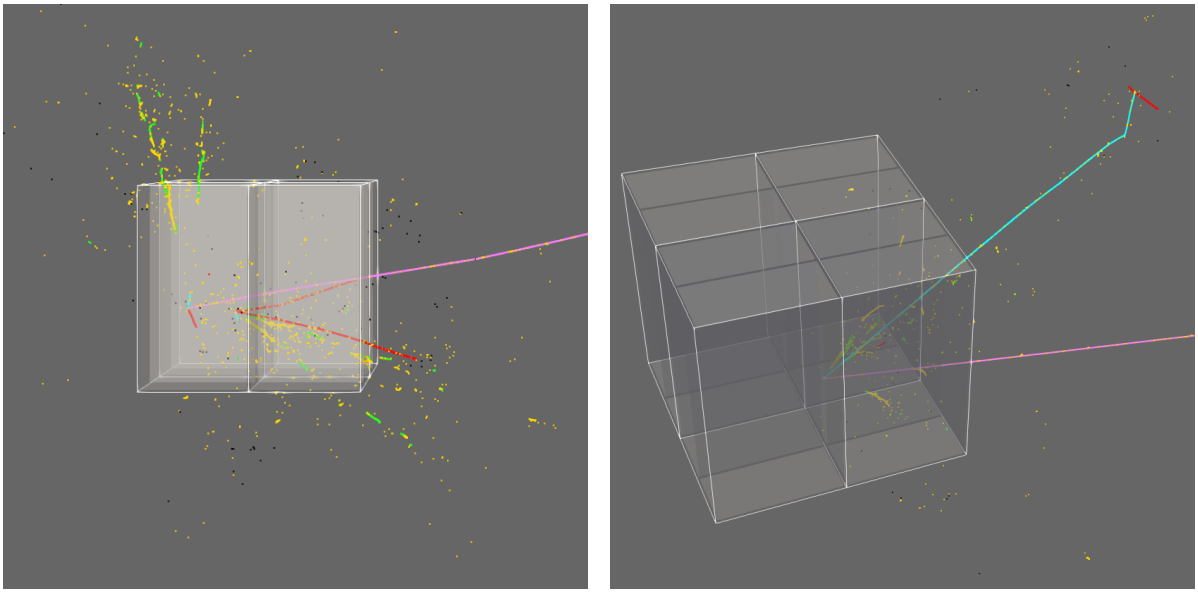

(c) $E_\nu = 4.83\,\text{GeV}$ **(d)** $E_\nu = 9.37\,\text{GeV}$

Figure 5.19.: Example ν_μ interactions in LAr simulated with ArgonBox for a number or different incident neutrino energies, and with the ArgonCube 2×2 Demonstrator geometry superimposed but not simulated. The event vertices are randomly distributed within the active volume of the 2×2 Demonstrator. Energy deposits are color-coded according to the particle type: $\pi^\pm$ – blue; $\mu^\pm$ – purple; e^+ – green; e^- – yellow; protons – red; recoiling nuclei – black.

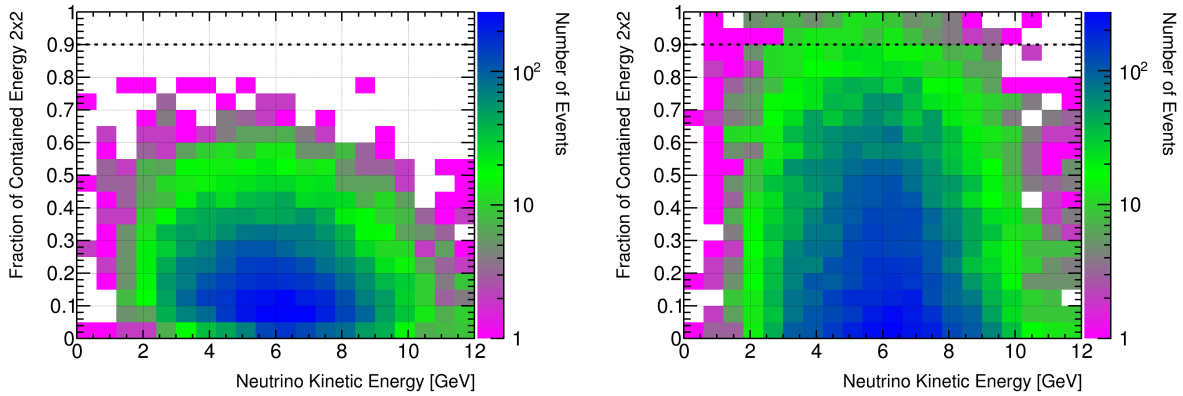

(a) w/ primary muons **(b)** w/o primary muons

Figure 5.20.: Fraction of neutrino energy contained in the active volume of the ArgonCube 2×2 Demonstrator as a function of the incident neutrino energy, colored by the number of events. In the left-hand plot, the energy carried away by any particles produced in the interaction has been taken into account, while in the right-hand plot, the energy carried away by primary muons produced in CC interactions has been ignored and subtracted from the neutrino energy. An event is classed as contained if $\geq 90\,\%$ of the incident neutrino energy is contained in the 2×2 active volume (events above the horizontal dashed line).

the horizontal dashed line). The containment efficiencies in each neutrino-energy bin have been derived from Figures 5.20a and 5.20b, and are represented by the fraction of events above the dashed lines compared to the total number of events in the respective bin. These efficiencies are visible in Figure 5.21. The simulation clearly shows that

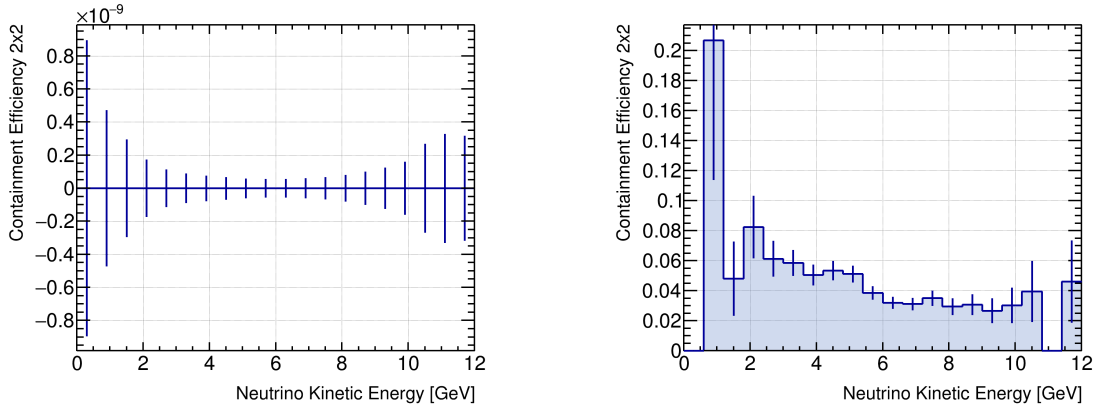

(a) w/ primary muons **(b)** w/o primary muons

Figure 5.21.: Efficiencies for containing neutrino events in the ArgonCube 2×2 Demonstrator, as a function of the neutrino energy. In the left-hand plot, the energy carried away by any particles produced in the interaction has been taken into account, while in the right-hand plot, the energy carried away by primary muons produced in CC interactions has been ignored and subtracted from the neutrino energy. An event is classed as contained if $\geq 90\,\%$ of the incident neutrino energy is contained in the 2×2 active volume.

the ArgonCube 2×2 Demonstrator is too small to fully contain neutrino events, which is mainly due to the escaping primary muon produced in CC interactions. However, ignoring the primary muon, a valuable sample of contained events ($\pm 4\,\%$ of all events) will be available for detector studies in the ArgonCube 2×2 Demonstrator test at FNAL.

In order to test how well the reconstruction can identify shower depth, a sample of fully contained EM showers would be extremely useful. Additionally, a sample of $\pi^0 \rightarrow \gamma\gamma$ decays, where both photons produce showers that are fully contained in the ArgonCube 2×2 active volume, would be very helpful to measure the EM shower resolution. Respective containment efficiencies are shown as a function of initiator-particle energy in Figure 5.22, for EM showers and π^0 decays. Only neutrino interactions with the vertex inside the fiducial volume have been considered in the study, both ν_μ CC and NC. A shower is classed as contained if $\geq 90\,\%$ of the shower energy is contained in the active volume of the detector. Both single EM showers and pairs of EM showers induced by π^0 decay are contained up to initiator-particle energies of $\sim 3\,\text{GeV}$.

Neutrons pose a big problem in LArTPCs because they are not visible and can carry away significant amounts of energy. An extensive discussion about neutron detection in LArTPCs will follow in the chapter 6.

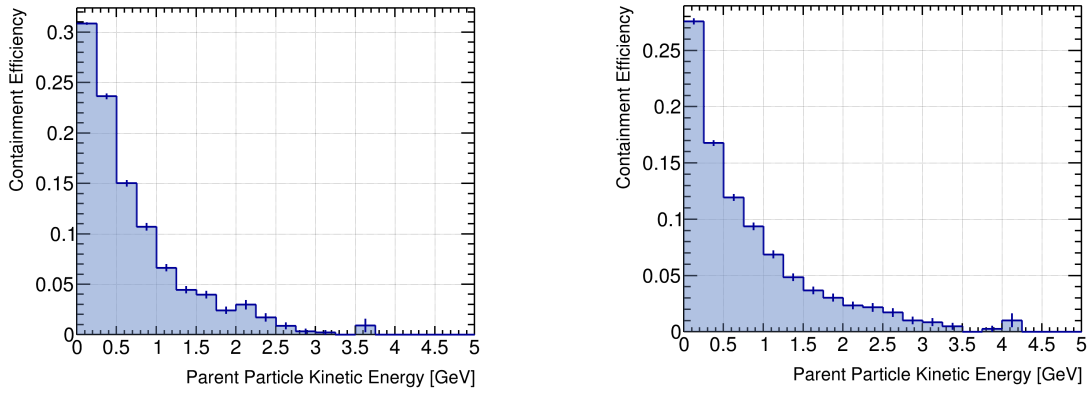

(a) EM shower **(b)** $\pi^0 \to \gamma\gamma$

Figure 5.22.: Efficiencies for containing EM showers (a) and both photon-induces showers from π^0 decays (b) in the ArgonCube 2×2 Demonstrator, as a function of the initiator-particle energy. A shower is classed as contained if $\geq 90\,\%$ of the shower energy is contained in the active volume of the detector.

5.4.4. Additional Studies Including a Muon Tracker

Many muons produced in neutrino events in the DUNE ND will not be contained in the ND-LAr. Therefore, a magnetized muon spectrometer will be place downstream of ND-LAr in order to determine the energies of escaping forward-going muons, which is essential for the neutrino-energy reconstruction. These muons need to be matched between the ND-LAr and the muon spectrometer.

Similarly, ProtoDUNE-ND will place detector components re-purposed from the Main Injector Experiment for ν-A (MINERνA) downstream of the ArgonCube 2×2 Demonstrator, acting as a muon tracker. The tracker will be used to demonstrate the ability to match tracks between the ArgonCube modules, with slow charge and fast light readout, and other, fast detector components. Additionally, the tracking will broaden the phase-space over which events of interest can be reconstructed in ProtoDUNE-ND. For example, it will be able to provide a valuable sample of fully contained electromagnetic showers, where the shower would not be contained the active volume of the stand-alone 2×2 Demonstrator. Such an event is shown in Figure 5.23.

Additional scintillator planes will be placed upstream and downstream of the ArgonCube 2×2 Demonstrator in ProtoDUNE-ND. This will allow to tag muons originating from the surrounding rock independently of the ArgonCube system, providing an ideal sample to be used for calibration purposes, e.g. for measuring electric field uniformities with crossing muons. [23]

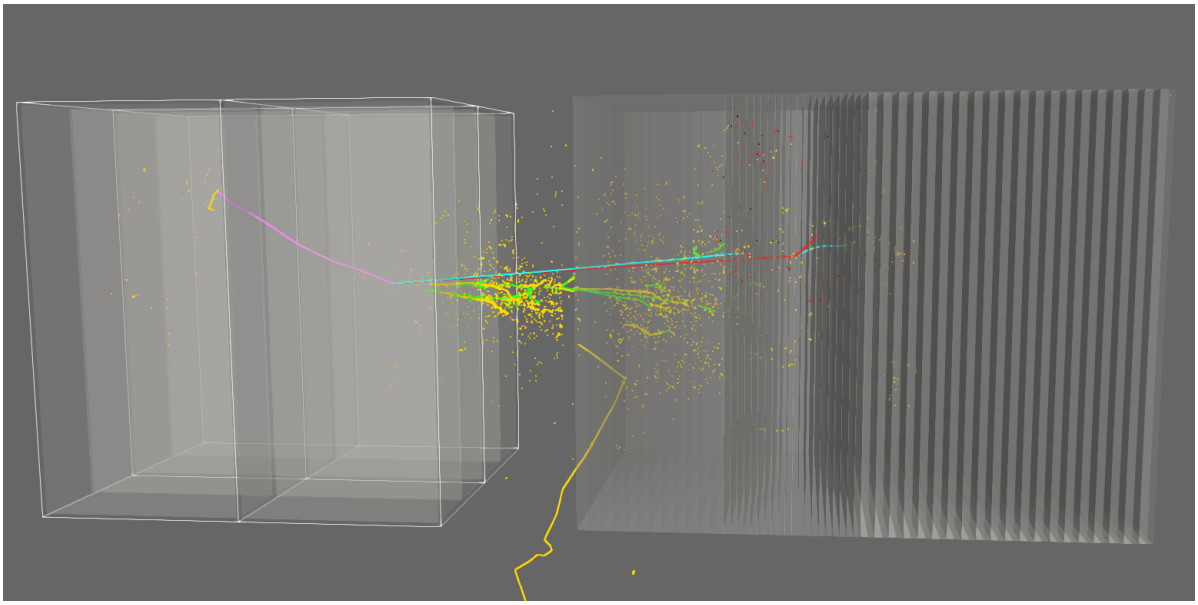

Figure 5.23.: Example CC interaction of a 7 GeV ν_μ in LAr simulated with ArgonBox. The ArgonCube 2×2 Demonstrator with downstream muon-tracker geometry is superimposed but not simulated. Particles/showers not contained in the the 2×2 Demonstrator exit downstream, and are seen in the muon spectrometer re-purposed from MINERνA detector components. Energy deposits are color-coded according to the particle type: $\pi^\pm$ – blue; $\mu^\pm$ – purple; e^+ – green; e^- – yellow; protons – red; recoiling nuclei – black.

6. Neutron Tagging in LArTPCs

Neutrons emerging from the neutrino interaction vertex can carry away more than 25 % of the neutrino energy. Being electrically neutral particles, neutrons do not ionize atoms when traversing LAr, and consequently are not visible in LArTPCs. Therefore, the reconstructed neutrino energy of events with neutrons is underestimated. In this chapter, I will present a novel approach to indirectly detect fast neutrons in LAr, based on simulations performed with the ArgonBox software. The goal of this method is to tag neutrino interactions for missing reconstructed neutrino energy in detectors using the LArTPC technology.

6.1. Motivation

The future long-baseline neutrino-oscillation experiment DUNE aims for high-precision measurements of neutrino-oscillation parameters with LArTPCs. A proper reconstruction of the neutrino energy is essential for those measurements because oscillations are a function of the neutrino energy (see Chap. 3). Many neutrino interactions on LAr do not follow two-body kinematics, such that the energy is usually reconstructed with the so-called calorimetric method. The calorimetric method sums up the total energy of all particles produced in the neutrino-nucleus interaction, according to Equation 6.1.

$$E_{\nu,reco} = \underbrace{E_{\mu}}_{leptonic} + \underbrace{\sum_{i=\mathrm{p},\pi^{\pm}} E_i}_{hadronic} + \underbrace{\sum_{i=\pi^0,\mathrm{e},\gamma} E_i}_{EM-showers} \tag{6.1}$$

Being electrically neutral particles, neutrons do not interact with the electronic shells of argon nuclei. Consequently, neutrons are not reconstructed by LArTPCs and the neutrino energy obtained from the calorimetric method is underestimated, up to 25 %, if neutrons are produced in the neutrino interaction.

Energy that is missed due to escaping neutrons leads to a bias of the reconstructed neutrino energy that can be corrected for, presuming we know the average number and energy of these neutrons. I will derive that bias for both NC and CC neutrino interactions on LAr simulated with the GENIE event generator. I will further show that the number of neutrons produced in these events and their energy underly big variations. These variations can not be corrected for and reduce the neutrino energy resolution in LArTPCs. I will present a method to indirectly detect neutrons by exploiting the fast response of the light-readout systems in order to assign these neutrons to the proper neutrino interaction vertices, given the high-rate environment at the DUNE-ND site. That method can be used for the tagging of single events that suffer a mis-reconstructed neutrino energy due

to energy carried away by neutrons. Ultimately, I will present how much the uncertainty on the reconstructed neutrino energy can be improved when neutron-tagged events are excluded from the analysis.

6.2. Simulation Sample

A sample of $\sim 10^6$ neutrino interactions on argon has been produced with the GENIE[1] event generator, and was later used to seed the detector simulation. Neutrino flux files with an energy spectrum and beam composition comparable to the future FNAL FHC and 3-horn optimized beamline have been used to sample the events. The sample composition is shown in Figure 6.1, as a function of neutrino energy. It is dominated

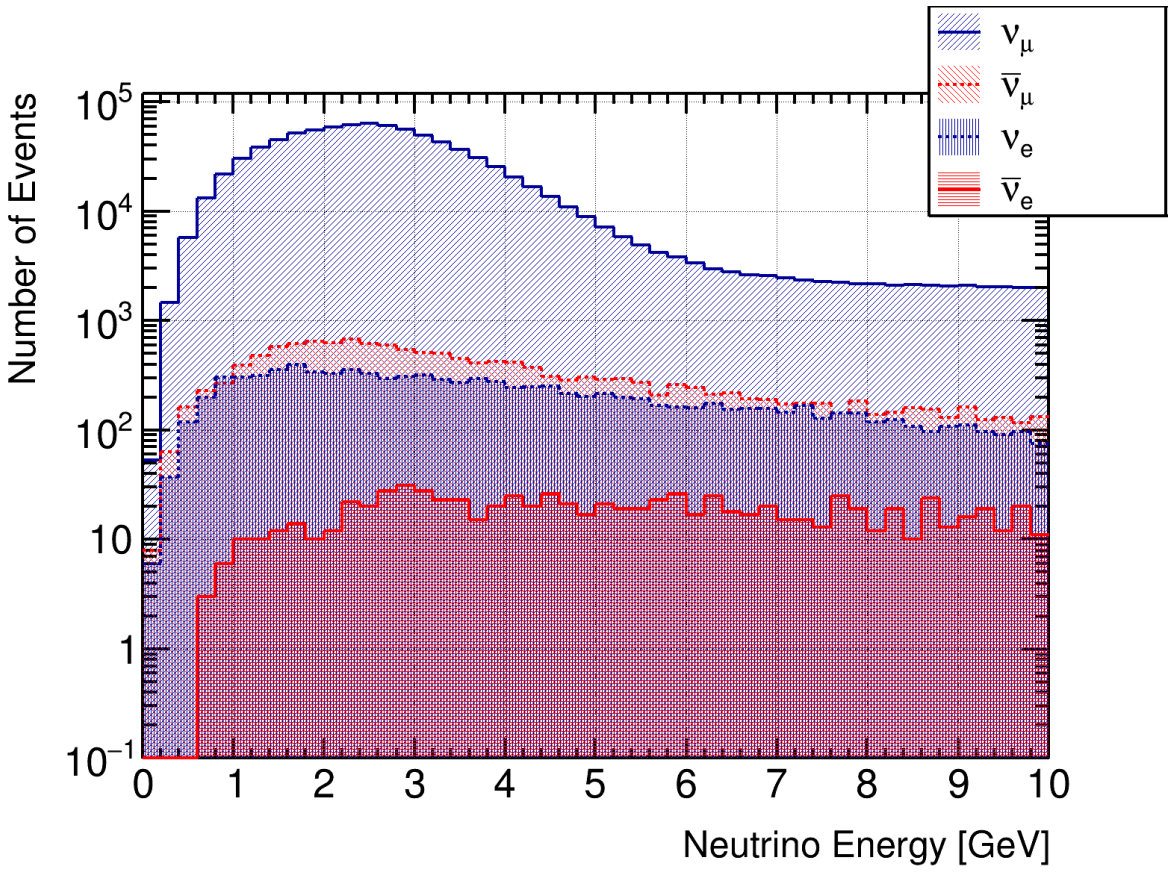

Figure 6.1.: Composition of the neutrino event sample used for the simulation, as a function of the neutrino energy. Neutrino flux files with an energy spectrum and beam composition comparable to the future FNAL FHC and 3-horn optimized beamline have been used to sample the events.

by muon neutrinos with a peak energy between 2 and 3 GeV. Other neutrino types

[1] GENIE version 2.12.8, with *ValenciaQE2p2hBergerSehgalCOHRES* configuration

contaminating the beam are roughly two orders of magnitude less frequent ($\overline{\nu}_\mu$ and ν_e) than muon neutrinos, or of negligibly small abundance ($\overline{\nu}_e$).

Figure 6.2 shows the neutrino energy spectrum of the event sample broken down by the interaction type, i.e. CC or NC, for the different muon-type neutrinos. The difference

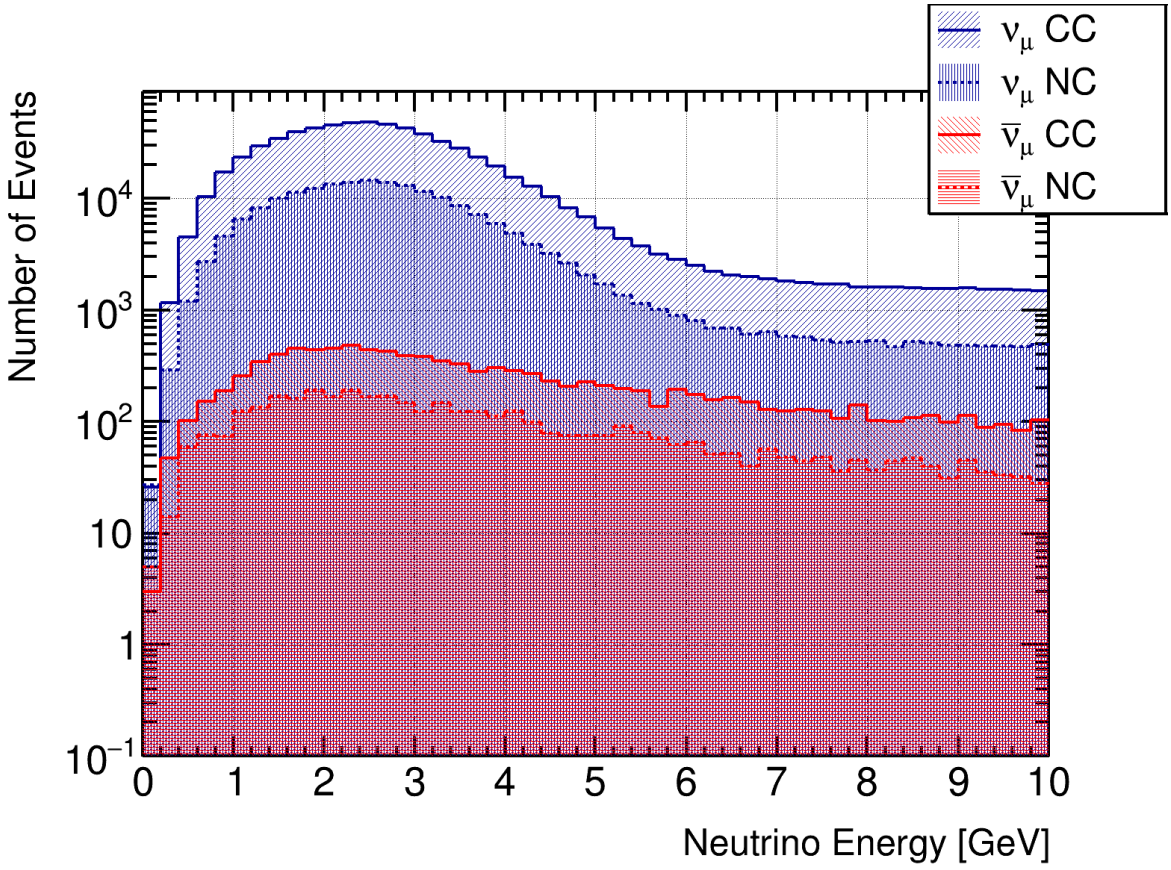

Figure 6.2.: Neutrino energy spectrum of the event sample broken down by the interaction type, i.e. CC or NC, for muon neutrinos and muon anti-neutrinos. We can see, that for neutrinos with energies typical for the FNAL beamline, interactions happen more often by CC exchange, for both muon neutrinos and muon antineutrinos.

between the occurrence of NC and CC interactions reflects the respective cross-section ratio ($\sim 1/3$). Due to lepton-number conservation, the outgoing primary lepton in a ν_μ CC interaction is a muon with negative electric charge, while in a $\overline{\nu}_\mu$ CC interaction, the primary lepton is a anti-muon with positive electric charge. If we consider the CC QE process, an antineutrino scattering off the nucleus produces a neutron and a neutrino scattering off the nucleus produces a proton, in oder to conserve electric charge. Consequently, we expect a higher abundance of neutrons in the final state of antineutrino CC interactions than in NC interactions, and a lower abundance of neutrons in the final state of neutrino CC interactions than in NC interactions. Figure 6.3 shows the

fraction of events in the sample with at least one primary neutron (directly emerging from the neutrino interaction vertex) produced in the interaction for both ν_μ and $\overline{\nu}_\mu$, broken down by the interaction type and as a function of the neutrino energy. No significant

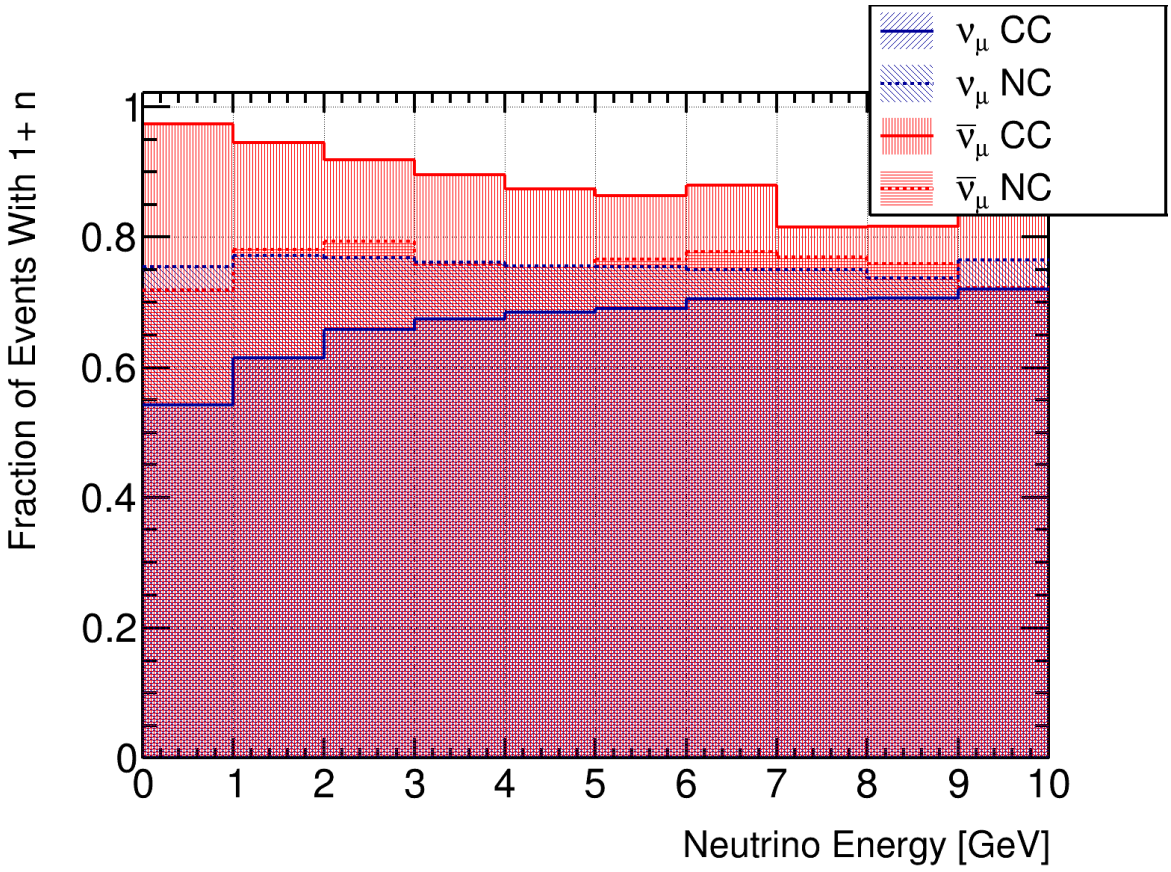

Figure 6.3.: Fraction of events with at least one primary neutron (directly emerging from the neutrino interaction vertex) produced in the interaction for both ν_μ and $\overline{\nu}_\mu$, broken down by the interaction type and as a function of the neutrino energy. Due to charge conservation, a higher primary-neutron yield is observable for antineutrino CC interactions, and a lower primary-neutron yield is observable for neutrino CC interactions.

difference is observable by comparing neutrino and antineutrino NC interactions. Primary neutrons are involved in roughly 80 % of the events. However, a slightly higher fraction is observable for antineutrino CC interactions, and a slightly lower fraction is observable for neutrino CC interactions, which is in agreement with our expectation. These differences decrease with an increase in neutrino energy as more energy becomes available to break up nuclei in DIS interactions.

6.2.1. Primary Neutrons in the Sample

Let us assume, that we have a hypothetical, perfect detector that allows us to reconstruct the kinetic energy of any particles produced in our sample, including neutrons. If we sum up the kinetic energy of all primary particles produced in an event, and compare that with the sum of the kinetic energy carried away by primary neutrons only, we can see that on average $\sim 10\,\%$ of the total kinetic energy is carried away by primary neutrons. Respective plots are shown in Figure 6.4, for muon neutrinos and for muon antineutrinos, as a function of the neutrino energy and broken down by the interaction type. Furthermore, a small discrepancy between the parent neutrino's kinetic energy and the total kinetic energy of primary particles produced in the events is observable. The deficit in primary kinetic energy is due to the energy consumption in the break-up processes of nuclei and/or nucleons, and due to energy consumed to produce new matter particles, predominately pions. The latter is illustrated in Figure 6.5, which shows the deficit in primary kinetic energy as a function of the pion multiplicity, i.e. the number of primary pions produced in the interaction. The error bands shown in these plots represent the 1σ profile-width of the respective distribution in each bin.

Next, we're going to have a look on the subsample of CC events, in which at least one primary neutron is emerging from the event vertex (indicated by "1+ n" in the labels). Figure 6.6 shows the multiplicity of primary neutrons in those events as a function of the parent neutrino's energy. Interestingly, the neutrino type (ν_μ or $\overline{\nu}_\mu$) seems to affect the number of events with primary neutrons involved, but not the neutron multiplicity, which is on average three neutrons for both muon neutrinos and muon antineutrinos. A possible explanation for that behavior is that the mean might be influenced by a long tail where FSI liberates many nucleons, a feature unique to GENIE which may or may not be present in reality.

The fraction of energy, w.r.t. the parent neutrino energy, that is carried away by the primary neutrons, is shown in Figure 6.7, as a function of the neutrino energy. On average, $\sim 10\,\%$ of the neutrino's energy is missed in those events, if we apply the calorimetric method for neutrino-energy reconstruction. That fraction increases to more than a quarter of the neutrino energy if many primary neutrons are present. The same plot is shown in Figure 6.8, but with the fractional energy replaced by the sum of the absolute kinetic energy carried away by primary neutrons.

6.2.2. Summary of Findings

We have seen that primary neutrons are involved in about $80\,\%$ of neutrino-argon interactions, at neutrino energies corresponding to the FNAL beamline. That number is slightly higher for $\overline{\nu}_\mu$ CC-interactions, and slightly lower for $\overline{\nu}_\mu$ CC-interactions. In those events with primary neutrons involved, a mean energy corresponding to $\sim 10\,\%$ of the parent neutrino's kinetic energy is carried away by primary neutrons. That energy is distributed among three primary neutrons, on average. It is important to mention that these findings depend on the event generator. Neutrino-argon interactions are not perfectly understood and the used interaction model might not reflect the reality well.

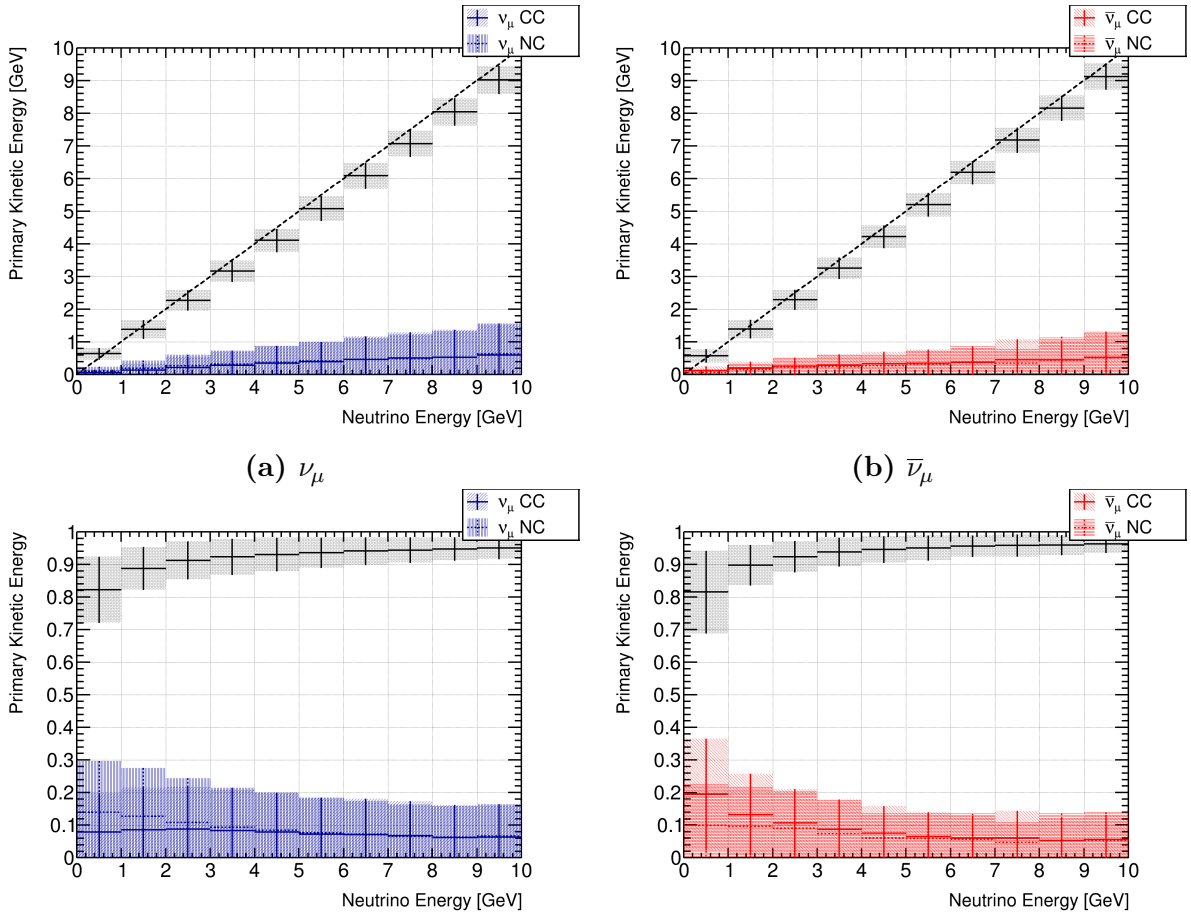

(a) ν_μ **(b)** $\overline{\nu}_\mu$

(c) ν_μ **(d)** $\overline{\nu}_\mu$

Figure 6.4.: Sum of the kinetic energy carried away by all primary particles (black) and primary neutrons only (blue, red) produced in the neutrino event as a function of the neutrino energy. The diagonal line represents the line of equality, and the gray bands indicate the total kinetic energy of all primary particles produced in the event, while the labeled bands indicate the sum of the kinetic energy carried away by primary neutrons only. Absolute energies are shown in the upper plots and relative energies with respect to the neutrino kinetic energy are shown in the lower plots. The error bands represent the 1σ profile-width of the respective distribution in each bin.

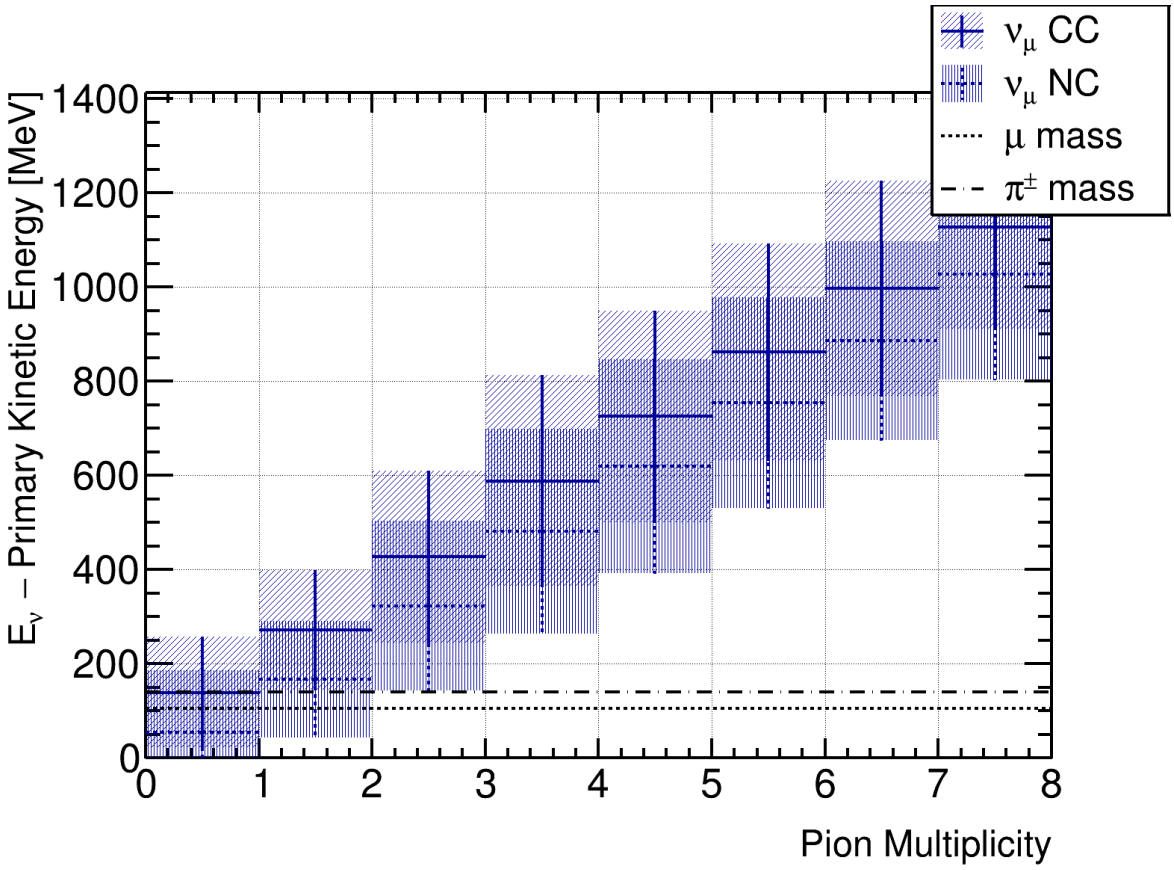

Figure 6.5.: Difference between the neutrino energy and the sum of the kinetic energy carried away by all primary particles produced in the neutrino event, with respect to the number of π mesons produced in the neutrino event. The dotted and dashed lines indicate the mass of the muon and the charged pion, respectively. The error bands represent the 1σ-uncertainty.

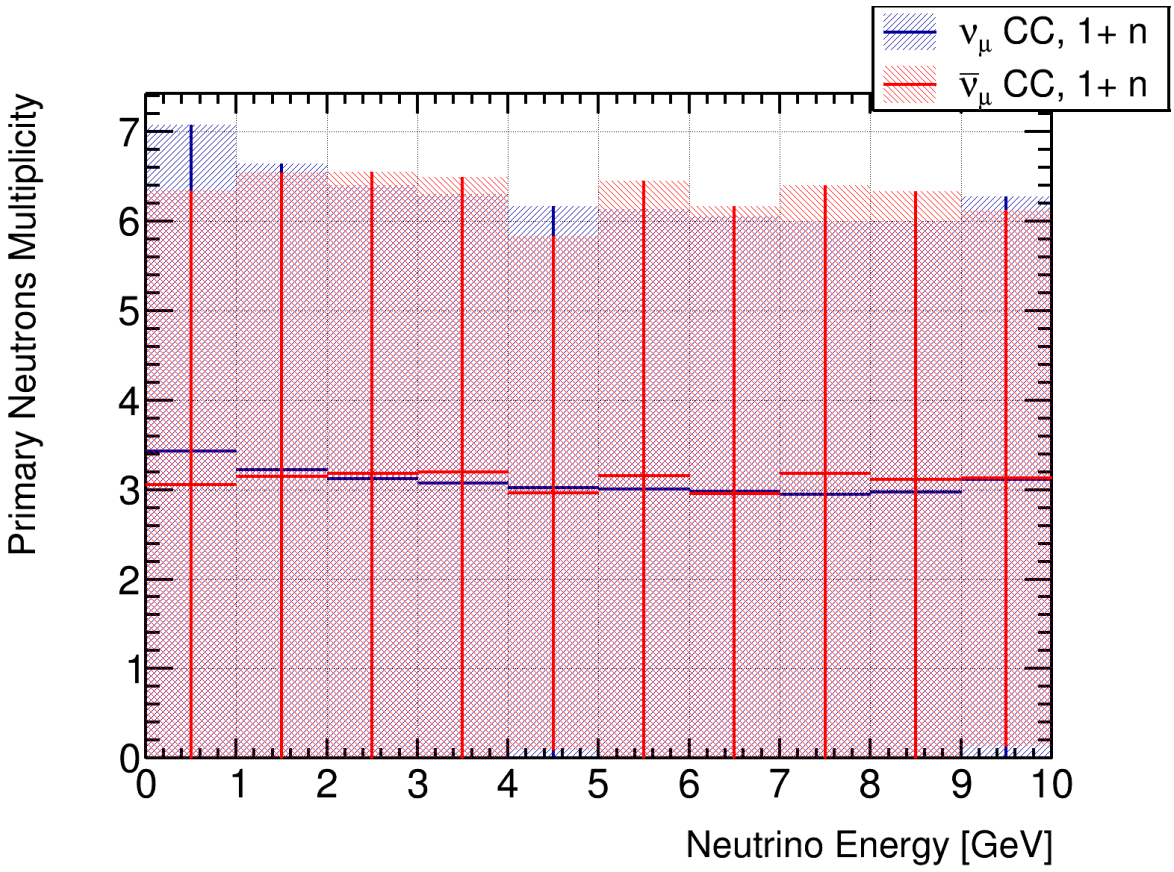

Figure 6.6.: Average number of primary neutrons produced in the neutrino event as a function of the neutrino energy. The error bands represent the 1σ-uncertainty.

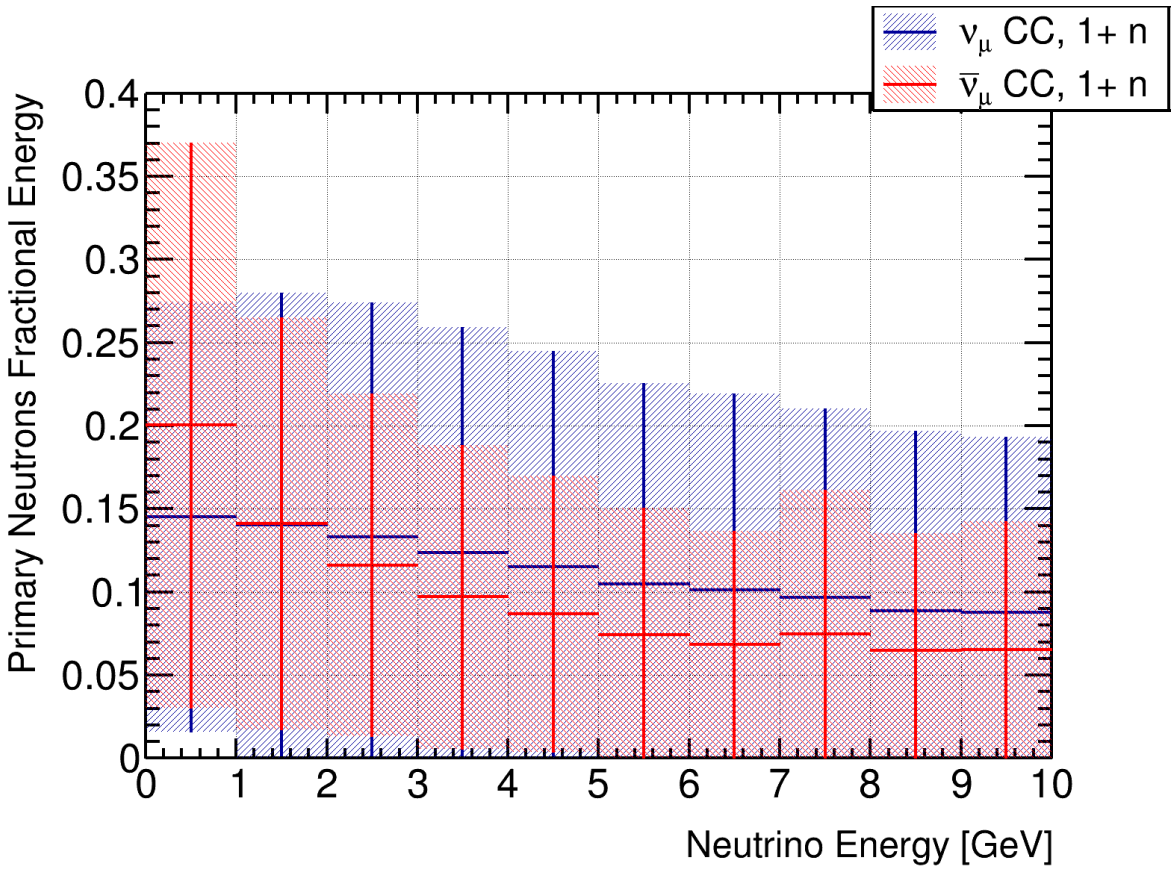

Figure 6.7.: Sum of the kinetic energy carried away by primary neutrons produced in the neutrino event as a function of the neutrino energy and normalized by the neutrino energy. The error bands represent the 1σ-uncertainty.

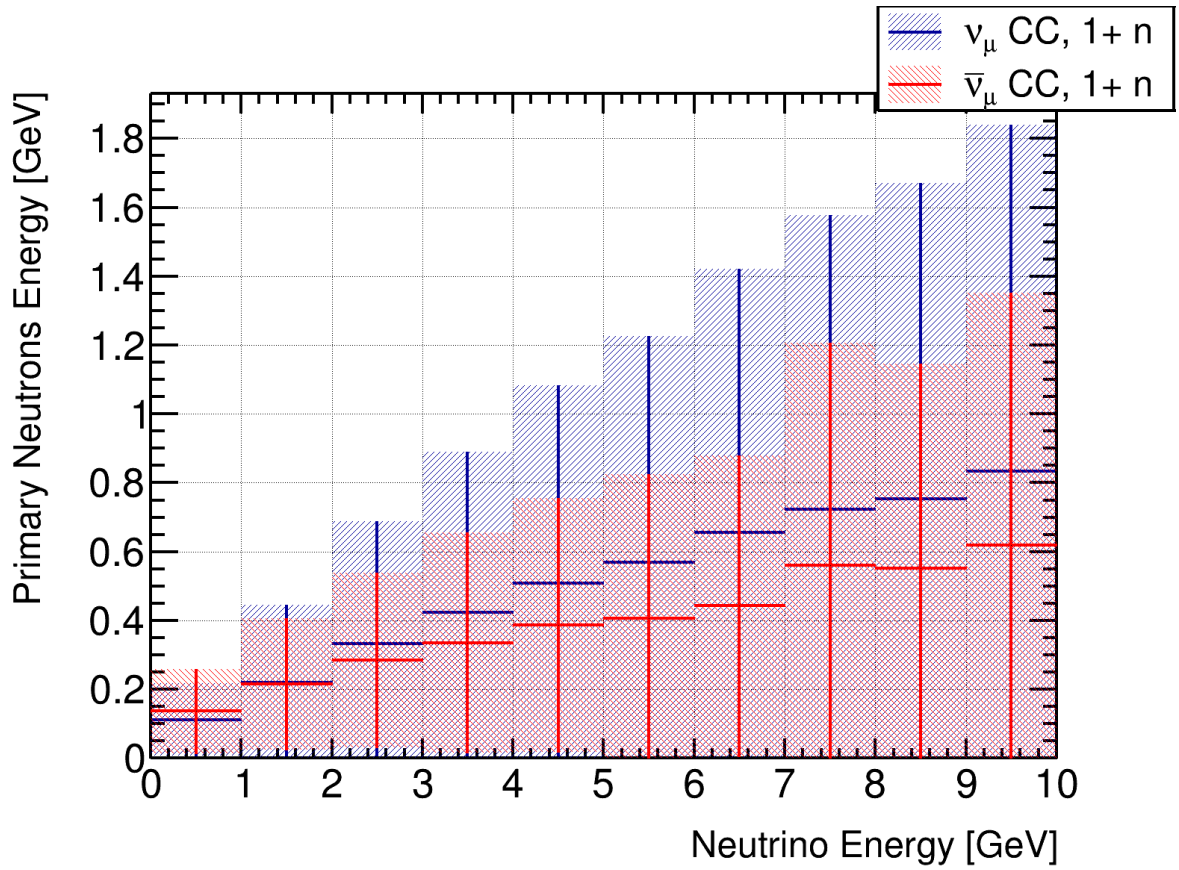

Figure 6.8.: Sum of the kinetic energy carried away by primary neutrons produced in the neutrino event as a function of the neutrino energy. The error bands represent the 1σ-uncertainty.

Anyways, with these findings taken as a rough estimate for how much neutrino energy is mis-reconstructed with the calorimetric method due to missed neutrons ($\sim 10\,\% \pm 15\,\%$), it seems absolutely worth investigating in potential methods of detecting neutrons in LArTPCs.

6.3. Simulation Setup

A Monte-Carlo (MC) simulation was used to perform the studies presented in this work. Therefore, the final-state particles of the GENIE sample presented above were used to seed the GEANT4 based ArgonBox program. In ArgonBox, a large LAr volume of 200 m × 200 m × 200 m side length serves as the detector material. The program provides propagation and tracking of the final-state particles, and allows to store the respective energy deposits.

6.3.1. Detector Definition

DUNE's ND-LAr will consist of 35 modules arranged in an array 7 modules wide and with 5 modules along the beam axis. A single module measures 1 m × 3.5 m × 1 m (W × H × L) and contains two LArTPCs separated by a central cathode plane. Each TPC having an active volume of $0.5\,\mathrm{m} \times 3\,\mathrm{m} \times 1\,\mathrm{m} = 1.5\,\mathrm{m}^2$ the detector will provide a total active volume of $105\,\mathrm{m}^3$. With a LAr density of $\rho_{LAr} \simeq 1.4\,\mathrm{kg\,L}^{-1}$ these dimensions correspond to an active target mass of $\sim 147\,\mathrm{t}$. Accordingly, a rectangular cuboid of the dimensions 7 m × 3 m × 5 m was defined as the simulation's active volume.

To emulate particles produced in neutrino interactions in the rock and support structures surrounding the LArTPCs, and then entering the detector's active volume, the LAr volume used for simulations was extended beyond the limits of the active volume: 5 m upstream, 2 m at both sides and 1.5 m below and above the active volume. This results in a total target volume of $11\,\mathrm{m} \times 6\,\mathrm{m} \times 10\,\mathrm{m} = 660\,\mathrm{m}^2$, corresponding to 924 t of LAr and containing ~ 100 neutrino events per beam spill (at 1 MW beam power).

An early version (4 × 5 modules configuration) of the detector geometry used for the simulation is shown in Figure 6.9. A cut through the emulated rock volume (dark gray) allows a view into the detector. Energy deposits of a simulated spill at 1 MW beam power are visible in the active detector volume composed of 4 × 5 modules. An updated 7 × 5 modules configuration was used for the simulation studies presented in this work.

6.3.2. Beam Spill

Full neutrino-beam spills were simulated for pile-up studies. The number of neutrino events in the individual spills are generated according to a Poisson distribution using the average number of neutrino events per spill in the target volume as the expected number of occurrences. Event vertices were then randomly distributed within the total target volume, the active volume included. The neutrino-vertex times were generated

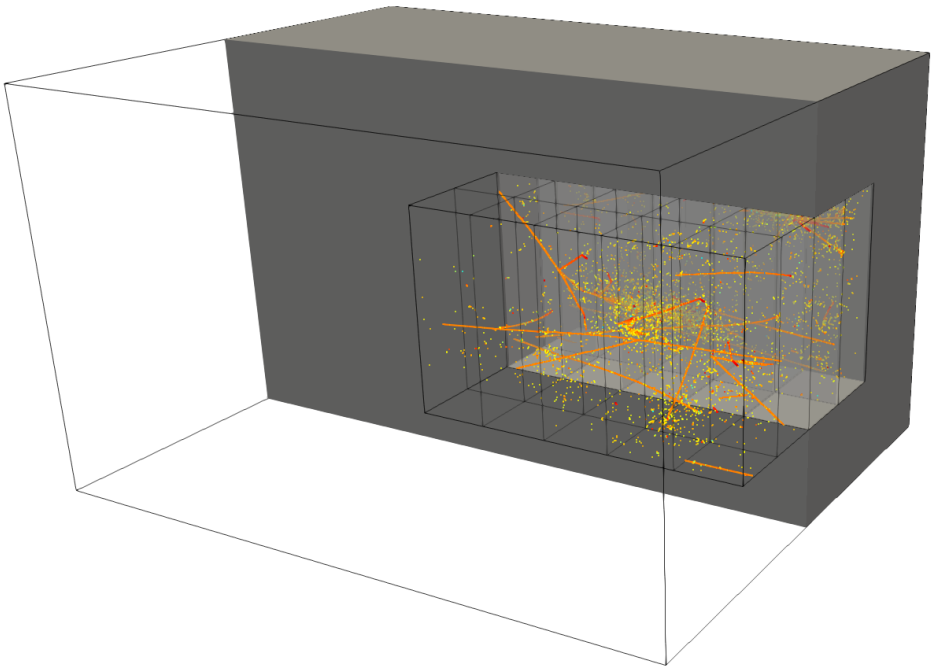

Figure 6.9.: Early version (4×5 modules configuration) of the detector geometry used for the simulation. A cut through the emulated rock volume (dark gray) allows a view into the detector. Energy deposits of a simulated 1 MW beam spill are visible in the active detector volume composed of 4×5 modules. The beam is coming from the left. An updated 7×5 modules configuration was used for the simulation studies presented in this work.

following a uniform distribution within an interval length equal to the neutrino beam spill-length [75].

The simulation has shown that particles produced in neutrino interactions outside of the detector and entering the detector's active volume increases the number of seen muons per spill from on average 15 to 55. The separation time between consecutively seen events in the beam spill is shown in Figure 6.10. On average, the events registered in the active volume of the detector are separated by 179 ns.

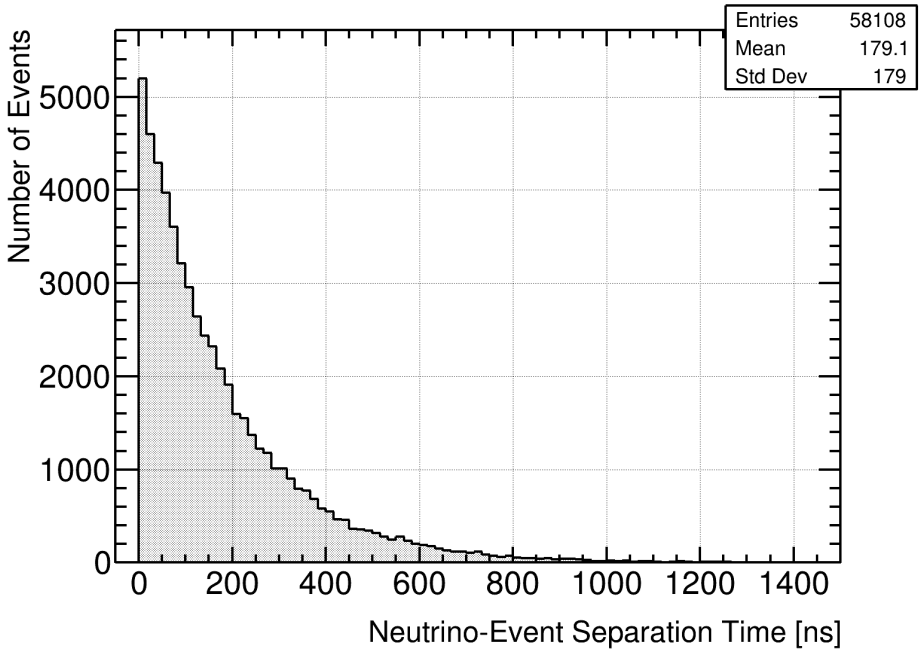

Figure 6.10.: Separation time between consecutively seen neutrino events within the same neutrino beam spill. Only events visible in the 105 m^3 active volume are considered. On average, the events registered in the active volume of the detector are separated by 179 ns.

6.4. Neutron Detection in LArTPCs

As already mentioned, neutrons are not reconstructed in LArTPCs. Consequently, the only way to detect neutrons are indirect methods. Two promising methods for indirect detection of neutrons in LArTPCs are:

1. Detection of thermal neutrons of the $\mathcal{O}(1)$ keV through neutron capture. This is usually achieved by coating the detector walls or PMTs with a neutron affine material, e.g. gadolinium, or to dope the material directly into the active medium of the detector. The radiation emitted from excited nuclei after having captured a neutron is interaction-specific and thereby serves as an indicator for slow neutrons.

2. Detection of fast neutrons of the $\mathcal{O}(1)$ MeV or greater through recoiling charged particles after a collision of a neutron with an argon nucleus. The recoiling particle can be the argon nucleus as a whole, or, if the neutron exceeds the nuclear binding energy of $\sim 5\,\mathrm{MeV}$, a knock-out proton or heavier nuclear fragments, like deuterons.

6.4.1. Neutron Capture

Thermal neutrons (0.025 eV neutrons) can be detected through neutron capture. Natural gadolinium (Gd) has a thermal-neutron [2] capture cross-section of 46 000 b, including a 15.65 % abundance of the $^{157}_{64}$Gd isotope with a thermal neutron-capture cross section of 255 000 b [107]. The absorption of the neutron leaves the $^{158}_{64}$Gd in an excited state that releases energy through emission of high-energy gamma rays, low-energy gamma rays, x-rays, internal-conversion electrons and Auger Coster-Kronig conversion electrons [107]. The major decay channels of excited $^{158}_{64}$Gd are summarized in Figure 6.11. 19.1 % of the

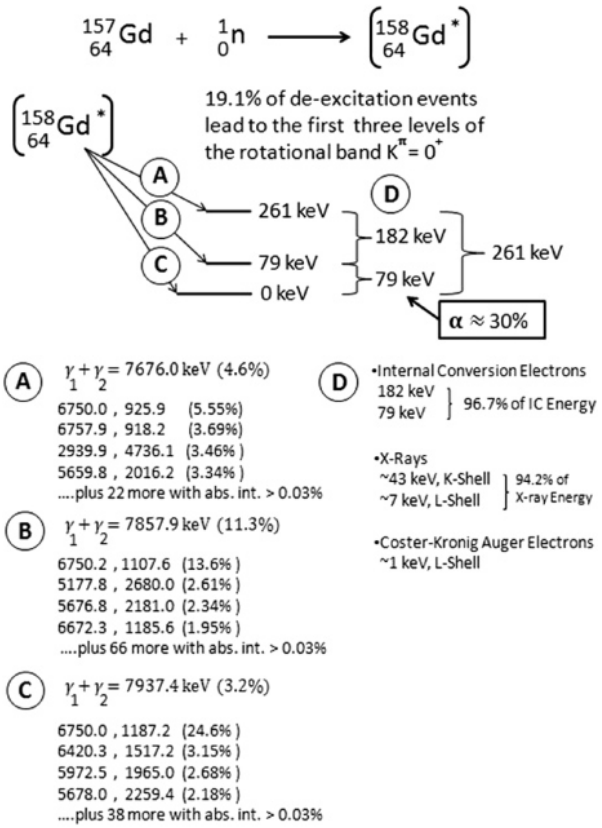

Figure 6.11.: Major decay channels of an excited $^{158}_{64}$Gd nucleus. [107]

de-excitation events lead to multi-MeV gamma rays (channels A + B + C) [107]. With the EM radiation length of LAr, $X_0 = 18\,\mathrm{cm}$ [108], these gamma rays will eventually

[2] Neutron energy $< 0.1\,\mathrm{eV}$ [106].

form small EM showers to be measured with calorimetric methods in order to identify neutron captures.

Gadolinium has an electronegativity of 1.2 and would drastically reduce the electron lifetime in LArTPCs if it was doped to the LAr directly. Another possibility is to apply a gadolinium coating to the inside of the detector walls. The current ArgonCube design discussed above does not provide un-instrumented surfaces for such methods, and the acceptance might be rather low unless light-readout tiles would be interrupted to allow a higher gadolinium coverage. Furthermore, a negative neutron-scattering resonance was calculated for ^{40}Ar, which makes LAr almost transparent to neutrons with an energy of $\sim$ 57 keV. At the resonance, the effective mean free path of neutrons in natural argon is $\sim$ 30 m. The fractional energy loss per neutron scatter is 4.8 %, and with the resonance window 20 keV wide most neutrons above the resonance energy could fall into the window. [109] The most compelling reason to ignore neutron capture techniques arises due to event-pileup though. Slow neutrons propagate slowly and travel far compared to the module dimensions, which means there is no localization, in either space or time. Consequently, there will be hundreds of neutron captures per neutrino beam spill without the chance to associate them to any neutrino interaction.

The fraction of events that include primary neutrons with kinetic energies below 100 keV is shown in Figure 6.12a, as a function of neutrino energy. It is less than one in

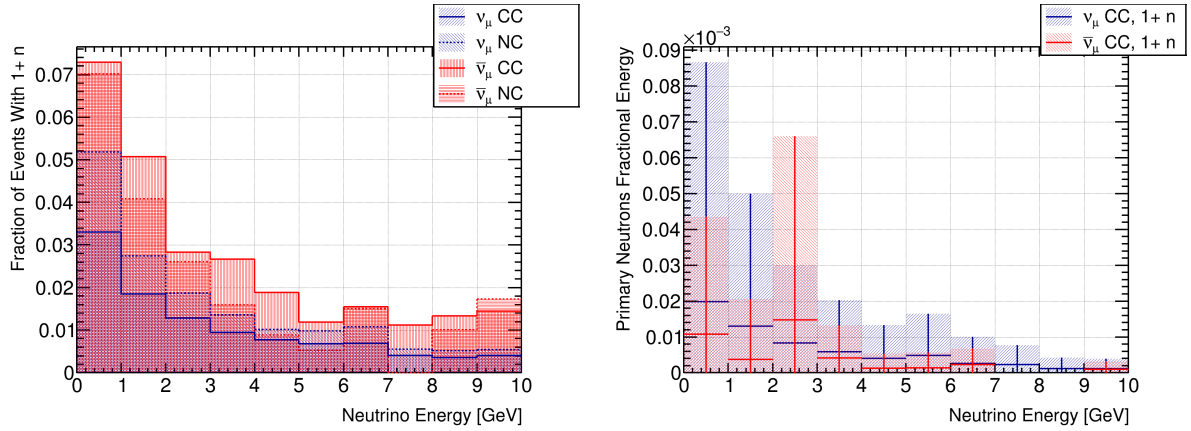

(a) **(b)**

Figure 6.12.: Subsample of events that include primary neutrons with kinetic energies below 100 keV. The fractional occurrence of those events is shown in (a) as a function of the neutrino energy. It is less than one in ten neutrino interactions that produce such low-energetic neutrons. The fractional energy, w.r.t. the neutrino energy, carried away by those neutrons is shown in (b), as a function of the neutrino energy. The error bands represent the 1σ-uncertainty.

ten neutrino interactions that produce such low-energetic neutrons. Accordingly small is the fractional energy, w.r.t the neutrino energy, carried away by these neutrons, which is shown in Figure 6.12b. Consequently, we will not further analyze the method of neutron

capture in LAr, but focus on the second method, the detection of fast neutrons through recoiling charged particles.

6.4.2. Neutron Induced Recoils

Fast neutrons ($E_{\text{kin}} > 100\,\text{keV}$) travel on average $\sim 80\,\text{cm}$ in LAr until they scatter off an argon nucleus. If the transferred momentum is below a few MeV, then the argon nucleus can be seen in the LArTPC as a recoiling charged particle. On the other hand, if the transferred momentum exceeds the nuclear binding energy ($\sim 5\,\text{MeV}$), then the nucleus may break such that recoiling charged nuclear fragments produced in the collision can be detected in LAr. From now on, we will refer to these recoiling argon nuclei and nuclear fragments as neutron induced recoils, and presuppose that these neutron induced recoils are so-called secondary charged particles produced by primary neutrons only.

6.4.3. Fiducial Volume Definition

A detector fiducial volume was defined to increase the detection efficiency of neutron induced recoils. The distance between the neutron induced recoil and the neutrino vertex, as a function of the primary neutron's polar angle (w.r.t. the beam), is shown in Figure 6.13a. The respective transverse and longitudinal components of the vertex distance are shown in Figures 6.13b and 6.13c. Absolute values are taken for the transverse vertex distance, positive longitudinal vertex distances correspond to forward going neutrons and negative longitudinal vertex distances correspond to backward going neutrons.

Most primary neutrons are forward boosted such that many neutron induced recoils occur within 20 cm along the transverse axis. With a fiducialization of 30 cm at both sides as well as the bottom and top of the active LAr volume, roughly 90 % of sideways going neutron-induced recoils are contained for those events with the vertex at the very edge of the Fiducial Volume (FV). Recoils of forward going neutrons are harder to contain. With a 30 cm fiducialization at the downstream edge of the detector, only roughly 50 % of the recoils are contained in the detector's active volume, for those events with the vertex at the downstream end of the FV. The containment does not improve a lot if we restrict the FV to 50 cm from the downstream edge of the detector, namely to $\sim 64\,\%$.

Ultimately, the detector's FV was defined 30 cm from all sides (incl. bottom and top) of the active LAr volume, and 30 cm from the downstream edge of the active LAr volume. With a total of only $\sim 10\,\%$ backward going primary neutrons, no fiducialization was applied to the upstream edge of the detector's active volume. From now on, if not other declared, only events the the neutrino vertex in the detector's FV and only recoils visible in the detector's active volume are considered in the analysis.

6.4.4. Properties of Neutron Induced Recoils

The most abundant recoiling nuclear fragments produced by neutrons in LAr, independent of neutron energy, have been determined from 10 838 neutrino interactions, and are listed

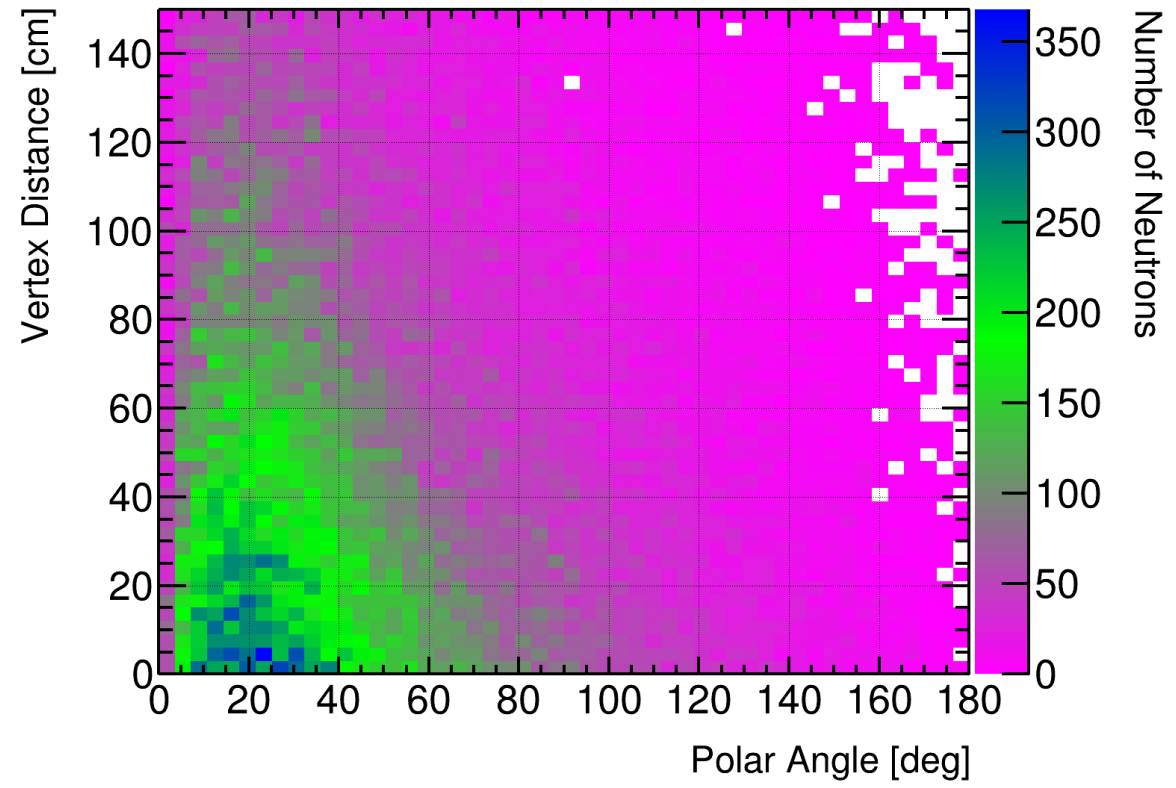

(a) Total

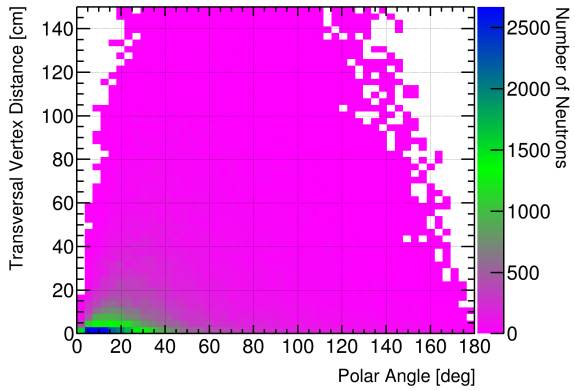

(b) Transversal

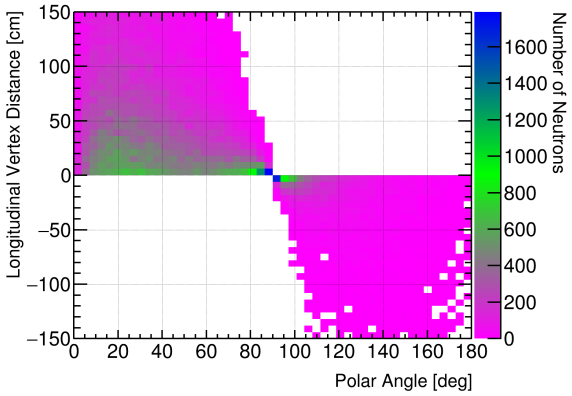

(c) Longitudinal

Figure 6.13.: Distance between the neutron induced recoil and the neutrino vertex, as a function of the primary neutron's polar angle w.r.t. the beam (a), and the respective transverse (b) and longitudinal (c) components of the vertex distance. Absolute values are taken for the transverse vertex distance, positive longitudinal vertex distances correspond to forward going neutrons and negative longitudinal vertex distances correspond to backward going neutrons.

in Table 6.1. The second column denotes the total number of neutron induced recoils

Table 6.1.: The most abundant recoiling nuclear fragments produced by neutrons in LAr, derived from a sample of 10 838 neutrino interactions. The second column denotes the total number of neutron induced recoils partially or fully contained in the active volume of the detector, and the third column denotes the recoil multiplicity per event, for the subsample of events with at least one primary neutron.

Nuclear Fragment	**Number of Recoils**	**Number of Recoils per Event**
$^{40}_{18}$Ar	24 269	3.10
p	8438	1.14
$^{39}_{18}$Ar	3631	0.49
$^{38}_{18}$Ar	2986	0.40
$^{4}_{2}$He	1211	0.16
d	855	0.12
$^{37}_{18}$Ar	844	0.11
$^{37}_{17}$Cl	834	0.11
$^{34}_{16}$S	651	0.09
$^{39}_{17}$Cl	580	0.08

partially of fully contained in the active volume of the detector, and the third column denotes the recoil multiplicity per event, for the subsample of events with at least one primary neutron.

On average, ~ 3 (4) recoiling $^{40}_{18}$Ar cores (incl. other argon isotopes) and ~ 1 recoiling proton are produced by events with primary neutrons. These numbers heavily fluctuate and have a dependence on neutron energy, as it is shown Figure 6.14 for argon (incl. any isotopes listed above), proton, helium and deuteron recoils. Argon nuclei are the dominating recoils by means of multiplicity up to a neutron energy of ~ 200 MeV, while protons are the dominating recoils above that energy. Other nuclear fragments play a subordinate role.

The kinetic energy of neutron induced recoils is shown in Figure 6.15, again for argon (incl. any isotopes listed above), proton, helium and deuteron recoils, as a function of the primary neutron's kinetic energy. Having kinetic energies of the $\mathcal{O}(1)$ MeV, argon

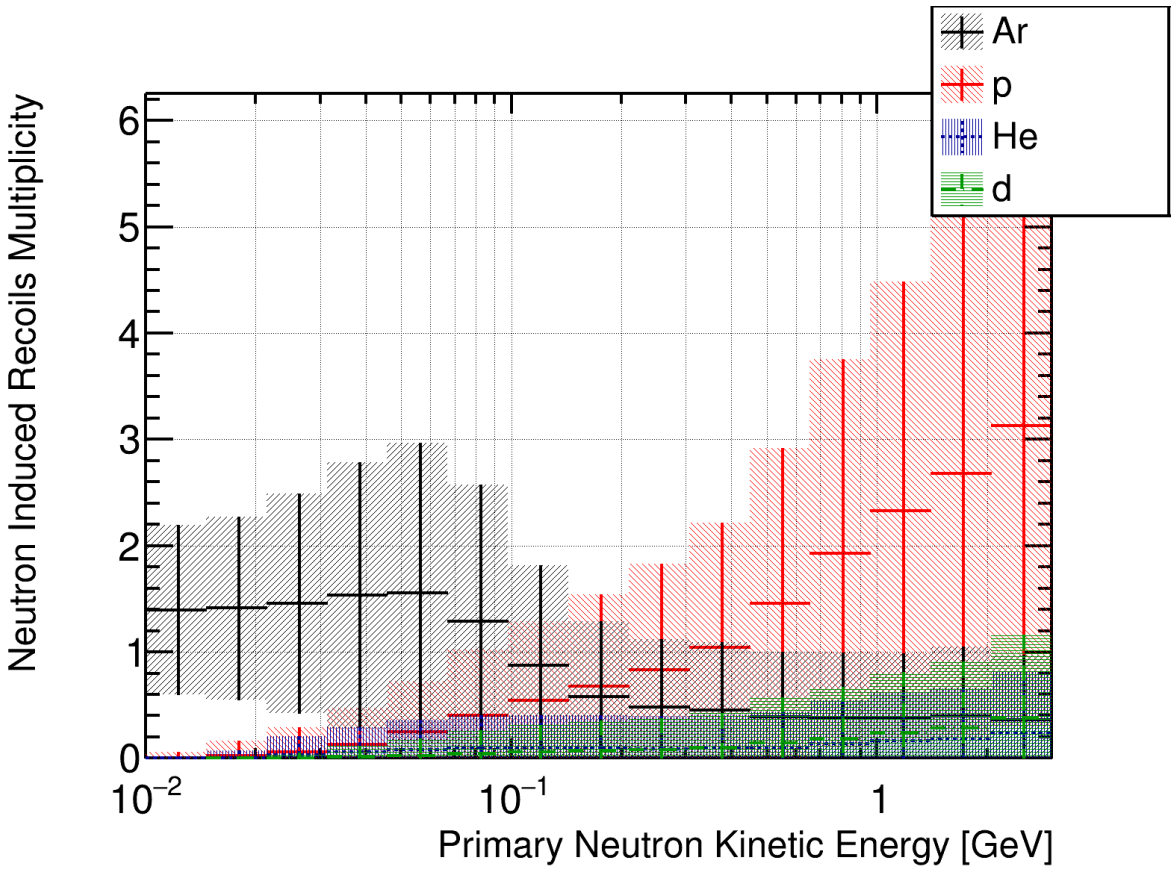

Figure 6.14.: Multiplicity of the most frequent recoiling, nuclear fragments induced by a primary neutron, as a function of the primary neutron kinetic energy. Argon nuclei are the dominating recoils by means of multiplicity up to a neutron energy of $\sim 200\,\mathrm{MeV}$, while protons are the dominating recoils above that energy. Other nuclear fragments play a subordinate role. The error bands represent the 1σ-uncertainty.

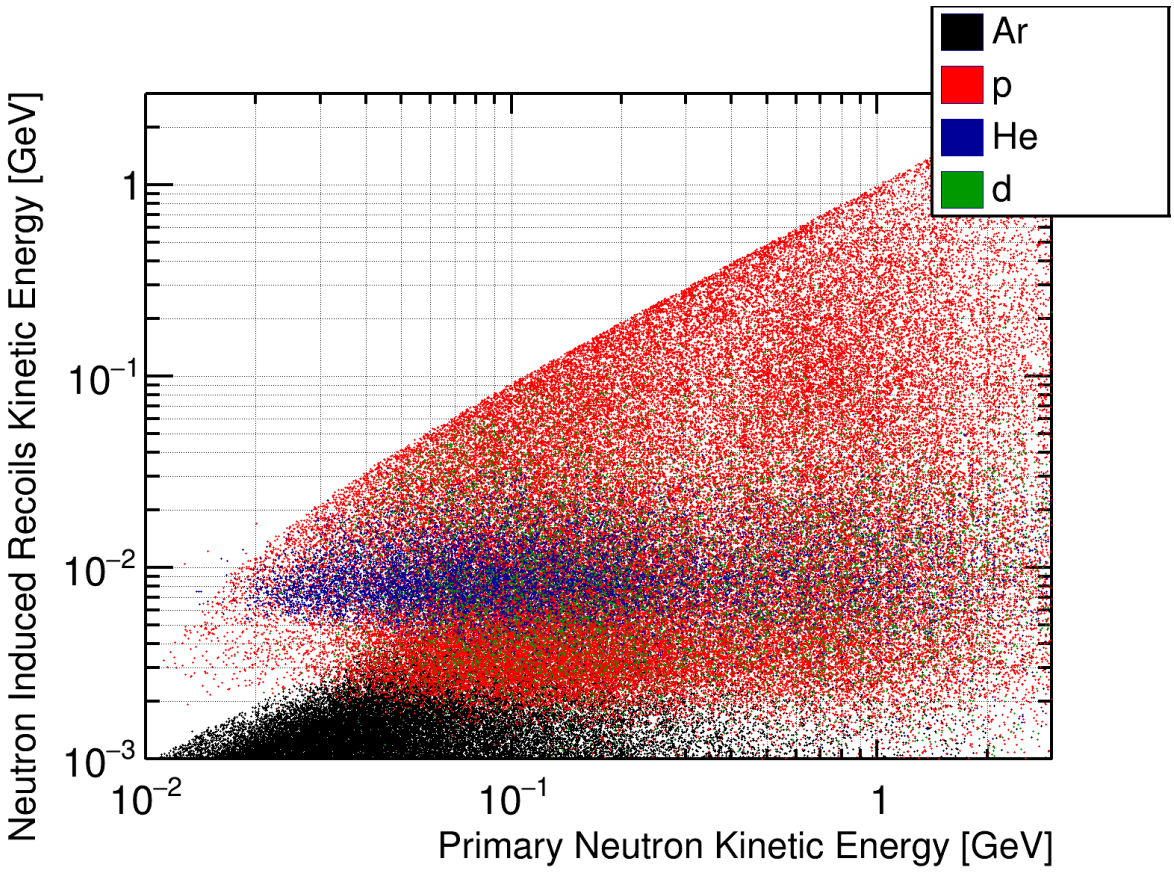

Figure 6.15.: Kinetic energy distribution of the most frequently recoiling particles induced by a primary neutron with respect to the primary neutron kinetic energy. Argon recoils have kinetic energies of the $\mathcal{O}(1)$ MeV, while recoiling protons and other light nuclear fragments have kinetic energies of the $\mathcal{O}(10)$ MeV to $\mathcal{O}(1)$ GeV. Proton recoils start to appear a neutron energies $\gtrsim 10\,\mathrm{MeV}$, because the neutron needs to break the nuclear binding energy of $\sim 5\,\mathrm{MeV}$.

recoils are hard to identify [3] within all the activity of a neutrino interaction seen in the LArTPC. On the other hand, recoiling protons and other light nuclear fragments have kinetic energies of the $\mathcal{O}(10)$ MeV to $\mathcal{O}(1)$ GeV. Consequently, for simplicity, it was decided to exclude particles with initial kinetic energies below 10 MeV from the analysis, and to focus on neutron induced proton recoils with kinetic energies ≥ 10 MeV.

The effect of setting such a kinetic energy limit is shown in Figure 6.16. Six event displays – a side view – are shown for the same neutrino-beam spill, with coloring according to the deposited energy, and with energy deposits colored in red for proton recoils and blue for any other particles. The top displays show the raw response, i.e. the energy deposits of particles produced in the neutrino interactions during the beam-spill, without cutting any particles. Accordingly high is the density of energy deposits, which makes it very difficult to identify the signals of detached, neutron-induced recoils. The center displays show energy deposits of all particles produced in the interactions that have initial kinetic energies ≥ 10 MeV. Clean tracks are visible and neutron-induced proton recoils show up as detached energy deposits and tracks that are well separable from other spill activities. The bottom displays show energy deposits of particles with initial kinetic energies below 10 MeV only, i.e. whatever is cut in the center displays. These deposits do not show up as connected tracks but separated deposits along the trajectories of more energetic particles, but also as randomly distributed blips in the whole detector. The latter, most probably being registered as single-pixel hits, one should be able to fairly easy reject in the analysis of charge signals acquired with true-3D pixel-readout systems.

Focusing on proton recoils with kinetic energies above 10 MeV means limiting to primary neutrons with kinetic energies of at least 20 MeV, which is evident from Figure 6.15. The fraction of events that include primary neutrons with kinetic energies above 20 MeV is shown in Figure 6.17a, as a function of neutrino energy. These neutrons are way more abundant than epithermal neutrons, and they carry away the biggest fraction of energy, w.r.t the neutrino energy, as it is shown by Figure 6.17b.

The track length of proton recoils is shown in Figure 6.18, as a function of the proton's kinetic energy. Up to kinetic energies of ~ 20 MeV, neutron-induced proton recoils most probably show up as single-pixel hits, assuming a pixel pitch of 4.4 mm. Above that energy, proton recoils start to show up as tracks, and I thought about method of extrapolating the track back towards the interaction vertex of the neutrino, in order to associate these detached recoils with the respective neutrino event, given a high-multiplicity environment comparable to the DUNE ND. Figure 6.27d shows the angle between the momentum vector of recoiling protons and the connecting line between the start position of the proton and the neutrino vertex, as a function of the proton kinetic energy. For protons of the $\mathcal{O}(10)$ MeV, that angle strongly varies between 10° and 160°. Consequently, tracing back to the neutrino vertex from the track of neutron-induced proton recoils does not work.

Another possibility to make the association between detached proton recoils and neutrino vertices is timing by exploiting the fast scintillation light. Proton recoils

[3] The Micro Booster Neutrino Experiment (MicroBooNE) Collaboration has proven that MeV-scale physics with LArTPCs is technically possible [110].

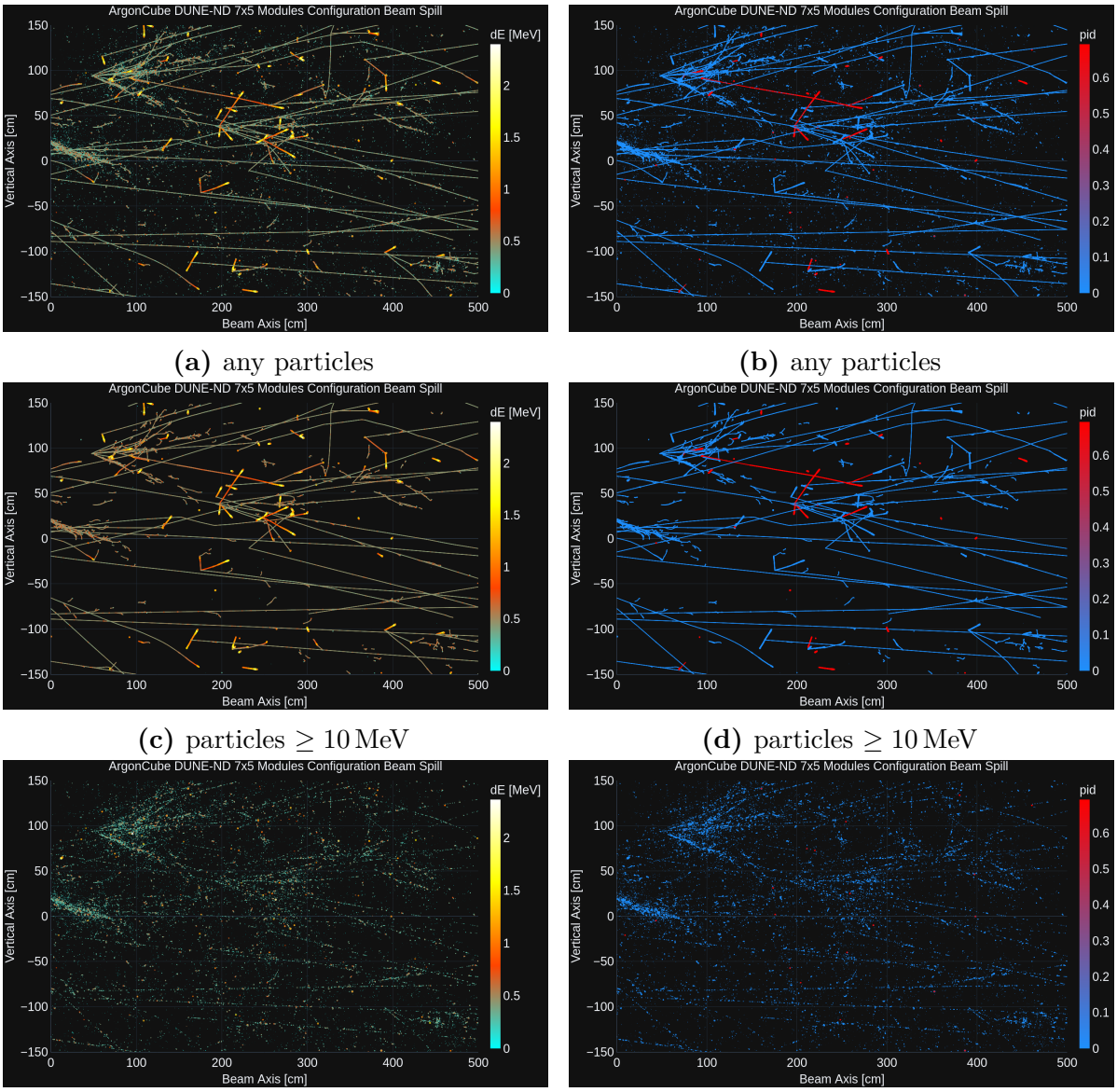

(a) any particles

(b) any particles

(c) particles $\geq 10\,\mathrm{MeV}$

(d) particles $\geq 10\,\mathrm{MeV}$

(e) particles $< 10\,\mathrm{MeV}$

(f) particles $< 10\,\mathrm{MeV}$

Figure 6.16.: Event displays of a neutrino beam spill, with coloring according to the deposited energy (left column), and with energy deposits colored in red for proton recoils and blue for any other particles (right column). No cut is applied in the top displays. Only particles with kinetic energies $\geq 10\,\mathrm{MeV}$ are shown in the center displays, and only particles with kinetic energies $< 10\,\mathrm{MeV}$ are shown in the bottom displays.

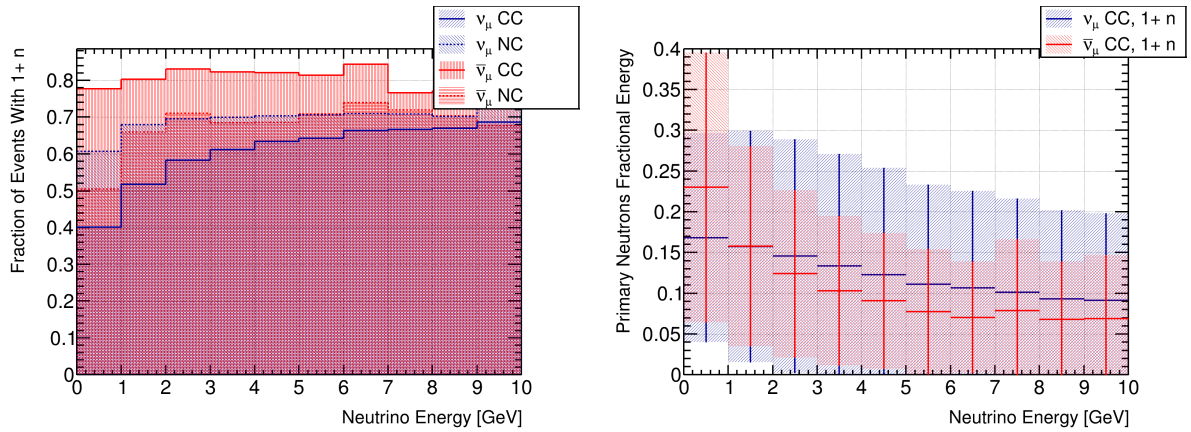

(a) **(b)**

Figure 6.17.: Subsample of events that include primary neutrons with kinetic energies $\geq 20\,\text{MeV}$. The fractional occurrence of those events is shown in (a) as a function of the neutrino energy. More than 50 % of the events produce such fast neutrons. The fractional energy, w.r.t. the neutrino energy, carried away by those neutrons is shown in (b), as a function of the neutrino energy. Fast neutrons are those neutrons that carry away the biggest fraction energy in neutrino interactions. The error bands represent the 1σ-uncertainty.

appear nearly instantly (a few ns) after the actual neutrino interaction. That is evident from Figure 6.20, which shows the time delay of recoiling protons, w.r.t. the neutrino interaction, as a function of the distance between the proton recoil and the interaction vertex. The black line denotes the speed of light in vacuum. In the next section, we will investigate in such a method exploiting the fast scintillation light provided by the optical detectors, in order to tag fast neutrons, and to assign them to the proper neutrino-interaction vertex.

6.4.5. Optical Neutron Tagging

We saw in Section 6.3.2 that the mean neutrino-event separation time is $\sim 179\,\text{ns}$. Most proton recoils, in contrary, appear within less than 10 ns after the interaction. If the light-readout system is able to time-stamp such neutron recoils, with a timing resolution of the $\mathcal{O}(10)$ ns, these proton recoils can be assigned to a neutrino-interaction vertex. That principle is illustrated in Figure 6.21, which shows the temporal distribution of energy deposits that appear within a 2 µs long window in the 10 µs neutrino-beam spill. The color axis indicates the number of energy deposits related to proton recoils, and stars indicate energy deposits due to other neutron-induced nuclear fragments. All energy deposits appear immediately (a few ns) after the respective neutrino interaction. Some of the neutrino interactions appear blank because particles do not enter the detector's active volume.

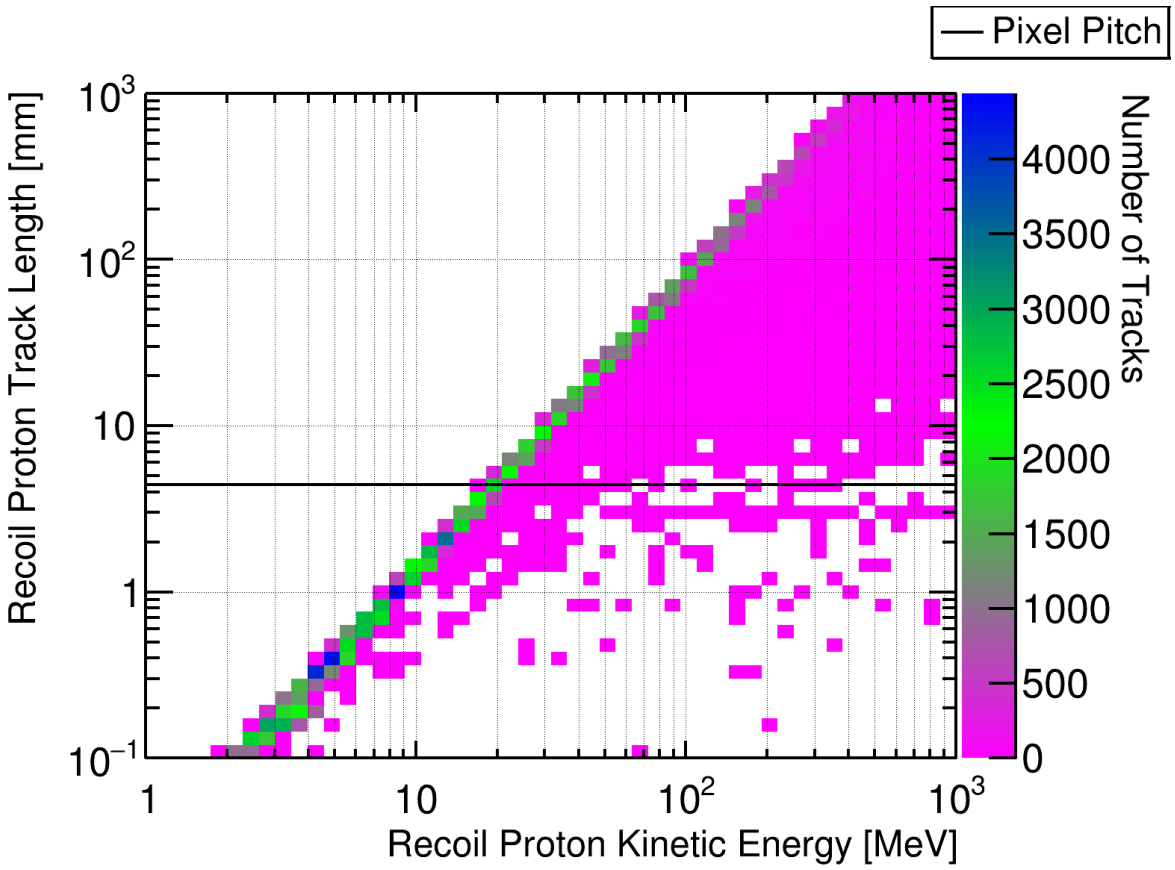

Figure 6.18.: Track length of recoiling protons as a function of the proton kinetic energy. Proton recoils with kinetic energies above $\sim 20\,\mathrm{MeV}$ start to show up as tracks, assuming a pixel pitch of 4.4 mm.

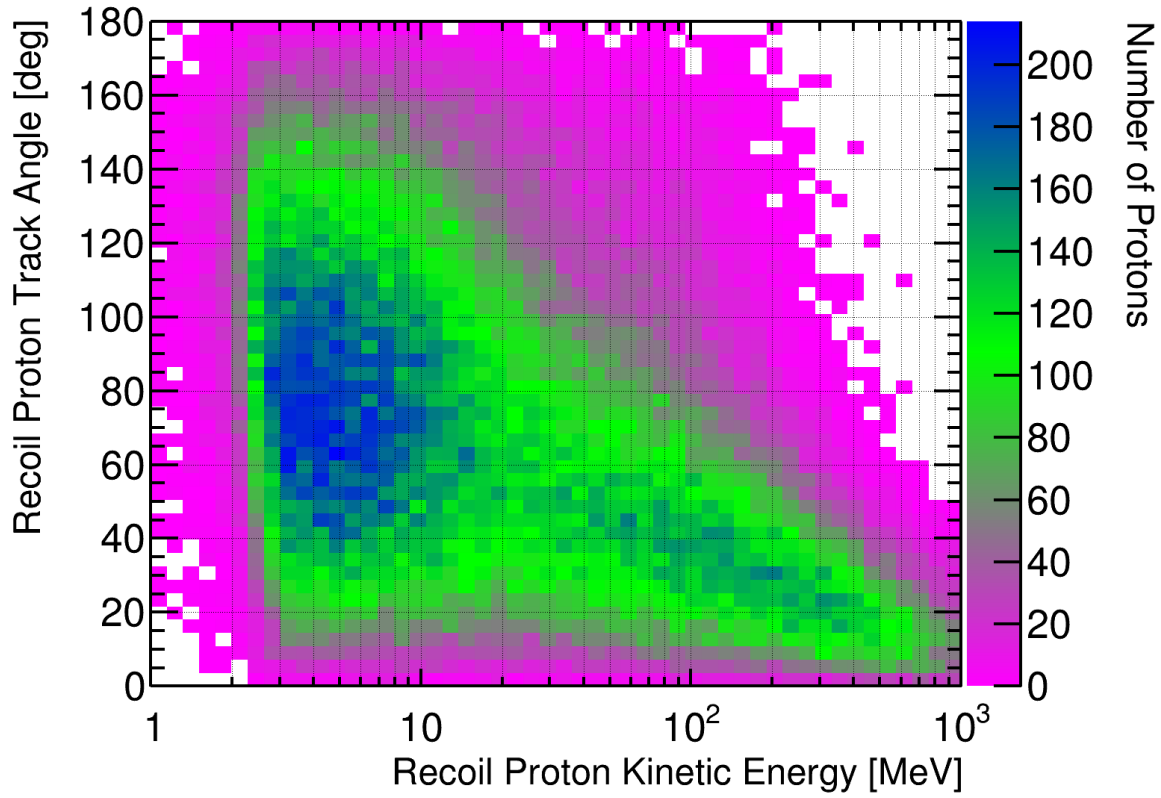

Figure 6.19.: Angle between the recoil-proton track (start-to-end vector) and the connecting line between the proton track start position and the neutrino vertex, with respect to the proton kinetic energy. Even for protons at the $\mathcal{O}(100)$ MeV, that angle strongly varies between 10° and 80°. Consequently, tracing back to the neutrino vertex from the track of neutron-induced proton recoils does not work.

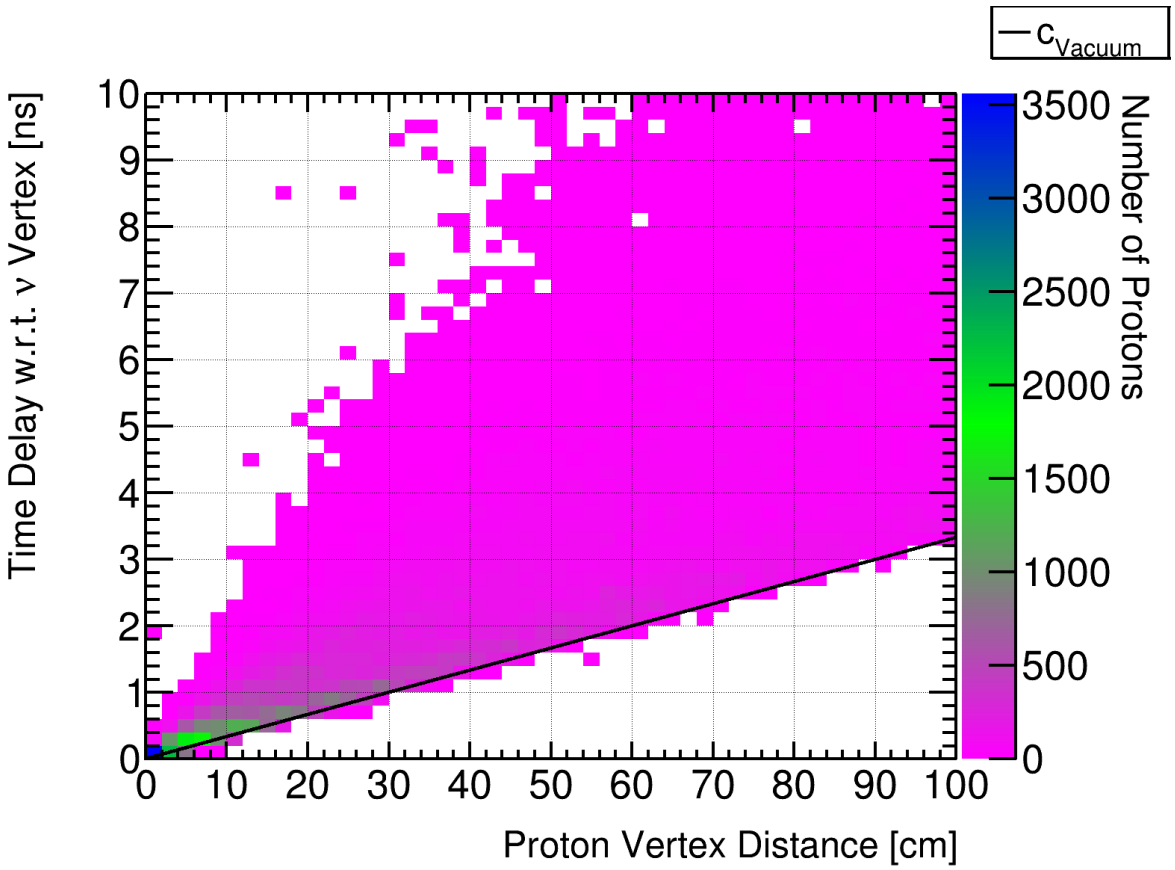

Figure 6.20.: Time delay of recoiling protons, w.r.t. the neutrino interaction, as a function of the distance between the proton recoil and the interaction vertex. Proton recoils appear nearly instantly (a few ns) after the actual neutrino interaction. The black line denotes the speed of light in vacuum.

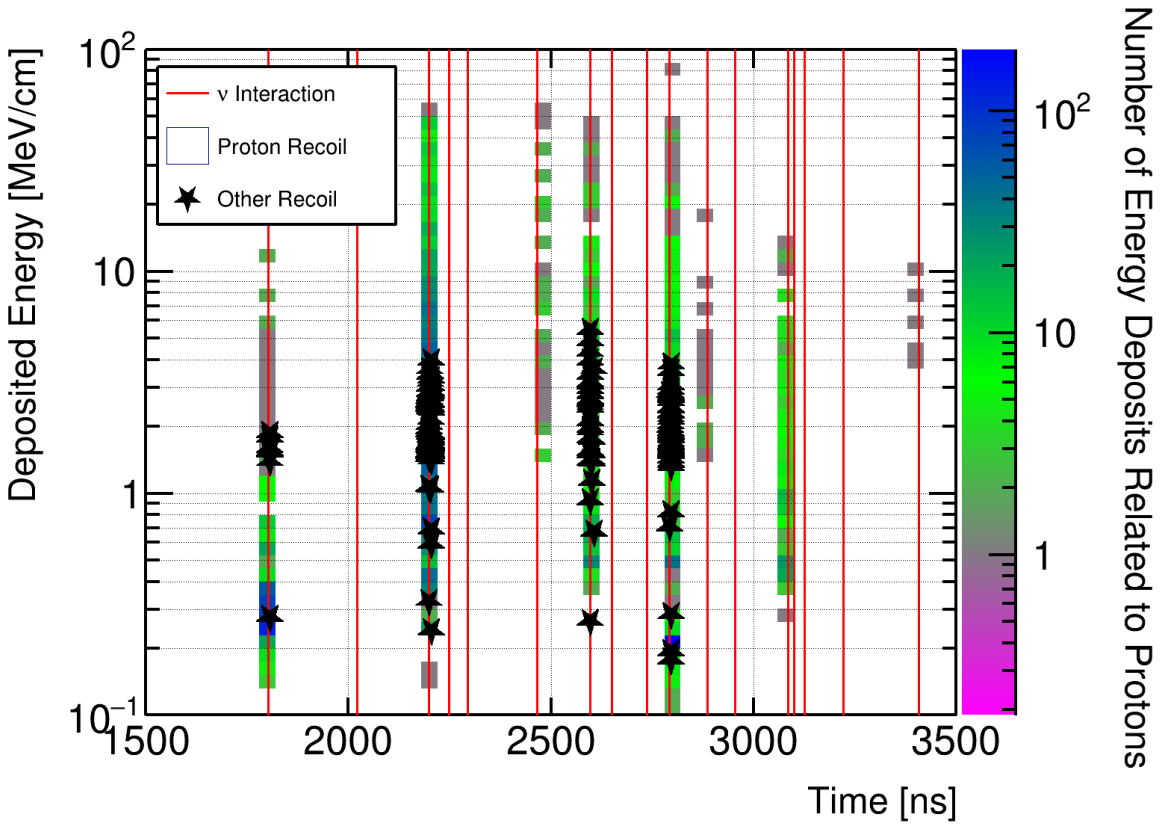

Figure 6.21.: Temporal distribution of energy deposits that appear within a 2 µs long window in the 10 µs neutrino beam spill. Vertical red lines are drawn whenever a neutrino interaction occurs. The color axis indicates the number of energy deposits related to proton recoils, and stars indicate energy deposits due to other neutron-induced nuclear fragments. All energy deposits appear immediately (a few ns) after the respective neutrino interaction. Some of the neutrino interactions appear blank because particles do not enter the detector's active volume.

Timing might not work well if the proton recoil appears in the same TPC as the interaction, due to the high activity and light yield close to the vertex. However, a second light signal, separated in time, would be expected if the neutron recoil belonged to another event. By that means, the exclusion principle can be applied to verify the vertex affiliation of the detached proton recoil, presuming that light and charge signals can be matched. Similarly, a proton that appears in another module than the interaction vertex can be assigned to its actual vertex by matching the time stamps. We will refer to that method as optical neutron tagging (or optical n-tagging) from now on.

Obviously, optical n-tagging requires not only a fast light-readout system, with a timing resolution of the $\mathcal{O}(10)$ ns, but the light-readout also needs to provide spatial resolution, in order to assign individual time stamps to the proper energy depositions seen by the charge readout. The required spatial resolution was evaluated by calculating the minimum 3D-distance from proton recoils ($\geq 10\,\mathrm{MeV}$) to any energy deposits ($\geq 10\,\mathrm{MeV}$) arising from other neutrino interactions in the same beam spill. The respective histograms are shown in 6.22, for 1 MW neutrino-beam spills (a) and for 2 MW neutrino-beam spills (b). If the light-readout systems are able to detect fast scintillation light with a spatial

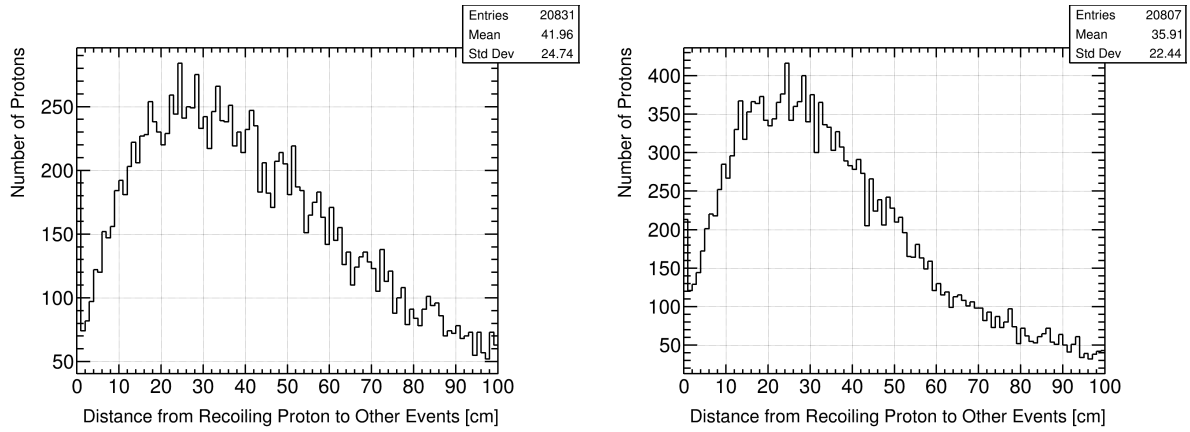

(a) 1 MW beam, 97 % > 5 cm. **(b)** 2 MW beam, 96 % > 5 cm.

Figure 6.22.: Minimum 3D-distance from proton recoils ($\geq 10\,\mathrm{MeV}$) to any energy deposits ($\geq 10\,\mathrm{MeV}$) arising from other neutrino interactions in the same beam spill. If the light-readout systems are able to detect fast scintillation light with a spatial resolution of $\sim 5\,\mathrm{cm}$, then 97 % (96 %) of neutron induced recoils can be assigned an individual time stamp, independent of other activity in the same TPC, at a beam power of 1 MW (2 MW). The peak at zero is caused by overlapping neutrino events.

resolution of $\sim 5\,\mathrm{cm}$, then 97 % (96 %) of neutron induced recoils can be assigned an individual time stamp, independent of other activity in the same TPC, at a beam power of 1 MW (2 MW). A preliminary study concerning the expected spatial resolution of the ArgonCube light-readout system will be discussed in Chapter 7.

6.4.6. Neutron Tagging by Range

A further method for neutron tagging, independent of the light-readout system, becomes available, if we simply use the distances between proton recoils and neutrino vertices as an estimator for the protons' affiliation. The mean free path (Eq. 4.9) of neutrons in LAr is inversely proportional to the respective neutron cross-section. The total neutron cross-section on argon between 100 and 800 MeV has been measured in the Cryogenic Apparatus for Precision Tests of Argon Interactions with Neutrinos (CAPTAIN) experiment [111]. A comparison with Monte Carlo generators has shown that the values extracted from GEANT4 are consistent with the measured data. Accordingly, we are going to assume that neutron-argon interactions are modeled well, and that we can reduce the dependence of the described method on modeling neutrino-argon interactions.

The distance between proton recoils and neutrino vertices is shown in Figure 6.26, for a beam power of 1 MW (a) and 2 MW (b). The horizontal axis indicates the distance

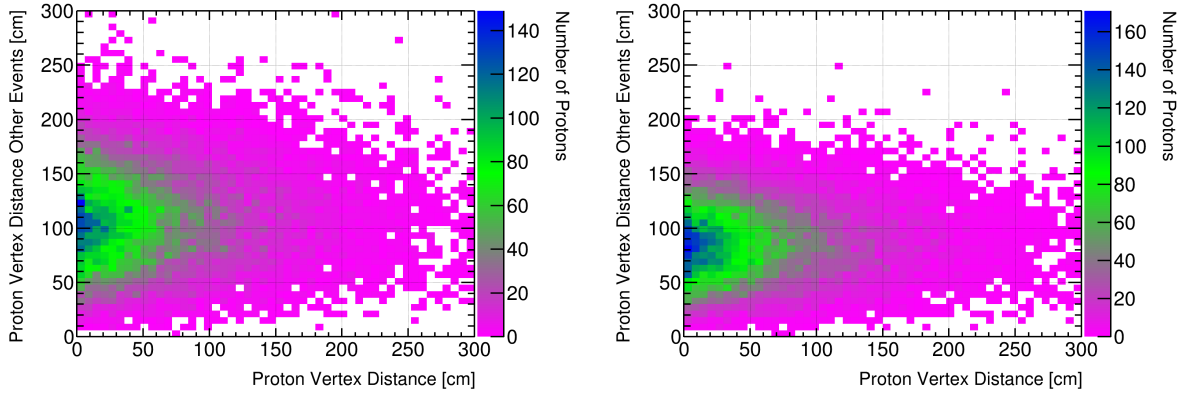

(a) 1 MW beam. **(b)** 2 MW beam.

Figure 6.23.: Distance between proton recoils and neutrino vertices, for proton recoils with kinetic energies > 10 MeV. The horizontal axis indicates the distance from the proton recoil to the actual neutrino interaction vertex of its origin, while the vertical axis indicates the distance from the proton recoil to the closest other neutrino interaction vertex. Most proton recoils appear closer to the vertex of their origin than to any other interaction vertex in the same beam spill. And barely any proton recoil appears closer than 50 cm to any other interaction vertex in the same spill at all.

from the proton recoil to the actual neutrino interaction vertex of its origin, while the vertical axis indicates the distance from the proton recoil to the closest other neutrino interaction vertex. Most proton recoils appear closer to the vertex of their origin than to any other interaction vertex in the same beam spill. And barely any proton recoil appears closer than 50 cm to any other interaction vertex in the same spill at all.

6.5. Application in DUNE ND

Now, I'm going to show how the discussed methods of neutron tagging affect the uncertainty of reconstructed neutrino-energy, resulting from the calorimetric method (Eq. 6.1). I assume a modular LArTPC with a module footprint of 1 m × 1 m, and the modules are supposed to use the novel detection technologies introduced with the ArgonCube concept. The total active LAr volume is of the sames dimensions as the planned DUNE ND-LAr. The neutrino beam intensity and spectrum are chosen according to the LBNF beamline, resulting in an event pile-up comparable to the expected pile-up at the future DUNE-ND site. Only neutrino events with the interaction vertex inside the FV as defined above, and neutron-induced proton recoils inside the active LAr volume are considered in the analysis. Proton recoils with kinetic energies below 10 MeV are not used for n-tagging.

6.5.1. Optical Neutron Tagging

The fractional energies carried away by all primary neutrons produced in a neutrino event, and the corresponding 1σ uncertainties, serve as the starting point of the analysis, and are shown in Figure 6.24a as a function of the neutrino energy. Any events, whether there are primary neutrons or not, are considered. Figure 6.24b shows the same plot,

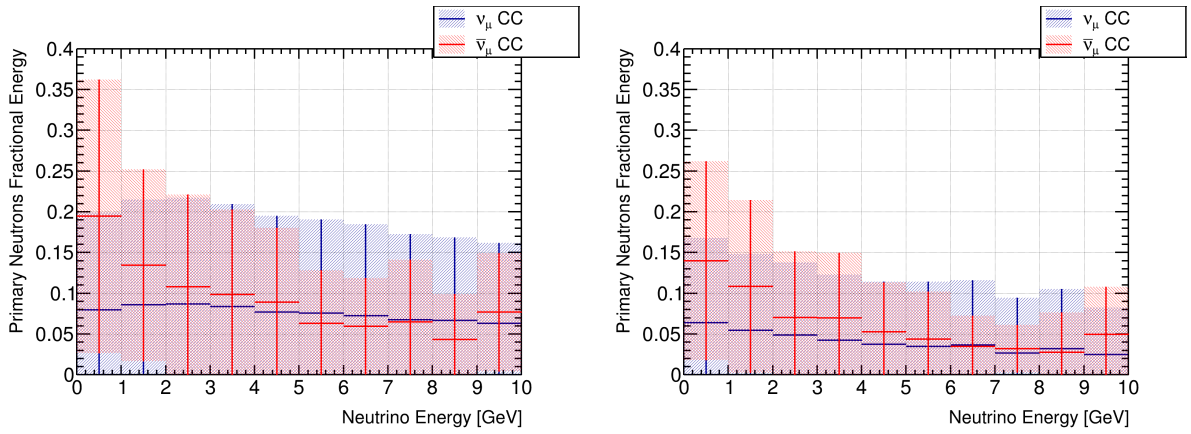

(a) w/o n-tagging **(b)** optical n-tagging

Figure 6.24.: Fractional kinetic energy, w.r.t the neutrino energy, carried away by primary neutrons produced in the neutrino event, as a function of the neutrino energy. The same plot is shown for all neutrino events in the sample (a), and with the events that allow for optical n-tagging excluded (b). Excluding the n-tagged events reduces mean value of the missed energy, i.e. the bias of reconstructed neutrino energy, and it also reduces the uncertainty on the reconstructed neutrino energy. Only recoil protons with kinetic energies $\geq$ 10 MeV are considered for tagging. The error bands represent the 1σ-uncertainty.

but events with neutron-induced proton recoils have been excluded. Here, we assume that we are able to identify all proton recoils with kinetic energies above 10 MeV, and that we are able to assign them to the proper neutrino interaction vertex by optical n-tagging. The efficiency of optical n-tagging is $\sim 36\,\%$, i.e. from a sample of $\sim 104\,486$ simulated events as many as 70 438 events have at least one primary neutron produced in the interaction, and the method of optical n-tagging allows to tag 25 357 of those events. Excluding the n-tagged events reduces the mean value of the missed energy, i.e. the bias of reconstructed neutrino energy, and more important, it also reduces the uncertainty on the reconstructed neutrino energy.

The uncertainties on the reconstructed neutrino energy due to missed neutrons, with and without optical n-tagging, are compared in Figure 6.25, for ν_μ CC events. For the

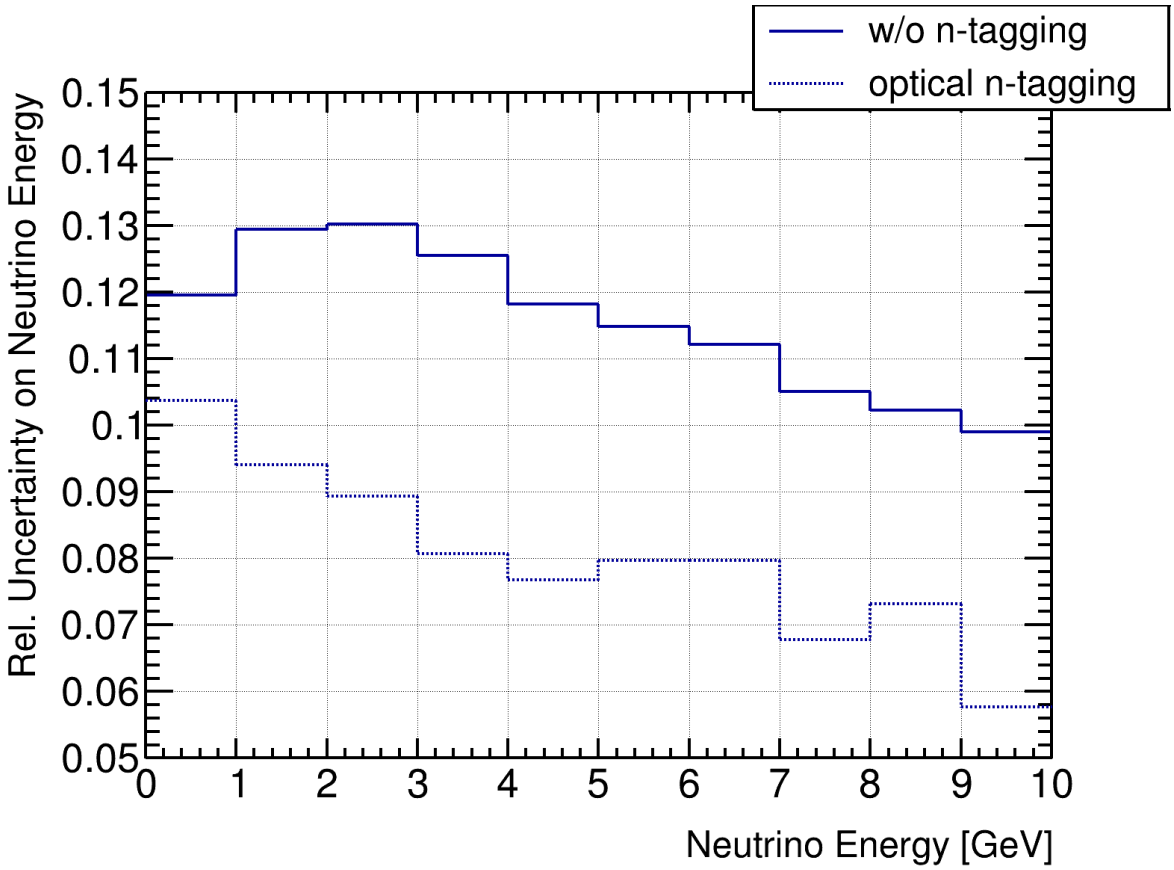

Figure 6.25.: Comparison of the energy uncertainties of ν_μ CC events due to missed primary neutrons, with and without optical n-tagging. Only recoil protons with kinetic energies ≥ 10 MeV are considered for tagging.

energy bin including the most interactions ($2\,\text{MeV} < E_\nu < 3\,\text{MeV}$), the energy uncertainty due to missed primary neutrons reduces from 13 % to 9 %. Similar improvements are observable for most of the other energy bins.

6.5.2. Neutron Tagging by Range

Slightly lower tagging efficiencies are expected for n-tagging by range, because the considered volume to look for proton recoils is limited to a sphere with a radius of some 10s of cm around the interaction vertex. As demonstrated in Section 6.4.6, most proton recoils appear closer to the vertex of their origin than to any other interaction vertex in the same beam spill, and barely any proton recoil appears closer than 50 cm to any other interaction vertex in the same spill at all. Accordingly, we are going to cut off any events with a neutron-induced proton recoil closer than 50 cm to the interaction vertex, regardless whether the proton recoil was induced by a primary neutron originating from that interaction of from any other interaction in the spill.

The distance between proton recoils and neutrino vertices is shown in Figure 6.26, for a beam power of 1 MW (a) and 2 MW (b). The horizontal axis indicates the distance

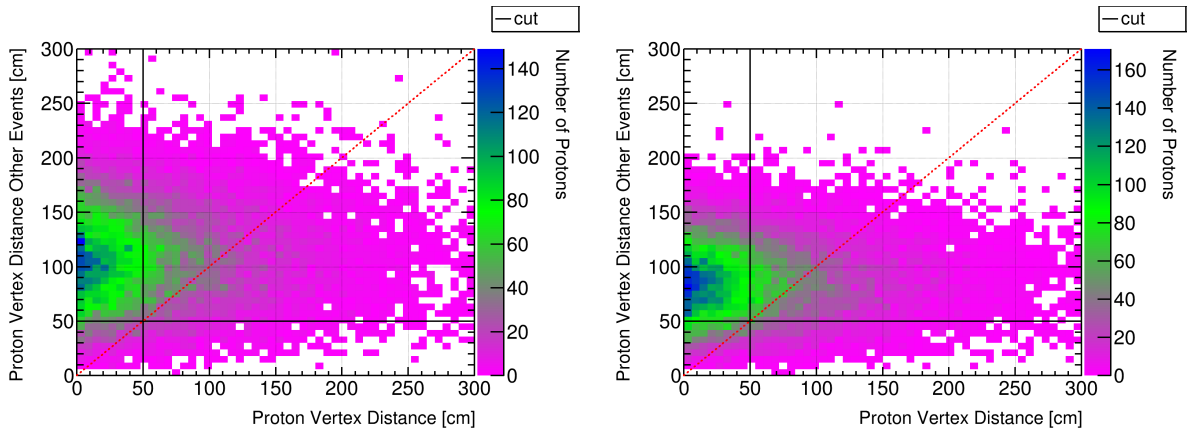

(a) 1 MW beam. **(b)** 2 MW beam.

Figure 6.26.: Neutron tagging by range. The axes label the same quantities as in Figure 6.23. Events with a hit to the left of the vertical black line (at 50 cm), or events with a hit below the horizontal black line (at 50 cm), are being tagged to contain primary neutrons. That procedure allows for an efficient rejection of events with primary neutrons, however, a small fraction of events are being wrongly tagged (those with hits below the horizontal black line).

from the proton recoil to the actual neutrino interaction vertex of its origin, while the vertical axis indicates the distance from the proton recoil to the closest other neutrino interaction vertex. Events with a hit to the left of the vertical black line (at 50 cm), or events with a hit below the horizontal black line (at 50 cm), are being tagged to contain primary neutrons. That procedure allows for an efficient rejection of events with primary neutrons, however, a small fraction of events are being wrongly tagged (those with hits below the horizontal black line), which can be a draw-back for experiments that rely on large samples for statistical significance.

Table 6.2 summarizes the efficiencies and purities to assign a neutron-induced proton recoil correctly to its interaction vertex, for both 1 MW and 2 MW beam power, and for a cut range of 50 cm as well as for an alternative cut range of 100 cm. Independent of the

Table 6.2.: Purity and efficiency of neutron-vertex association by range, for both 1 MW and 2 MW beam power. Two different ranges 50 cm and 100 cm have been considered. The purity denotes the fraction assigned proton recoils that have been assigned to the correct neutrino interaction vertex, and the efficiency denotes the fraction of proton recoils that appear within the respective range of the proper neutrino interaction vertex. The used subsample contains a total of 104 486 events.

Nuclear Fragment	Beam Power	Recoils	Threshold	Range	Purity	Efficiency
p	1 MW	45 094	10 MeV	50 cm	93 %	54 %
p	1 MW	45 094	10 MeV	100 cm	76 %	80 %
p	2 MW	45 094	10 MeV	50 cm	88 %	54 %
p	2 MW	45 094	10 MeV	100 cm	68 %	80 %

beam power, 54 % of the proton recoils appear within 50 cm to the proper interaction vertex, and 80 % of the proton recoils appear within 100 cm to the proper interaction vertex. At 1 MW beam power, 7 % (24 %) are assigned wrongly for a cut range of 50 cm (100 cm), and at 2 MW beam power, 12 % (32 %) are assigned wrongly for a cut range of 50 cm (100 cm).

The efficiency for n-tagging by range is $\sim 21\,\%$ ($\sim 30\,\%$) for a cut range of 50 cm (100 cm), i.e. from a sample of $\sim 104\,486$ simulated events as many as 70 438 events have at least one primary neutron produced in the interaction, and the method of neutron tagging by range allows to tag 14 792 (21 131) of those events. The respective fractional energies carried away by all primary neutrons produced in a neutrino event, and the corresponding 1σ uncertainties, are shown in Figure 6.27 as a function of the neutrino energy. The two left-hand plots (a and c) show the energy fractions without n-tagging and serve as a reference, while the two right-hand plots show the respective energy fractions with n-tagging by range, for a cut range of 50 cm (b) and of 100 cm (d).

The uncertainties on the reconstructed neutrino energy due to missed neutrons, with and without n-tagging by range, are compared in Figure 6.25, for ν_μ CC events.

6.5.3. Summary

A summary of the tagging efficiencies resulting from the two methods discussed above is given in Table 6.3. Optical n-tagging is the most effective method, but it requires a

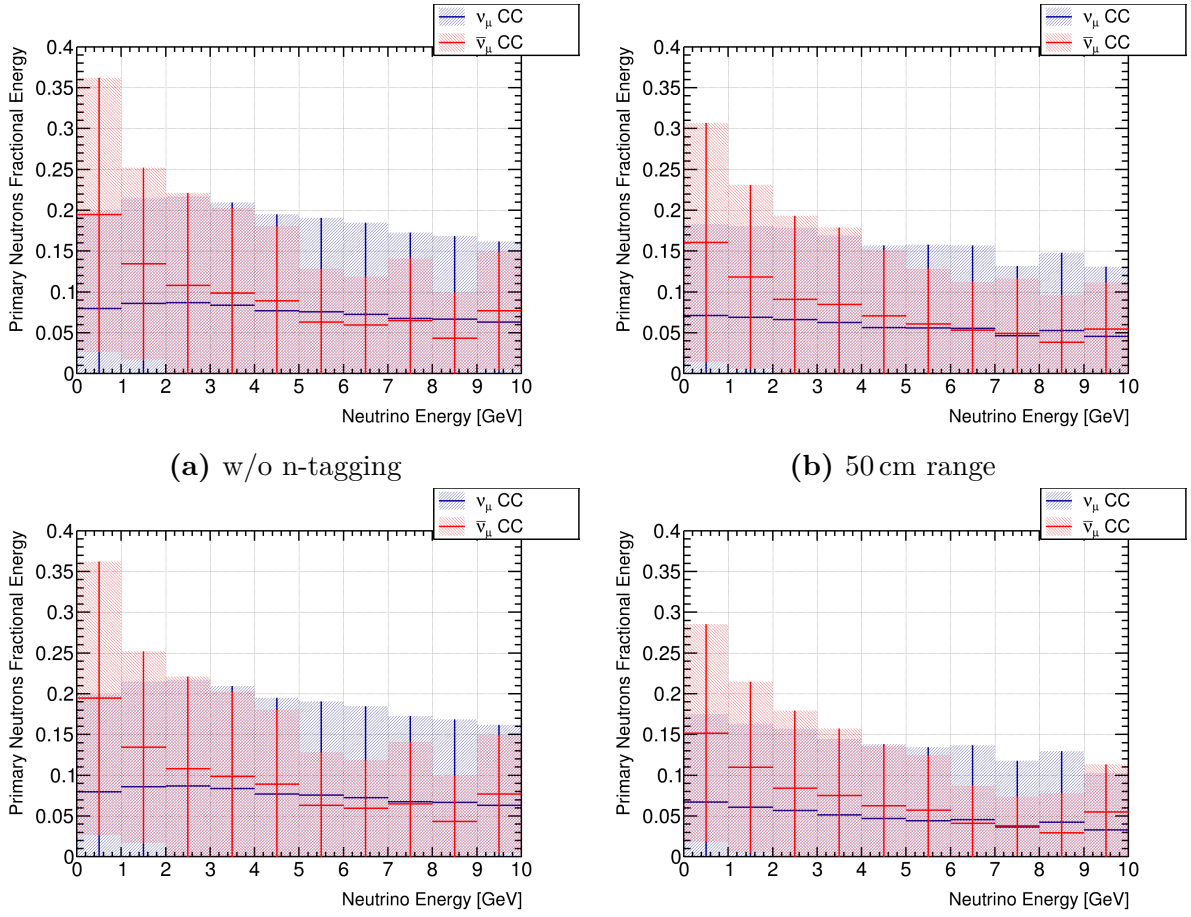

(a) w/o n-tagging

(b) 50 cm range

(c) w/o n-tagging

(d) 100 cm range

Figure 6.27.: Fractional kinetic energy, w.r.t the neutrino energy, carried away by primary neutrons produced in the neutrino event, as a function of the neutrino energy. The same plot is shown for all neutrino events in the sample (a and c), and with the events that allow for n-tagging by range excluded, for a vertex range of 50 cm (b) aand a vertex range of 100 cm (d). This method is less effective in reducing the neutrino energy uncertainties than optical tagging, because the considered volume to look for proton recoils is limited to a sphere with a radius of some 10s of cm around the interaction vertex. Only recoil protons with kinetic energies ≥ 10 MeV are considered for tagging. The error bands represent the 1σ-uncertainty.

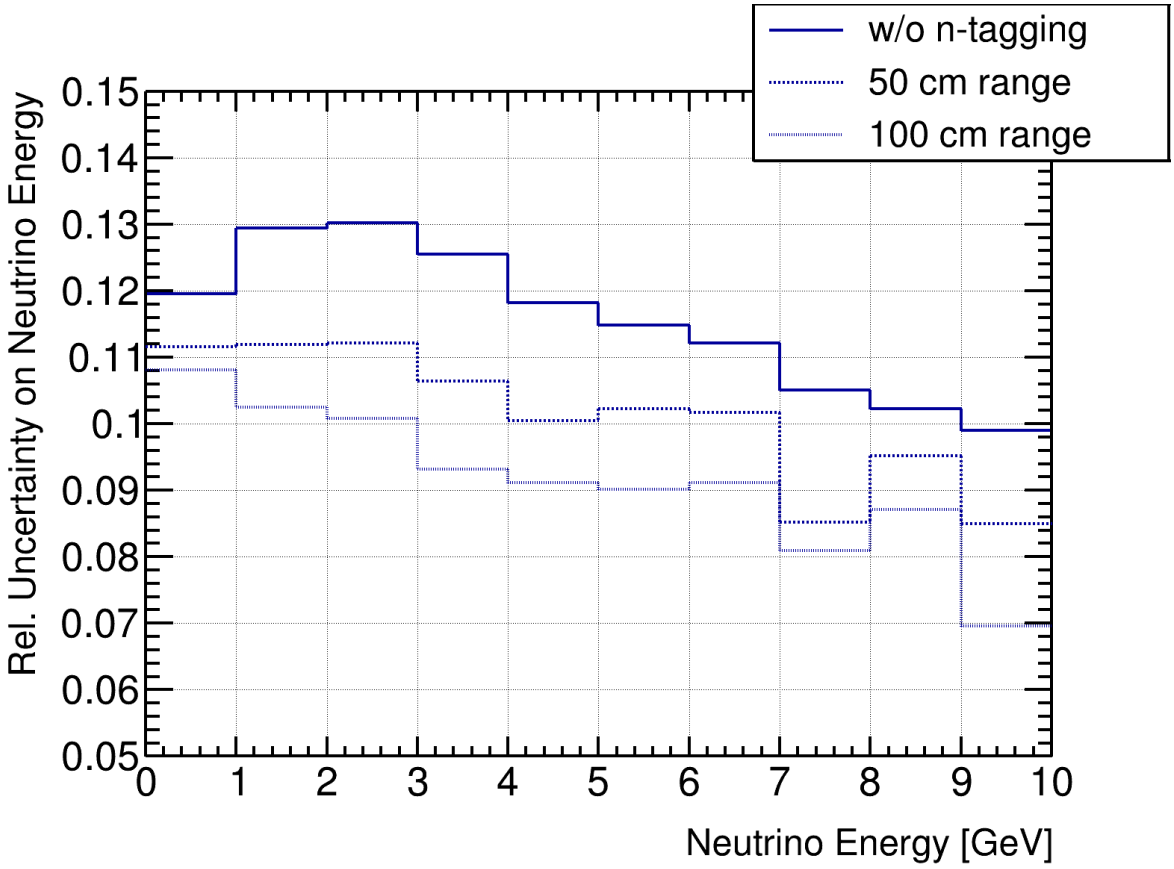

Figure 6.28.: Comparison of the energy uncertainties of ν_μ CC events due to missed primary neutrons, with and without n-tagging by range. Only recoil protons with kinetic energies $\geq 10\,\mathrm{MeV}$ are considered for tagging.

Table 6.3.: Summary on tagging efficiencies of fast neutrons with the methods of optical n-tagging and n-tagging by range. The used subsample contains a total of 104 486 events.

Nuclear Fragment	Beam Power	1+ n	Threshold	Range	Optical	Efficiency
p	1 MW	70 438	10 MeV	w/o	w/	36 %
p	1 MW	70 438	10 MeV	50 cm	w/o	21 %
p	1 MW	70 438	10 MeV	100 cm	w/o	30 %

dedicated light-readout system with a timing resolution of the $\mathcal{O}(10)$ ns as well as the ability to spatially resolve recoiling protons with a resolution of $\sim 5\,\text{cm}$. The spatial resolution of the light-readout systems will be calculated with simulations in Chapter 7. The uncertainty on the reconstructed neutrino energy due to missed neutrons drops by roughly a third for most of the energy bins if optical n-tagging is applied.

Neutron tagging by range is possible using the charge signals only, however, the uncertainty on the reconstructed neutrino energy improves less and some of the proton recoils are assigned to wrong neutrino interaction vertices, which results in smaller event samples if applied in analysis. If the optical n-tagging lacks efficiency, one can applying the two complementary approaches as a combined method of n-tagging.

So far, the presented methods for n-tagging have only been applied to raw neutrino beam sample. The performance of the methods might be different if applied analysis specific subsamples, e.g. a subsample selected for a low-ν analysis in order to characterize the neutrino beam.

7. Optical Simulation

The future ND-LAr will sit in the most intense neutrino beam ever built and will register the signals from as many as ~ 55 neutrino interactions per beam spill. Each of the 70 optically isolated LArTPCs will see particles from on average five interactions per spill. With a drift window roughly ten times as long as the spill duration, the charge readout will see a more or less instantaneous picture of the whole spill. The novel, pixelated charge readout provides unambiguous and true-3D imaging, which helps to disentangle piled-up events. Detached energy deposits pose a problem, because they can not be accurately assigned to an interaction vertex. The light readout will be able to temporally resolve the signals from the scintillation light at the $\mathcal{O}(1)$ ns, which is much shorter than the mean event separation time of 179 ns at 1 MW beam power. This is crucial for the method of optical n-tagging discussed in Chapter 6, and additionally necessitates the light readout to spatially resolve light signals with a resolution of $\sim$ 5 cm. In this last chapter, we're going to discuss the requirements on the ND-LAr's light-readout system, and we will exemplary simulate the light response of the ArgonCube 2×2 Demonstrator TPC, in order to evaluate the optical spatial resolution.

7.1. Optical Design Requirements

As mentioned earlier, there are two basic requirements on the ArgonCube light-readout system in order to assign detached energy deposits to neutrino-interaction vertices:

1. Timing resolution of $\mathcal{O}(10)$ ns is required to temporally resolve the fast scintillation signals from single events in the neutrino-beam spill.

2. Spatial resolution of ~ 5 cm is required to assign the timestamps of detached energy deposits to the corresponding charge signals.

Further design requirements that were discussed earlier in this work are the high coverage of active volume and the minimization of dead volume in the detector.

7.2. Optical Simulation

An optical simulation has been implemented in GEANT4 using the *Optical Photon Processes* libraries[1]. The simulation was performed with a geometry according to the

[1] https://geant4-userdoc.web.cern.ch/UsersGuides/ForApplicationDeveloper/html/TrackingAndPhysics/physicsProcess.html#optical-photon-processes

TPC design that will be used in the ArgonCube 2×2 Demonstrator test. Therefore, the active LAr volume (corresponding to one TPC) was divided into 32 × 128 × 64 voxels (along the drift, vertical and beam axis, respectively) with an equal size of roughly 9 mm × 10 mm × 10 mm each. As many as 10^7 photons have been simulated per voxel, randomly distributed within the voxel, resulting in a total of 2.62 billion simulated photons. The ionization and charge-conversion processes are not part of the optical simulation. The simulated times for photons only account for the propagation time of the photons from the point where they have been created to the surface of the SiPMs, including delays from the absorption and re-emission of wavelength shifting processes. The output of the simulation has then be used to build a photon Look-Up-Table (LUT), which serves as a light-weight tool for optical analysis. A preliminary comparison of the optical response simulated with the photon LUT and the optical data collected in the partially instrumented Module0 configuration is shown in Appendix A.

7.3. Geometry

The simulation geometry was built with a software called Dune-ND-GGD, a tool to build proposal geometries for the DUNE ND. Dune-ND-GGD is based on a pure Python module called General Geometry Description (GGD)[2] that allows to generate a description of a constructive solid geometry as specifically used by GEANT4 or ROOT applications, and which is represented in the GDML[3] file-format.

The geometry produced for the ArgonCube 2×2 Demonstrator TPC is illustrated in Figure 7.1a, and the stand-alone geometries produced for the light- and charge-readout tiles are shown in Figures 7.1b, 7.1c and 7.1d. For simplicity, the optical fibers are implemented as straight tubes. A 100 % reflective interface is implemented at the fiber ends, close to the cathode plane, in order to prevent coupled-in photons to escape. Similarly, an effective SiPM-sensitive area is implemented along all fiber ends close to the charge-readout plane, in order to prevent coupled-in photons from being absorbed by the SiPM PCBs. Configuration files allow to adjust the dimensions of the geometry in order to simplify scaling, i.e. to the reference size of the ND-LAr TPC. The geometries of the ArgonCube 2×2 Demonstrator module, and of an actual 2×2 array of such modules, can be found in Appendix A.

A visualization of the optical simulation (photon traces in green) is shown in Figure 7.2. 1000 photons with a wavelength of 128 nm and isotropically distributed pointing vectors are generated at the center of the TPC. Many photons head straight into the central cathode or the charge-readout plane, where they are mostly absorbed. Some other photons are being trapped in the dielectric plastic sheets of ArCLight tiles and eventually absorbed at one of the coupled SiPMs (e.g. top left tile in the visualization). Yet other photons couple into the optical fibers of LCM tiles, highlighting the shape of individual fibers due to the many reflections on their path to the SiPMs positioned at the fiber ends.

[2] `https://github.com/brettviren/gegede`
[3] `http://gdml.web.cern.ch/GDML/`

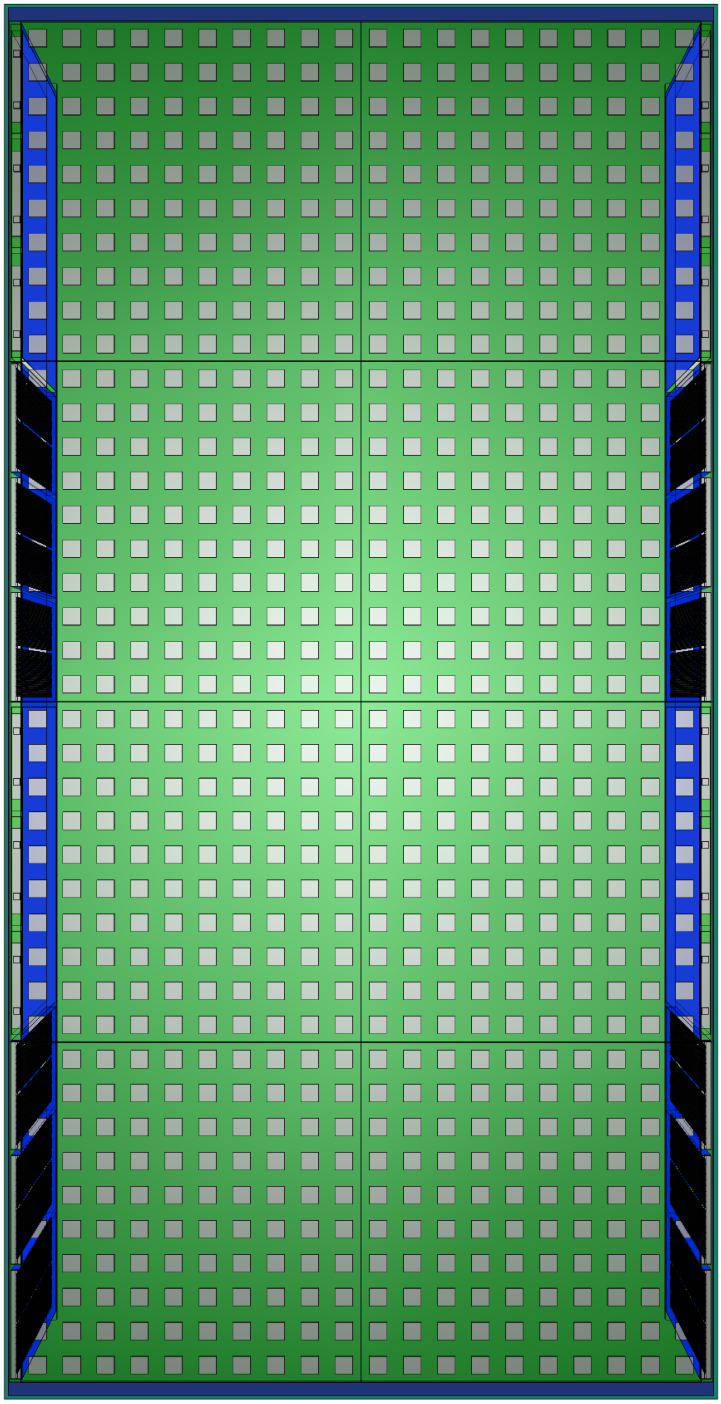

(a) TPC.

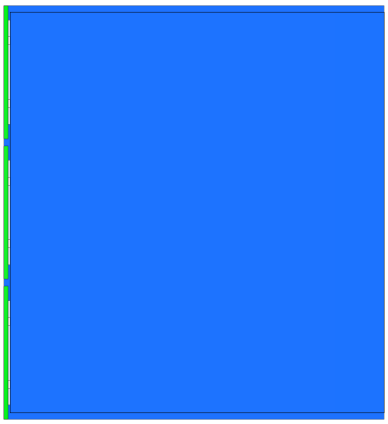

(b) ArCLight tile.

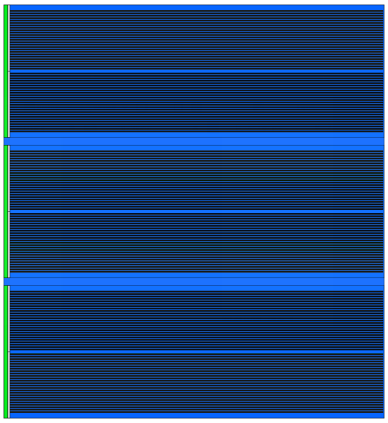

(c) LCM tile.

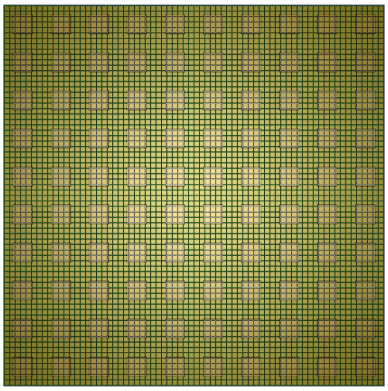

(d) Pixel Tile.

Figure 7.1.: GDML geometries produced for the optical simulation of the ArgonCube 2×2 Demonstrator TPC (a), and the stand-alone geometries of the light- and charge-readout tiles (a – ArCLight and b – LCM) as well as the charge readout (d) .

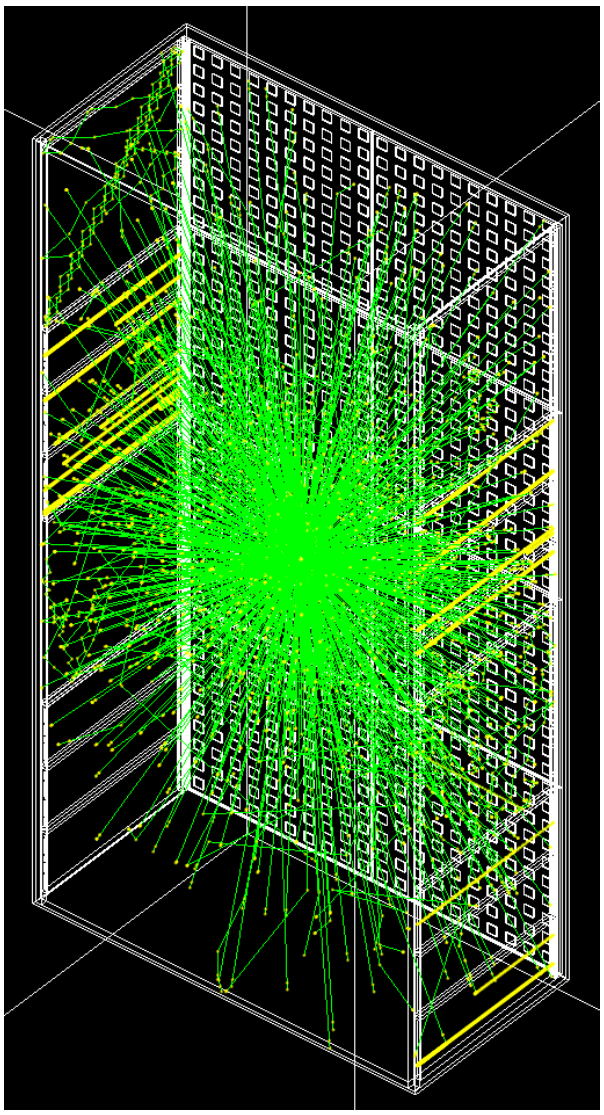

Figure 7.2.: Visualization of the optical simulation. The traces of 1000 photons produced at the center of the TPC and with isotropically distributed pointing vectors are drawn in green. Many photons head straight into the central cathode or the charge-readout plane, where most of them are absorbed. Other photons are being trapped in the dielectric plastic sheets of ArCLight tiles and eventually killed at one of the coupled SiPMs (e.g. top left tile in the visualization). Yet other photons couple into the optical fibers of LCM tiles, highlighting the shape of individual fibers du to the many reflections on their path to the SiPMs positioned at the fiber ends.

7.4. Photon Look-up-Table

The photon LUT is a ROOT file that contains the summarized information acquired with the optical simulation. Each entry corresponds to a specific voxel–SiPM pair, and contains two variables, the propagation time and the detection probability (or visibility). Accordingly, the LUT contains nearly as many entries as the number of voxels multiplied by the number of SiPMs in the TPC (slightly less because entries with zero visibility are being ignored). The propagation time is in nanoseconds and represents the minimum time required for the photons produced in a specific voxel to travel to a specific SiPM. The detection probability is a number between zero and one, and represents the probability for the photons produced in a specific voxel to be detected at a specific SiPM. In case of LCM, the probabilities of each two SiPMs have been averaged, in order to account for the fact that the fibers are bent by 180° and the ends are coupled to two SiPMs each.

7.4.1. Propagation Time

Projections of the minimum propagation time onto the drift axis, beam axis and vertical axis are shown in Figure 7.3, for both ArCLight and LCM. The time values represent mean values that were averaged among all voxels that share an identical coordinate on the respective axis. Axis coordinates are given in unit lengths of the respective voxel dimensions and slightly differ for the different axes because the voxels are not perfect cubes. The considered SiPMs are located close to the axis origin on both the drift and the beam axes, and are located close to 50 cm (ArCLight) and 80 cm (LCM) on the vertical axis. The difference of the propagation time for different positions in the TPC is at the same order as the respective propagation time of light in LAr, which is roughly 1.4 ns to cross the TPC along its shortest dimension (~ 30 cm). By other words, the spread of the propagation time among different voxels is approximately proportional to the distance form the voxels to the respective light-readout tiles. The absolute time values are then further shifted towards higher values, which is due to the additional path the photons travel in the dielectric photon traps.

7.4.2. Visibility

Figure 7.4 shows the same plots as above, but colored by the visibility, for both ArCLight and LCM. In general, the visibility in LCM is roughly one order of magnitude higher than the visibility in ArCLight, which agrees with expectations due to the different designs. The intensity of the scintillation light produced in a single spot of the TPC is expected to decrease proportional to the square of the traveled distance. Accordingly, a SiPM detects much more photons from a relatively close voxel than from a voxel at the other end of the TPC. The visibility does not change a lot among voxels that are shifted along the drift axis, because the light-readout tiles completely cover the inside of the walls parallel to that axis. However, voxels close to the light-readout tiles (beam axis $\simeq 0$ cm) benefit a much higher visibility, by roughly a factor of ten, than voxels further away (beam axis $\simeq 60$ cm). Similarly, voxels that are at the same vertical level as the SiPMs

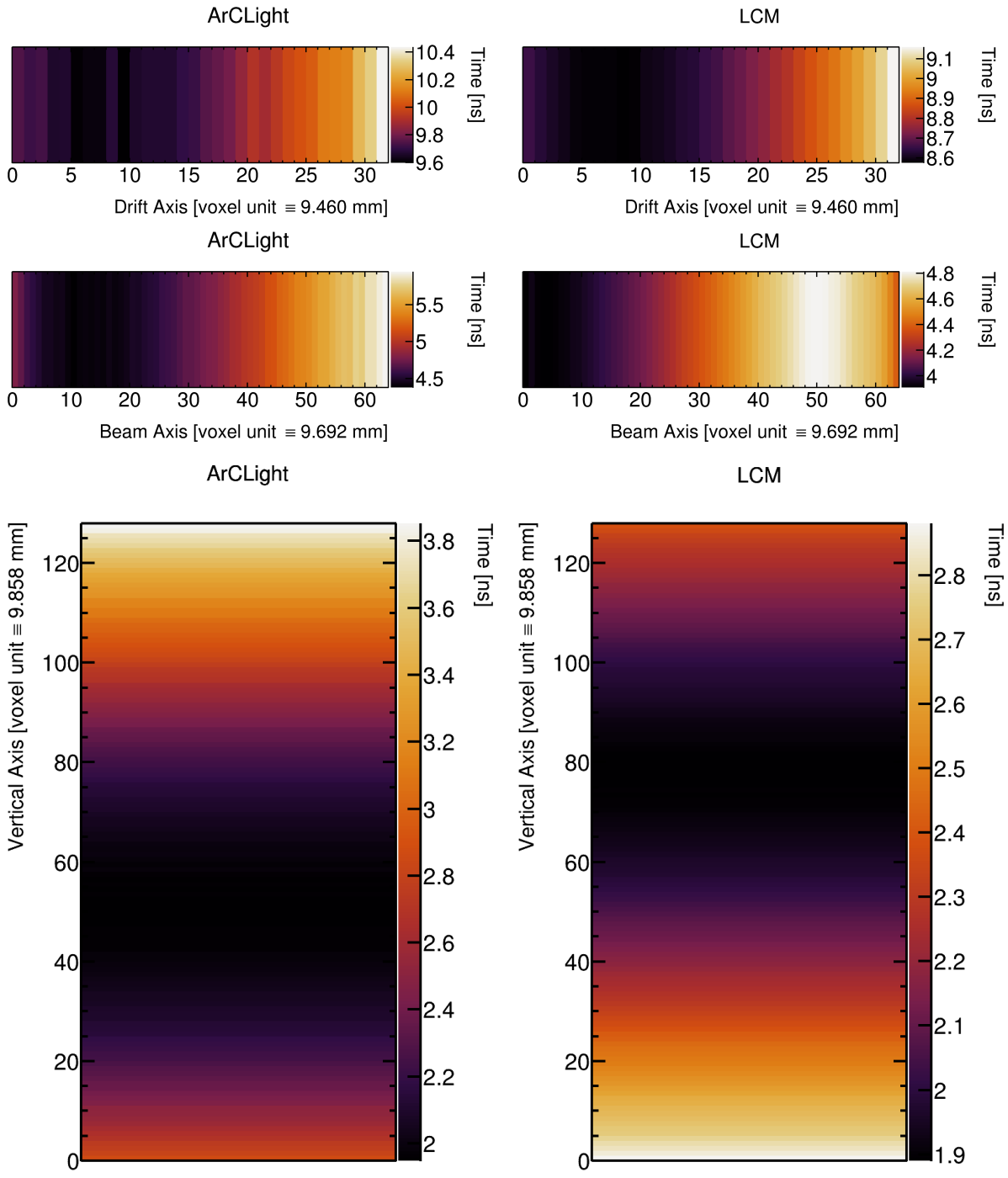

Figure 7.3.: Projection of the mean photon propagation time for different voxel positions along the drift, beam and vertical axis, for ArCLight (left) and LCM (right).

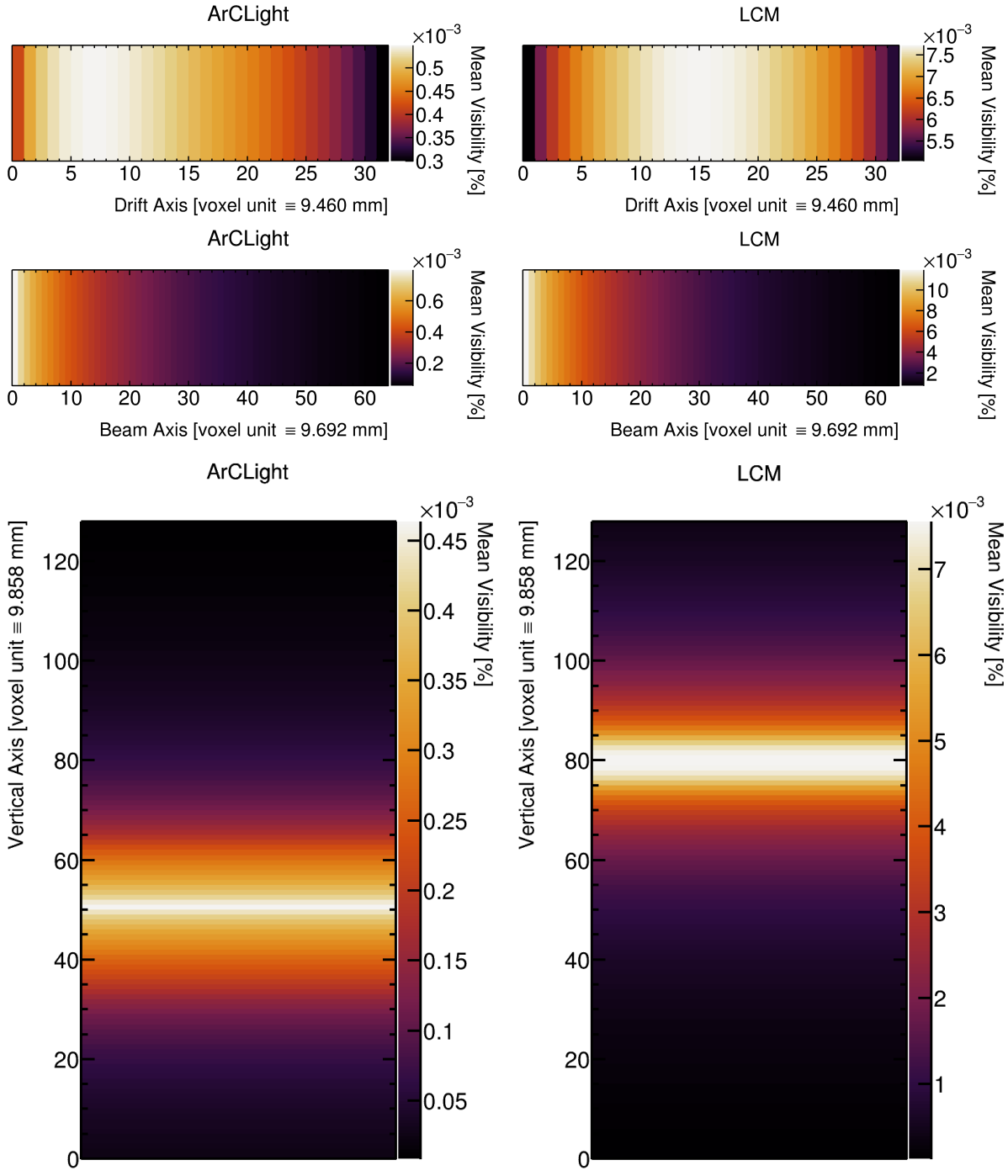

Figure 7.4.: Projection of the mean photon visibility for different voxel positions along the drift, beam and vertical axis, for ArCLight (left) and LCM (right).

show visibilities up to nearly one order of magnitude higher compared to voxels located at the very top or bottom in the TPC.

7.4.3. Findings

Comparing the 1D projections of the timing and the visibility, it seems like the visibility provides much higher discrimination power, by means of spatial resolution, along the beam axis and along the vertical axis. The spread of propagation times among the TPC is at the $\mathcal{O}(1)$ ns, which is comparable to the timing resolution of the light-readout system. The number of photons that arrive at the SiPMs, on the other hand, is of $\mathcal{O}(10)$ MeV^{-1}, while the light-readout has the ability to resolve single photons. Consequently, for a 10 MeV deposit, the signal registered form a voxel close to the SiPM ($\sim$ 250 counts) appears to be $\mathcal{O}(10)$ times stronger than the signal registered from a voxel far away to the SiPM ($\sim$ 25 counts), while the uncertainty is at the $\mathcal{O}(1)$ count. None of the two variables seems to provide the information and/or accuracy needed for spatial resolution along the drift axis. On one hand, the temporal separation along the drift axis is less than the timing resolution of the light-readout system, on the other hand, the visibility stays approximately the same along the drift axis.

As a consequence of these findings, we will be focusing on the visibility only in order to derive the spatial resolution provided by the light-readout system. Further visualizations of the visibility (2D projection) can be found in Appendix A.

7.4.4. Voxel Optimization

Before applying the photon LUT, I want to evaluate the optimal voxel size for the LUT, in order to exploit the maximum amount of information provided by the simulation, but also to keep the computation time as small as possible. Therefore, 100 vertical and through going (entering at the top and exiting at the bottom of the TPC) cosmic-muon tracks have been simulated in the GDML that was built for the optical simulation. The light yield was calculated using the Birks' model developed by the ICARUS collaboration [89], resulting in 25 236 photon/cm at 0.5 kV cm^{-1}. The number of photons arriving at the SiPMs was then evaluated using the photon LUT, for one LCM tile (SiPM numbers 14 to 17) and for one ArCLight tile (SiPM numbers 18 to 23). Photons were generated with different sampling step-lengths along the muon tracks, with the smallest step length equal to 3 mm (7570.8 photons per step) and the longest step length equal to 300 mm (757 080 photons per step). The results are shown in Figure 7.5. Surprisingly, the number of detected photons is almost exactly the same for all SiPMs and for any sampling step-lengths between 3 mm and 100 mm. Clear deviations are observable for the LCM SiPMs closer to the edge of the TPC (numbers 12 to 15). Consequently, it was decided to produce a smaller photon LUT with $8 \times 26 \times 14$ voxels (2912 in total), resulting in a voxel size of 37.840 mm $\times$ 48.534 mm $\times$ 44.307 mm. This LUT was finally used to evaluate the spatial resolution of the light-readout system.

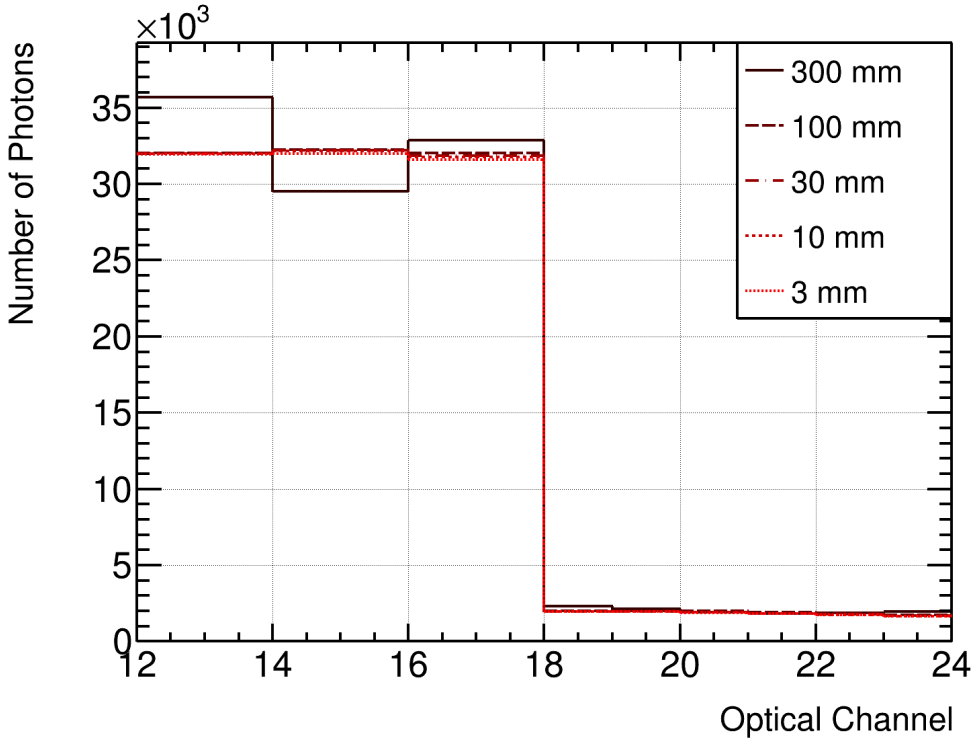

Figure 7.5.: Number of photons arriving at the SiPMs for different sampling step-lengths calculated with the photon LUT (LCM: optical channels 12-17, ArCLight: optical channels 18-23). 100 vertical and through going (entering at the top and exiting at the bottom of the TPC) cosmic-muon tracks have been simulated. The light yield was calculated using the Birks' model: 25 236 photon/cm at 0.5 kV cm^{-1}.

7.5. Spatial Resolution

In Figure 7.4 the visibility changes by up to one order of magnitude for energy deposits at different positions along beam axis and the vertical axis. The SiPMs are arranged in a line along the vertical axis such that the intensities of the signals between different SiPMs can be used to derive a rough position of the energy deposit along that axis. That method should work for tracks of different lengths as long as the track's vertical extension is small compared to the distance between the SiPMs. A similar method can be used for the resolution along the beam axis by comparing the intensities of the signals of the upstream light-readout plane with the intensities of the signals of the downstream light-readout plane.

7.5.1. Vertical Spatial Resolution

All SiPMs in the TPC, 48 in total, were used to evaluate the vertical spatial resolution, i.e. 4×6 SiPMs from ArCLight tiles, 2 tiles at the upstream and 2 tiles at the downstream module wall, and 4×6 SiPMs from LCM tiles, 2 tiles at the upstream and 2 tiles at the downstream module wall. A total of 100 000 horizontal and through-going cosmic-muon tracks have been simulated. These tracks were randomly distributed inside the active volume of the TPC, and with random orientations. Birks' model was used to estimate the light yield along the tracks, with a step length of 50 mm, and the LUT was used to get the number of photons detected at each SiPM in turn. The numbers of photons detected at LCM tiles were normalized with a factor that corresponds to the fraction between the total visibility of ArCLight SiPMs and the total visibility of LCM SiPMs in the LUT. The Center of Gravity (CoG) was used to estimate the vertical position from the number of photons detected at the SiPMs. The CoG is defined as

$$\mathrm{CoG} = \frac{\sum_{i=0}^{n} (y_i * \gamma_i)}{\sum_{i=0}^{n} \gamma_i}, \tag{7.1}$$

where y_i is the vertical position of the i-th SiPM in the TPC, γ_i is the number of photons detected at the i-th SiPM and n is the total number of SiPMs in the TPC.

The results of the simulation are shown in Figure 7.6. The residual between the estimated vertical position (the CoG) and true vertical position of the tracks is shown in Figure 7.6a, as a function of the true vertical position. The mean value and the 1σ uncertainty of the residuals were fitted for each vertical slice, and plotted as a function of the true vertical position in Figures 7.6b and 7.6c, respectively. From the mean values, it is evident that the estimated vertical position agrees well with the true vertical position for tracks at the center of the TPC. The positions are estimated too high towards the bottom of the TPC, and too low towards the top of the TPC, up to ~ 10 cm, which is because of the limited angular acceptance at the TPC bottom and top. The vertical spatial resolution is interpreted as the residual uncertainty, and, similar to the mean values, increases towards the TPC bottom on top. From that simulation, we conclude that the vertical spatial resolution provided by the light-readout system is $\lesssim 5$ cm at

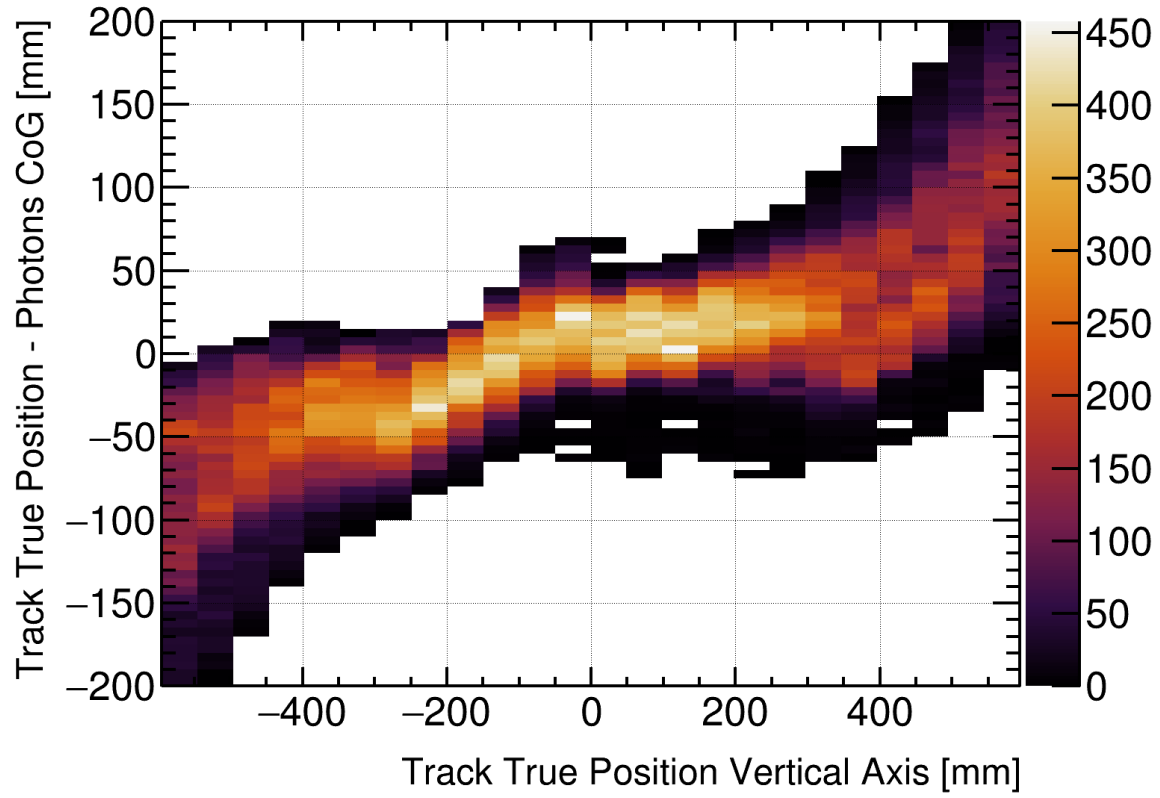

(a) Center of gravity residuals.

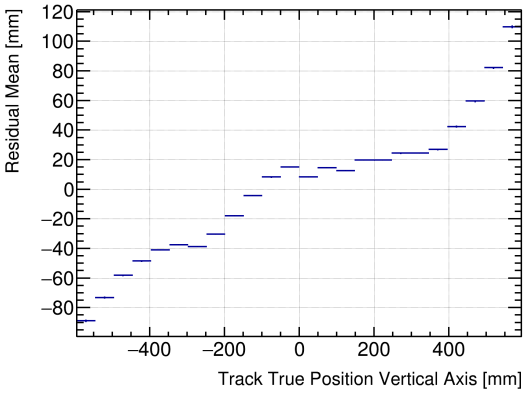

(b) Center of gravity residual mean.

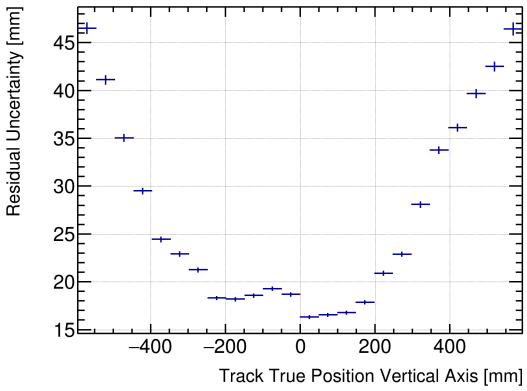

(c) Center of gravity residual uncertainty.

Figure 7.6.: Vertical spatial resolution derived from the optical simulation. The residual between the estimated vertical position (the CoG) and true vertical position of the tracks is shown in sub-figure **a**, as a function of the true vertical position. The mean value and the 1σ uncertainty of the residuals were fitted for each vertical slice, and plotted as a function of the true vertical position in sub-figures **b** and **c**, respectively. A total of 100 000 horizontal and through-going cosmic-muon tracks have been simulated and were sampled with a step length of 50 mm.

any position in the TPC, which is roughly the same size as the distance between two adjacent SiPMs.

7.5.2. Spatial Resolution Along the Beam Axis

The resolution along the beam axis (between the light panels) was derived by comparing the intensities of the signals of the upstream light-readout plane with the intensities of the signals of the downstream light-readout plane. An illustration comparing the visibilities between upstream and downstream SiPMs along the beam axis is shown in Figure 7.7, for ArCLight (a) and LCM (b). The visibility is shown for two SiPMs, one at the upstream

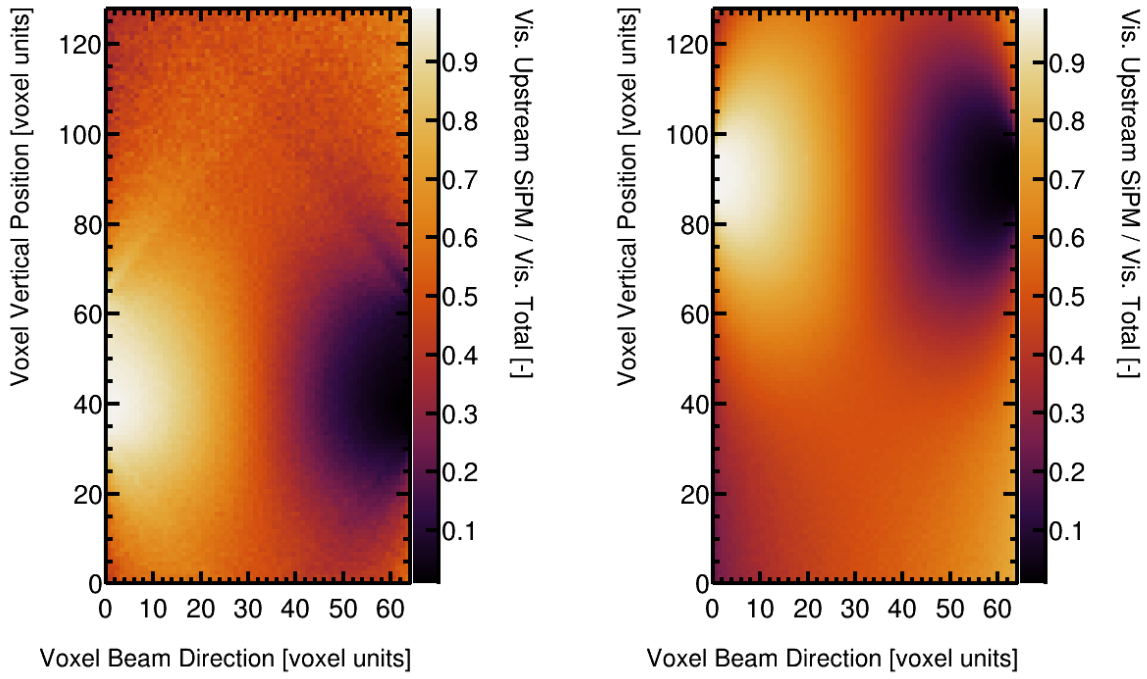

(a) ArCLight **(b)** LCM

Figure 7.7.: Comparison between the visibilities of upstream and downstream SiPMs along the beam axis, for ArCLight (a) and LCM (b). The visibility is shown for two SiPMs, one at the upstream light-readout (at 0 on the horizontal axes) and one at the downstream light-readout plane, both at the same vertical level. The color encodes the relative visibility of the upstream SiPM with respect to the sum of the visibilities of both the upstream and the downstream SiPM. Accordingly, one (or white) means that a voxel is exclusively seen by the upstream SiPM while zero (or black) means that a voxel is exclusively seen by the downstream SiPM, and 0.5 means that the visibility is the same for both SiPMs.

light-readout (at voxel 0 on the horizontal axes) and one at the downstream light-readout

plane, both at the same vertical level. The color encodes the relative visibility of the upstream SiPM with respect to the sum of the visibilities of both the upstream and the downstream SiPM. Accordingly, one (or white) means that a voxel is exclusively seen by the upstream SiPM while zero (or black) means that a voxel is exclusively seen by the downstream SiPM, and 0.5 means that the visibility is the same for both SiPMs.

The optical spatial resolution along the beam axis was derived from a sample of 100 000 through-going cosmic-muon tracks, but with random orientations in vertical planes normal to the beam axis (i.e. all deposits that belong to the same track have the same position on the beam axis). The CoG was used to estimate the track position along the beam axis from the number of photons detected at the SiPMs.

$$\mathrm{CoG} = \frac{\sum_{i=0}^{n} (z_i * \gamma_i)}{\sum_{i=0}^{n} \gamma_i}, \tag{7.2}$$

The results of the simulation are shown in Figure 7.6. The residual between the estimated position (the CoG) and true position along the beam axis of the tracks is shown in sub-figure **a**, as a function of the true position along the beam axis. The mean value and the 1σ uncertainty of the residuals were fitted for each vertical slice, and plotted as a function of the true position along the beam axis in sub-figures **b** and **c**, respectively. As visible from Figure 7.8b, the residual means are distributed within a fairly narrow band of $< 3\,\mathrm{cm}$ around zero. The respective uncertainties, which are interpreted as the spatial resolution along the beam axis, are below 2 cm for all positions along the beam axis.

7.5.3. Results

The spatial resolution along the vertical axis as well as the beam axis was derived with the optical simulation of the ArgonCube 2×2 Demonstrator, for a single TPC representing an optically isolated unit. The spatial resolution along the vertical axis was found to be $< 5\,\mathrm{cm}$ for all positions along the respective axis, and the spatial resolution along the beam axis was found to be $< 2\,\mathrm{cm}$ for all positions along the respective axis. Assuming that these two resolutions are uncorrelated, we can determine the spatial resolution in the vertical/beam plane to be $< 5.4\,\mathrm{cm}$.

In Chapter 6 (Fig. 6.22a), we figured out that the minimum distance from recoiling protons to other events ($\geq 10\,\mathrm{MeV}$) is $< 5\,\mathrm{cm}$ for 97 % of the protons at, 1 MW beam power. Now, that we know we actually can achieve a spatial resolution of $< 5.4\,\mathrm{cm}$ in the plane normal to the drift axis, we want to reproduce that result for the more conservative case, where we only consider the distance from recoiling protons to other events in the respective plane. That means that any spatial separation along the drift axis will not enhance the ability to assign proton recoils to event vertices by using the optical readout. Figure 7.9 shows the minimum distance of recoiling protons to other events, not in 3D space but only in the 2D projection onto the plane perpendicular to the drift axis (YZ plane), for a 1 MW beam power. Still 90 % of the proton recoils (kinetic energy $\geq 10\,\mathrm{MeV}$) can be assigned to a neutrino vertex with the method of optical n-tagging, if we make the conservative assumption of an optical spatial resolution of 6 cm in the plane perpendicular to the drift axis.

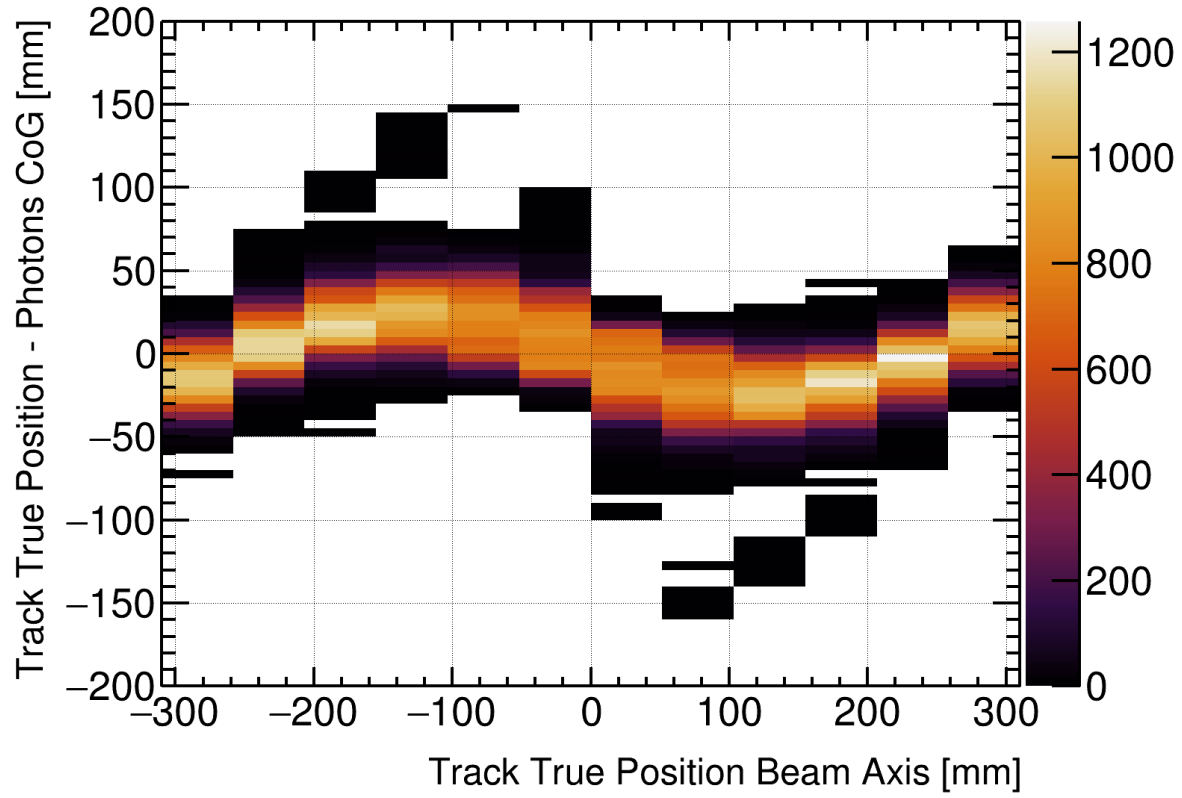

(a) Center of gravity residuals.

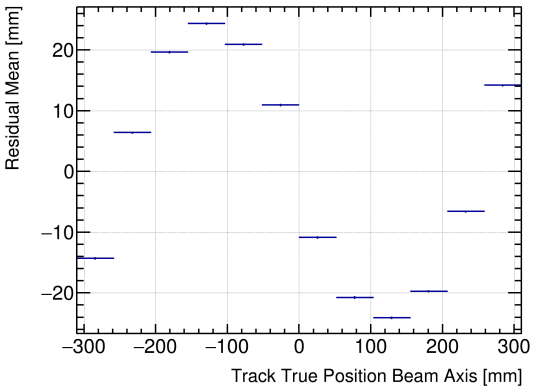

(b) Center of gravity residual mean.

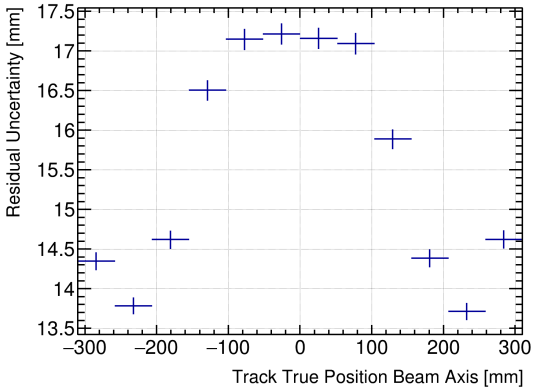

(c) Center of gravity residual uncertainty.

Figure 7.8.: Spatial resolution along the beam axis derived from the optical simulation. The residual between the estimated position (the CoG) and true position along the beam axis of the tracks is shown in sub-figure **a**, as a function of the true position along the beam axis. The mean value and the 1σ uncertainty of the residuals were fitted for each vertical slice, and plotted as a function of the true position along the beam axis in sub-figures **b** and **c**, respectively. A total of 100 000 through-going cosmic-muon tracks with random orientations in vertical planes normal to the beam axis have been simulated and were sampled with a step length of 50 mm.

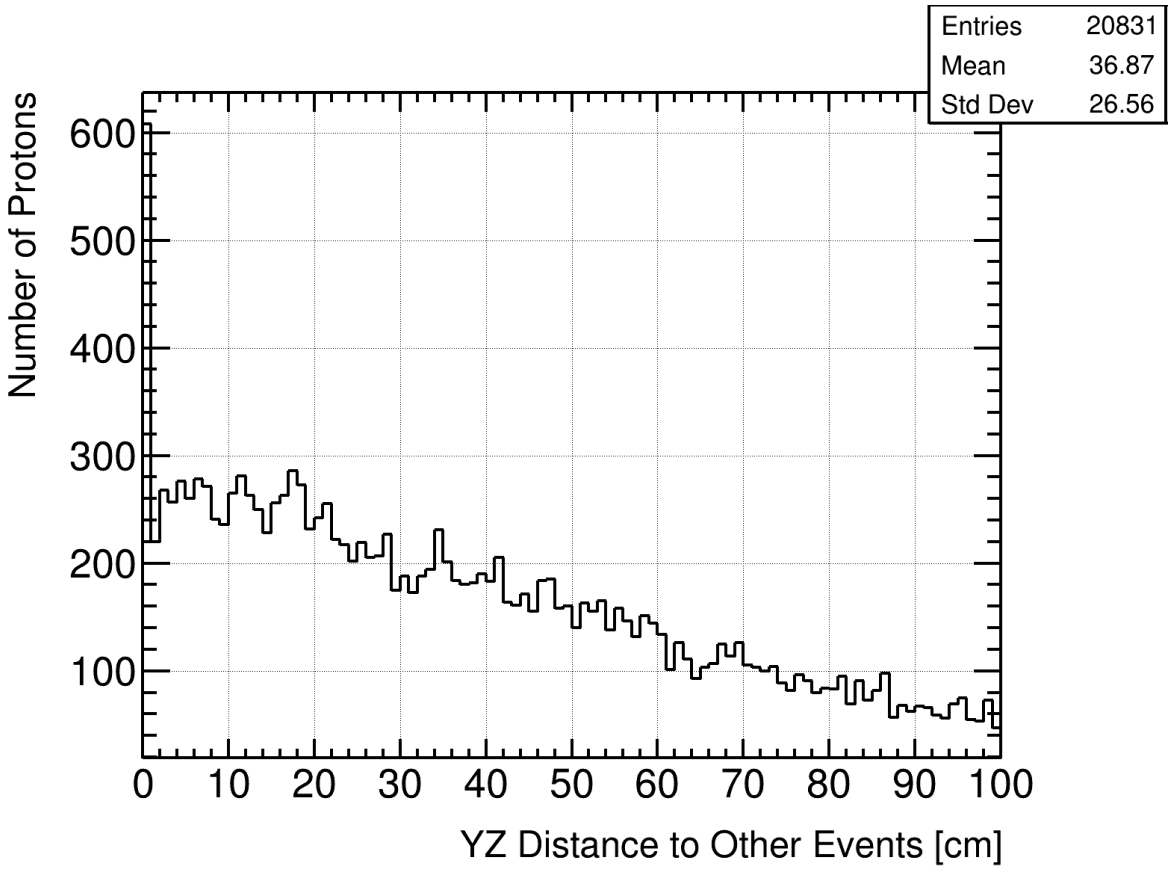

Figure 7.9.: Minimum distance of recoiling protons to other events, projected onto the plane perpendicular to the drift axis. If the light-readout systems are able to detect fast scintillation light with a spatial resolution of 5 cm (6 cm) in the respective plane, then 92 % (90 %) of neutron induced recoils can be assigned an individual time stamp, independent of other activity in the same TPC. The peak at zero is caused by overlapping neutrino events.

8. Conclusion

The DUNE experiment is a long-baseline neutrino-oscillation experiment that is realized in the USA. The oscillated signal will be measured with four cryogenic 10 kt LArTPCs representing the FD, located 1300 km from the neutrino source at SURF. The un-oscillated signal at the FD will be predicted from measurements of the un-oscillated neutrino beam at FNAL. These measurements will be performed with the ND located 574 m from the neutrino source, using a LArTPC as the detector's core component. This component is called ND-LAr and uses the same target nucleus and the same fundamental detection principle as the FD, thus reducing the sensitivity to nuclear effects and detector-driven systematic uncertainties in the extraction of the oscillation signal at the FD.

ND-LAr will be exposed to the world's most intense high-energy neutrino beam, such that on average ~ 15 neutrinos per beam spill will interact in the detector's 147 t active LAr target, at 1 MW beam power. Moreover, it will see the signals form a total of ~ 55 events per beam spill, if we consider additional interactions in the surrounding rock and support structures. Traditional projective wire-readout TPCs reconstruct 3D images from multiple 2D projections, which introduces ambiguities. Therefore, this technology is not able to disentangle piled-up events, as they will occur in ND-LAr.

The ArgonCube concept modularizes the ND-LAr into a number of self-contained LArTPCs with a drift length of 50 cm. Furthermore, it uses novel technologies to mitigate the problem of event pile-up. The charge signals are detected with a pixelated charge-readout system enabling true-3D event reconstruction. ASICs specifically developed for this purpose are capable of cold amplification and digitization, thus reducing the number cryostat penetrations, and dissipate as few as 61 µW of energy per readout channel. Two complementary light readout systems that allow for the efficient detection of the LAr scintillation light are used in the ArgonCube concept. Both systems are based on dielectric structures and can be deployed in electromagnetic fields with high field strengths, avoiding the need for additional dead volume in the modular design of ArgonCube. The electric drift field is shaped by a resistive shell that is a carbon-loaded polyimide foil laminated directly onto the cathode plane and the module walls. The polyimide foil has a resistivity of $\mathcal{O}(1)$ GΩ per square at LAr temperatures and provides a continuous linear potential distribution along the drift direction. Compared to conventional field cages, the resistive shell drastically reduces the component count and, therefore, also the number of potential points of failure. And in the case of an electric breakdown the resistive shell limits the power release.

Neutrino oscillations are a function of the neutrino energy, and in order to determine the oscillation parameters, the neutrino energy needs to be measured with both the ND and the FD. The energy of a neutrino interacting with a multi-nucleon target is usually reconstructed with the calorimetric method because of the unknown initial state of the

target nucleus and FSI. Neutrons emerging from the interaction vertex can carry away more than 25 % of the neutrino energy. That energy is missed by applying the calorimetric method because neutral particles are not reconstructed in LArTPCs. Simulations using the GENIE event generator have shown that primary neutrons are involved in about 80 % of neutrino-argon interactions, at neutrino energies corresponding to the FNAL beamline. In those events with primary neutrons involved, a mean energy corresponding to ~ 10 % of the parent neutrino's kinetic energy is carried away by primary neutrons, and the relative uncertainty on the reconstructed neutrino energy can exceed 13 %. The energy is distributed among three primary neutrons, on average, an more than 90 % of that energy is carried away by fast neutrons with kinetic energies ≥ 20 MeV.

Neutrons can be identified in LArTPCs by secondary charged particles that are produced if the neutron interacts with an argon nucleus. The most abundant nuclear fragments are argon nuclei, up to a neutron energy of ~ 200 MeV, and protons that are knocked out of an argon nucleus, at higher neutron energies. The kinetic energy of recoiling argon nuclei is of the $\mathcal{O}(1)$ MeV, showing up as single blips in TPCs, and therefore are hard to identify among all the activity produced by neutrino interactions. Recoiling protons, on the other hand, have kinetic energies of the $\mathcal{O}(10)$ MeV to $\mathcal{O}(1)$ GeV, depending on the neutron energy. Setting a threshold of 10 MeV on the kinetic energy of all particles produced in neutrino interactions cuts off low-energetic activity sprinkled among the TPC, leaving a much clearer image that allows identifying detached energy deposits produced by proton recoils. At kinetic energies ≥ 20 MeV, these proton recoils can be resolved as short tracks, however, extrapolating the track back to a neutrino interaction vertex does not work because of the inelastic character of the collisions producing protons.

The DUNE beam spill has a duration of 10 µs, while the charge-readout window at 0.5 m drift length is nearly 300 µs long, at an electric field strength of 0.5 kV cm^{-2}. Accordingly, the charge readout sees all the activity deposited within a beam spill as a single image. Therefore, the charge readout can not make the association between detached energy deposits and neutrino interaction vertices. Neutrino interactions show up in LAr-ND with a mean event separation time of 179 ns. The ArgonCube light-readout systems, having a time resolution of the $\mathcal{O}(1)$ ns, can easily resolve the light signals produced by individual neutrino interactions in the beam spill. The modularization introduced by the ArgonCube concept drastically reduces the pile-up of optical signals, and increases the localization of scintillation light. While the mean distance between proton recoils and tracks from other neutrino interactions is 42 cm, 97 % of all protons can be assigned to the correct interaction vertex if the optical system can provide a spatial resolution of 5 cm, at 1 MW beam power. Assuming that neutrino events with primary-neutron induced proton recoils can be tagged for mis-reconstructed neutrino energy, the relative uncertainty on the reconstructed neutrino energy due to missed neutrons drops to less than 10 % for the most populated energy bins (between 1 MeV and 5 MeV).

A second option to tag neutrons using the charge signals only is by range. Most proton recoils appear closer to the vertex of their origin than to any other interaction vertex in the same beam spill, and barely any proton recoil appears closer than 50 cm to any

other interaction vertex in the same spill at all. Excluding events with a neutron-induced proton recoil closer than 50 cm to the interaction vertex reduces the relative uncertainty on the reconstructed neutrino energy by $\sim 3-4\%$ for the most populated energy bins. A drawback of that method is that some of the proton recoils are assigned to wrong neutrino interaction vertices, resulting in smaller event samples if applied in analysis.

An optical simulation was performed with GEANT4 to derive the spatial resolution provided by the ArgonCube light-readout systems. A purpose-built detector geometry of the LArTPC, according to the dimensions of the Module0 prototype, and the same design as it will be used in the ArgonCube 2×2 Demonstrator test, was implemented to simulate and track VUV photons. The results were stored in a photon LUT, that allows a simplified handling for further studies of the optical detector-response, and that allows for a simple integration in high-level reconstruction software. Studies using the LUT have shown that the light-readout systems are able to provide a spatial resolution of $\lesssim 5$ cm along the vertical detector axis, at any position in the TPC, which is roughly the same size as the distance between two adjacent SiPMs. Furthermore, the light-readout systems are able to provide a spatial resolution of $\lesssim 2$ cm along the beam axis, which is perpendicular to the drift axis. No spatial resolution is provided along the drift axis. Consequently, the minimum distance between proton recoils and tracks produced by other neutrino interactions was re-evaluated, ignoring the contribution from the separation along the drift axis. It was shown that still 90 % of the proton recoils (kinetic energy ≥ 10 MeV) can be assigned to a neutrino vertex with the method of optical neutron tagging, which makes this method a valuable option to reduce the uncertainty on the reconstructed neutrino energy.

The neutron yield of atmospheric neutrinos in water has been measured in Super-Kamiokande [112], and ANNIE [113] is measuring the neutron yield of beam neutrinos in water. Up to now, no similar measurements have been performed in LAr. Measurements that allow to characterize the neutron yield of neutrino interactions in LAr would be very valuable, not only for DUNE, but for any neutrino experiment using the LArTPC technology. Such measurements could be performed with the ArgonCube 2×2 Demonstrator using the proposed methods of neutron tagging, and would simultaneously serve as a proof of principle of those methods. On the other hand, a direct exposure of a LArTPC to neutrons of known energy could help to understand the phenomenology of neutron induced recoils. Studies of low-level background rejection in DUNE would further allow to optimize the identification of proton recoils within all the activity sprinkled among the TPCs by the multiple events per beam spill.

I have performed a preliminary comparison between the optical response simulated with the photon LUT and the optical data collected in the partially instrumented Module0. The results are shown in Appendix A.3. The measured shape and the ratio of light yield between the LCM (channels 13 - 18) and ArCLight (channels 19 - 24) light-readout systems roughly agree with expectations. Discrepancies in the shape of LCM channels might occur because different WLS coatings have been tested in the experiment, and the photon LUT was built with the simulation of TPB coating only. The magnitude of photons measured with LCM is by about a factor three lower than what is simulated, which indicates that the efficiency resulting from the simulation is too optimistic. The

magnitude of photons measured with ArCLight agrees well with the simulation, although single channels seem to lack unstable operation in some of the recorded events.

Similar comparisons with the data from the fully instrumented Module0 runs, or the planned ArgonCube 2×2 Demonstrator, would help to verify the performance of the optical simulation and allow to tune the LUT for further applications, if necessary. Furthermore, a sample of through going, vertical cosmic-ray muons, and a sample horizontal muons produced by neutrino interactions, would allow to derive the respective optical spatial resolutions from actual data, in the same way as it was derived from the simulation. Last but not least, analyzing the optical response of piled-up neutrino events in ArgonCube, separated in time, would help to understand how well detached energy deposits can be localized in the detector, and how pile-up of the slow component of the scintillation light might affect such measurements.

Acknowledgements

A big thank you goes to my supervisor **Prof. Dr. Michele Weber**, director of LHEP, to whom I owe the possibility to have done my doctorate at the Laboratory for High Energy Physics. It was always very inspiring to talk about neutrino physics and to discuss latest results from neutrino experiments with you. Your availability to students and your commitment to LHEP in general was always outstanding.

A big thank you goes also to **Prof. Dr. Antonio Ereditato**, former director of LHEP, and second key person who made all of this possible. It was you who definitively awakened my passion for particle physics – especially neutrino physics – attending your courses during my undergraduate studies. You opened me the door to the particle physics world and I had the great experience to be a member of the world-class T2K Collaboration during my Master's already.

Thank you to **Prof. Dr. Christopher Marshall** for being my external examiner, for reading my PhD thesis and for giving me valuable input during my studies. And thank you to **Prof. Dr. Thomas Becher** for chairing my PhD defense.

A special thank you goes to **Dr. James Sinclair**, my mentor during my PhD, and to **Dr. Callum Wilkinson**, my mentor during my Master's. I've learned so much form you guys, not only what concerns physics but also how to enjoy life as an internationally committed physicist with all its pros and cons. It was always fun to spend time with you – during work, during the free time and while traveling – and you became great friends that I hope to meet again whenever and wherever after the completion of my PhD.

I want to express my greatest possible gratitude to my friends **Roman Berner**, **Thomas Mettler** and **Patrick Stähli**, all of whom already became a Doctor of Physics meanwhile – congratulation guys! We first met in 2012, nearly a decade ago, and spent so many hours together in the lecture rooms at the University of Bern. We learned together and we supported each other, but we also motivated each other, which I think is one of the main reasons why we all became great scientists. But also spending time with you while just bullshitting around, playing kicker or having a Guinness at Nelson Pub was always big fun that I never wanted to miss.

Thank you to **Prof. Dr. Igor Kreslo** and to **Dr. Francesco Piastra**, two very passionate and among the most productive physicists I have met during my time at the University of Bern. You always supported my work and a big piece of my success is owed to you. And thank you to **Dr. Yifan Chen**, you did an excellent job hosting the internal Neutrino Meeting, which was very valuable for everyone presenting his work. You were always ready to ask questions and gave a lot of input during discussions.

Ultimately, I want to say thank you to everyone that was a member of the **Liquid Argon Neutrino Group** during my time at LHEP, but was not personally mentioned above. Thank you to the **Mechanical Workshop**, thank you to the **Electronics**

Workshop and thank you to the **Secretariat** for your support. You were always very productive collaborators and it was always a pleasure to work with you.

Bibliography

[1] W. Pauli. 'Dear radioactive ladies and gentlemen'. In: *Phys. Today* 31N9 (1978), p. 27 (cit. on pp. 1, 5).

[2] H. Massey and N. Feather. 'James Chadwick. 20 October 1891 – 24 July 1974'. In: *Biographical Memoirs of Fellows of the Royal Society* 22 (1976), pp. 11–70. ISSN: 00804606. URL: http://www.jstor.org/stable/769732 (cit. on pp. 1, 5).

[3] J. Chadwick. 'The intensity distribution in the magnetic spectrum of beta particles from radium (B + C)'. In: *Verh. Phys. Gesell.* 16 (1914), pp. 383–391 (cit. on pp. 1, 5).

[4] E. Fermi. 'Versuch einer Theorie der β-Strahlen. I'. In: *Zeitschrift für Physik* 88.3 (Mar. 1934), pp. 161–177. ISSN: 0044-3328. DOI: 10.1007/BF01351864. URL: https://doi.org/10.1007/BF01351864 (cit. on pp. 1, 5).

[5] F. Reines et al. 'Detection of the Free Antineutrino'. In: *Phys. Rev.* 117 (1 Jan. 1960), pp. 159–173. DOI: 10.1103/PhysRev.117.159. URL: https://link.aps.org/doi/10.1103/PhysRev.117.159 (cit. on pp. 1, 6, 7).

[6] C. Giunti and C. W. Kim. *Fundamentals of Neutrino Physics and Astrophysics.* OCLC: 476241776. Oxford: Oxford University Press, UK, 2007. ISBN: 9780198508717 (cit. on pp. 1, 17, 18, 27).

[7] C. Giganti, S. Lavignac and M. Zito. 'Neutrino oscillations: The rise of the PMNS paradigm'. In: *Progress in Particle and Nuclear Physics* 98 (2018), pp. 1–54. ISSN: 0146-6410. DOI: https://doi.org/10.1016/j.ppnp.2017.10.001. URL: https://www.sciencedirect.com/science/article/pii/S014664101730087X (cit. on pp. 1, 15).

[8] B. Abi et al. 'Deep Underground Neutrino Experiment (DUNE), Far Detector Technical Design Report, Volume II DUNE Physics'. In: (Feb. 2020). arXiv: 2002.03005 [hep-ex] (cit. on pp. 1, 3, 36, 37, 41, 51–54).

[9] A. D. Sakharov. 'Violation of CP Invariance, C asymmetry, and baryon asymmetry of the universe'. In: *Sov. Phys. Usp.* 34.5 (1991), pp. 392–393. DOI: 10.1070/PU1991v034n05ABEH002497 (cit. on pp. 1, 8).

[10] P. Lipari. 'Introduction to neutrino physics'. In: (2003). DOI: 10.5170/CERN-2003-003.115. URL: http://cds.cern.ch/record/677618 (cit. on pp. 1, 2, 18, 21, 27–30).

[11] S. F. King. 'Neutrino mass and mixing in the seesaw playground'. In: *Nuclear Physics B* 908 (2016). Neutrino Oscillations: Celebrating the Nobel Prize in Physics 2015, pp. 456–466. ISSN: 0550-3213. DOI: https://doi.org/10.1016/j.nuclphysb.2015.12.015. URL: https://www.sciencedirect.com/science/article/pii/S0550321315004356 (cit. on pp. 2, 18, 19).

[12] B. Abi et al. 'Volume III. DUNE far detector technical coordination'. In: *Journal of Instrumentation* 15.08 (Aug. 2020), T08009–T08009. DOI: 10.1088/1748-0221/15/08/t08009. URL: https://doi.org/10.1088/1748-0221/15/08/t08009 (cit. on p. 2).

[13] K. Abe et al. 'The T2K experiment'. In: *Nuclear Instruments and Methods in Physics Research Section A: Accelerators, Spectrometers, Detectors and Associated Equipment* 659.1 (2011), pp. 106–135. ISSN: 0168-9002. DOI: https://doi.org/10.1016/j.nima.2011.06.067. URL: https://www.sciencedirect.com/science/article/pii/S0168900211011910 (cit. on pp. 2, 14).

[14] D. S. Ayres et al. 'The NOvA Technical Design Report'. In: (Oct. 2007). DOI: 10.2172/935497. URL: https://www.osti.gov/biblio/935497 (cit. on pp. 2, 14).

[15] I. Esteban et al. 'The fate of hints: updated global analysis of three-flavor neutrino oscillations'. In: *Journal of High Energy Physics* 2020.9 (Sept. 2020), p. 178. ISSN: 1029-8479. DOI: 10.1007/JHEP09(2020)178. URL: https://doi.org/10.1007/JHEP09(2020)178 (cit. on pp. 2, 14, 30, 31).

[16] F. Capozzi et al. 'Global constraints on absolute neutrino masses and their ordering'. In: *Phys. Rev. D* 95 (9 May 2017), p. 096014. DOI: 10.1103/PhysRevD.95.096014. URL: https://link.aps.org/doi/10.1103/PhysRevD.95.096014 (cit. on p. 2).

[17] G. Fogli et al. 'Global analysis of three-flavor neutrino masses and mixings'. In: *Progress in Particle and Nuclear Physics* 57.2 (2006), pp. 742–795. ISSN: 0146-6410. DOI: https://doi.org/10.1016/j.ppnp.2005.08.002. URL: https://www.sciencedirect.com/science/article/pii/S0146641005000980 (cit. on p. 2).

[18] E. Majorana. 'Teoria simmetrica dell'elettrone e del positrone'. In: *Il Nuovo Cimento (1924-1942)* 14.4 (Sept. 2008), p. 171. ISSN: 1827-6121. DOI: 10.1007/BF02961314. URL: https://doi.org/10.1007/BF02961314 (cit. on pp. 2, 16).

[19] M. Aker et al. 'Improved Upper Limit on the Neutrino Mass from a Direct Kinematic Method by KATRIN'. In: *Phys. Rev. Lett.* 123 (22 Nov. 2019), p. 221802. DOI: 10.1103/PhysRevLett.123.221802. URL: https://link.aps.org/doi/10.1103/PhysRevLett.123.221802 (cit. on p. 2).

[20] A. Loureiro et al. 'Upper Bound of Neutrino Masses from Combined Cosmological Observations and Particle Physics Experiments'. In: *Phys. Rev. Lett.* 123 (8 Aug. 2019), p. 081301. DOI: 10.1103/PhysRevLett.123.081301. URL: https://link.aps.org/doi/10.1103/PhysRevLett.123.081301 (cit. on p. 2).

[21] K. Abe et al. 'Hyper-Kamiokande Design Report'. In: (May 2018). arXiv: 1805.04163 [physics.ins-det] (cit. on pp. 2, 39, 40).

[22] B. Abi et al. 'Volume I. Introduction to DUNE'. In: *Journal of Instrumentation* 15.08 (Aug. 2020), T08008–T08008. DOI: 10.1088/1748-0221/15/08/t08008. URL: https://doi.org/10.1088/1748-0221/15/08/t08008 (cit. on pp. 2, 3, 36, 38, 40, 50).

[23] A. Abed Abud et al. 'Deep Underground Neutrino Experiment (DUNE) Near Detector Conceptual Design Report'. In: (Mar. 2021). arXiv: 2103.13910 [physics.ins-det] (cit. on pp. 3, 40, 44, 46–50, 54, 78, 99, 100, 108).

[24] D. Göldi. 'A Novel Liquid Argon Time Projection Chamber Detector: The Argon-Cube Concept'. PhD thesis. Bern U., 2018. DOI: 10.7892/boris.116931 (cit. on pp. 3, 44, 74).

[25] D. Dwyer et al. 'LArPix: demonstration of low-power 3D pixelated charge readout for liquid argon time projection chambers'. In: *Journal of Instrumentation* 13.10 (Oct. 2018), P10007–P10007. DOI: 10.1088/1748-0221/13/10/p10007. URL: https://doi.org/10.1088/1748-0221/13/10/p10007 (cit. on pp. 3, 81–83).

[26] J. Chadwick. 'Possible Existence of a Neutron'. In: *Nature* 129.3252 (Feb. 1932), pp. 312–312. ISSN: 1476-4687. DOI: 10.1038/129312a0. URL: https://doi.org/10.1038/129312a0 (cit. on p. 5).

[27] F. Perrin. 'Possibilité d'émission de particules neutres de masse intrinsèque nulle dans les radioactivités β'. In: *C. R. Acad. Sci. (Paris)* 197 (1933), pp. 1625–1627. URL: http://www.neo-classical-physics.info/uploads/3/4/3/6/34363841/perrin_-_neutrino.pdf (cit. on p. 5).

[28] H. BETHE and R. PEIERLS. 'The "Neutrino"'. In: *Nature* 133.3362 (Apr. 1934), pp. 532–532. ISSN: 1476-4687. DOI: 10.1038/133532a0. URL: https://doi.org/10.1038/133532a0 (cit. on p. 5).

[29] R. Davis. 'Attempt to Detect the Antineutrinos from a Nuclear Reactor by the $Cl^{37}(\overline{\nu}, e^-)A^{37}$ Reaction'. In: *Phys. Rev.* 97 (3 Feb. 1955), pp. 766–769. DOI: 10.1103/PhysRev.97.766. URL: https://link.aps.org/doi/10.1103/PhysRev.97.766 (cit. on p. 6).

[30] C. S. Wu et al. 'Experimental Test of Parity Conservation in Beta Decay'. In: *Phys. Rev.* 105 (4 Feb. 1957), pp. 1413–1415. DOI: 10.1103/PhysRev.105.1413. URL: https://link.aps.org/doi/10.1103/PhysRev.105.1413 (cit. on p. 6).

[31] M. Goldhaber, L. Grodzins and A. W. Sunyar. 'Helicity of Neutrinos'. In: *Phys. Rev.* 109 (3 Feb. 1958), pp. 1015–1017. DOI: 10.1103/PhysRev.109.1015. URL: https://link.aps.org/doi/10.1103/PhysRev.109.1015 (cit. on p. 6).

[32] G. Danby et al. 'Observation of High-Energy Neutrino Reactions and the Existence of Two Kinds of Neutrinos'. In: *Phys. Rev. Lett.* 9 (1 July 1962), pp. 36–44. DOI: 10.1103/PhysRevLett.9.36. URL: https://link.aps.org/doi/10.1103/PhysRevLett.9.36 (cit. on p. 7).

[33] R. Davis, D. S. Harmer and K. C. Hoffman. 'Search for Neutrinos from the Sun'. In: *Phys. Rev. Lett.* 20 (21 May 1968), pp. 1205–1209. DOI: 10.1103/PhysRevLett.20.1205. URL: https://link.aps.org/doi/10.1103/PhysRevLett.20.1205 (cit. on pp. 8, 9).

[34] B. T. Cleveland et al. 'Measurement of the Solar Electron Neutrino Flux with the Homestake Chlorine Detector'. In: *The Astrophysical Journal* 496.1 (Mar. 1998), pp. 505–526. DOI: 10.1086/305343. URL: https://doi.org/10.1086/305343 (cit. on pp. 8, 23).

[35] M. L. Perl et al. 'Evidence for Anomalous Lepton Production in $e^+ - e^-$ Annihilation'. In: *Phys. Rev. Lett.* 35 (22 Dec. 1975), pp. 1489–1492. DOI: 10.1103/PhysRevLett.35.1489. URL: https://link.aps.org/doi/10.1103/PhysRevLett.35.1489 (cit. on p. 8).

[36] M. L. Perl et al. 'Properties of the proposed τ charged lepton'. In: *Physics Letters B* 70.4 (Oct. 1977), pp. 487–490. ISSN: 0370-2693. DOI: https://doi.org/10.1016/0370-2693(77)90421-X. URL: https://www.sciencedirect.com/science/article/pii/037026937790421X (cit. on p. 8).

[37] K. S. Hirata et al. 'Experimental study of the atmospheric neutrino flux'. In: *Physics Letters B* 205.2 (Apr. 1988), pp. 416–420. ISSN: 0370-2693. DOI: https://doi.org/10.1016/0370-2693(88)91690-5. URL: https://www.sciencedirect.com/science/article/pii/0370269388916905 (cit. on p. 8).

[38] D. Casper et al. 'Measurement of atmospheric neutrino composition with the IMB-3 detector'. In: *Phys. Rev. Lett.* 66 (20 May 1991), pp. 2561–2564. DOI: 10.1103/PhysRevLett.66.2561. URL: https://link.aps.org/doi/10.1103/PhysRevLett.66.2561 (cit. on p. 8).

[39] L. Wan et al. 'Measurement of the neutrino-oxygen neutral-current quasielastic cross section using atmospheric neutrinos at Super-Kamiokande'. In: *Phys. Rev. D* 99 (3 Feb. 2019), p. 032005. DOI: 10.1103/PhysRevD.99.032005. URL: https://link.aps.org/doi/10.1103/PhysRevD.99.032005 (cit. on p. 10).

[40] K. S. Hirata et al. 'Real-time, directional measurement of ^{8}B solar neutrinos in the Kamiokande II detector'. In: *Phys. Rev. D* 44 (8 Oct. 1991), pp. 2241–2260. DOI: 10.1103/PhysRevD.44.2241. URL: https://link.aps.org/doi/10.1103/PhysRevD.44.2241 (cit. on p. 11).

[41] A. Blondel. 'The Number of Neutrinos and the Z Line Shape'. In: (2016). DOI: 10.1142/9789814733519_0008. URL: https://cds.cern.ch/record/2217139 (cit. on p. 11).

[42] Y. Fukuda et al. 'Measurement of a small atmospheric ν_μ/ν_e ratio'. In: *Physics Letters B* 433.1 (1998), pp. 9–18. ISSN: 0370-2693. DOI: https://doi.org/10.1016/S0370-2693(98)00476-6. URL: https://www.sciencedirect.com/science/article/pii/S0370269398004766 (cit. on p. 11).

[43] Y. Fukuda et al. 'Study of the atmospheric neutrino flux in the multi-GeV energy range'. In: *Physics Letters B* 436.1 (1998), pp. 33–41. ISSN: 0370-2693. DOI: https://doi.org/10.1016/S0370-2693(98)00876-4. URL: https://www.sciencedirect.com/science/article/pii/S0370269398008764 (cit. on p. 11).

[44] Z. Li et al. 'Measurement of the tau neutrino cross section in atmospheric neutrino oscillations with Super-Kamiokande'. In: *Phys. Rev. D* 98 (5 Sept. 2018), p. 052006. DOI: 10.1103/PhysRevD.98.052006. URL: https://link.aps.org/doi/10.1103/PhysRevD.98.052006 (cit. on p. 12).

[45] K. Kodama et al. 'Observation of tau neutrino interactions'. In: *Physics Letters B* 504.3 (2001), pp. 218–224. ISSN: 0370-2693. DOI: https://doi.org/10.1016/S0370-2693(01)00307-0. URL: https://www.sciencedirect.com/science/article/pii/S0370269301003070 (cit. on p. 12).

[46] Q. R. Ahmad et al. 'Direct Evidence for Neutrino Flavor Transformation from Neutral-Current Interactions in the Sudbury Neutrino Observatory'. In: *Phys. Rev. Lett.* 89 (1 June 2002), p. 011301. DOI: 10.1103/PhysRevLett.89.011301. URL: https://link.aps.org/doi/10.1103/PhysRevLett.89.011301 (cit. on p. 13).

[47] S. M. Bilenky. 'Bruno Pontecorvo and Neutrino Oscillations'. In: *Advances in High Energy Physics* 2013 (Sept. 2013), p. 873236. ISSN: 1687-7357. DOI: 10.1155/2013/873236. URL: https://doi.org/10.1155/2013/873236 (cit. on p. 12).

[48] S. Ahn et al. 'Detection of accelerator-produced neutrinos at a distance of 250 km'. In: *Physics Letters B* 511.2 (2001), pp. 178–184. ISSN: 0370-2693. DOI: https://doi.org/10.1016/S0370-2693(01)00647-5. URL: https://www.sciencedirect.com/science/article/pii/S0370269301006475 (cit. on p. 13).

[49] M. H. Ahn et al. 'Measurement of neutrino oscillation by the K2K experiment'. In: *Phys. Rev. D* 74 (7 Oct. 2006), p. 072003. DOI: 10.1103/PhysRevD.74.072003. URL: https://link.aps.org/doi/10.1103/PhysRevD.74.072003 (cit. on p. 13).

[50] A. Gando et al. 'Reactor on-off antineutrino measurement with KamLAND'. In: *Phys. Rev. D* 88 (3 Aug. 2013), p. 033001. DOI: 10.1103/PhysRevD.88.033001. URL: https://link.aps.org/doi/10.1103/PhysRevD.88.033001 (cit. on p. 13).

[51] D. G. Michael et al. 'Observation of Muon Neutrino Disappearance with the MINOS Detectors in the NuMI Neutrino Beam'. In: *Phys. Rev. Lett.* 97 (19 Nov. 2006), p. 191801. DOI: 10.1103/PhysRevLett.97.191801. URL: https://link.aps.org/doi/10.1103/PhysRevLett.97.191801 (cit. on p. 13).

[52] D. Adey et al. 'Measurement of the Electron Antineutrino Oscillation with 1958 Days of Operation at Daya Bay'. In: *Phys. Rev. Lett.* 121 (24 Dec. 2018), p. 241805. DOI: 10.1103/PhysRevLett.121.241805. URL: https://link.aps.org/doi/10.1103/PhysRevLett.121.241805 (cit. on p. 14).

[53] J. K. Ahn et al. 'RENO: An Experiment for Neutrino Oscillation Parameter θ_{13} Using Reactor Neutrinos at Yonggwang'. In: (Mar. 2010). arXiv: 1003.1391 [hep-ex] (cit. on p. 14).

[54] Y. Abe et al. 'Indication of Reactor $\overline{\nu}_e$ Disappearance in the Double Chooz Experiment'. In: *Phys. Rev. Lett.* 108 (13 Mar. 2012), p. 131801. DOI: 10.1103/PhysRevLett.108.131801. URL: https://link.aps.org/doi/10.1103/PhysRevLett.108.131801 (cit. on p. 14).

[55] R. Patterson. 'The NOvA experiment: status and outlook'. In: *Nuclear Physics B - Proceedings Supplements* 235-236 (2013). The XXV International Conference on Neutrino Physics and Astrophysics, pp. 151–157. ISSN: 0920-5632. DOI: https://doi.org/10.1016/j.nuclphysbps.2013.04.005. URL: https://www.sciencedirect.com/science/article/pii/S0920563213001266 (cit. on pp. 14, 25).

[56] K. Abe et al. 'Search for CP Violation in Neutrino and Antineutrino Oscillations by the T2K Experiment with 2.2×10^{21} Protons on Target'. In: *Phys. Rev. Lett.* 121 (17 Oct. 2018), p. 171802. DOI: 10.1103/PhysRevLett.121.171802. URL: https://link.aps.org/doi/10.1103/PhysRevLett.121.171802 (cit. on p. 14).

[57] K. Abe et al. 'Constraint on the matter–antimatter symmetry-violating phase in neutrino oscillations'. In: *Nature* 580.7803 (Apr. 2020), pp. 339–344. ISSN: 1476-4687. DOI: 10.1038/s41586-020-2177-0. URL: https://doi.org/10.1038/s41586-020-2177-0 (cit. on p. 14).

[58] K. Abe et al. 'Indication of Electron Neutrino Appearance from an Accelerator-Produced Off-Axis Muon Neutrino Beam'. In: *Phys. Rev. Lett.* 107 (4 July 2011), p. 041801. DOI: 10.1103/PhysRevLett.107.041801. URL: https://link.aps.org/doi/10.1103/PhysRevLett.107.041801 (cit. on p. 14).

[59] N. Agafonova et al. 'Discovery of τ Neutrino Appearance in the CNGS Neutrino Beam with the OPERA Experiment'. In: *Phys. Rev. Lett.* 115 (12 Sept. 2015), p. 121802. DOI: 10.1103/PhysRevLett.115.121802. URL: https://link.aps.org/doi/10.1103/PhysRevLett.115.121802 (cit. on p. 14).

[60] B. Pontecorvo. 'Inverse beta processes and nonconservation of lepton charge'. In: *Sov. Phys. JETP* 7 (1958), pp. 172–173. URL: http://www.jetp.ac.ru/files/pontecorvo1958_en.pdf (cit. on p. 15).

[61] Z. Maki, M. Nakagawa and S. Sakata. 'Remarks on the Unified Model of Elementary Particles'. In: *Progress of Theoretical Physics* 28.5 (Nov. 1962), pp. 870–880. ISSN: 0033-068X. DOI: 10.1143/PTP.28.870. eprint: https://academic.oup.com/ptp/article-pdf/28/5/870/5258750/28-5-870.pdf. URL: https://doi.org/10.1143/PTP.28.870 (cit. on p. 15).

[62] P. D. Group et al. 'Review of Particle Physics'. In: *Progress of Theoretical and Experimental Physics* 2020.8 (Aug. 2020). 083C01. ISSN: 2050-3911. DOI: 10.1093/ptep/ptaa104. eprint: https://academic.oup.com/ptep/article-pdf/2020/8/083C01/34673722/ptaa104.pdf. URL: https://doi.org/10.1093/ptep/ptaa104 (cit. on pp. 18, 60–62, 66, 76).

[63] J. N. Bahcall, M. H. Pinsonneault and S. Basu. 'Solar Models: Current Epoch and Time Dependences, Neutrinos, and Helioseismological Properties'. In: *The Astrophysical Journal* 555.2 (July 2001), pp. 990–1012. DOI: 10.1086/321493. URL: https://doi.org/10.1086/321493 (cit. on p. 23).

[64] A. Bellerive. 'Review of Solar Neutrino Experiments'. In: *Int. J. Mod. Phys. A* 19 (Dec. 2003), pp. 1167–1179. URL: https://cds.cern.ch/record/692828 (cit. on p. 23).

[65] N. G. Cooper. 'Los Alamos Science, Number 25 – 1997: Celebrating the neutrino'. In: (Dec. 1997). DOI: 10.2172/569122. URL: https://www.osti.gov/biblio/569122 (cit. on p. 24).

[66] F. P. An et al. 'Observation of Electron-Antineutrino Disappearance at Daya Bay'. In: *Phys. Rev. Lett.* 108 (17 Apr. 2012), p. 171803. DOI: 10.1103/PhysRevLett.108.171803. URL: https://link.aps.org/doi/10.1103/PhysRevLett.108.171803 (cit. on p. 25).

[67] J. J. Evans. 'The MINOS Experiment: Results and Prospects'. In: *Advances in High Energy Physics* 2013 (Nov. 2013), p. 182537. ISSN: 1687-7357. DOI: 10.1155/2013/182537. URL: https://doi.org/10.1155/2013/182537 (cit. on p. 25).

[68] P. A. Machado, O. Palamara and D. W. Schmitz. 'The Short-Baseline Neutrino Program at Fermilab'. In: *Annual Review of Nuclear and Particle Science* 69.1 (2019), pp. 363–387. DOI: 10.1146/annurev-nucl-101917-020949. eprint: https://doi.org/10.1146/annurev-nucl-101917-020949. URL: https://doi.org/10.1146/annurev-nucl-101917-020949 (cit. on p. 26).

[69] L. Wolfenstein. 'Neutrino oscillations in matter'. In: *Phys. Rev. D* 17 (9 May 1978), pp. 2369–2374. DOI: 10.1103/PhysRevD.17.2369. URL: https://link.aps.org/doi/10.1103/PhysRevD.17.2369 (cit. on pp. 27, 30).

[70] S. P. Mikheyev and A. Y. Smirnov. 'Resonant amplification of ν oscillations in matter and solar-neutrino spectroscopy'. In: *Il Nuovo Cimento C* 9.1 (Jan. 1986), pp. 17–26. ISSN: 0390-5551. DOI: 10.1007/BF02508049. URL: https://doi.org/10.1007/BF02508049 (cit. on p. 30).

[71] Hyper-Kamiokande. *Gallery : Hyper-Kamiokande*. http://www.hyper-k.org/en/gallery.html. Accessed: 2021.06.15 (cit. on p. 39).

[72] J-PARC Center. *The Hyper-Kamiokande project is officially approved.* http://www.j-parc.jp/c/en/topics/2020/02/12000416.html. Accessed: 2021.06.11. Feb. 2020 (cit. on p. 40).

[73] Fermi Research Alliance, LLC. *Neutrino beam.* https://lbnf-dune.fnal.gov/how-it-works/neutrino-beam/. Accessed: 2021.02.16 (cit. on pp. 41, 42).

[74] Fermi Research Alliance, LLC. *Construction begins on international mega-science experiment to understand neutrinos.* https://news.fnal.gov/2017/07/construction-begins-international-mega-science-experiment-understand-neutrinos/. Accessed: 2021.06.15 (cit. on p. 41).

[75] J. Strait et al. 'Long-Baseline Neutrino Facility (LBNF) and Deep Underground Neutrino Experiment (DUNE): Conceptual Design Report, Volume 3: Long-Baseline Neutrino Facility for DUNE June 24, 2015'. In: (Jan. 2016). arXiv: 1601.05823 [physics.ins-det] (cit. on pp. 42–44, 122).

[76] F. Matichard. 'ND I&I Overview'. DUNE Collaboration Meeting. May 2021. URL: https://indico.fnal.gov/event/46503/contributions/215447/ (cit. on p. 45).

[77] K. Abe et al. 'T2K ND280 Upgrade - Technical Design Report'. In: (Jan. 2019). arXiv: 1901.03750 [physics.ins-det] (cit. on p. 48).

[78] R. Acciarri et al. 'Long-Baseline Neutrino Facility (LBNF) and Deep Underground Neutrino Experiment (DUNE): Conceptual Design Report, Volume 2: The Physics Program for DUNE at LBNF'. In: (Dec. 2015). arXiv: 1512.06148 [physics.ins-det] (cit. on p. 51).

[79] B. Povh et al. *Particles and Nuclei: An Introduction to the Physical Concepts.* Springer, 2008 (cit. on p. 56).

[80] W. R. Leo. *Techniques for nuclear and particle physics experiments: a how-to approach.* Springer, 1994 (cit. on pp. 58, 59, 61, 62, 64, 66, 67).

[81] C. W. Fabjan and T. Ludlam. 'Calorimetry in High-Energy Physics'. In: *Annual Review of Nuclear and Particle Science* 32.1 (Dec. 1982), pp. 335–389. ISSN: 0163-8998. DOI: 10.1146/annurev.ns.32.120182.002003. URL: https://doi.org/10.1146/annurev.ns.32.120182.002003 (cit. on p. 66).

[82] Los Alamos National Security, LLC. *ENDF/B-VII.1 Incident-Neutron Data.* https://t2.lanl.gov/nis/data/endf/endfvii.1-n-pdf/ar40.pdf. Accessed: 2021.09.22. Dec. 2011 (cit. on p. 68).

[83] J. N. Marx and D. R. Nygren. 'The Time Projection Chamber'. In: *Phys. Today* 31N10 (1978), pp. 46–53. DOI: 10.1063/1.2994775 (cit. on p. 69).

[84] R. Berner et al. 'First Operation of a Resistive Shell Liquid Argon Time Projection Chamber: A New Approach to Electric-Field Shaping'. In: *Instruments* 3.2 (2019). ISSN: 2410-390X. DOI: 10.3390/instruments3020028. URL: https://www.mdpi.com/2410-390X/3/2/28 (cit. on pp. 69, 86, 88).

[85] W. Willis and V. Radeka. 'Liquid-argon ionization chambers as total-absorption detectors'. In: *Nuclear Instruments and Methods* 120.2 (1974), pp. 221–236. ISSN: 0029-554X. DOI: https://doi.org/10.1016/0029-554X(74)90039-1. URL: https://www.sciencedirect.com/science/article/pii/0029554X74900391 (cit. on p. 70).

[86] C. Rubbia. *The liquid-argon time projection chamber: a new concept for neutrino detectors*. Tech. rep. Geneva: CERN, 1977. URL: https://cds.cern.ch/record/117852 (cit. on p. 70).

[87] Brookhaven National Lab. *Liquid Argon Properties (Tables and Calculators)*. https://lar.bnl.gov/properties/. Accessed: 2021.07.01. Jan. 2021 (cit. on p. 71).

[88] N. E. Holden et al. 'IUPAC Periodic Table of the Elements and Isotopes (IPTEI) for the Education Community (IUPAC Technical Report)'. In: *Pure and Applied Chemistry* 90.12 (2018), pp. 1833–2092. DOI: doi:10.1515/pac-2015-0703. URL: https://doi.org/10.1515/pac-2015-0703 (cit. on p. 70).

[89] T. Yang. 'Calibration of Calorimetric Measurement in a Liquid Argon Time Projection Chamber'. In: *Instruments* 5.1 (2021). ISSN: 2410-390X. DOI: 10.3390/instruments5010002. URL: https://www.mdpi.com/2410-390X/5/1/2 (cit. on pp. 72, 153).

[90] B. Jones. 'Introduction to Scintillation Light in Liquid Argon'. LArTPC R&D Workshop, Fermilab. July 2014. URL: http://microboone-exp.fnal.gov/public/talks/LArTPCWorkshopScintLight_bjpjone_2014.pdf (cit. on p. 73).

[91] M. Auger et al. 'A Concept for the Fourth DUNE Far Detector Module'. DUNE-doc-10419-v2. 2018. URL: https://docs.dunescience.org/cgi-bin/private/ShowDocument?docid=10419&asof=2019-11-1 (cit. on p. 78).

[92] J. Asaadi et al. 'A pixelated charge readout for Liquid Argon Time Projection Chambers'. In: *Journal of Instrumentation* 13.02 (Feb. 2018), pp. C02008–C02008. DOI: 10.1088/1748-0221/13/02/c02008. URL: https://doi.org/10.1088/1748-0221/13/02/c02008 (cit. on p. 79).

[93] G. De Geronimo et al. 'Front-End ASIC for a Liquid Argon TPC'. In: *IEEE Transactions on Nuclear Science* 58.3 (2011), pp. 1376–1385. DOI: 10.1109/TNS.2011.2127487 (cit. on p. 79).

[94] J. Asaadi et al. 'First Demonstration of a Pixelated Charge Readout for Single-Phase Liquid Argon Time Projection Chambers'. In: *Instruments* 4.1 (2020), p. 9. DOI: 10.3390/instruments4010009. arXiv: 1801.08884 [physics.ins-det] (cit. on pp. 79, 80).

[95] C. Grace et al. 'A 32-Channel ASIC for the Readout of Pixelated Liquid Argon Time Projection Chambers'. In: *2018 IEEE Nuclear Science Symposium and Medical Imaging Conference Proceedings (NSS/MIC)*. 2018, pp. 1–3. DOI: 10.1109/NSSMIC.2018.8824340 (cit. on p. 79).

[96] M. Kuźniak and A. M. Szelc. 'Wavelength Shifters for Applications in Liquid Argon Detectors'. In: *Instruments* 5.1 (2021). ISSN: 2410-390X. DOI: 10.3390/instruments5010004. URL: https://www.mdpi.com/2410-390X/5/1/4 (cit. on p. 83).

[97] M. Auger et al. 'ArCLight—A Compact Dielectric Large-Area Photon Detector'. In: *Instruments* 2.1 (2018), p. 3. DOI: 10.3390/instruments2010003. arXiv: 1711.11409 [physics.ins-det] (cit. on p. 83).

[98] L. Calivers. 'Development and Characterisation of a Novel Light Detector: ArCLight'. PhD thesis. Bern U., 2021 (cit. on pp. 83, 84, 86).

[99] N. Anfimov et al. 'Development of the Light Collection Module for the Liquid Argon Time Projection Chamber (LArTPC)'. In: *JINST* 15.07 (2020), p. C07022. DOI: 10.1088/1748-0221/15/07/C07022 (cit. on pp. 83, 86).

[100] B. Abi et al. 'Volume IV. The DUNE far detector single-phase technology'. In: *Journal of Instrumentation* 15.08 (Aug. 2020), T08010–T08010. DOI: 10.1088/1748-0221/15/08/t08010. URL: https://doi.org/10.1088/1748-0221/15/08/t08010 (cit. on p. 86).

[101] F. Drielsma. 'ND-LAr Demonstrator High Voltage System'. DUNE Collaboration Meeting. Sept. 2020. URL: https://indico.fnal.gov/event/22617/contributions/198002/attachments/135025/167288/20200924_demonstrator_hv_dune.pdf (cit. on pp. 86, 87).

[102] S. A. Kharusi et al. 'nEXO Pre-Conceptual Design Report'. In: (May 2018). arXiv: 1805.11142 [physics.ins-det] (cit. on p. 89).

[103] A. Mastbaum. 'ND-LAr Simulation and Analysis Update'. DUNE Collaboration Meeting. May 2021. URL: https://indico.fnal.gov/event/46503/contributions/215714/attachments/143224/181095/20210519_nd-lar-sw.pdf (cit. on pp. 95, 96).

[104] A. Lambert. 'ND LAr Design Status'. DUNE Collaboration Meeting. Sept. 2020. URL: https://indico.fnal.gov/event/22617/contributions/197623/attachments/135024/167286/DUNE_CM_09242020_v2.pptx (cit. on p. 98).

[105] M. Auger et al. 'ProtoDUNE-ND: proposal to place the ArgonCube 2x2 Demonstrator on-axis in NuMI'. DUNE-doc-12571-v1. Jan. 2019. URL: https://docs.dunescience.org/cgi-bin/private/ShowDocument?docid=12571 (cit. on pp. 102–104).

[106] G. H. Lee, Y. Chang and T.-J. Kim. '2 - Properties and possible application areas'. In: *Ultrasmall Lanthanide Oxide Nanoparticles for Biomedical Imaging and Therapy*. Ed. by G. H. Lee, Y. Chang and T.-J. Kim. Woodhead Publishing, 2014, pp. 15–28. ISBN: 978-0-08-100066-3. DOI: https://doi.org/10.1533/9780081000694.15. URL: https://www.sciencedirect.com/science/article/pii/B9780081000663500024 (cit. on p. 123).

[107] D. Schultz et al. 'The K-shell Auger electron spectrum of gadolinium obtained using neutron capture in a solid state device'. In: *Journal of Physics D: Applied Physics* 43.7 (Feb. 2010), p. 075502. DOI: 10.1088/0022-3727/43/7/075502. URL: https://doi.org/10.1088/0022-3727/43/7/075502 (cit. on p. 123).

[108] M. Tanabashi et al. 'Review of Particle Physics'. In: *Phys. Rev. D* 98 (3 Aug. 2018), p. 030001. DOI: 10.1103/PhysRevD.98.030001. URL: https://link.aps.org/doi/10.1103/PhysRevD.98.030001 (cit. on p. 123).

[109] J. Wang. 'Pulsed Neutron Source for Liquid Argon TPC Calibration'. Workshop on Calibration and Reconstruction for LArTPC Detectors, Fermilab. Dec. 2018. URL: https://indico.fnal.gov/event/18523/contributions/47916/attachments/29843/36746/20181210_Pulsed_Neutron_Source-compressed.pdf (cit. on p. 124).

[110] T. M. Collaboration. 'MeV-scale Physics in MicroBooNE'. MICROBOONE-NOTE 1076-PUB. 2020. URL: https://microboone.fnal.gov/wp-content/uploads/MICROBOONE-NOTE-1076-PUB.pdf (cit. on p. 130).

[111] B. Bhandari et al. 'First Measurement of the Total Neutron Cross Section on Argon between 100 and 800 MeV'. In: *Phys. Rev. Lett.* 123 (4 July 2019), p. 042502. DOI: 10.1103/PhysRevLett.123.042502. URL: https://link.aps.org/doi/10.1103/PhysRevLett.123.042502 (cit. on p. 138).

[112] H. Zhang. 'Neutron tagging and its application to physics in Super-Kamiokande IV'. In: *32nd International Cosmic Ray Conference*. Vol. 4. 2011, p. 71. DOI: 10.7529/ICRC2011/V04/0353 (cit. on p. 163).

[113] V. Fischer and A. Weinstein. 'ANNIE: Neutron multiplicity in neutrino interactions and new technologies'. In: *Journal of Physics: Conference Series* 1468 (Feb. 2020), p. 012226. DOI: 10.1088/1742-6596/1468/1/012226. URL: https://doi.org/10.1088/1742-6596/1468/1/012226 (cit. on p. 163).

A. Optical Simulation

A.1. ArgonCube 2x2 Demonstrator GDML

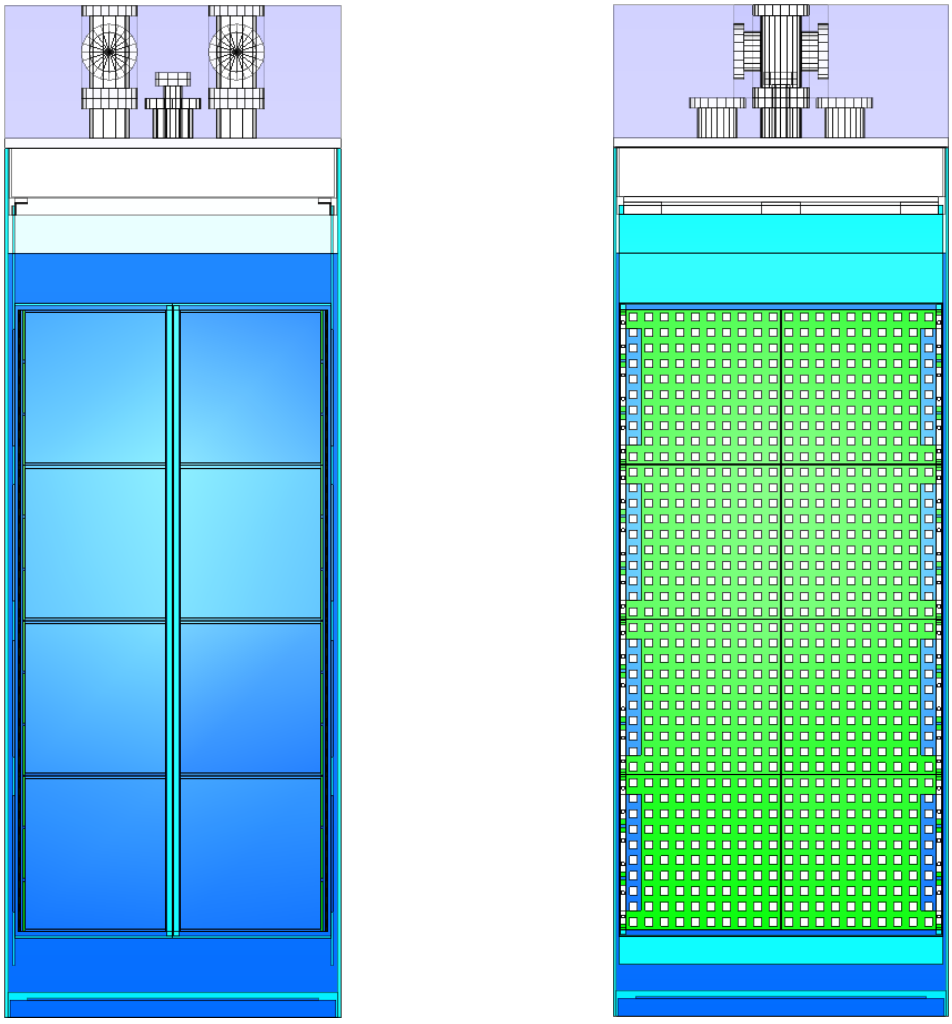

(a) **(b)**

Figure A.1.: A side-view of the ArgonCube 2×2 Module GDML, showing the details of the light-readout plane (a) and the pixelated charge-readout plane (b).

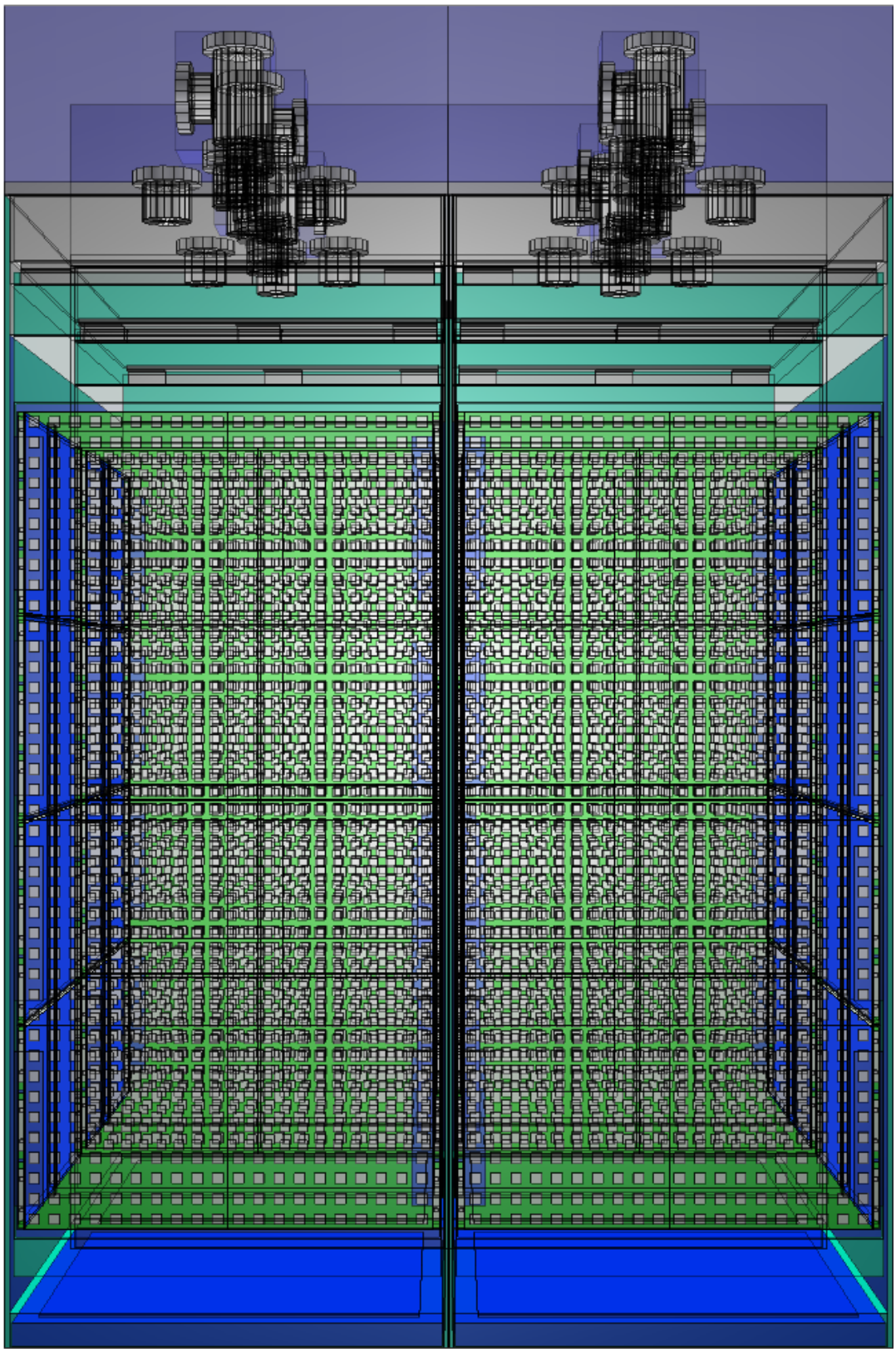

Figure A.2.: A perspective side-view of the ArgonCube 2×2 Demonstrator GDML

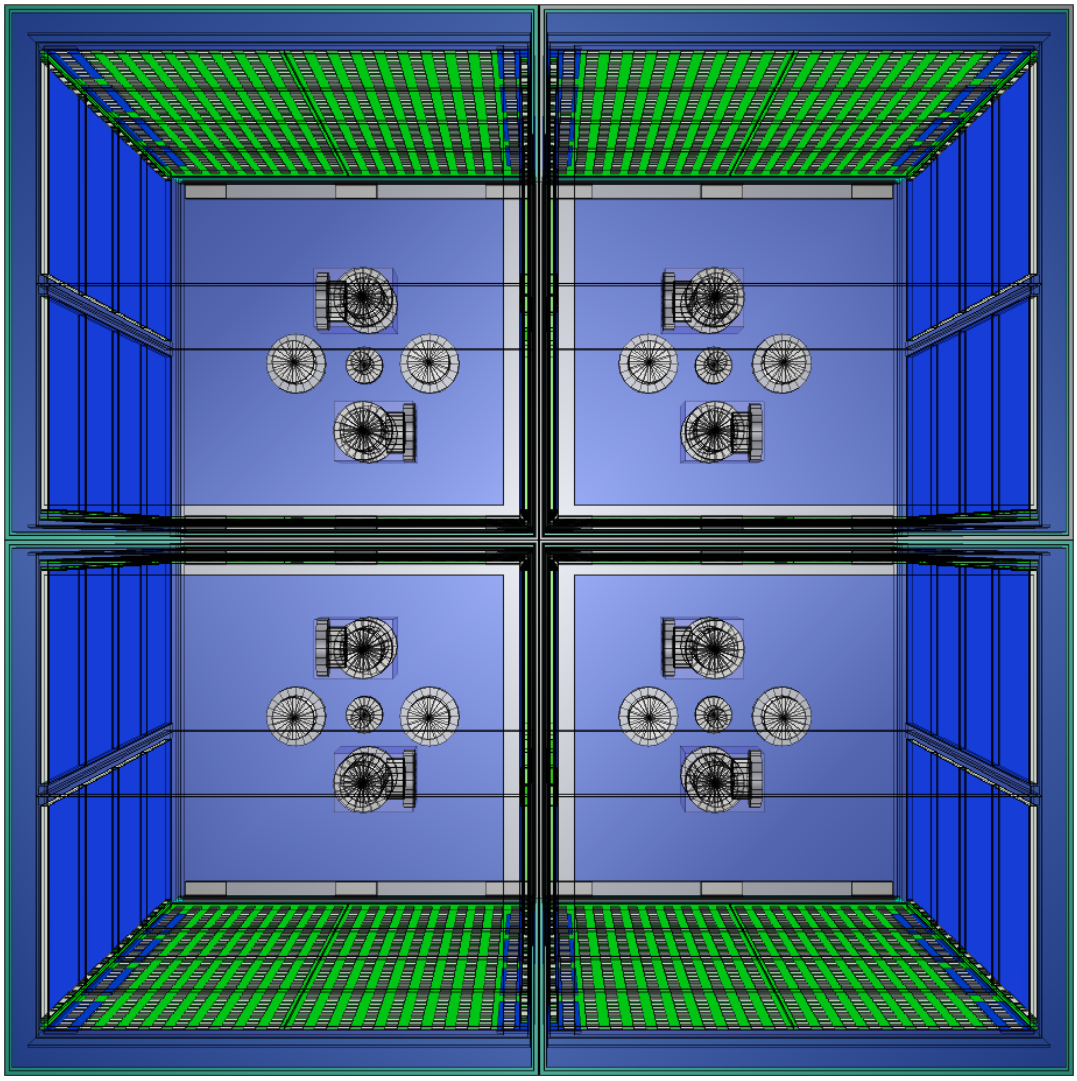

Figure A.3.: A perspective top-view of the ArgonCube 2×2 Demonstrator GDML

A.2. Photon Look-up-Table

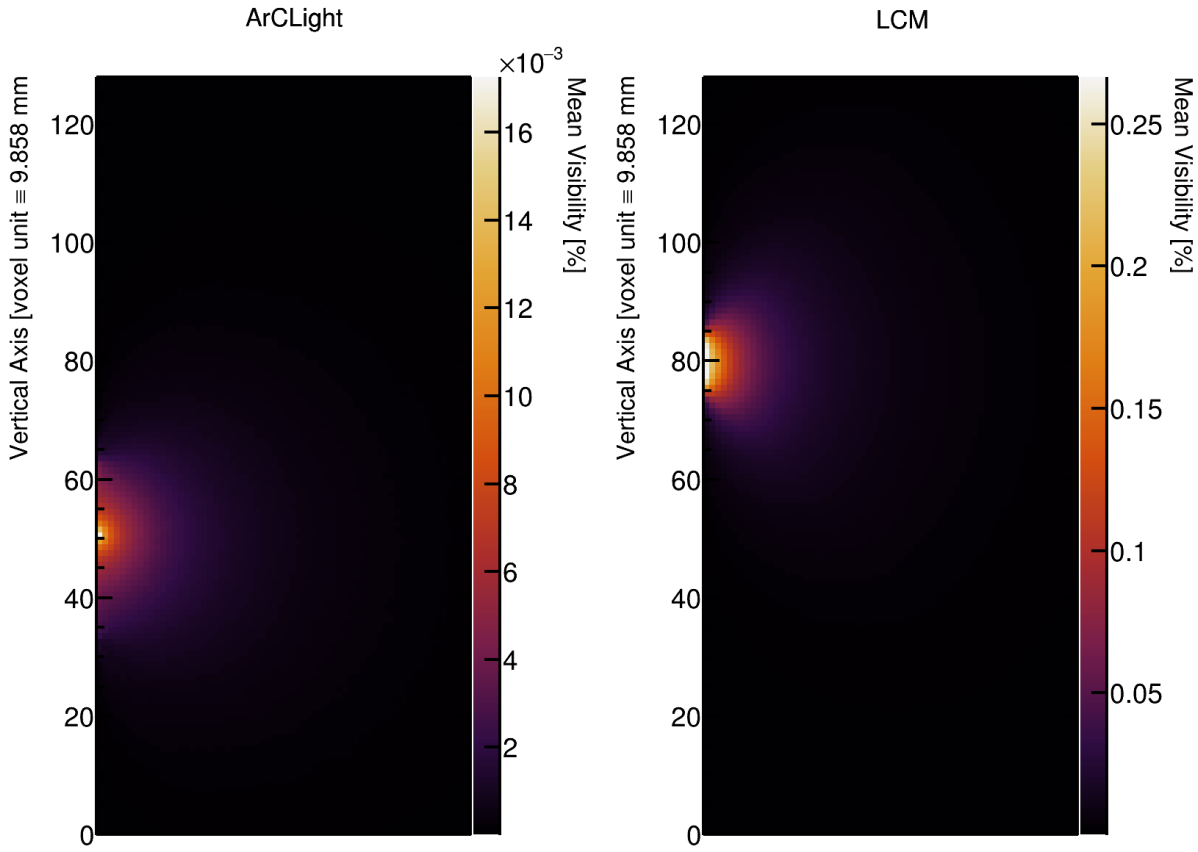

Figure A.4.: 2D-projection of the visibility onto the plane perpendicular to the drift axis, for one ArCLight SiPM (left) and a pair of coupled LCM SiPMs (right).

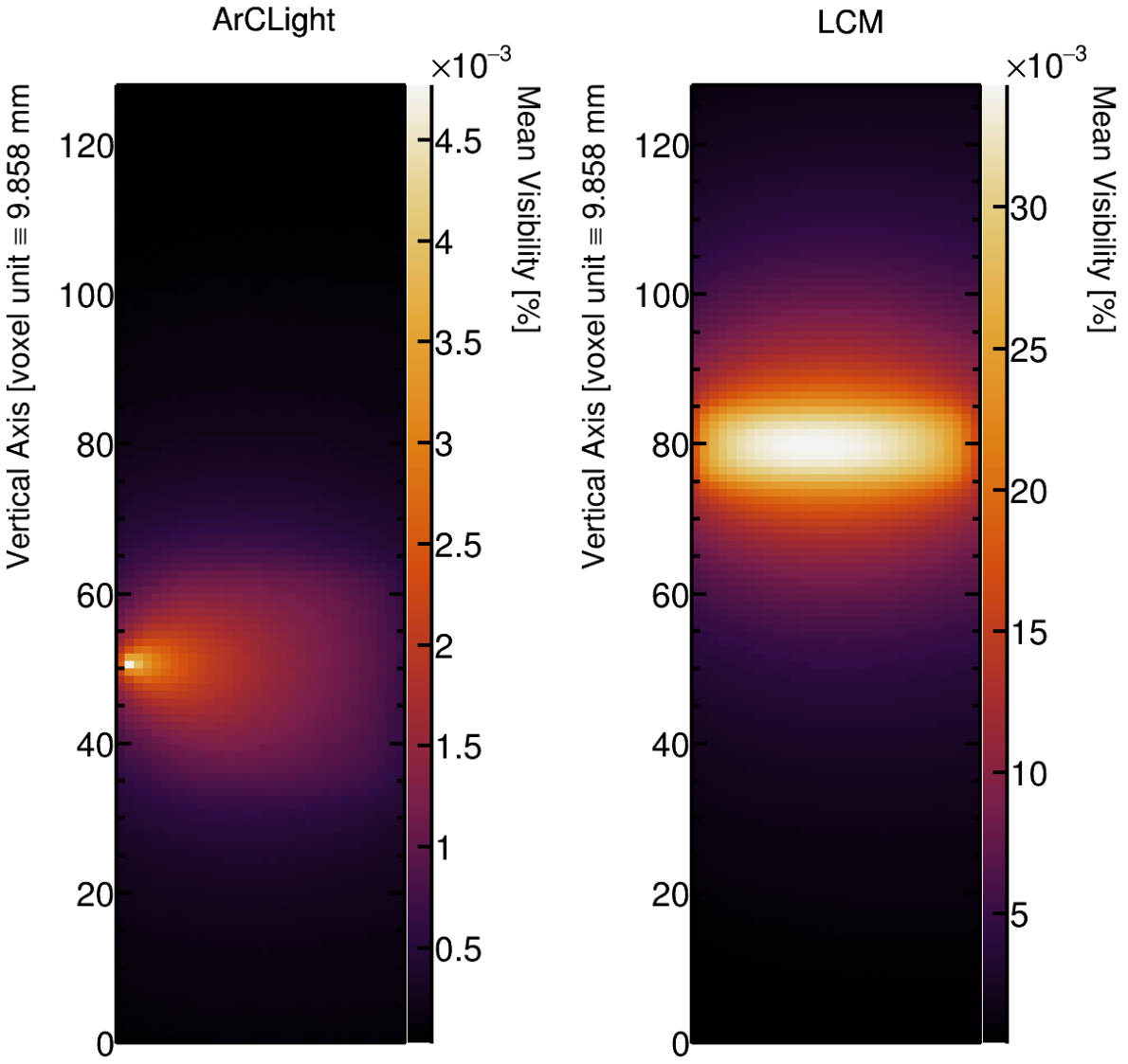

Figure A.5.: 2D-projection of the visibility onto the plane perpendicular to the beam axis, for one ArCLight SiPM (left) and for a pair of coupled LCM SiPMs (right). The visibility outlines the shapes of the light-readout tiles.

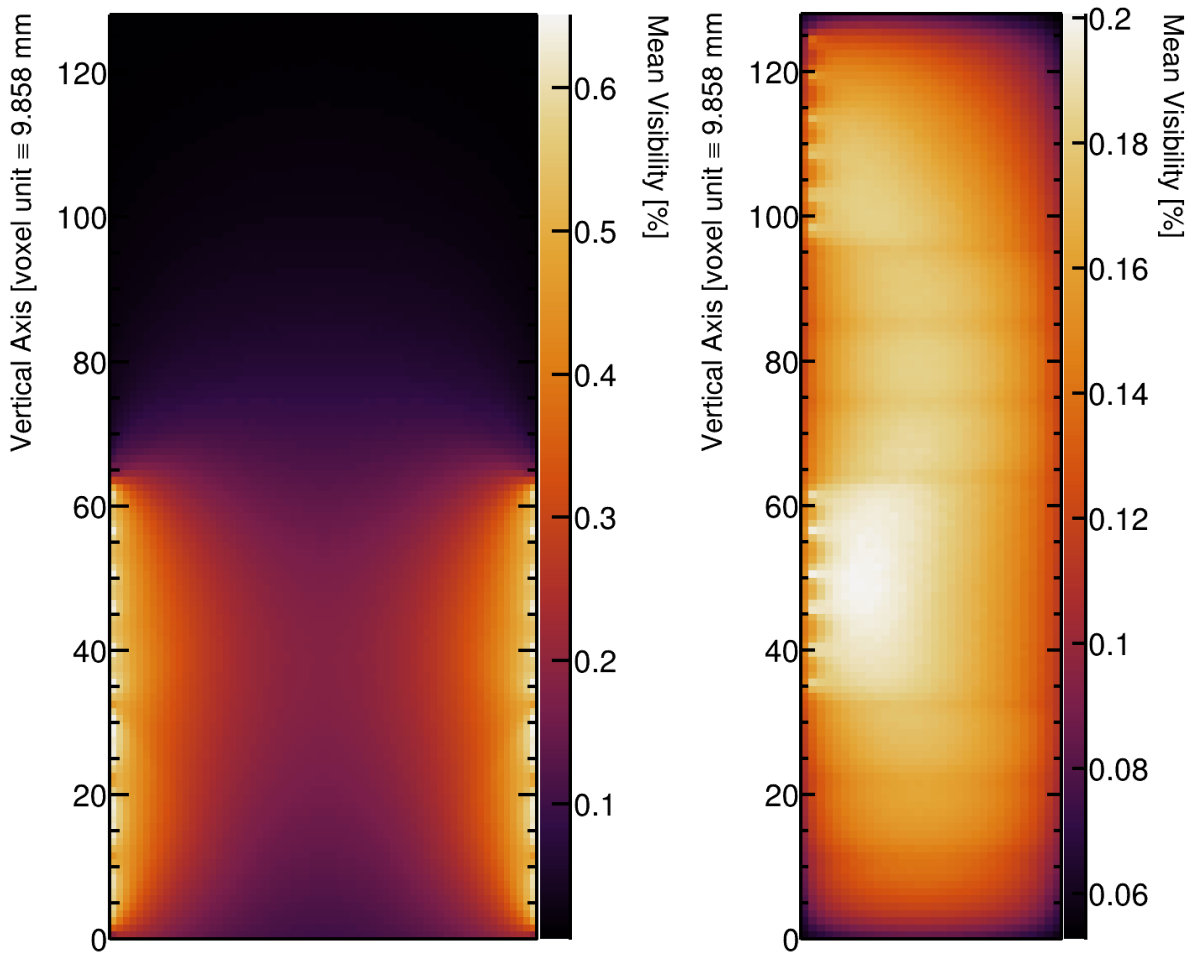

Figure A.6.: 2D-projections of the combined visibility of multiple SiPMs. The combined visibility of all SiPMs placed in the bottom half of the module, projected onto the plane perpendicular to the beam axis, is shown on the left. The combined visibility of all SiPMs of a light-readout plane, projected onto the plane perpendicular to the drift axis, is shown on the right.

A.3. LUT/Data Comparison

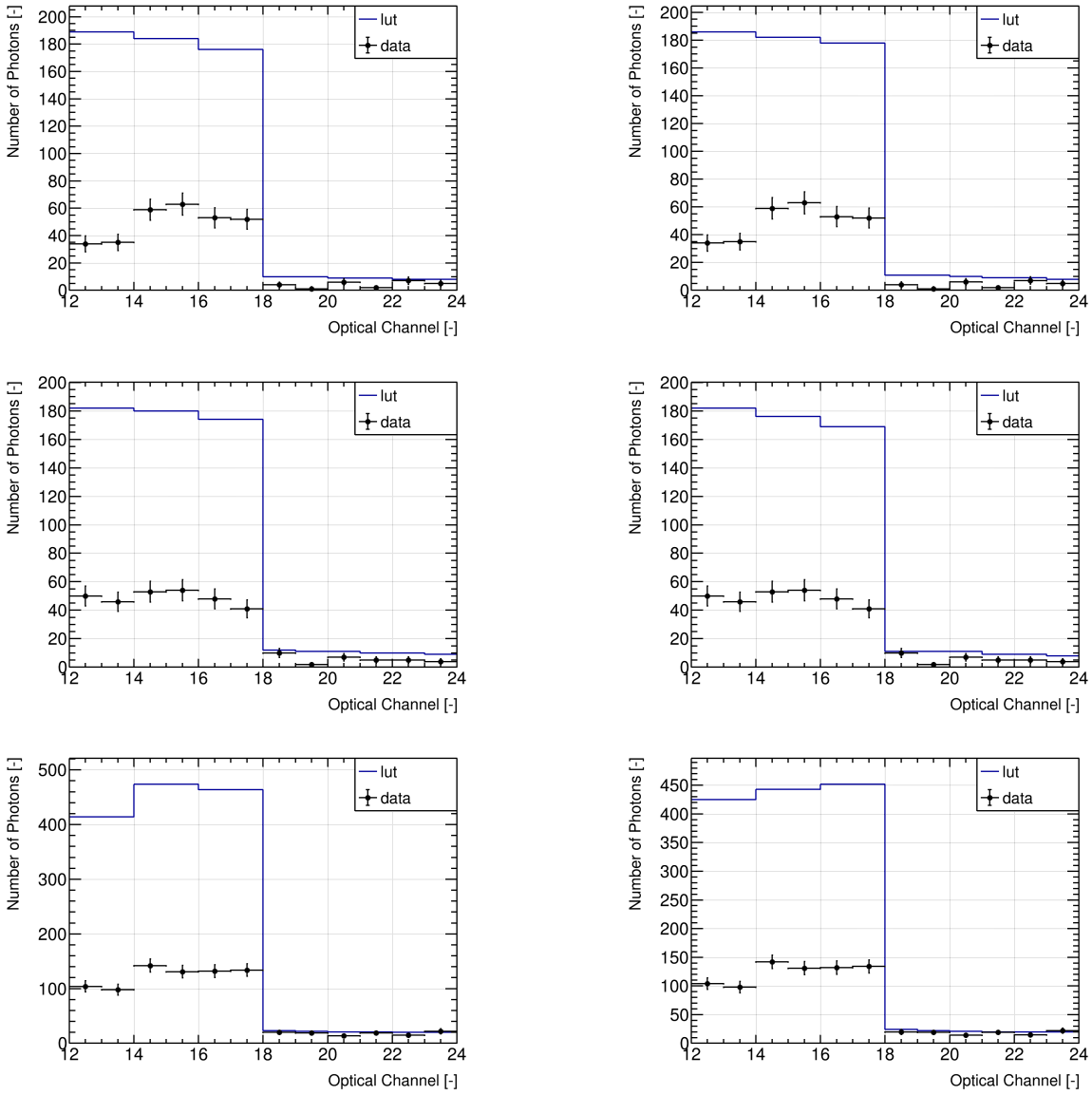

Figure A.7.: Comparison between the simulated and measured light response in the partially instrumented Module0 prototype. The number of photons arriving at the SiPMs is shown for one LCM tile – optical channels 12-17, and one ArCLight tile – optical channels 18-23. The comparison is shown for three through-going (entering at the top and exiting at the bottom of the TPC) cosmic-muon tracks (rows), using both the 2912-voxels LUT (left) and the 262 144-voxels LUT (right). The light yield was calculated using the Birks' model: 25 236 photon/cm @ 0.5 kV cm^{-1}. The error bars represent the statistical uncertainty.